Charles University
Faculty of Science
Department of Physical and Macromolecular chemistry

Macromolecular Chemistry

MSc. Roberto Fernandez Alvarez

Design nanostruktur založených na klastrových sloučeninách bóru ve vodných roztocích
Design of boron cluster-containing nanostructures in solution

Doctoral Thesis

Supervisor: doc. RNDr. Pavel Matějíček, Ph.D.
Advisor: Ing. Mariusz Uchman, Ph.D.

Prague 2020

Acknowledgments

I want to acknowledge the countless people who helped me finish this thesis either directly or indirectly. I cannot possibly name you all, but I will try.

A special acknowledgment to my supervisor, prof. Pavel Matějíček, for putting your trust in me and giving me the opportunity to start this journey. Your continued support and lightheartedness when discussing science made it possible for me to approach you for advice whenever it was needed.

I would also like to thank my advisor, Mariusz Uchman, for his sincere advice and stern corrections to help me improve not only my publications but my way of doing science.

I would also like to acknowledge the help of the Soft-Matter group for the discussions which made me improve the understanding on my own research. Specifically, to Mirek Štepanek for taking the time to answer virtually any question I ever asked him on complex experimental techniques with detail and patience. Further, many thanks to Zdeněk Tošner for always receiving my NMR samples with a smile and being open to new NMR experiments no matter how uncertain the chances of success were.

I would like to thank the whole B Team, both present and past. Vlado, Eva, David, Jianwei and Somdeb, our fun and insightful talks about scientific (and non-scientific) problems in the lab showed me a great example of how collaboration among colleagues should look like. A special mention to Vlado for helping me navigate the Czech world in my early days and for his continued support despite leaving the lab. And to Jianwei, thank you for always having a kind word to say, innumerable stories about Chinese culture and for your constant push to make our science better and more impactful.

I would like to acknowledge Carlos Vieira for taking much more time than he should have to correct my publications, and for teaching me the proper ways of scientific writing along the process. Without your lessons the writing quality in this thesis would be many levels below what is shown here.

My sincere gratitude to my family, Jorge, Norma, Jose Pablo and Alejandra, for their life-long support and affection and for making me feel at home once a week despite being so far away.

Lastly, to my wife, Zlatica, for her support and motivation. Thank you for making me believe that there is always a chance and that is worth fighting for it.

Abstract

The main objective of this thesis is the study of boron cluster compounds in solution, their interaction with polymers and the formation of nanostructures. Most of the work was focused around cobalt bis(dicarbollide) (COSAN) but the incorporation of carborane into polymers was also studied. The idea was to close the knowledge gap around the way COSAN aggregates and continue the line of the laboratory in leading this topic. Therefore, we performed in-depth analysis of isothermal titration calorimetry curves to determine the aggregation number at concentrations around the critical micellar concentration (CMC). Thus, the aggregation number obtained was an improvement over previous data obtained a much higher concentration. The use of acetonitrile as a cosolvent in the micellization process helped formulate a model describing how C-H bonds in the COSAN micelles are directed towards the inside of the micelle. Furthermore, COSAN was used as a model drug for loading nanocarriers composed of hydrophobic core and charged corona. The importance of this work relies on the creation of guidelines for drug loading into similar polymeric vectors in order to determine how the nanocarrier will be affected. With the help of coarse-grained simulations, we determined that changes in the hydrophobicity of the loaded drug will have a deep impact on the solubility of the nanocarrier. Notably, a slight increase in hydrophobicity of loaded drug triggers the collapse of polymer chains in the corona therefore limiting the loading capacity of such systems. Lastly, a triblock terpolymer containing carboranes was used to determine the effect of such clusters in the self-assembly. To determine the direct effect of carborane a diblock copolymer was synthesized with the exact composition as the terpolymer minus the short carborane block. The carborane block allowed for terpolymer to self-assemble either as worms or spherical micelles depending on the solvent mixture, whereas the diblock was only capable of forming spherical micelles. Furthermore, the terpolymer micelles worked as a dual stimuli responsive system to F^- ions and pH change. The changes were tracked via fluorescence with pH working as an ON/OFF switch for the fluorescence of the micelles.

Abstrakt

Náplní této disertační práce bylo studium roztokového chování klastrových sloučenin bóru a jejich interakce s polymery, s důrazem na pochopení zákonitostí vedoucích k tvorbě příslušných nano-struktur. Kromě polymerního systému obsahujícího o-karboran, byl výzkum zaměřen zejména na chování kobalt bis(dikarbollidového) aniontu (COSAN). Hlavní myšlenkou bylo pochopit některé dosud nejasné aspekty micelizace COSANu v souladu s dlouhodobými badatelskými plány v naší skupině. Z toho důvodu byla provedena detailní kalorimetrická studie, která umožnila kromě dalších termodynamických parametrů stanovit hodnotu agregačního čísla solí COSANu při koncentracích blízkých kritické micelární koncentrace (KMK), což je obtížně dostupné pomocí jiných experimentálních technik. Použití acetonitrilu jako příměsi ve vodném roztoku COSANu se ukázalo jako velmi účinný prostředek pro získání alespoň přibližné představy o vnitřní struktuře micel COSANu, což je z experimentálního hlediska jinak velmi obtížné. Z provedených fyzikálně chemických experimentů plyne, že C-H skupiny COSANu pravděpodobně směřují dovnitř nano-agregátů. Dále byla studována solubilizace COSANu v micelách s hydrofobním jádrem a polyelektrolytovou slupkou, kde byl použit COSAN jako modelové léčivo kombinující elektrostatický náboj s hydrofobním charakterem. Význam tohoto projektu spočívá v predikci základních scénářů chování polymerních nosičů léčiv s ohledem na jejich vnitřní strukturu a morfologii, což má značný vliv na jejich stabilitu a množství solubilizovaného modelového léčiva. Posledním projektem bylo studium nanočástic tvořených trojblokovým terpolymerem s obsahem výrazně hydrofobního o-karboranu. Cílem bylo objasnit vliv karboranového bloku na vznik a vnitřní strukturu studovaných polymerních částic, přičemž bylo porovnáno chování amfifilního dvojblokového kopolymeru bez karboranu a trojblokového terpolymeru s karboranovým blokem. Studie prokázala, že zatímco dvojblokový systém vytváří kulovité nanočástice, může vést přítomnost silně hydrofobního karboranového bloku ke vzniku cylindrických micel. Vznik karboranových domén uvnitř těchto micel však nebyl prokázán. Poměrně nečekanou vlastností těchto nanostruktur však je zdvojená citlivost na vnější podněty. Jednak to je vliv pH na náboj poly(4-hydroxystyrenu) a pak zejména reakce F- iontů s o-karboranovými jednotkami, která má vliv na náboj uvnitř těchto nanočástic a také na jejich fotofyzikální chování. To umožňuje přepínání fluorescence micel ze stavů vypnuto/zapnuto.

Declaration

I declare that I have written this thesis on my own. If already published results are used, they are included in the list of references. I agree with lending the thesis to anyone who may be interested. This thesis is not substantially the same as any work that has been or is being submitted to any other university for any degree, diploma or any other qualification.

Prague, 02.10.2020

....

Signature

Prohlášení

Prohlašuji, že jsem závěrečnou práci zpracoval samostatně a že jsem uvedl všechny použité informační zdroje a literaturu. Tato práce ani její podstatná část nebyla předložena k získání jiného nebo stejného akademického titulu.

V Praze, 02. 10. 2020

….………………………………..

Podpis

Workload Distribution

Student Roberto Fernandez Alvarez (RFA) performed most physical chemistry characterization techniques as well as the analysis of such. RFA participated in figure preparation and manuscript preparation in each of the publications. In detail, for Publication I and II: all sample preparations, the measurements of ITC and ionic conductivity. In Publication III: NMR measurement and interpretation, self-assembly of nanoparticles, fluorescence, design of dual-stimuli responsive system, SAXS interpretation and DLS. Finally, in Publication IV:

In Publication II Medoš Ž. and Bešter-Rogač M. designed the model equation for COSAN micellization, Hervø-Hansen S. and Lund M. conducted all atomic molecular dynamics simulations; Tošner Z. measured NMR and Zhigunov A. measured and analyzed SAXS data. Rodzeń K. and Strachota A. synthesized the polymers for Publication III. Cabrera-González J. and Núñez R. synthesized the carborane containing monomer for Publication III. Hlavatovičová, E. assisted with fluoresecence and self-assembly experiments for Publication III. Kereïche, S. measured cryo-TEM for Publication III and IV. Nová L., Uhlík F., and Košovan P. performed coarse grain simulations for Publication IV.

Matějíček, P. and Uchman, M. contributed with design of experiments, writing of publications and overal guidance towards the completition of this thesis.

…………………………………….

Supervisor‘s Signature

Table of Contents

Acknowledgments iii

Abstract iv

Table of Contents viii

List of abbreviations x

Preface xii

1- Theoretical Background 1

  1.1- General information about boron clusters 1

    1.1.1- Aromaticity of boron clusters 4

    1.1.2- Redox characteristics 6

    1.1.3- Solution behavior 8

  1.2- Modifications to the boron cluster framework. 14

    1.2.1- Modifying the cluster framework 14

    1.2.2- Applications 19

  1.3- Incorporation into polymers 22

    1.3.1- Polymers with boron clusters as pendant groups 22

    1.3.2- Polymers with carboranes in the main chain 23

  1.4- Future perspectives 24

  References 25

2- Experimental section 29

  2.1- Main characterization methods 29

    2.1.1- Light Scattering (DLS, SLS) 29

    2.1.2- Nuclear Magnetic Resonance (NMR) spectroscopy 31

    2.1.3- Isothermal Titration Calorimetry (ITC) 33

    References 34

  2.2- Experimental Set up 35

    2.2.1- NMR 35

    2.2.2- SAXS 35

    2.2.3- Fluorescence 36

    2.2.4- TEM (cryo) 36

    2.2.5- Conductometry 37

    2.2.6- Electrophoretic light Scattering 37

    2.2.7- Isothermal titration calorimetry 37

3- Research aims 38

4- Results 39

4.1- Publication I..40
4.2- Publication II...72
4.3- Publication III 112
4.4- Publication IV 140
5-Summary and general conclusions 175

List of abbreviations

2c–2e	Two-center, two-electron
3c–2e	Three-center, two-electron
ABCCs	Anionic Boron Cluster Compounds
AFM	Atomic force microscopy
AIBN	Azobisisobutyronitrile
BNCT	Boron neutron capture therapy
CAC	Critical aggregation concentration
CMC	Critical micelle concentration
COSAN	Cobalt sandwich
Cryo-TEM	Cryogenic transmission electron microscopy
DHB	Dihydrogen bond
DLS	Dynamic light scattering
DOSY	Diffusion-ordered spectroscopy
ESI-MS	Electrospray ionization mass spectroscopy
TFA	Trifluoroacetic acid
GPC	Gel permeation chromatography
HPLC	High-performance liquid chromatography
ITC	Isothermal titration calorimetry
LS	Light scattering
MD	Molecular Dynamics
MS	Mass spectrometry
NMR	Nuclear magnetic resonance
NICS	Nucleus independent chemical shifts
P2VP	Poly(2-vinylpyridine)
PEO	Poly(ethylene oxide)
PSEPT	Polyhedral skeletal electron pair theory
RAFT	Reversible Addition-Fragmentation chain-Transfer polymerization
SANS	Small-angle neutron scattering
SAXS	Small-angle X-ray scattering
SDS	Sodium dodecyl sulfate
SEP	Skeletal electron pairs
SLS	Static light scattering
SI	Supporting information
ss-NMR	Solid-state nuclear magnetic resonance
THF	Tetrahydrofuran
UV-Vis	Ultraviolet–visible
WAXS	Wide-angle X-ray scattering

Preface

The search for new materials and new technologies is what pushes humanity ever forward, in this search a series of sequential steps are necessary. First, through fundamental research researchers describe the properties and interactions of a particular molecule or group of molecules. Second, this knowledge is used to attempt to solve current problems and limitations of existing technologies. Lastly, a third step involves transforming the proofs of concept into tangible technological advances. The second step requires a large exercise of creativity and imagination. The researcher not only needs to be acutely aware of the properties of his specific system but also to have a broad enough view of current technologies. Therefore, this step is not always accomplished or even attempted., this will depend on many other outside factors that have to do little with science. The third step might be the hardest one. Not only a substantial improvement on current technology is needed but it should be done for a reasonable price. It is the job of researchers to undergo the first two steps repeatedly and as often possible in order to carry on a handful of projects into the third step. It must be noted that the various steps might be stretched through decades, or even done by multiple research groups who might or might not communicate with one another.

This dissertation deals mainly with the first step of the above-mentioned process. Nonetheless the second step was always “kept in mind” and some work done during the completion of this PhD dealt with the proof of concept necessary in the second step. Unfortunately, such work could not be completed in time but has initiated the process towards the final step.

1- Theoretical Background

1.1- General information about boron clusters

Neutral boranes were first synthesized in 1912 but this water and air sensitive compounds were not suitable for further development.[1] Anionic boranes are much more stable and were later synthesized by Hawthorne and Pitochelli in 1960. Their major stability has given them greater importance until becoming the key building blocks in nanochemistry that they are today (further mention of boranes will refer to anionic boranes). Boranes result from the catenation of boron, which is part of the selective few elements (also S, C and Si) capable of forming bond of the same elements into chains. The catenation of boron often results in 3 dimensional deltahedra (polyhedrons with regular triangular faces) as opposed to carbon and silicon which form almost exclusively chains. These structures, commonly known as boron clusters, follow the formula $B_nH_n^{2-}$ with n values going from 5 to 12. (Figure 1.1)

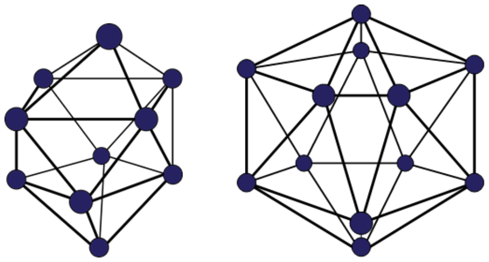

Figure 1.1. Selected example of boranes with formula $B_nH_n^{2-}$ for n = 10,12.

As one of the first major challenges, boron chemists had to develop the correct way of determining the structure of boron clusters from their chemical formula. Boron clusters are composed of a mixture of classical 2c-2e bonds (two centers-two electrons) and the less common 3c-2e bonds (three centers-three electrons). The later occurs when a molecule has more atomic orbitals than bonding electrons. This has led to equivocally labelling boranes as "electron deficient" structures, which contradicts the high stability observed in some of them (specially $B_6H_6^{-2}$, $B_{10}H_{10}^{-2}$, $B_{12}H_{12}^{-2}$). On the one hand, 2c-2e bonds are formed when 2 atoms provide 2 atomic orbitals which form 1 bonding orbital and 1 antibonding orbital. On the other hand, 3c-2e are formed when the atomic orbitals of 3 different atoms interact to form 1 bonding orbital and 2 antibonding orbitals. As a way of correctly predicting the structure of boranes Lipscomb proposed the topological model.[2–4] It describes the distribution of 2c-2e and 3c-2e bonds in boron clusters. In short: (i) all B-H bonds are 2c-2e, (ii) orbitals used are the 1s orbital of H and four sp^3 orbitals of B, (iii) the B-H-B 3c-2e bridge bonds are formed by electrons filling the bonding orbital formed by 1s from H and $1sp^3$ orbital from each B (iv) orbitals and electrons of B atoms are first allocated to B-H bonds and B-H-B bridges, remaining ones are used as skeletal molecular orbitals to construct the clusters framework. These rules laid the framework to properly predict cluster structure based on the chemical formula.

Later, a set of principles were formulated by Wade to successfully predict the shape of deltahedron boron clusters. The system is based around the number of skeletal electron pairs (SEP) and molecular orbitals. These principles or rules are officially known as Polyhedral Skeletal Electron Pair Theory (PSEPT) but commonly referred to as the Wade-Mingos rules. The more general rules are summarized as follows: (i) each vertex is considered a building block of the clusters which contributes a certain number of SEP. SEP are defined as the electrons used for cage bonding. As an example, a unit like B-H has four valence electrons, two of which are used for B-H bond formation and the remaining ones are used for framework bonds. Therefore B-H is considered as a 2 SEP donor. Electrons that are use in exo-cluster bonding (B-H, C-H bonds e.g.) are not participating in the cage bonding, the same is true for electrons in non-bonding orbitals. (ii) The structure of the cluster is derived from the number of SEP after counting all participating groups. A *closo*-cluster will have n vertex with n = SEP - 1. The molecular orbital are n+1, where there is a unique hybrid *sp* orbital at the center of the cluster formed from the overlap of sp^z orbitals from each vertex. (iii) The removal of a vertex from a deltahedron does not change the number of skeletal bonding molecular orbitals. The last rule is especially important when predicting architecture of *nido* and *arachno* compounds, which are deltahedron with one or two vertexes removed respectively (Figure 1.2).

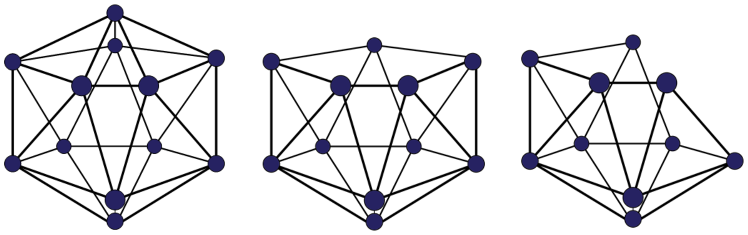

Figure 1.2. $B_{12}H_{12}^{2-}$ borane with its *closo, nido* and *arachno* form.

Boron clusters are not exclusively composed of B-H bonds. Namely, the substitution of a B-H group for a C-H group in the cluster produces a carborane. Their structures and existence were first predicted by Lipscomb and Hoffmann[5–7] and they follow the formula $C_nB_mH_{n+m}^{n-2}$. Twelve vertex mono-carboranes ($CB_{11}H_{12}^-$) and dicarboranes ($C_2B_{10}H_{12}$) are the most studied due to their stability, facile synthesis and versatile functionalization. Carbon atoms are located at the least connected vertex of the cluster. Dicarboranes can have several possible isomers, the relative position of C-H towards each other it leads to *orto*, meta or *para* isomer (Figure 1.3).Carboranes have a more variated chemistry than boranes in account of their acidic C-H bonds which can be functionalized using common organic chemistry. For example, by the sequential addition of *n*-butyllithium and an electrophile a new group can be introduced into the C atoms (see Chapter 1.2). These clusters still share many of the characteristics of boranes and their structure can be predicted by the Wade-Mingos rules with C-H is a 3 SEP donor.

Carboranes undergo the loss of a B-H group in a process known as deboronation, in the case of $C_2B_{10}H_{12}$ it loses a B-H to produce a *nido* cluster known as dicarbollide ($C_2B_9H_{11}^{2-}$). After deboronation, a flat face is formed where the B-H group is formed. The atoms at the flat face have the same hybridization as flat polygonal systems (e.g. benzene, cyclopentadienyl), meanwhile atoms at the interior retain the normal hybridization of cluster compounds. This characteristic hybridization at the flat face allows this *nido* compounds to act as ligands and form complexes with transition metals. (Figure 1.4)

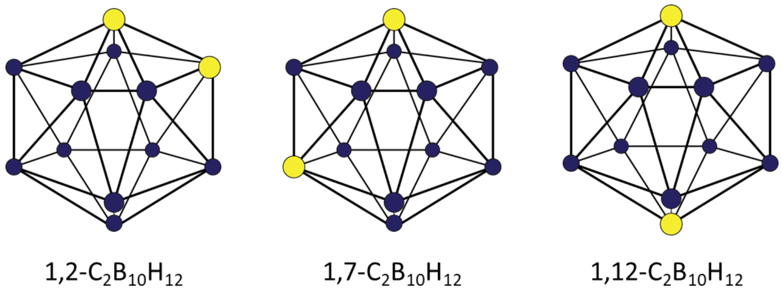

Figure 1.3. Chemical structure of dicarboranes isomers (from left to right) *orto*, *meta* and *para*.

One or two dicarbollide ligands can complex a transition metal forming a metallacarboranes (strict labelling would be *endo*-metallacarboranes but will be further referred to only as metallacarboranes). They were first synthesized by Hawthorne et al. in 1967.[8] Dicarbollide acts as a η^5 ligand and is isolobal with cyclopentadienyl ligands. Several metals have been complexed this way (e.g: Cr, Fe, Cu, Co) with complexes including one or two dicarbollides. Of special interest are bis-dicarbollide compounds. These complexes have a structural resemblance to metallocenes (e.g ferrocene) although dicarbollide-metal bonds have a higher covalent character than cyclopentadienyl-metal which results in a much stronger bond and stability of the formed complex. Out of these, the most studied one is the cobalt bisdicarbollide complex commonly known as COSAN (CObalt SANdwich). Bisdicarbollide compounds are obtainable with 7,8-$C_2B_9H_{11}^{2-}$, and 7,9-$C_2B_9H_{11}^{2-}$ but has not been observed for the 2,9-$C_2B_9H_{11}^{2-}$ (obtained from deboronation of *para*-dicarborane). Metal insertion is possible with both the presence or absence of the bridging proton on the planar C_2B_3 face of *nido* species. Despite not being highly researched bisdicarbollide species formed with the 7,9-$C_2B_9H_{11}^{2-}$ isomer are the most stable.

Bisdicarbollide compounds formed with 7,8-$C_2B_9H_{11}^{2-}$ ligand can form different isomers (rotamers) depending on the relative position of the C-H bonds across the B10-B10' axis (Figure 1.4). Namely, bisdicarbollide compounds form *cisoid, gauche* and *transoid* isomers. It should be noted that B-H and C-H bonds at the C2B3 face are not coplanar. Instead, there is a 50°C angle deviation from planarity which causes an impediment for free rotation and creates the three above mentioned rotamers.[9] Extensive studies about the energy profile of the different rotamers of COSAN have been conducted, mainly using ab initio and density-functional methods. Nonetheless, which rotamer is the most stable is still debated and depends on the environment of the molecule.

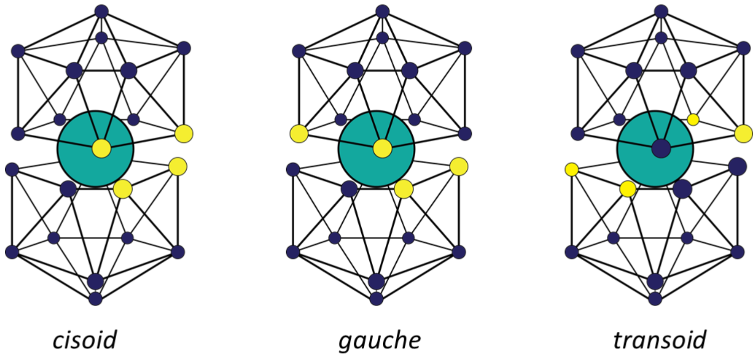

Figure 1.4. Depiction of the three rotamer configurations of metallacarboranes.

Quantum chemical calculations for *in vacuo* show the *trans*oid rotamer as the most stable followed by the *gauche* with almost the same energy. The energy difference between *transoid* and *cisoid* rotamers is only 11 kJ/mol.[10] Meanwhile, the results for solid state are confusing. At times, crystal structures show more than one conformation and both purely *transoid* and *cisoid* crystals have been reported. Ultimately, the larger amount of reported *cisoid* crystalline structures (90% in the Cambridge Crystallographic Data Center) indicates it has a larger stability in the solid state. Furthermore, the formation of intermolecular C-H···H-B bonds stabilizes the *cisoid* rotamer and is absent in the *transoid* conformation.[11] In aqueous state, there is still not a clear answer about the rotamer distribution or if this changes once the COSAN molecules self-assemble. DFT calculations in implicit water solvent show the cisoid conformation as the most stable by 8.36 kJ mol^{-1}. Furthermore, around 86% of COSAN molecules are present in this conformation at room temperature.[12]

A key aspect of metallacarboranes is the possibility to alter the oxidation state of the sandwiched metal in a reversible way. This has found multiple applications from redox catalysis to solar cells. Furthermore, Hawthorne described how the reduction from Ni^{IV} to Ni^{III} causes a transition from *cis* to *trans* configuration of the dicarbollide ligands. [13] This kind of control over molecular configuration inspired research around metallacarboranes as nanomachines. Therefore, a lot of effort has been made to modulate the redox potential of metallacarboranes mainly by careful halogenation of B-H bonds. This sequential process can modulate the redox potential of COSAN ($[Co(C_2B_9H_9)_2]^-$) from -1.51 V to -0.52 V after 9 halogenations $[Co(C_2B_9Cl_9)_2]^-$ (see Chapter 1.1.2).

1.1.1- Aromaticity of boron clusters

Closo-Borohydrides and carboranes have unusually high stability due to their aromaticity. Many studies in the early years of boron clusters were centered around the idea of aromaticity despite being far from the molecules usually recognized as aromatic (flat, conjugated double bonds, hydrocarbons). Boron clusters have three-dimensional aromaticity and it was first theorized by Lipscomb et al. in 1959 in account of the high stability and benzene-like reactivity of boranes.[14] A graph-theory model analogous to Huckel's method for conjugated hydrocarbons was first used by King to interpret three-dimensional delocalization in the clusters.[15] Pioneering calculations by Aihara sorted the anionic boranes $B_nH_n^{2-}$ ($5 \leq n \leq 12$) in order of aromaticity. In his work resonance energies were calculated with another graph-theory method. Aihara determined that for $B_nH_n^{2-}$ compounds the aromaticity criteria was met for n ≤ 6-12 and that n = 4-5 were not aromatic. In contrast, Schleyer and King claimed $B_5H_5^{2-}$ is indeed an aromatic compound by using different parameters to define aromaticity.[16]

In the cases of carboranes, they have been termed as superaromatic compounds. Their stabilization trend mirrors that of boranes, that is, stabilization increases with cluster size. Albeit the trend is more predictable than in boranes. Notably, when the reaction energy of clusters is plotted against cluster size an almost linear correlation is obtained. Deviations from this trend are the biggest for $B_nH_n^{2-}$, smaller for $CB_nH_{n+1}^{-}$ and the smallest for $C_2B_nH_{n+2}$. In contrast with two-dimensional aromaticity where delocalization occurs over unhybridized *p* orbitals in three-dimensional aromaticity electrons are delocalized over *sp* hybrid orbitals. Each vertex of the clusters has a *sp* orbital directed towards the inner part of the cluster, the overlap of this orbitals is how electron delocalization occurs in the cluster.

Closo-boranes of the kind $B_nH_n^{2-}$ with n≥ 13-17 are known as supraicosahedral clusters. It was previously mentioned that stability of clusters increases with size, this fact is in direct contradiction with the lack of synthetic strategies to obtain n≥ 13 clusters. Theoretical approaches have determined that their structure is aromatic and, in some cases (n = 16,17), their formation energy is more favorable than $B_{12}H_{12}^{2-}$. Lipscomb calculations still show $B_{12}H_{12}^{2-}$ as the most stable cluster but shows high stability and aromaticity for supraicosahedral clusters. An explanation for this is that the high energetic stability of $B_{12}H_{12}^{2-}$ acts as an energy sink when attempting the synthesis of larger clusters.

Experimental demonstrations of three-dimensional aromaticity are rarely mentioned in contemporary literature, but it is necessary to revisit the methods to fully understand the discussion about aromaticity. The main experimental methods are magnetic susceptibility exaltation (Λ), nucleus independent chemical shifts (NICS), and bond length difference. First, Λ is a measure of the difference between calculated and experimental magnetic susceptibility. Aromatic molecules have higher experimental values than the calculated values. Thus, negative Λ values indicate aromaticity. Values of Λ increase not only with aromaticity but with surface area and size. Therefore, larger clusters will have large values and not necessarily reflect an increase in aromaticity. Nonetheless, Λ is a good criterion to adjudicate aromaticity or antiaromaticity. Second, NICS shows the magnetic environment at a desired point in the molecule. For boron clusters the center of the cluster is always used. Negative values of NICS indicate a diatropic magnetic field. Third, a small bond length difference indicates length uniformity among the bonds. Small values (0-0.05 nm) are typical of aromatic molecules. In summary, the trends of stability and aromaticity do not exactly match when comparing the different methods. On the one hand, magnetic susceptibility exaltation and calculation of ΔH of formation indicate an almost linear increase in stability and aromaticity with increase in cluster size. On the other hand, NICS and bond length show a non-linear trend with increasing cluster size. Uniquely, various degrees of aromaticity are seen with $B_6H_6^{2-}$ and $B_{12}H_{12}^{2-}$ showing notable aromaticity above the other clusters. Even though aromaticity does not always correlate with stability[17] (especially true for carborane isomers where topological factors need to be considered in stability), it seems the results from NICS and bond length measurements are more in line with the observed stability. Notably, NICS is currently the most used experimental method for determination of (anti)aromaticity.[18]

Chemist have tried all along to relate the structure of boron clusters to their corresponding aromatic hydrocarbon counterparts. Contribution to the theory were made by Teixidor group a special analogy between 2D hydrocarbon aromatic compounds and how to "convert" these into 3D aromatic borohydrides.[19]

1.1.2- Redox characteristics

The redox stability of boron clusters has been widely studied (boranes, carboranes and metallacarboranes) and it has become key knowledge for their application into various processes. Nuñez et al. recollected electrochemical information about boron clusters and normalized the redox potential to the Fc/Fc^+ reference.[20] Similarly to organic molecules, boron clusters redox potential is greatly impacted by substituents both in C and B atoms. In Figure 1.5 a visual guide on the oxidation/reduction of different boron cluster shows the difference between them and the general effect substituents can have on them depending on the nature of the substituent and the substituted atoms (C or B).

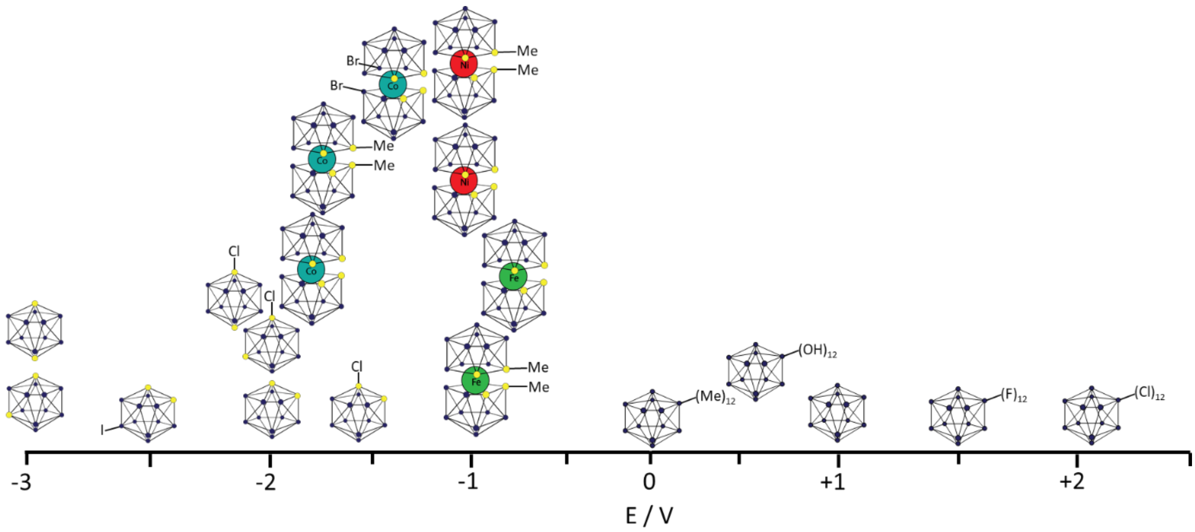

Figure 1.5. Reduction potential of boranes, carboranes, metallacarboranes and their derivatives. All values are reference to Fe^{III}/Fe^{II} pair. In all cases only the first oxidation/reduction is depicted. For metallacarboranes all values refer to the M^{III}/M^{II} change. Data obtained from reference[21].

The redox process can be pictured as a molecule in solution encountering an electrode, their relative energy levels will determine whether the molecule undergoes reduction or oxidation. Briefly, in order to reduce a molecule, the energy of electrodes needs to be higher (more negative potentials) than the potential energy of molecular orbital of the analyte so electrons can “jump” to the analyte. Whereas, decreasing the potential energy of the electrode (positive potentials) creates an energetically favorable environment for electrons to flow from the analyte to the electrode, thus oxidizing the analyte.

In the case of boranes, dodecaborate is the most studied cluster. It is irreversibly oxidized to $[B_{24}H_{23}]^{3-}$ at E=+1.05 V which consist of two $B_{12}H_{11}$ clusters joined by a H atom. On the other hand, the reduction of $[B_{12}H_{12}]^{2-}$ has never been observed. The use of electron donating substituents on $[B_{12}H_{12}]^{2-}$ produces reversible redox pairs, thus improving the usefulness of electrochemical applications of $[B_{12}H_{12}]^{2-}$. The persubstitution ($[B_{12}Y_{12}]^{2-}$) leads to reversible 1 and 2 e^- oxidations. Depending on the substituent the products of oxidation are stable radical and neutral species, respectively. Their stability is ascribed to electron donating effect of Y groups and the steric encumbrance that originates from a persubstituted cluster. Furthermore, the addition of halogen groups makes oxidation more difficult (more positive potential) whereas the addition of hydroxy groups facilitates it (more negative potential).[22]

In the same way that reduction of $[B_{12}H_{12}]^{2-}$ has never been observed there is no evidence of reduction of $[CB_{11}H_{12}]^-$ either. Conversely, oxidation on $C_2B_{10}H_{12}$ has not yet been registered for any of its isomers (1,2-,1.7-, and 1,12- $C_2B_{10}H_{12}$). It seems the addition of a carbon atoms to the clusters improves their resistance to oxidation. Oxidation in monocarboranes depends heavily on the substituents. For example, only highly methylated monocarboranes undergo oxidation and the process is reversible only in cases where the antipodal B(12) is substituted. On the other hand, reduction of dicarboranes always occur as a 2 e$^-$ process. The electron can be added in sequential matter or in one step. In general, bulky substituents in the C will give reduction resistance to the cluster and dividing the reduction process into a 2-step reaction. Reduction occurs with the rupture of the C-C bonds making reversibility a rare event. The result is a nido compound of the type [*nido*-7,9-$C_2B_{10}H_{12}$]$^{2-}$. Recently, a reversible 2 e$^-$ of dicarboranes was reported, reversibility was possible due to double functionalization of C with phosphate groups.[23] In summary, unsubstituted [$CB_{11}H_{12}$]$^-$ is a molecule highly resistant to both oxidation and reduction. Meanwhile, $C_2B_{10}H_{12}$ has high resistance to oxidation but undergoes (usually) irreversible reduction processes due to the cleavage of C-C bond.

The redox potential of metallacarboranes, specifically bisdicarbollide compounds, has been subject to intensive research. Partly due to the reversibility of the process similar to that observed in ferrocene. Unlike ferrocene, metallacarboranes can undergo numerous modifications (22 vs 10 potential modification sites in metallacarboranes and ferrocene respectively) which allows for a finer tuning of the electrochemical potential. As usual when it comes to metallacarboranes cobalt complexes are the most studied. Most work has been done by Teixidor's group who has managed to modulate the redox potential by sequential addition of halogen groups to COSAN. In short, each addition of Cl decreases in 0.1 V the redox potential of COSAN ($Co^{2+} \rightarrow Co^{3+}$) allowing an effective range of E from -1.51 to -0.52, all in a single platform. Spokoyny et al. studied redox nickel bisdicarbollide (NISAN) with various substituents in the B(9) position. Perhaps the most known work involving NISAN is that of Hawthorne in which the reduction of the nickel induces a switch from cis to trans rotamer in the metallacarborane. Nonetheless, this kind of control over rotamers has not been observed in any other bisdicarbollide-transition metal complex

1.1.3- Solution behavior

In previous section the distinctive features of boron clusters were detailed, in here the effect that such traits have in the solution behavior will be explained. Several papers have described the solution behavior of boron clusters but cobalt bisdicarbollide remains the most highly studied. COSAN's solution behavior has been examined with numerous techniques both experimental and theoretical. In recent years, the solution behavior of boranes such as $B_{12}H_{12}^{2-}$ has attracted attention since the coinage of the superchaotropic term.

1.1.3a- Intermolecular interactions of boron clusters

To understand the solution behavior of boron clusters it is necessary to understand how they interact with the surrounding molecules. Several types of interactions have been identified mainly through crystal structures and they will be briefly detailed here in order of strength. First, the weak hydrogen bonding is formed between C-H groups (as H-donors) and rich electron density groups (O, N, Cl, I and π-aromatic systems). This has been observed for carboranes both in crystal structures and in solution by NMR. Second, dihydrogen bonding is formed between proton donors of the type Y-H (Y= N, O, S, C) and σ-bonding electron pair X-Y (X= electropositive atoms, B, metal alkali). Spectroscopic and structural evidence have proved their existence and their strength increases with the acidity of the Y-H group. Third, weak bonding between B-H and π-electrons has been observed but is believed to exist only in solid state where it is forced by steric factors. Lastly, the σ-hole bonding has a role in crystal packing of halogenated carboranes. The pairs of unshared electrons in R-X (X= Cl, Br, I) bonds form a belt of negative electrostatic potential and a positive hole at the end of the bond centered around the R-X bond axis. This σ-hole interacts with negative regions of other molecules. Overall, the former two bond-types have the biggest impact on the solution behavior of boron clusters.

1.1.3b- Boron clusters in aqueous solvent - their place in the Hofmeister series

The idea of water as a structured liquid and its manipulation through ions has existed for more than 120 years. In 1888 Franz Hofmeister tested the effect of salts on the solubility of proteins. The result was a series of cations and anions indicating those with the most facility to precipitate the proteins (salting-out). That series is now known as the Hofmeister series. Later, experiments in water viscosity by Jones and Dole brought the idea that some ions induce order/disorder in water structure. Small ions with high charge density increased the viscosity of water, thus the overall order in the system. These ions were named kosmotropes.[24] On the other hand, large ions with low charge density decreased viscosity and were thought to break the order in water. They were named chaotropes. This offered some explanation to the Hofmeister series (for the anions), kosmotropes withdraw water from the hydration layer of proteins causing precipitation and chaotropes do the opposite.

It is necessary to mention that the existence of kosmotropes and chaotropes and their effect on water structures has many detractors. Many researchers have called to stop the usage of Hofmeister series as an explanation and to focus on ion-specific interactions.[25,26] Many arguments point to “blind spots” in the theory that the Hofmeister series fails to explain, these are briefly mentioned here: i) ions do not have a long range effect on water structure, ii) the Hofmeister series is reversed in some specific cases, iii) the Hofmeister effects are seen even at low concentrations and iv) the confusing salting-in behavior in proteins is observed in kosmotropes for anions and in chaotropes for cations. Despite its detractors the use of terms as kosmotropes and chaotropes continues to be generally used to explain behavior of ions in solution. The popularity of the idea resides in the simplicity to explain experimental observations.

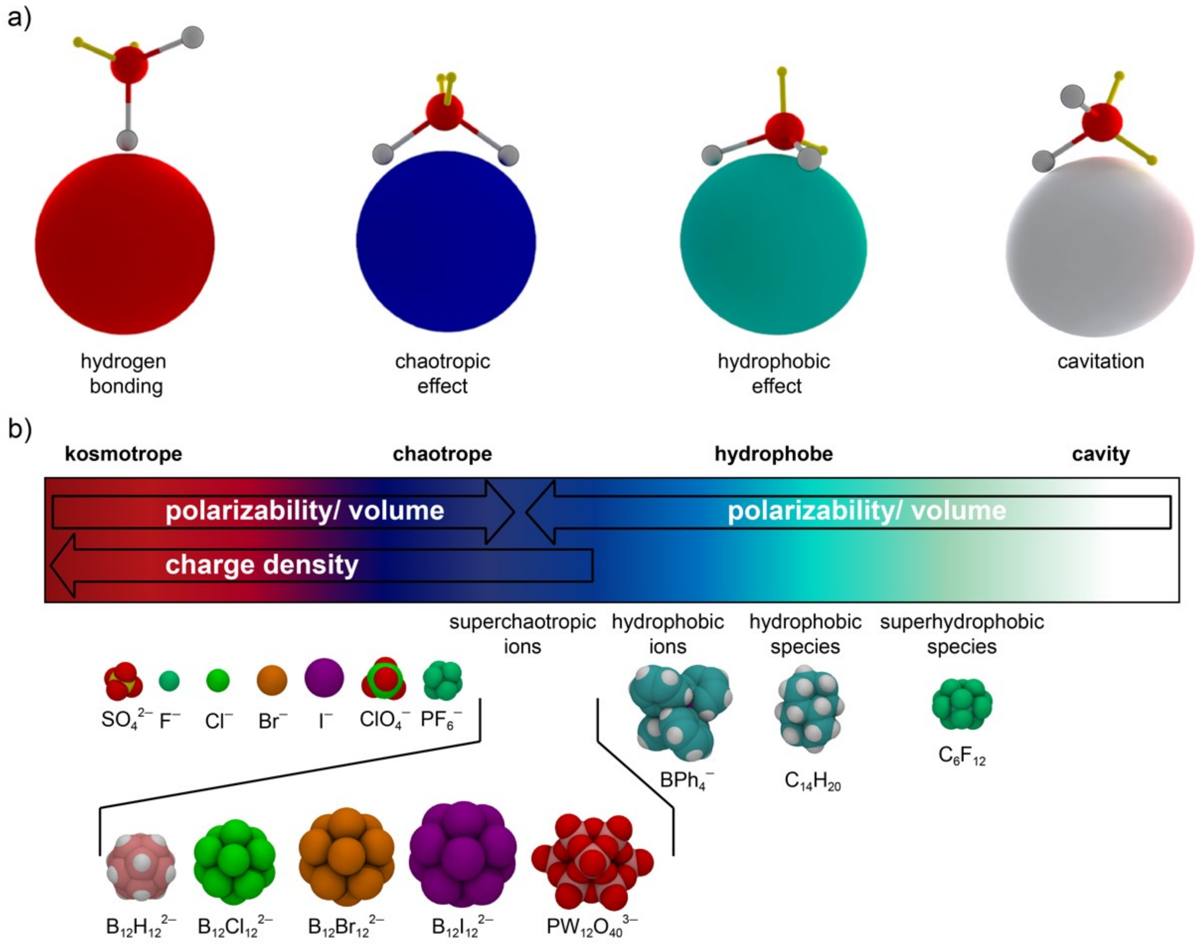

Figure 1.6. a) Depiction of presumed favorable orientations of water molecules around a cavity and at the surface of solutes with various properties: kosmotropic and chaotropic ions, hydrophobic molecules, and void space (cavitation). b) Extension of the original Hofmeister scale with specific section added: superchaotropic, hydrophobic ionic, and superhydrophobic regions. Figure obtained from reference[27]

Some boranes and metallacarboranes are anions soluble in water which gives them a place in the Hofmeister series (Figure 1.6b). Assaf and Nau defined the chaotropic effect and made a distinction between it and the hydrophobic effect.[28] Chaotropic behavior is studied by the binding of ions to surfaces or molecules containing cavities (e.g. proteins, cyclodextrins). A series of publications dealing with inclusion complexes between boron clusters and cyclodextrins signals this method as the favored one to study chaotropic behavior. The underlying principle relies on molecules suffering a desolvation effect upon binding. Hydrophobic molecules show a characteristic entropy driven interaction due to the loss of "structured water" (hydrophobic effect). In contrast, chaotropic molecules are characterized by an enthalpy driven process. Therefore, the lack of structured hydration water around chaotropic molecules leads to a small ΔS of desolvation. In both scenarios the relative contribution of entropy and enthalpy to Δ*G* is temperature dependent. Meaning that at low temperatures ΔS will acquire more importance in the process and the opposite is true at high temperatures. Consequently, thermodynamic parameters (Δ*G*, Δ*H*, Δ*S*) are the main experimental tool to determine chaotropic/kosmotropic behavior. Furthermore, specific parameters were stablished to classify molecule as chaotropic based on their changes to water viscosity and their hydration entropy. Dodecaborate and derivatives excel in these parameters as compared to known chaotropes. Thus, they were classified as superchaotropes. So far, the superchaotropic description has been extended to COSAN and bigger boranes ($B_{21}H_{18}^{2-}$)

The interaction of boron cluster with aqueous solvents has been studied mainly through molecular dynarkimics (MD) simulations. Notably, the partial negative charge of H atoms in B-H bonds precludes the formation of classical hydrogen bonding with water but allows the formation of dihydrogen bonds. For dodecaborate, simulations described the first layer of hydration water around it and its derivatives. Results show a patchy hydration shell with hydrogen atoms pointing towards the cluster and forming dihydrogen bonding.[29] Likewise, MD simulations of COSAN in water show the same patchy water structure around the cluster (Figure 1.7.[30] The first layer hydration shell defines the properties of the whole hydration shell. Therefore, MD studies on this have been key contributions to understand how boron clusters behave in aqueous solutions and supports claims of superchaotropic behavior.

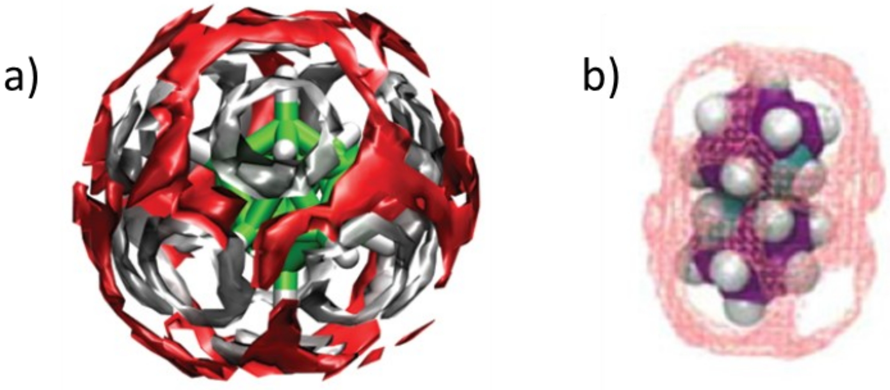

Figure 1.7. Spatial density distribution of water molecules around (a) dodecaborate and COSAN (b). Images taken from reference [29] and [30].

1.1.3c- Self-assembly of boron clusters

As mentioned above the solution behavior of metallacarboranes is the most studied, specifically the anion COSAN. First reports of self-assembly were done in 2006 by Matejicek et al. in a study based on light scattering (DLS, SLS), SEM and AFM. In here, researchers found large aggregates with concentration-dependent size. Later, Bauduin et al. reported a study based on SANS/SAXS focusing on self-assembly at smaller concentrations than previous work and attributed the self-assembly to intermolecular B-H···H-C dihydrogen bonding. Reportedly, at low concentrations COSAN aggregates exist only as monolayer vesicles (R=20 nm, 0.01 mM).

After concentration increases above 18.6 mM smaller micelles form (R=1.86 nm) and coexist with the vesicles. Other reports indicate that vesicles are only a small portion of the aggregates and the small micelles are predominant. Additionally, the observation of large vesicles could be due to presence of nanobubbles.[31] Furthermore, studies via ITC, DOSY and conductimetry determined the correct CMC to be around 10 mM. At higher concentrations, the presence of worm-like micelles was observed via cryo-TEM and lyotropic lamellar phases are observed upon the iodination of B(8) and B(8′) in COSAN.

After initial reports describing COSAN aggregation in general terms notable efforts were made to elucidate more details from the process. The comparison of COSAN to classical surfactants (e.g. sodium dodecyl sulfate) helped to contextualize and define its surfactant behavior. Despite the lack of a head-and-tail structure (a hydrophilic “head” and a hydrophobic “tail” is the structure most known for surfactant molecules) its behavior mirrors that of classical surfactants. Terms such as intrinsic amphiphile, stealth-amphiphile and theta-amphiphile have all been used to describe COSAN as an attempt to capture its odd solution behavior. The incorporation of thermodynamic methods (ITC) into the study of micellization revealed abundant new information about COSAN. Primarily, that COSAN micellization is an enthalpy driven process independently of the temperature. In contrast, micellization of classical surfactants is entropy driven (at low temperatures) due to the release hydration water around the hydrophobic segments (hydrophobic effect). The dominant enthalpic contribution in COSAN aggregation sharply resembles the observation made for superchaotropic ions. Additionally, the high enthalpic contribution to ΔG indicates that additional effects besides B-H···H-C dihydrogen bonding are involved in the micellization. Furthermore, recent work from Assaf et al. denotes that dihydrogen bonding contribution to boron clusters-cyclodextrin interaction is only important in solid and gaseous state but becomes less important in solution due to dihydrogen bonding with water. Even though the work was done for $B_{21}H_{18}^{2-}$ -cyclodextrin interaction the same conclusion of dihydrogen bonding can be extrapolated to the COSAN micellization system.[32] Currently, experimental evidence and theoretical approaches indicate that the solvation water is a key participant in the micellization of COSAN. Albeit it remains unanswered if the chaotropic effect is involved or some other explanation is necessary.

Two independent groups studied the effect of counterion in the aggregation of COSAN (H^+, Li^+, Na^+, K^+) (one of them is included in this Thesis, for more details see Section 4.2). In both cases no significant changes were found in aggregation number, counterion binding, concentration related NMR shifts, or CMC. Nonetheless, small variations in thermodynamic parameters suggest that the role of counterions is still not completely deciphered. The lack of a marked effect of counterion could be attributed to the high charge delocalization of COSAN which leads to small attraction with the counterion. Furthermore, ITC studies showed that COSAN does not conform to the pseudo-phase separation model followed by most classic surfactants.

Therefore, COSAN is unable to create pseudo-phase separation in solution despite its similarities to classical surfactants. Possibly for lacking large hydrophobic part relative to its polar part.

Agreement between simulations and experimental results have solidified the view that researchers have on the micellization process of COSAN. For example, the extremely low counterion condensation on micelles was also observed in MD simulations (Figure 1.8). Specifically, a counterintuitive repulsion between COSAN and Na^+ was found at small distances. Moreover, an attraction between COSAN molecules was observed at short distances despite being like-charged. These simulation results mimic the observation in experiments.

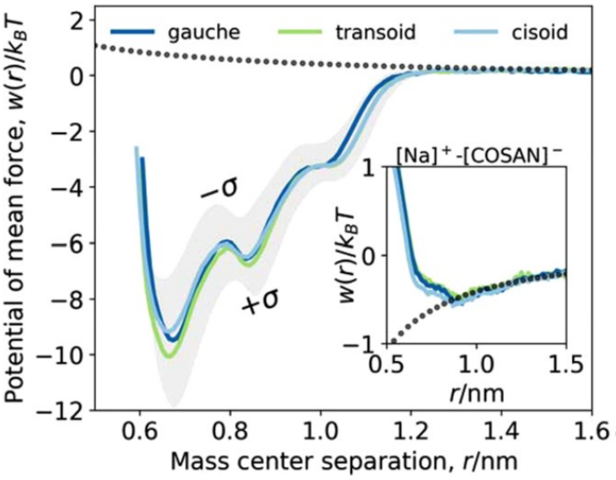

Figure 1.8. Simulated potential of mean force for COSAN···COSAN and Na···COSAN (inset) interactions in all three COSAN configurations (gauche, cisoid and transoid). Image reproduced from reference [30].

The solution behavior of other boron clusters has been much less explored. Experiments are mostly limited to a publication by Dordovic et al. which investigated the hydrophobicity, and surface tension (γ) of boranes such as $Na_2B_{12}H_{12}$, $NaB_{10}H_{10}$, NaCOSAN and $KCB_{11}H_{12}$.[33] Analysis of surface tension curves and reverse phase HPLC indicate a variating degree of hydrophobicity for these boron clusters. They can be ordered by increasing hydrophobicity as follows: NaCOSAN, > $KCB_{11}H_{12}$> $Na_2B_{12}H_{12}$> $NaB_{10}H_{10}$. Regarding the surface activity, all tested clusters decrease the γ of water. However, the analysis of γ curves show that only NaCOSAN produces a clear formation of aggregates. The other clusters need an extremely high concentration (>0.5 M) to reach the point where γ stops decreasing (usually indicating phase separation), at such high concentration other factors could contribute to the shown behavior such as ion pairing or nonideality of the solution, therefore it is no clear indication of aggregation.

Open questions remain about micellization/aggregation of boron clusters. For example, the exchange rate of COSAN molecules from solution to micelle is unknown. Also, the isomeric form of COSAN in aggregation is still not fully elucidated. *Cis*-COSAN is the most stable in solution but whether this remain true in the micelles is not known. Furthermore, the debate about large vesicles existence and their relative abundance in solution is not clear and further experiments in nanobubbles are imperative to discern. For dodecaborate is necessary to distinguish if what is observed is aggregation of simply ion pairing at high concentrations.

1.2- Modifications to the boron cluster framework.

Over many years since the discovery of boron clusters their applications are numerous and in different fields. Application in the fields of medicine, catalysis, optoelectronics and more have demonstrated its versatility. In here, the common ways to modify boron clusters will be outlined. Later, the main applications of dodecaborate, carboranes and metallacarboranes will be briefly mentioned with a few selected examples. A more complete list can be found in books and reviews. Lastly, their incorporation into polymers and nanostructures will be detailed due to its relevance with the current work.

1.2.1- Modifying the cluster framework

1.2.1a- Modifications in dodecaborate

Any molecular scaffold needs a developed toolkit of chemical modifications in order to achieve its potential applications. In the case of dodecaborate, its modifications are scarcer than carboranes and metallacarboranes due to the symmetry and stability of the molecule. The symmetry implies difficult functionalization of specific B-H bonds and deficient control over subsequent modifications. Therefore, persubstituted and monosubstituted dodecaborate are the most useful and sought for reactions. A near complete list of modifications can be found in reviews by Sivaev.[34] Three types of derivatives are commonly used for dodecaborate: 1) halogenation, 2) hydroxylation and 3) oxonium derivatives.

The perhalogenation of $B_{12}H_{12}^{2-}$ were some of the earliest modifications performed, mainly carried out by Knoth and coworkers. [35,36] Reactions were conducted in both water and ethanol with fast rates of reaction achieving good yields of perhalogenation with F, Cl, Br and I. Miscellaneous modifications such as a single substitution of a B-H bond by a halogen, -OH, -NH_2 or other groups have also been accomplished.

The perhydroxilation of $B_{12}H_{12}^{2-}$ was first discovered by Hawthorne's group and has since been used as a starting point for polyfunctionalization of dodecaborate.[37] $B_{12}(OH)_{12}^{2-}$ is synthesized by treating the parent closo-$B_{12}H_{12}^{2-}$ with 30% hydrogen peroxide at reflux temperature for several days. Naturally, esterification[38] and benzylation[39] followed the discovery of $B_{12}(OH)_{12}^{2-}$, again by Hawthorne's group. Said reactions had long reaction times and acceptable yields but were key to discover the redox properties of persubstituted dodecaborate. After full functionalization, the clusters are capable of a quasi-reversible two-step oxidation passing by a radical species, $B_{12}R_{12}^{2-} \rightarrow B_{12}R_{12}^{\cdot -} \rightarrow B_{12}R_{12}$. The presence of these species is revealed by color in the reaction. Furthermore, the stability of the radical and neutral species ($[B_{12}R_{12}]^{\cdot -}$, $[B_{12}R_{12}]^{0}$) depends on the substituents.[40] Later, bioactive groups were incorporated into the $B_{12}(OH)_{12}^{2-}$

cluster via carbamate linkers, showing the advantages of this system for biomedical applications.[41] Afterwards, the use of microwaves led to outstandingly shorten reaction times and improved yields.[40] Additionally, the high rate of reaction under microwaves enables the work even without inert atmosphere and strictly dry conditions. The improvements of control over dodecaborate modifications has led to fully covalent nanoparticles with atomic precision.[42]

Finally, the oxonium derivatives have offer one of the most versatile ways of incorporating dodecaborate into different molecular scaffolds. The incorporation of an oxonium group provides an "activated" electrophilic site to functionalize $B_{12}H_{12}^{2-}$. Most commonly $[B_{12}H_{11}O(CH_2)]^-$ and $[B_{12}H_{11}O(CH_2CH_2)_2O]^-$ are synthesized and later functionalized with a nucleophile. Said derivatives are produced by the reaction of tetrahydrofuran and dioxane with dodecaborate, respectively, and follow two synthetic strategies. First, reflux of $B_{12}H_{12}^{2-}$ in the presence of $F_3B{*}Et_2O$.[43] Second, reflux of $B_{12}H_{12}^{2-}$ in acidic media (Scheme 1.1).[44] The later is more tolerable to air and humidity, thus it can be done without strict inert atmosphere conditions with good yields. In both cases the group that attaches to the boron clusters is the nucleophile most present in the reaction mixture. Consequently, this reaction is done using the desired group as solvent (e.g. tetrahydrofuran or dioxane) and water should be excluded as much as possible.

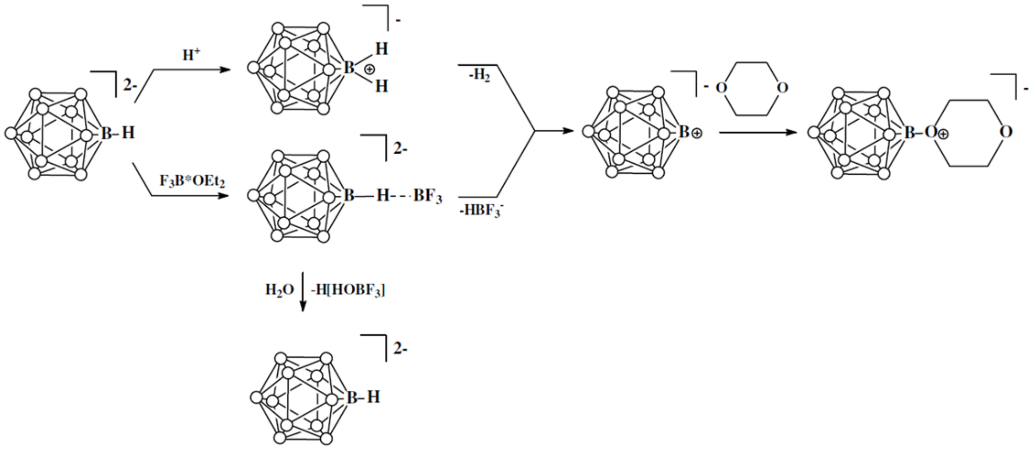

Scheme 1.1. Synthesis of dioxonate derivative of dodecaborate. Bottom route corresponds to the original synthesis whereas the top route is the newest one with fewer decomposition products. Reproduced from reference [44].

1.2.1b- Modification for carboranes (closo-$C_2B_{10}H_{12}$, closo- $CB_{11}H_{12}^-$ and nido-$C_2B_9H_{10}^{2-}$)

Monocarborane ($CB_{11}H_{12}^-$) has a rich and versatile chemistry with possibilities to functionalize both C and B sites, extensive reviews by Michl and coworkers are excellent sources of information.[45] Additionally, $CB_{11}H_{12}^-$ polarity confers it water solubility. C-modifications are possible via cluster modification or cluster synthesis. The cluster modification occurs through proton abstraction of the C-H bond by *n*-butyllithium and subsequent modification with an electrophile. This method produces species $RCB_{11}H_{12}^{-}$ with a great variety of R group (R=alkyl, alkenyl, aryl, silyl, phosphino, carboxylic acid, alcohol, hydroxy). Furthermore, C-H abstraction is possible despite other substituents in the cluster.[46] Also, R groups can be directly inserted while synthesizing the cluster. This is achieved by treating $B_{11}H_{14}^{-}$ with and arylhalocarbene ((*p*-XC_6H_4)CCl: , X= Cl, Br, Br, I, Ph). The ease of C-H functionalization and the polarity of $CB_{11}H_{12}^{-}$ present advantages over dodecaborate while maintaining its characteristic high thermal stability.

B-modifications are possible with electrophilic reagents and are determined by the proximity to the carbon atom. The polarity of $CB_{11}H_{12}^{-}$ (Figure 1.9) defines three distinct regions: the upper belt is comprised of B(2-6)-H, the middle belt includes B(7-11)-H and the antipodal region is only the B(12)-H. The ease of electrophilic substitution increases with distance from C atom (antipodal > middle belt > upper belt) due to the increased electron density at B12. Halogenations on B12 can be done selectively under mild conditions, an increase in temperature often leads to halogenation in the middle belt. Furthermore, perhalogenation is achieved at high temperatures and strong acid conditions (200 °C and CF_3COOH). Notably, the upper belt can be protected against substitution by using a bulky group at the C-R site.

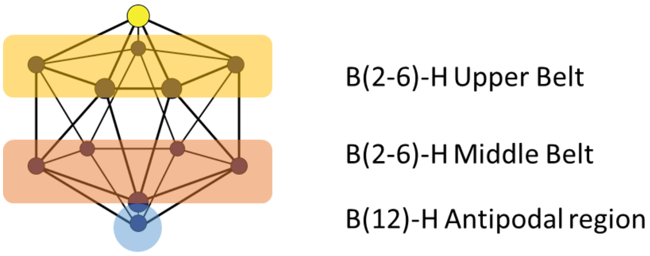

Figure 1.9. Areas of B-H reactivity for $CB_{11}H_{12}^{-}$. Detailed explanation in text.

The *closo*-1,2-dicarbaborane (*orto*-carborane) is the most used carborane. The C-substitutions are similar to that of $CB_{11}H_{12}^{-}$, but with the complications expected in a system with two C-H bonds. Namely, lithiation and subsequent nucleophilic attack results in a mixture of mono and disubstituted product. This effect occurs due to an equilibrium in which mono-, di-lithiated and parent carborane coexist. Reports indicate that using dimethoxyethane favors the mono substituted product.[46] After C-substitution the cluster is still subjectable to deboronation forming the *nido*-7,8-dicarborane. In the case of 1,7-$C_2B_{10}H_{12}$ and 1,12-$C_2B_{10}H_{12}$ (*meta* and *para*-carborane respectively) the C-H protons are less acidic compared to 1,2-$C_2B_{10}H_{12}$, partly due to a more even electron distribution across the cluster (reduced polarity). Metalation of *m*-carborane results in mono C-substituted products with higher yields than o-carborane. [46]

B-substitution in $C_2B_{10}H_{12}$ recently underwent fast progress via the use of metallic catalysts which are necessary for regioselective reactions.[47] The charge density in $C_2B_{10}H_{12}$ increases with distance from the C-cage atoms which conditions the reactivity of the different B atoms. For *o*-

carborane the B-H bonds can be divided in four groups (Figure 1.10), in order of electron density they are: B(9,12) > B(8,10) > B(4,5,7,11) > B(3,6). An electron deficient transition metal catalyst is needed to activate the most electron rich sites, B(9,12/ 8,10) and B(4,5,7,11). Non-specific catalyst include $AlCl_3$ which induces alkylation in all groups except B(3,6) and occurs in the presence of RX (R=alkly group, X=halogen). Alkylation in the presence of $AlCl_3$ proceeds stepwise from higher to lower electron density. Specific activation of B(4,5,7,11) needs a directing group and an electron deficient catalyst. A carboxylic group directly attached to C atom is used for directing due to its effectiveness and possibility to remove it after the reaction. In contrast, the activation of B(3,6) proceeds with an electron rich catalyst. Electrophilic B-halogenation also occurs in the presence of a transition metal catalyst ($AlCl_3$, $FeCl_3$) or a strong protonic acid with a preference for electron density rich B-sites. Additionally, B-modification with S, N and C groups has been achieved through various methods.[48] Furthermore, Quan's group achieved the regioselective hydroxylation[49] and amination[50] of B(4) which opens up new possibilities for functionalization and applications of carboranes.

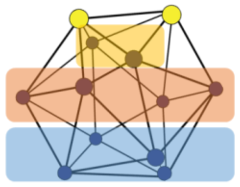

B(3,6)-H electron rich with transition metal catalyst

B(4,5/7,11)-H Directing group plus electron-deficient transition metal catalyst

B(8,10/9,12)-H electron-deficient transition metal catalyst

Figure 1.10. Specific conditions needed for B-H activation and substitution in 1,2-$C_2B_{10}H_{12}$.

Modifications on *nido*-carboranes (7,8-$C_2B_9H_{12}^-$) are usually more challenging due to the high reactivity of these clusters. Incorporation of ether and thioether groups is accomplished in position B(9) and B(10) when catalyzed by strong acids (2-4 mol L^{-1}). The use of weak acids or strong acids outside the mentioned range results in no reaction or sharply reduced yields, respectively. Furthermore, reactions in acidic media often result in some degree of boron cage degradation. Therefore, the preferred route is modification on the *closo*-cluster followed by deboronation (the process of losing a B-H vertex). Deboronation occurs under reflux conditions in the presence of an ethoxide group (MeO^-, EtO^-).[51] Alternatively, mild conditions for deboronation were discovered by Yoo et al.[52] In this case deboronation also needs reflux conditions but the alkoxide reagent is substituted by cesium fluoride. Therefore, making possible the deboronation of *closo*-carboranes containing groups sensitive to alkoxides.

1.2.1c- Modification for metallacarboranes

In here modifications concerning bisdicarbollide-type metallacarboranes will be addressed, modifications of other kind of metallacarboranes can be found elsewhere. Changes to the structure of metallacarboranes can be done following two routes. Namely, changes can be introduced before or after the complexation of the transition metal by dicarbollide groups. The post-complexation route takes advantage of the general resilience that metallacarboranes have to harsh conditions. Meanwhile, the pre-complexation route is a multi-step process involving modification to *closo*-carborane, deboronation to obtain the modified dicarbollide anion and finally the complexation of a transition metal.

Modifications on cluster pre- metal complexation are identical to modifications for *closo*-carboranes and are found in the previous section (Chapter 1.2.1b). Substituents can affect the yield of metal complexation and, in some cases, precludes the formation of metallacarboranes, especially when substitution occur at the η^5 face. Nonetheless, this route is the most efficient way to obtain metallacarboranes with selective B-substituents other than in B(8).

Modifications post-metallacarboranes formation are focused on the B(8) which is in opposite direction to the C-C bonds across in the η^5 face. B(8) contains the most electron density and its easily activated with Lewis acids such as BF_3 or $AlCl_3$. Modifications on the B(8) include $-NH_2$, -OH, $-NC_5H_5$, -I and PPh_3.[48] Alternatively, both B(8) and B(8′) can be modified either with identical or dissimilar groups on each dicarbollide ligand. Furthermore, the linkage of the B(8) and B(8′) sites result in a metallacarboranes with fixed *cisoid* geometry. Most studies on linking bisdicarbollide cages in COSAN were done by Plesek and coworkers. Among the different linking groups phosphates, benzene and other aromatic rings are distinguished for conserving the -1 charge in the complex. Conversely, N-R, O-R, S-R linking groups all generate zwitterions. In all cases a Lewis acid is needed as catalyst. In general, substitutions on different B atoms require high temperatures and often result in mixtures of two or more products. An exception to this is iodination with ICl. This compound is highly effective for halogenation of B(8, 9, 12) in COSAN (boron atoms with highest electron density) and presents very high yield. Exceptionally, this iodination occurs without the need of a catalyst. Furthermore, this route offers an easy route for methylation of the B vertices through a 2-step process. First, iodination with ICl. Second, methylation of iodinated vertices with a Grignard reagent (MeMgBr).[53]

Additionally, C atoms can be modified with “classic” organic chemistry after metallacarboranes formation. Buthyl lithium is used to deprotonate C-H bonds which can later be modified with an electrophile (e.g: CH_3-I, CO_2, CH_3-$(CH_2)_5$-Br). In COSAN the removal of one C-H proton is characterized by the production of a deep purple compound, an additional C-H proton removal produces a dark blue product. It is not always easy to differentiate between the color of these products due to the dark hue of both. Nonetheless, both are isolable as Li-salts (sensitive to moisture) and can later undergo substitution or return to the original COSAN by quenching with water. Removing more than two C-H protons at the same time results in decomposition of the parent metallacarboranes in the form of a brown precipitate. Notably, bulky substituents in B(8) and B(8′) preclude the C-H proton abstraction. Bond angles of dicarbollide atoms at the η^5 face are not in plane with the flat face but rather have an 50° angle. Therefore, to accommodate two bulky substituents in B(8,8′) COSAN is forced into the *transoid* rotamer.

Consequently, the B(8,8′) substituents are located in the middle of the C-C bond of the opposite dicarbollide ligand, effectively blocking the hydride abstraction through steric hindrance.

The introduction of an oxonium group (identical to that used for dodecaborates) is a popular modification used to attach metallacarboranes to an ever-growing variety of molecules. After its synthesis by Plešek et al.[54] the use of COSAN-oxonium derivatives has been widely implemented due to its convenience. There are two possible mechanisms for the formation of the oxonium derivative: i) electrophilic-aromatic substitution which involves the B-H bond activation by a Lewis acid and is used for 2D-aromatic systems, and ii) electrophile-induced nucleophilic substitution (EINS) consists in protonation of B-H, subsequent lost of -H_2 followed by a nucleophilic attack from the most abundant nucleophile, even weak ones. The opening of the oxonium ring occurs under mild conditions and usually high conversions are observed. A nucleophilic attack on the carbon adjacent to the $B\text{-}O^+\text{-}R_2$ effectively incorporates numerous groups such as azo, ethyl, phenyl, carboxylic, alkoxy, and more. Therefore, it is the preferred route when incorporating metallacarboranes into proteins, nucleosides[55] or other sensitive groups.

1.2.2- Applications

Applications of boron clusters make use of all their inherent characteristics, temperature resistance, redox resistance, rich modification chemistry, aromaticity and hydrophobicity. Their applications are vast thus only selected examples from the most traditional areas (medicine, radionuclei radio extraction and catalysis). Nonetheless, recent advances have broadened the areas in which boranes contributions make a difference. For example, the literature on their use for non-linear optics and liquid crystals has grown in recent years. Also, the properties of carboranes have been exploited in synthesis of metal-organic frameworks. Moreover, the use carborane enabled a breakthrough in metal-organic frameworks by producing reversible structure capable of switching from 3D to 2D and back.

1.2.2a- Uses in Medicine

Boron clusters can be incorporated into medicine in two main ways: i) as the active species itself (e.g as BNCT agents, enzymatic inhibitors) or ii) they can be used as pharmacophores on existing drugs to improve their pharmacokinetic properties. Reviews dealing with medicinal applications of boron clusters exist and can be found here.[56–58] The price of boron clusters is often cited as a weakness to their applications but in drugs development the price of boron clusters is usually only a small fraction of the price.

It is impossible to relate boron cluster to medicine without mentioning their role in boron neutron capture therapy (BNCT). The irradiation of ^{10}B with low-energy thermal neutrons produces a α particle ($^{4}He^{2+}$), $^{7}Li^{3+}$ and a photon (γ)

$$^{10}B + n \rightarrow {}^{7}Li^{3+} + \alpha + \gamma$$

This highly energetic ions (2.31 MeV of kinetic energy) can travel the average diameter of a cell (5-9 µm) and potentially be deadly for the cell. Therefore, the accumulation of ^{10}B in cancerous cells can lead to a controlled destruction of tumor tissue without harm to healthy tissue. Nonetheless, a concentration of 30 µg ^{10}B/g of tumor is needed for an effective treatment. ^{10}B is used due to its high neutron capture cross-section, which is several orders of magnitude higher than other elements normally found in tissues. Thus, irradiation with low energy neutrons is mostly harmless and highly specific for ^{10}B. Even since the many years since its discovery still only two boron compounds have been clinically used for BNCT, boronophenylalanine and borocaptate ($Na_2B_{12}H_{12}S$), the being the only boron cluster currently in use for this purpose. Considering the high concentration of boron needed per g of tumor it becomes clear why boron clusters present such a big advantage over other boron compounds. A single boron cluster can add up to 18 ^{10}B atoms per molecule (metallacarboranes). Whereas compounds such as boronophenylalanine contributes 1 ^{10}B per molecule. Nonetheless, both compounds exhibit low cellular uptake and limited permeability across the brain-blood barrier (BBB) which hampers their effective application for brain tumors.

Orto-carboranes have been a great tool for medicinal chemistry to enhance the pharmacokinetic and targeting properties of small molecule drugs. Their high hydrophobicity improves their ability to cross the cellular membrane and the brain blood barrier. Also, they are naturally resistant to enzymatic degradation in account of their inorganic nature. Finally, their 3-dimensional structure gives them an advantage over other lipophilic moieties (benzene, adamantane) which can only be modified in 2 dimensions thus have lower degrees of control over the final structure and its interactions. These traits have led to their use in a myriad of targets as inhibitors, in many cases the structure is that of a known drug albeit with the phenyl ring substituted by a carborane. In some cases, carboranes are used as the active compound itself and not only as a modifier of a known drug. A clear example is the use of *orto*-carborane and its derivatives as inhibitors of carbonic anhydrase. This enzyme has been related to several diseases such as cancer and epilepsy among others.[59] Furthermore, if the hydrophobicity of the drug affects the solubility the carboranes can undergo deboronation producing a *nido*-carboranes with a -1 charge. This improves water solubility and its hydrophobicity can be tuned by counterion choice.[58] Besides BNCT, boron clusters have been used for mixed therapies by incorporating them into phthalocyanines for BNCT/photodynamic therapy. Therefore, combining the ability of phthalocyanines to produce cytotoxic oxygen species (singlet oxygen, hydroxyl radicals and superoxide anions) upon irradiation with red laser light with the high boron content of boranes.

Metallacarboranes have fewer uses in medicine when compare to carboranes but still have been used for key targets. For example, COSAN is known as potent and specific inhibitors of HIV-1 protease with a IC_{50} =1.1 µM.[60] It acts by binding to hydrophobic pockets in the active site of the protease at a ratio of 2:1 (COSAN:HIV-1) through a competitive binding mechanism.

Furthermore, modifications consisting on joining two COSAN molecules by various linkers greatly increased its specificity and potency with $IC_{50} \leq 200nM$.[61,62] This represents one of the few clinically available drugs based on metallacarboranes. Additionally, metallacarboranes have been used to modify adenosine to act as platelet function inhibitors. The study was made by covalently attaching various boron clusters to adenosine, COSAN-adenosine specifically activates the release of proteins from platelets.

1.2.2b- Catalysis

The use of monocarboranes in catalyst species relies on their highly delocalized charge. This gives them the ability to form loose bond pairs, thus leaving their metallic counterion exposed. For example, $LiCB_{11}H_{12}$ catalyzes rearrangement of pericyclic hydrocarbons and radical polymerization of terminal alkenes as a result of an extremely active Li^+ ion. $CB_{11}H_{12}^-$ also forms complexes with transition metals and improves their catalytic power when compared with other big anions (BF_4^-, ClO_4^-, OTf^-)

Chemists take advantage of the structural rigidity of o-carboranes ($C_2B_{10}H_{12}$) to design catalyst by building the framework from the C-H carboranes bonds. Phosphino-carboranes can be used for mono-, bi- and tridentate ligand design. Extensive review about phosphino-carboranes and their catalytic properties can be found here.[63] The development of specialized chemical modifications in boron clusters has made possible the synthesis of complex catalysts. Some exploit the deboronation reaction to alter the solubility of catalysts while maintaining catalytic activity. *Nido*-carboranes are used as catalyst both in the form of exo-nido metal complexes and as metallacarboranes. Notably, *nido*-carboranes often substitute cyclopentiendyl groups in metallocene-type catalysts for olefin polymerization. Nonetheless, bis-dicarbollide metallacarboranes rarely see any use as catalyst except for COSAN. Namely, COSAN works as a photoredox catalyst in water for the oxidation of aliphatic and aromatic alcohols.[64]

1.2.2c- Radioactive radii extraction

The extraction of metallic ions from nuclear waste is one of the oldest and largest scale applications for boranes, specifically metallacarboranes. The extractions process occurs on high acidic concentrations (HNO_3, 3M) and is necessary to complex the ions (e.g: Cs^+, Sr^{2+}, Am^{3+}) and transport them into the organic phase. The problem is that to operate under such acidic concentrations the extraction agent must not form a complex with H^+ and remain stable. The successful use of COSAN in this process stems from its amphiphilic behavior, its highly delocalized charge, and its stability. The delocalized charge provides characteristics of a superacid; thus it remains dissociated even at high acidic concentration. The amphiphilic behavior makes it soluble both in water and organic solvents with the solubility variating with the counterion. Nonetheless, COSAN is only able to extract monovalent Cs^+ on its own. Modifications on COSAN (e.g: short polyethylene oxide chains) have been implemented to aid in the complexation and extraction of polyvalent lantanides. Alternatively, additives such as crown-ethers are used alongside COSAN to improve the extraction of multivalent cations.

Remarkably, recent advances on carboranes synthesis yielded a carboranes capable of reversible redox reactions. Upon reduction the bite size of the modified carboranes changes allowing the complexation of uranyl ion. After oxidation and successful reformation of *orto*-carborane the uranyl is released, thus solving the problem of release of uranyl ion that other system presented.

1.3- Incorporation into polymers

Polymers are a major component of every-day life in modern societies. Their modernization is paramount to the advancement of both common and specialized technological applications. Even early after the discovery of carboranes, their incorporation into polymers has been a great motivation to further their research. In general, polymers featuring carboranes exhibit increased temperature and oxidative resistance. Polymers with boranes (decaborane, dodecaborane) are not frequently found in literature and are mostly limited to polymers made to fabricate ceramics. Even then, most examples are over 20 years old which gives the impression that the field is stagnated. This is caused, in part, by the facility with which carboranes are functionalized and incorporated into polymeric chains. Thus, providing similar benefits to the polymer than what boranes would provide but with a much more developed toolset (carboranes vs boranes). There are two different ways of including carboranes and boranes into the polymeric chain: as pendant groups or as part of the main chain, each method with its advantages and disadvantages.

1.3.1- Polymers with boron clusters as pendant groups

Adding carboranes as pendant groups offers much more flexibility than incorporating them into the polymeric chain. For example, any existing polymer with capacity to modify its side chains can thus be modified with carboranes. This multiplies the number of polymers available for carboranes modification without having to optimize polymerizations with carborane-containing monomers. Nonetheless, the thermal stability granted by carboranes to polymers is decreased when included as pendant groups.

Furthermore, carborane pendant groups can be further modified by deboronation which adds functionalities to the polymer. For example, a carborane-containing fluorescent copolymer film suffered a fluorescence intensity increase up to 3.6 times upon deboronation. This kind of stimuli responsive films could find applications as sensors. [65] Additionally, the pendant *nido*-carboranes can complex transition metals to form crosslinked polymers.

Monomers suitable for polymerization can be modified with carboranes and still undergo different kinds of polymerization. Radical polymerization has been used to synthesize various vinyl carborane polymers, including homopolymers and copolymers. Nonetheless, this kind of monomers show decreased reactivity towards radical polymerization due to steric hindrance and electron withdrawing effect of carboranes. Additionally, ring opening polymerization (ROMP) is also compatible with monomers containing monocarboranes, dicarboranes and metallacarboranes. Different norbornene-based polymers were synthesized through ROMP using a Grubbs catalyst yielding up to 100 repetitive units. It was reported that this bulky groups slow down the polymerization but not to a great extent. Furthermore, polymerization proceeded despite of an *endo/exo*-norbornene mixture.

The incorporation of metallacarboranes as pendant groups has fewer examples than carboranes. The high price of metallacarboranes is partially the reason of this. One of the earliest examples by Vohlidal et al. exploited the reaction between dicarbollides/metallacarboranes functionalized with reactive basic groups (NH_3, NH_2-O, H_2-N-NH_2) and dibromide alkyl compounds to form a polymer.[66] The strategy was effective for different metals complexes (Co, Ni) and different ligands (1,2-$C_2B_9H_{11}^{2-}$, $CB_{10}H_{11}^{2-}$) and yielded pH responsive metallacarboranes polymers (the amino groups granted the pH responsiveness). Nonetheless, the polymers were poorly characterized and should be revisited and characterized with modern techniques and considering new applied fields in which they could be exploited. A post-polymerization modification with metallacarboranes has also been achieved by using the LiNa[COSAN] carbanion on a chloromethylated polystyrene.

Despite its high price and difficulties involved in polymerization metallacarboranes can greatly improve the characteristics of polymers. A great example of this is the

1.3.2- Polymers with carboranes in the main chain

Main chain carborane polymers are usually made with either *para* or *meta*-carboranes. The relative position of the C-H to each other facilitates the linking of carboranes groups with linker groups. For example, the rubber product known as DEXSIL is one of the most successful commercialization products of carboranes. DEXSIL uses siloxane polymer chain to connect *meta*-carboranes groups through their C atoms. Carborane incorporation dramatically increases the temperature resistance of the rubber allowing it to perform even at ~480 °C. The improved thermal stability is ascribed to the bulkiness of carboranes. Its big size interferes with polymer crystallization and restrains molecular motion. Furthermore, due to their high resonance stability carboranes are hypothesized to act as energy sinks.[46]

Newer and creative ways to incorporate carboranes into the main chain include the synthesis of carborane-containing RAFT (reversible addition-fragmentation chain transfer) agents. This naturally integrates a carborane at the end-chain of the polymer.

In the case of bisdicarbollide metallacarboranes several examples have been prepared although just like their pendant group counterparts they have proved difficult to characterize. In each case the polymers were obtained using a different strategy and there is a lack of systematic approach to synthesize and to study their properties. Probably due to difficulty of the synthesis and characterization most research groups seem to synthesize these polymers as oddities and stop pursuing their characterization.

A creative synthetic strategy involved the carboxylation of two C atoms in COSAN and subsequent polycondensation with 1,6-hexanediamine following two different routes. First, the carboxylic groups were transformed into the reactive acid chloride which quickly reacted with the diamine to yield a insoluble compound. Second, a salt of the dicarboxylic COSAN was prepared with 1,6-hexanediamine ($Li[Co(C_2B_9H_{10})_2(COO^-)_2(^+H_3N(CH_2)_6NH_3^+])$) and polymerized by increasing the temperature to 300 °C. In both cases a brown product was obtained but little characterization was given besides IR spectra and H-NMR. Therefore, the number of repetitive units, solution behavior and mechanical properties are still unknown, and no new work has been done with the polymer since then.

Alternatively, a more refined approach was taken by Hawthorne's group using metallacarboranes (M= Ni, Co) linked by their apical boron atoms, B(10), to obtain linear polymers.[67] This is, so far, the only example of a metallacarboranes polymer in which the linking between clusters is done via the boron and not the carbon. The group followed to routes for the polymerization. On the one hand, the dicarbollide cages were linked by their B(10) with a linker and the polymerization occurred upon formation of the metallacarboranes. On the other hand, metallacarboranes with B(10,10')-I bonds were synthesized and subsequently polymerized through cross-coupling polymerization with a Pd catalyst. Out of the two routes only the later yielded polymers of 35-44 repeating units, as determined by ^{10}B-NMR analysis. The resulting polymers were rigid rods as expected, but characterization through GPC proved impossible, as usually occurs with metallacarborane containing polymers.

1.4- Future perspectives

Despite the myriad of properties of boranes and metallacarboranes their high price of production is still an obstacle to scale-up their research and incorporate them into daily-use applications. Efforts to reduce the price of production are few and mainly on the research level and not industrial level. A great example is the recent synthesis of $B_{12}H_{12}^{2-}$ and $B_{10}H_{10}^{2-}$ from inexpensive and relatively safe $NaBH_4$.[68] Alternative synthetic options to obtain such boranes includes synthetic procedures starting from toxic boranes such as BH_3, B_2H_6 or $B_{10}H_{14}$. In the area of metallacarboranes the use of Cobalt remains a problem as it is an expensive metal. Nonetheless, efforts to improve the synthesis of metallacarboranes were undertaken by Viñas group. They have successfully synthesized metallacarboranes in a solid-state synthesis with different functional groups in the C atoms. By combining dicarbollide anions, and $CoCl_2$ and heating the mixture to 350-470 °C for a few minutes yield of >90% are reported.[69] Lowering the prices of boron clusters will surely increase the amount of research groups able to work with them. Also, it might accelerate their incorporation into polymers which will bring them one step closer to daily-use applications.

References

(1) Stock, A. *Hydrides of Boron and Silicon*; Cornell University Press: Ithaca, New York, 1933.

(2) Dickerson, R. E.; Lipscomb, W. N. Semitopological Approach to Boron-Hydride Structures. *J. Chem. Phys.* **1957**, *27* (1), 212–217.

(3) Lipscomb, W. N. *Boron Hydrides*; Courier Corporation: New York, 2012.

(4) Muetterties, E. L. *Boron Hydride Chemistry*; Academic Press, Inc: London, 1975.

(5) Hoffmann, R.; Lipscomb, W. N. Theory of Polyhedral Molecules. I. Physical Factorizations of the Secular Equation. *J. Chem. Phys.* **1962**, *36* (8), 2179–2189.

(6) Hoffmann, R.; Lipscomb, W. N. Theory of Polyhedral Molecules. III. Population Analyses and Reactivities for the Carboranes. *J. Chem. Phys.* **1962**, *36* (12), 3489–3493.

(7) Hoffmann, R.; Lipscomb, W. N. Boron Hydrides: LCAO—MO and Resonance Studies. *J. Chem. Phys.* **1962**, *37* (12), 2872–2883.

(8) Hawthorne, M. F.; Young, D. C.; Andrews, T. D.; Howe, D. V; Pilling, R. L.; Pitts, A. D.; Reintjes, M.; Warren, L. F.; Wegner, P. A. π-Dicarbollyl Derivatives of the Transition Metals. Metallocene Analogs. *J. Am. Chem. Soc.* **1968**, *90* (4), 879–896.

(9) Teixidor, F.; Viñas, C. Boron and Carbon: Antagonistic or Complementary? Proposal for a Simple Prototype of a Molecular Clutch or Molecular Switch. *Pure Appl. Chem.* **2012**, *84* (11), 2457–2465.

(10) Bühl, M.; Hnyk, D.; Machácek, J. Computational Study of Structures and Properties of Metallaboranes: Cobalt Bis(Dicarbollide). *Chem. - A Eur. J.* **2005**, *11* (14), 4109–4120.

(11) Juárez-Pérez, E. J.; Núñez, R.; Viñas, C.; Sillanpä, R.; Teixidor, F. The Role of C-H···H-B Interactions in Establishing Rotamer Configurations in Metallabis(Dicarbollide) Systems. *Eur. J. Inorg. Chem.* **2010**, No. 16, 2385–2392.

(12) Malaspina, D. C.; Viñas, C.; Teixidor, F.; Faraudo, J. Atomistic Simulations of COSAN: Amphiphiles without a Head-and-Tail Design Display “Head and Tail” Surfactant Behavior. *Angew. Chemie - Int. Ed.* **2020**, *59* (8), 3088–3092.

(13) Hawthorne, M. F.; Zink, J. I.; Skelton, J. M.; Bayer, M. J.; Liu, C.; Livshits, E.; Baer, R.; Neuhauser, D. Electrical or Photocontrol of the Rotary Motion of a Metallacarborane. *Science.* **2004**, *303*, 1849–1851.

(14) Lipscomb, W. N.; Pitochelli, A. R.; Hawthorne, M. F. Probable structure of the $B_{10}H_{10}^{2-}$ ion. *J. Am. Chem. Soc.* **1959**, *81* (21), 5833–5834.

(15) King, R. B.; Rouvray, D. H. Chemical Applications of Group Theory and Topology. 7. A Graph-Theoretical Interpretation of the Bonding Topology in Polyhedral Boranes, Carboranes, and Metal Clusters. *J. Am. Chem. Soc.* **1977**, *99* (24), 7834–7840.

(16) King, R. B. Three-Dimensional Aromaticity in Polyhedral Boranes and Related Molecules. *Chem. Rev.* **2001**, *101* (5), 1119–1152.

(17) Schleyer, P. von R.; Najafian, K. Stability and Three-Dimensional Aromaticity of Closo - Monocarbaborane Anions, $CB_nH_{n+1}^-$, and Closo -Dicarboranes, $C_2B_n^{2-}$ H N. *Inorg. Chem.* **1998**, *37* (14), 3454–3470.

(18) Gershoni-Poranne, R.; Stanger, A. Magnetic Criteria of Aromaticity. *Chemical Society Reviews*. **2015**, *44*, 6597–6615.

(19) Poater, J.; Solà, M.; Viñas, C.; Teixidor, F. π Aromaticity and Three-Dimensional Aromaticity: Two Sides of the Same Coin. *Angew. Chemie.* **2014**, *53* (45), 12191–12195.

(20) Núñez, R.; Tarrés, M.; Ferrer-Ugalde, A.; De Biani, F. F.; Teixidor, F. Electrochemistry and Photoluminescence of Icosahedral Carboranes, Boranes, Metallacarboranes, and Their Derivatives. *Chem. Rev.* **2016**, *116* (23), 14307–14378.

(21) Núñez, R.; Tarrés, M.; Ferrer-Ugalde, A.; De Biani, F. F.; Teixidor, F. Electrochemistry and

Photoluminescence of Icosahedral Carboranes, Boranes, Metallacarboranes, and Their Derivatives. *Chem. Rev.* **2016**, *116* (23), 14307–14378.

(22) Knoth, W. H.; Sauer, J. C.; England, D. C.; Hertler, W. R.; Mtjetterties, E. L. Chemistry of Boranes. XIX.1 Derivative Chemistry of B10H10-2 and B12H12-. *J. Am. Chem. Soc.* **1964**, *86* (19), 3973–3983.

(23) Keener, M.; Hunt, C.; Carroll, T. G.; Kampel, V.; Dobrovetsky, R.; Hayton, T. W.; Ménard, G. Redox-Switchable Carboranes for Uranium Capture and Release. *Nature* **2020**, *577* (7792), 652–655.

(24) Jones, G.; Dole, M. The Viscosity of Aqueous Solutions of Strong Electrolytes with Special Reference to Barium Chloride. *J. Am. Chem. Soc.* **1929**, *51* (10), 2950–2964.

(25) Okur, H. I.; Hladílková, J.; Rembert, K. B.; Cho, Y.; Heyda, J.; Dzubiella, J.; Cremer, P. S.; Jungwirth, P. Beyond the Hofmeister Series: Ion-Specific Effects on Proteins and Their Biological Functions. *J. Phys. Chem. B* **2017**, *121* (9), 1997–2014.

(26) Salis, A.; Ninham, B. W. Models and Mechanisms of Hofmeister Effects in Electrolyte Solutions, and Colloid and Protein Systems Revisited. *Chem. Soc. Rev.* **2014**, *43* (21), 7358–7377.

(27) Assaf, K. I.; Nau, W. M. The Chaotropic Effect as an Assembly Motif in Chemistry. *Angew. Chemie.* **2018**, *57* (43), 13968–13981.

(28) Nau, W. M.; Assaf, K. The Chaotropic Effect as an Assembly Motif in Chemistry. *Angew. Chemie.* **2018**.

(29) Karki, K.; Gabel, D.; Roccatano, D. Structure and Dynamics of Dodecaborate Clusters in Water. *Inorg. Chem.* **2012**, *51* (9), 4894–4896.

(30) Uchman, M.; Abrikosov, A. I.; Lepšík, M.; Lund, M.; Matějíček, P. Nonclassical Hydrophobic Effect in Micellization: Molecular Arrangement of Non-Amphiphilic Structures. *Adv. Theory Simulations* **2017**, *1700002*, 1700002.

(31) Uchman, M.; Ďorďovič, V.; Tošner, Z.; Matějíček, P. Classical Amphiphilic Behavior of Nonclassical Amphiphiles: A Comparison of Metallacarborane Self-Assembly with SDS Micellization. *Angew. Chemie - Int. Ed.* **2015**, *54* (47), 14113–14117.

(32) Assaf, K. I.; Holub, J.; Bernhardt, E.; Oliva-Enrich, J. M.; Fernández Pérez, M. I.; Canle, M.; Santaballa, J. A.; Fanfrlík, J.; Hnyk, D.; Nau, W. M. Face-Fusion of Icosahedral Boron Hydride Increases Affinity to γ-Cyclodextrin: Closo,Closo-$[B_{21}H_{18}]^-$ as an Anion with Very Low Free Energy of Dehydration. *ChemPhysChem* **2020**, 21, 1–7.

(33) Ďorďovič, V.; Tošner, Z.; Uchman, M.; Zhigunov, A.; Reza, M.; Ruokolainen, J.; Pramanik, G.; Cígler, P.; Kalíková, K.; Gradzielski, M.; et al. Stealth Amphiphiles: Self-Assembly of Polyhedral Boron Clusters. *Langmuir* **2016**, *32* (26), 6713–6722.

(34) Sivaev, I. B.; Bregadze, V. I.; Sjöberg, S. Chemistry of Closo-Dodecaborate Anion [B12H12]2-: A Review. *Collect. Czechoslov. Chem. Commun.* **2002**, *67* (6), 679–727.

(35) Knoth, W. H.; Miller, H. C.; Sauer, J. C.; Balthis, J. H.; Chia, Y. T.; Muetterties, E. L. Chemistry of Boranes. IX. Halogenation of $B_{10}H_{10}^{2-}$ and $B_{12}H_{12}^{2-}$. *Inorg. Chem.* **1964**, *3* (2), 159–167.

(36) Knoth, W. H.; Miller, H. C.; Muetterties, E. L.; England, D. C.; Parshall, G. W. Derivative Chemistry of B10H10- and B12H12-. *J. Am. Chem. Soc.* **1962**, *84* (6), 1056–1057.

(37) Peymann, T.; Herzog, A.; Knobler, C. B.; Hawthorne, M. F. Aromatic Polyhedral Hydroxyborates: Bridging Boron Oxides and Boron Hydrides. *Angew. Chemie Int. Ed.* **1999**, *38* (8), 1061–1064.

(38) Maderna, A.; Knobler, C. B.; Hawthorne, M. F. Twelvefold Functionalization of an Icosahedral Surface by Total Esterification of $[B_{12}(OH)_{12}]^{2-}$: 12(12)-Closomers. *Angew. Chemie Int. Ed.* **2001**, *40* (9), 1661–1664.

(39) Peymann, T.; Knobler, C. B.; Khan, S. I.; Hawthorne, M. F. Dodeca(Benzyloxy)Dodecaborane, $B_{12}(OCH_2Ph)_{12}$: A Stable Derivative Ofhypercloso-B12H12. *Angew. Chemie Int. Ed.* **2001**, *40* (9), 1664–1667.

(40) Wixtrom, A. I.; Shao, Y.; Jung, D.; Machan, C. W.; Kevork, S. N.; Qian, E. A.; Axtell, J. C.; Khan, S. I.; Kubiak, C. P.; Spokoyny, A. M. Rapid Synthesis of Redox-Active Dodecaborane $B_{12}(OR)_{12}$ Clusters under Ambient Conditions. *Inorg. Chem. Front.* **2016**, *3* (5), 711–717.

(41) Jalisatgi, S. S.; Kulkarni, V. S.; Tang, B.; Houston, Z. H.; Lee, M. W.; Hawthorne, M. F. A Convenient Route to Diversely Substituted Icosahedral Closomer Nanoscaffolds. *J. Am. Chem. Soc.* **2011**, *133* (32), 12382–12385.

(42) Qian, E. A.; Wixtrom, A. I.; Axtell, J. C.; Saebi, A.; Jung, D.; Rehak, P.; Han, Y.; Moully, E. H.; Mosallaei, D.; Chow, S.; et al. Atomically Precise Organomimetic Cluster Nanomolecules Assembled via Perfluoroaryl-Thiol SNAr Chemistry. *Nat. Chem.* **2017**, *9* (4), 333–340.

(43) Sivaev, I. B.; Semioshkin, A. A.; Brellochs, B.; Sjöberg, S.; Bregadze, V. I. Synthesis of Oxonium Derivatives of the Dodecahydro-Closo-Dodecaborate Anion [B12H12]2-. Tetramethylene Oxonium Derivative of [B12H12]2- as a Convenient Precursor for the Synthesis of Functional Compounds for Boron Neutron Capture Therapy. *Polyhedron* **2000**, *19* (6), 627–632.

(44) Sivaev, I. B.; Kulikova, N. Y.; Nizhnik, E. A.; Vichuzhanin, M. V.; Starikova, Z. A.; Semioshkin, A. A.; Bregadze, V. I. Practical Synthesis of 1,4-Dioxane Derivative of the Closo-Dodecaborate Anion and Its Ring Opening with Acetylenic Alkoxides. *J. Organomet. Chem.* **2008**, *693* (3), 519–525.

(45) Körbe, S.; Schreiber, P. J.; Michl, J. Chemistry of the Carba-Closo-Dodecaborate(-) Anion, CB11H12-. *Chem. Rev.* **2006**, *106* (12), 5208–5249.

(46) Grimes, R. N. *Carboranes*, 3rd editio.; Academic Press, Inc: London.

(47) Quan, Y.; Qiu, Z.; Xie, Z. Transition-Metal-Catalyzed Selective Cage B−H Functionalization of o-Carboranes. *Chem. - A Eur. J.* **2018**, *24* (12), 2795–2805.

(48) Olid, D.; Núñez, R.; Viñas, C.; Teixidor, F. Methods to Produce B-C, B-P, B-N and B-S Bonds in Boron Clusters. *Chem. Soc. Rev.* **2013**, *42* (8), 3318–3336.

(49) Lyu, H.; Quan, Y.; Xie, Z. Rhodium-Catalyzed Regioselective Hydroxylation of Cage B−H Bonds of o-Carboranes with O2or Air. *Angew. Chemie .* **2016**, *55* (39), 11840–11844.

(50) Lyu, H.; Quan, Y.; Xie, Z. Transition Metal Catalyzed Direct Amination of the Cage B(4)-H Bond in o-Carboranes: Synthesis of Tertiary, Secondary, and Primary o-Carboranyl Amines. *J. Am. Chem. Soc.* **2016**, *138* (39), 12727–12730.

(51) Hawthorne, M. F.; Young, D. C.; Garrett, P. M.; Owen, D. A.; Schwerin, S. G.; Tebbe, F. N.; Wegner, P. A. The Preparation and Characterization of the (3)-1,2- and (3) -1,7-Dicarbadodecahydroundecaborate (–1) Ions. *J. Am. Chem. Soc.* **1968**, *90* (4), 862–868.

(52) Yoo, J.; Hwang, J. W.; Do, Y. Facile and Mild Deboronation of O-Carboranes Using Cesium Fluoride. *Inorg. Chem.* **2001**, *40* (3), 568–570.

(53) Mortimer, M. D.; Knobler, C. B.; Hawthorne, M. F. Methylation of Boron Vertices of the Cobalt Dicarbollide Anion. *Inorg. Chem.* **1996**, *35* (19), 5750–5751.

(54) Plešek, J.; Heřmánek, S.; Franken, A.; Císařová, I.; Nachtigal, C. Dimethyl Sulfate Induced Nucleophilic Substitution of the [Bis(1,2-Dicarbollido)-3-Cobalt(1-)]Ate Ion. Syntheses, Properties and Structures of Its 8,8′-μ-Sulfato, 8-Phenyl and 8-Dioxane Derivatives. *Collect. Czechoslov. Chem. Commun.* **1997**, *62* (1), 47–56.

(55) Wojtczak, B. A.; Andrysiak, A.; Grüner, B.; Lesnikowski, Z. J. “Chemical Ligation”: A Versatile Method for Nucleoside Modification with Boron Clusters. *Chem. - A Eur. J.* **2008**, *14* (34), 10675–10682.

(56) Stockmann, P.; Gozzi, M.; Kuhnert, R.; Sárosi, M. B.; Hey-Hawkins, E. New Keys for Old Locks: Carborane-Containing Drugs as Platforms for Mechanism-Based Therapies. *Chem. Soc. Rev.* **2019**, *48* (13), 3497–3512.

(57) Sivaev, I. B.; Bregadze, V. V. Polyhedral Boranes for Medical Applications: Current Status and Perspectives. *Eur. J. Inorg. Chem.* **2009**, No. 11, 1433–1450.

(58) Scholz, M.; Hey-Hawkins, E. Carbaboranes as Pharmacophores: Properties, Synthesis, and Application Strategies. *Chem. Rev.* **2011**, *111* (11), 7035–7062.

(59) Brynda, J.; Mader, P.; Šícha, V.; Fábry, M.; Poncová, K.; Bakardiev, M.; Grüner, B.; Cígler, P.; Řezáčová, P. Carborane-Based Carbonic Anhydrase Inhibitors. *Angew. Chemie.* **2013**, *52* (51), 13760–13763.

(60) Cígler, P.; Kožíšek, M.; Řezáčová, P.; Brynda, J.; Otwinowski, Z.; Pokorná, J.; Plešek, J.; Grüner, B.; Dolečková-Marešová, L.; Máša, M.; et al. From Nonpeptide toward Noncarbon Protease Inhibitors: Metallacarboranes as Specific and Potent Inhibitors of HIV Protease. *PNAS.* **2005**, *102* (43), 15394–15399.

(61) Hosmane, N. S. *Boron Science: New Technologies and Applications*; CRC Press: Boca Raton, 2012.

(62) Řezáčová, P.; Pokorná, J.; Brynda, J.; Kožíšek, M.; Cígler, P.; Lepšík, M.; Fanfrlík, J.; Řezáč, J.; Šašková, K. G.; Sieglová, I.; et al. Design of HIV Protease Inhibitors Based on Inorganic Polyhedral Metallacarboranes. *J. Med. Chem.* **2009**, *52* (22), 7132–7141.

(63) Popescu, A. R.; Teixidor, F.; Viñas, C. Metal Promoted Charge and Hapticities of Phosphines: The Uniqueness of Carboranylphosphines. *Coord. Chem. Rev.* **2014**, *269* (1), 54–84.

(64) Guerrero, I.; Kelemen, Z.; Viñas, C.; Romero, I.; Teixidor, F. Metallacarboranes as Photoredox Catalysts in Water. *Chem. - A Eur. J.* **2020**, *26* (22), 5027–5036.

(65) Eo, M.; Park, M. H.; Kim, T.; Do, Y.; Lee, M. H. Polynorbornene Copolymers with Pendent O-Carborane and Carbazole Groups: Novel Side-Chain Donor-Acceptor Copolymers for Turn-on Sensing of Nucleophilic Anions. *Polym.* **2013**, *54* (23), 6321–6328.

(66) Vohlídal, J.; Vangani, V. H.; Plešek, J.; Rajabi, F. H.; Blechta, V.; Němec, I. Synthesis of New Polymers Involving Deltahedral Carborane Units. *Macromol. Chem. Phys.* **1997**, *198* (1), 193–218.

(67) Pichaandi, K. R.; Safronov, A. V.; Sevryugina, Y. V.; Everett, T. A.; Jalisatgi, S. S.; Hawthorne, M. F. Rodlike Polymers Containing Nickel and Cobalt Metal Bis(Dicarbollide) Anions: Synthesis and Characterization. *Organometallics* **2017**, *36* (19), 3823–3829.

(68) Gigante, A.; Duchêne, L.; Moury, R.; Pupier, M.; Remhof, A.; Hagemann, H. Direct Solution-Based Synthesis of $Na_4(B_{12}H_{12})(B_{10}H_{10})$ Solid Electrolyte. *ChemSusChem* **2019**, *12* (21), 4832–4837.

(69) Bennour, I.; Cioran, A. M.; Teixidor, F.; Viñas, C. 3,2,1 and Stop! An Innovative, Straightforward and Clean Route for the Flash Synthesis of Metallacarboranes. *Green Chem.* **2019**, *21* (8), 1925–1928.

2- Experimental section

2.1- Main characterization methods

2.1.1- Light Scattering (DLS, SLS)

Static Light Scattering (SLS)

All light is a composed of radiomagnetic radiation, this mean light is composed of two components: an electric and a magnetic field.[1] When the electric field portion of light interacts with the electrons of a particle it induces an oscillation of their electric dipole. This oscillation at the same time emits electromagnetic radiation, also known as scattering of light. The intensity of the scattered light is going to depend on the polarizability of the molecule (α), and the intensity of the electric field of the incident light $\vec{E}$. The intensity of scattered light is described by

$$I(q) = \frac{16\pi^4 \alpha^2 I_0 cos\theta}{\lambda^4 r^2} \tag{2.1}$$

$$q = \frac{4\pi n_D \sin(\theta/2)}{\lambda} \tag{2.2}$$

Where θ is the scattering angle of, I_0 is the intensity of incident light, r is the distance from the sample to the detector and q is the scattering vector. q is defined only by the wavelength of the laser (λ), the scattering angle and the refractive index of the solvent (n_D). q defines the scale of observation in a scattering experiment. Low q values give us information about particles and their interactions. Meanwhile, larger q values are useful to determine inner structures of particles or study the chain conformation of polymers.

The scattering intensity variates depending on ϑ for particles larger than 20 nm. Particles over this "threshold size" scatter light as if they were composed of several individual scatterers. The scattered light from these individual scatterers is going to have a difference in phase, creating both destructive and constructive interference. The obtained interference pattern is known as form factor, $P(q)$, and gives information about the shape of the particle.

$$P(q) = 1 - \frac{1}{3} q^2 R_g^2 + \ldots \tag{2.3}$$

Where R_g is the radius of gyration. For particles smaller than $20/\lambda$ the intensity is independent of the scattering angle and depends only on the mass of the particle. For such cases $P(q) = 1$.

Equation 2.1 shows the scattered intensity depending on experimental conditions such as r. To obtain an absolute scattering intensity Static light scattering experiments use the Rayleigh ratio, R, which is defined by

$$R = \frac{4\pi^2}{\lambda^2} n_{D,0}^2 \left(\frac{\partial n}{\partial c}\right)^2 \frac{cM}{N_L} \tag{2.4}$$

Where $n_{D,0}^2$ is the refractive index of the solvent, c is the concentration of analyte, M is the molar mass of the scattering particles, and ($\delta n/\delta c$) is the refractive index increment. For non-ideal solutions the scattering intensity equations can be rearranged into a series expansion known as the Zimm Equation

$$\frac{Kc}{R} = \frac{1}{MP(q)} + 2A_2 c + \cdots \tag{2.5}$$

Where K is the contrast factor and A_2 is the second virial coefficient. The specific interactions of the particles with the solvent and their interference pattern are accounted for in the A_2 and the $P(q)$. A_2 is used as an indication of solute-solvent interaction. The contrast factor can be described by

$$K = \frac{4\pi n_0^2}{\lambda_0^4 N_A}\left(\frac{\partial n}{\partial c}\right)^2 \tag{2.6}$$

Where N_A is the Avogadro number. The Zimm equation can be used to determine M and R_g. By measuring several concentrations, the values can be extrapolated to vanishing concentration and vanishing scattering angle.

Dynamic Light scattering (DLS)

The local concentration of particles in solution variates with the thermal density fluctuations of the solvent, which causes the Brownian motion of particles. This means that the interparticle interference pattern also changes in time as the particles move around in solution. The intensity of scattered light decays with a relaxation time, τ_c.[2] If the τ_c is measured after a very short time interval ($\tau << \tau_c$) then the two measurements are related and the decay behavior can be extracted by evaluating the autocorrelation function $g(\tau)$ defined as

$$g(\tau) = \lim_{T\to\infty}\frac{1}{T}\int_0^T I(t)I(t+\tau)dt \tag{2.7}$$

Where $I(t)$ is the intensity of light measured at a time t, $I(t+\tau)$ is the intensity measured after a delay time τ which is variable. T represents the overall duration of the experiment. Experimentally the photons are detected by a photomultiplier and a hardware known as autocorrelator calculates the products of $I(t)\cdot I(t+\tau)$. From this autocorrelation function the τ_c can be evaluated. Furthermore, if all particles have the same diffusion coefficient $g(\tau)$ simplifies to

$$g(\tau) = I_0^2\left(1 + be^{-\tau/\tau_c}\right) \tag{2.8}$$

Where I_0 is the average light intensity and b is a constant. τ_c can then be obtained through curve fitting. τ_c can also be defined as

$$\tau_c = \frac{\lambda_0^2}{16\pi^2 n_0^2 D sin^2(\theta/2)} \tag{2.9}$$

Where D is the diffusion coefficient and n_0 is the refractive index. Once D is obtained it can be transformed into hydrodynamic radius (R_H) of the particles using the Stokes-Einstein equation

$$D = \frac{kT}{f} = \frac{kT}{6\pi\eta R_H} \tag{2.10}$$

Where k is the Boltzmann constant, T is temperature, f is the friction of solution, and η is the viscosity of the solution.

2.1.2- Nuclear Magnetic Resonance (NMR) spectroscopy

Nuclear magnetic resonance occurs when nuclei absorb energy in the way of radiofrequency and reemit it.[3] From this point of view NMR spectroscopy can be considered an absorption spectroscopy technique just like infrared and UV spectroscopy. Only atoms with a non-zero nuclear spin are active in NMR. Shortly, atoms with an even number of both protons and neutrons have no net nuclear spin. Atoms with an odd number of protons and even number of neutrons (or viceversa) have a half-integer spin (i.e. 1/2, 3/2). Lastly, atoms with both protons and neutrons are odd have an integer spin (i.e. 1,2). These integers represent the numerical values of the nuclear spin number I, and are related to the magnitude of the generated dipole by the formula

$$u = \gamma\, I \tag{2.11}$$

Where γ represents the gyromagnetic ratio, unique to each atom.

The overall spin number will dictate the number of orientations a nucleus can have under an external uniform magnetic field, B_0, through the formula $2I+1$. The most studied species ^{1}H and ^{13}C have a ½ spin which gives them 2 possible orientations and 2 energy levels. The protons will be distributed among the two energy levels according to the Boltzmann distribution with a slight excess in the lower energy level. The energy separating both energy levels is given by

$$\Delta E = (h\gamma/2\pi)B_0 \tag{2.12}$$

Where h is Planck's constant. Equation 2.12 shows how ΔE is directly proportional to the applied magnetic field, B_0.

A proton spinning under an external magnetic field precesses about its z axis. This causes that the net macroscopic magnetization, M_0, is aligned with the z axis in the same direction as B_0, but it has no magnetization in the xy plane. If radiofrequency is applied matching the precessional frequency of a proton (Larmor frequency) the proton enters the state of nuclear magnetic resonance

$$v_L = (\gamma/2\pi)B_0 \tag{2.13}$$

In this state the proton absorbs the radiofrequency and can rise to a higher energy state. In modern NMR spectrometers a strong radiofrequency pulse (v_1) is applied whose objective is to tip the net magnetization M_0 into the xy plane. The magnetic components generated in this plane are detected by a receiver coil as projection onto the y axis. All the protons are affected simultaneously by the pulse, and the signal detected represents the difference between the individual v_L of each proton and v_1. The signal obtained is known as FID which is later Fourier transformed to obtain the NMR spectrum.

Once the M_0 is tipped to the xy plane it precesses back towards the original z direction through a process of relaxation. There are two types of relaxation known as T_1 and T_2. Spin-lattice or longitudinal relaxation process (T_1) refers to the transfer of energy from the excited protons to the surrounding protons tumbling at appropriate frequencies. The spin-spin or transverse relaxation (T_2) is the process when there is an energy transfer among the precessing protons. As a rule for the magnitude $T_1 \geq T_2$. For small molecules $T_1 \approx T_2$, but for large molecules T_1 is usually much larger than T_2.

Both relaxation times have a relation to the shape and intensity of signals observed in an NMR spectrum. T_1 is related to the intensity of the peak. T_2 results in dephasing and is seen as line broadening or signal loss. If T1 is too long then the peak intensity is not proportional to the amount of that specific kind of proton, as it happens with ^{13}C.

When a nucleus is excited by the radiofrequency the proton spin can form a spin coupling with neighboring protons through the bonding electrons. The bonding electrons between two nuclei are paired in a way that the spins are antiparallel. When subjected to a magnetic field each nucleus pairs its spin with one of the bonding electrons, again in antiparallel fashion. This effect causes that the signal from a specific nucleus is slightly affected by the coupling leading to a split in the signal. For this splitting to be seen both nuclei need to be active species on NMR (have a non-zero integer number). This means coupling between ^{12}C and ^{1}H won't be visible but coupling between ^{13}C and ^{1}H would be. The coupling helps identify chemical structures by indicating what kind of protons and how many are in the vicinity of a specific nucleus. Nonetheless, in some scenarios it may over complicate the spectra. For example, the ^{1}H spectra of boron clusters. Both ^{10}B and ^{11}B are active NMR species and thus have an effect in the splitting of H atoms. To remove this effect proton spectra for boron clusters is usually obtained with a ^{11}B decoupling, formally written as $^{1}H\{^{11}B\}$. Decoupling is done by emitting a second radiofrequency pulse with the specific frequency of the atoms whose coupling needs to be eliminated.

NMR spectroscopy is mainly used to determine the structure of chemical species. Using the common ^{1}H and ^{13}C in combination with 2D-NMR it is possible to determine how individual atoms are connected to each other. Additionally, NMR of a surfactant at different concentration can be used to determine the critical micellar concentration (CMC). When a molecule changes from being in a monomeric form to being surrounded by others in a micelle the nuclear shielding of some atoms might change, and this is reflected in a shift of the signal. This technique was employed in Chapter 4.1 and 4.2. A similar application is obtained by Diffusion Ordered Spectroscopy (DOSY). This NMR variation is based on the creation of a magnetic field gradient within the NMR tube. This means that the strength of the magnetic field will be different across the tube. In short, the protons are excited via a radiofrequency pulse (90°). Then a magnetic gradient pulse is applied to the sample. Afterwards a second radiofrequency pulse is applied to invert the magnetization (180°). Finally, a second magnetic gradient pulse is applied which will refocus the signal. After the refocusing signal that moved across the gradient due to diffusion will have a decreased intensity. Repeating this process yields a signal decaying as the magnetic field gradient increases. From fitting the signal decay, it is possible to obtain the diffusion coefficient. Performing this experiment at different concentrations allows us to determine at which concentration micellization occurs. This will be shown as a decrease in the diffusion coefficient. This technique was used in Chapter 4.2.

In the polymer science NMR finds many applications. With polymer whose end-group signal is possible to determine NMR represents an excellent tool to determine molecular weight and degree of polymerization. Furthermore, it can be used to assess the mobility of different blocks in the polymer. For example, diblock copolymer micelles in a selective solvent for block-A (non-solvent for block-B) will cause block-B to form the core of the micelle. In scenarios where the T_g of block-B is high enough it can be considered as “frozen”. The lack of movement of the polymer segments in the core makes them “invisible” to typical liquid NMR measurements. This feature can be further utilized to track the mobility of segments upon certain action (i.e: the addition of a small molecule). The lose of mobility is observed in the NMR spectra as decreased intensity or broadening of the signal.[4] This was utilized in Chapter 4.4 to track the mobility of the polymer segments in the micellar corona of diblock copolymer micelles.

2.1.3- Isothermal Titration Calorimetry (ITC)

Isothermal titration calorimetry is a widely used method to directly measure the generated/absorbed heat by molecular interactions. ITC originates a complete thermodynamic profile (ΔH, ΔS, ΔG and *K_a,)* and its frequently used for protein-protein interaction and micellization (demicellization experiments). In our work is was used to study demicellization of boron clusters.

A common set-up consists of two identical cells made of heat conductive and inert materials. One is the reference cell, the other is the sample cell. A syringe coupled with a stirring paddle is inserted into the sample cell and seals the system to atmospheric environment. The syringe has a double function: to stir and to inject aliquots. The aliquots are injected sequentially, upon injection a release or absorption of heat occurs in the sample cell. This change in heat triggers a response which equilibrates the temperature of the sample cell. After the heat signal returns to a base value the automatic injector supplies another aliquot. The process repeats until the injection of aliquots releases no heat other than heat of dilution.

In a common demicellization experiment a syringe is filled with concentrated surfactant at a concentration at least x20 the value of CMC. The sample cell will be filled with the same solvent as the surfactant (e.g: water, saline solution). Once the micelles are injected into the sample cell the surfactant will dilute to a concentration below the CMC, thus demicellization occurs. In subsequent injections the process will repeat itself until the concentration in the sample cell is above CMC. Then no more micellization occurs.

The first injections will register the heat changes of three processes: micelle diffusion, surfactant diffusion and demicellization. In the last stages of the experiment the heat registered will correspond only to micelle and surfactant diffusion. To subtract the heat of non-demicellization processes it is necessary to conduct blank experiments. the heat of surfactant diffusion is determined by using a syringe filled with surfactant below CMC and titrating into the sample cell.

Several models have been used to described micellization. The pseudo-phase separation model was one of the earliest ones. Nonetheless, this model was not fitting for every system due to assumptions in the aggregation number. Afterwards the mass action model was developed. In it aggregation number and counterion condensation are used as important parameters to correctly describe the micellization. A simplified version of the mass action model is described here (more detailed model can be found in Chapter 4.2).

$$nS^- + \beta nB^+ \leftrightarrow M_n^{-(1-\beta)n} \qquad (2.14)$$

Where is *S* is the surfactant in monomeric form, *B* is the counterion, *β* is the counterion condensation and *M* is the micelle made up of *n* monomeric units.

At any given moment the total surfactant concentration (c_t^s), and the total counterion concentration (c_t^B) remain identical $c_t = c_t^s = c_t^B$. Nonetheless the concentration of individual components $[M_n{}^{(-(1-\beta)n)}]$, $[S^-]$ and $[B^+]$ changes. These quantities are related by the following equation

$$c_t = [S^-] + n \cdot [M_n^{-(1-\beta)n}] = [B^+] + \beta n \cdot [M_n^{-(1-\beta)n}] \qquad (2.15)$$

The micelle formation has the equilibrium constant

$$K = [M_n^{-(1-\beta)n}]/([S^-]^n[B^+]^{\beta n} \qquad (2.16)$$

$$\Delta G = -RT \ln K \qquad (2.17)$$

With equations 2.16 and 2.17 is possible to determine the concentration of the individual components at any concentration.

References

[1]- Schärtl, W. *Light Scattering from Polymer Solutions and Nanoparticle Dispersions*; Springer: Berlin, 2007.

[2]- Munk, P.; Aminabhavi, T. M. *Introduction to Macromolecular Science*; John Wiley & Sons, Inc; New York, 2002.

[3]- Silverstein, R. M.; Webster, F. X.; Kiemle, D. J. *Spectrometric Identification of Organic Compounds*; John Wiely & Sons, Inc; New York, 2005.

[4]- Kawaguchi, S.; Winnik, M. A.; Ito, K. Macromolecules **1996**, 29, 4465.

2.2- Experimental Set up

2.2.1- NMR

In all publications the NMR data for identification of structure and integrity of studied molecules were recorded using a Bruker AVANCE III spectrometer operating at the proton Larmor frequency of 600 MHz. ^{1}H, ^{13}C, and ^{15}N experiments were measured using a cold probe, whereas for ^{7}Li a broadband probe was used. ^{15}N chemical shift was observed indirectly by measuring ^{1}H−^{15}N HMBC correlation spectrum employing the long-range coupling constant of 5 Hz. The carbon T1 relaxation of COSAN and acetonitrile was estimated in two separate inversion recovery experiments using 9−12 values of variable delay adapted to the short (about 1 s) and very long (about 30 s) relaxation times.

In Publication I and II the double stimulated echo experiment with bipolar pulse field gradients was used to monitor translational diffusion for both ^{1}H and ^{7}Li signals. The diffusion time and the duration of gradients were optimized to follow signal decays down to at least 10% of the initial value in all cases. The diffusion coefficients were calibrated using a standard sample of 1% H2O in D2O (doped with GdCl3) assuming the diffusion coefficient 1.9 × 10−9 m2 s−1 for the HDO signal at 25 °C. For lithium, the effect of the magnetic field gradients was recalculated using the corresponding gyromagnetic ratio. Data were processed using the spectrometer software (Topspin 3.5, Bruker).

^{11}B and ^{19}F-NMR spectra were recorded on a Bruker Avance 400 spectrometer at 25 °C. When measuring ^{11}B special quartz NMR cuvettes were used in order to minimize the background signal from normal cuvettes.

In Publication III the polymer was characterized through Magic-angle spinning (MAS)-NMR using a Bruker Advance 500 spectometer at 25°C for ^{11}B and ^{13}C.

2.2.2- SAXS

For analysis of COSAN micelles in Section 4.1 and 4.2 the SAXS experiments were performed using a pinhole camera (Molecular Metrology SAXS System) attached to a microfocused X-ray beam generator (Osmic Micro-Max 002) operating at 45 kV and 0.66 mA (30 W). The camera was equipped with a multiwire gas-filled detector with an active area diameter of 20 cm (Gabriel design). Two experimental setups were used to cover the q range of 0.04−11 nm−1. Scattering vector q = (4πn/λ) sin θ, where λ = 0.154 nm is the wavelength and θ is the angle between the incident X-ray beam and the detector measuring the scattered intensity. Glassy carbon sample, obtained from Rigaku Company (Japan), was used to measure intensity.

In the case of Section 4.3 the SAXS experiments for polymeric solutions were carried out on the P12 BioSAXS beamline (PETRA III storage ring, EMBL/DESY, Hamburg, Germany), equipped with a Pilatus 2M detector. The measurement was carried out at 20 °C and the sample-detector distance 3 m, allowing for covering the q-range interval from 0.07 to 4.4 nm-1 for the X-ray wavelength lambda = 0.1 nm. The q range was calibrated using the diffraction patterns of silver behenate. The experimental data were normalized to the transmitted beam intensity and corrected for nonhomogeneous detector response, and the background scattering of the solvent was subtracted. The solvent scattering was measured before and after the sample scattering to control for possible sample holder contamination. 20 consecutive frames with 0.05 s exposures comprising the measurement of the solvent, sample, and solvent were performed. Data have been checked for radiation damage. The final scattering curves were processed by automated data acquisition software and recalculated to absolute scattering intensities. The data were fitted to different models as described in the Supporting Information using the SASfit 0.94.7 software.

2.2.3- Fluorescence

All steady-state fluorescence spectra were acquired on a Fluorolog FL-3-22 (Horiba Jobin Yvon, France) equipped with an excitation and emission double monochromators and a 450 W xenon lamp. Polymer concentrations were always kept at 0.5 mg ml^{-1}.

2.2.4- TEM (cryo)

In Publication III TEM and cryo-TEM were used. The later was used to analyze the nanoparticles in solution and the procedure is the same as for Publication IV. The standard TEM was used with various staining techniques in order to determine the real dimensions of core/corona and the possible existence of inner compartments. Three staining techniques were used: Uranyl acetate (negative staining), osmium tetroxide and ruthenium oxide (both positive staining). In short, the negative staining was prepared by directly adding the staining agent (2µl) into the carbon-coated copper grids after the blotting. For the positive staining the grids with sample were put in a close compartment with OsO_4 (crystals, 2 hours) or RuO_4 (freshly prepared solution, 5 minutes) after blotting. After staining the samples were immediately measured.

For Publication IV the cryo-TEM was used to visualize the formed nanoparticles. A 3 µl drop of the sample solution was applied to an electron microscopy grid with carbon-covered polymer supporting film (lacey-carbon grids LC200-CuC, Electron Microscopy Sciences), glow discharged for 30 s with 5 m*A* current. Sampled was blotted (Whatman No. 1 Filter paper) for 1 s, and the grid was immediately plunged into liquid ethane held at -183 °C. The sample was then transferred without rewarming into a Tecnai Sphera G20 electron microscope (FEI, Hillsboro, OR) using a Gatan 626 cryo-specimen holder (Gatan Inc., Pleasanton, CA). In both cases, images were recorded at an accelerating voltage of 120 kV and magnifications ranging from 11 500× to 50 000× using a Gatan UltraScan 1000 slow scan CCD camera in the low-dose imaging mode, with an electron dose not exceeding 1500 electrons per nm^2. The applied underfocus typically ranged between 1.5 and 2.7 µm. The specimen thickness varied between 100 and 300 nm.

2.2.5- Conductometry

Conductivity of COSAN salts was measured with a CDM 230 Radiometer. All measurements were carried out at temperature 25°C by submerging the measuring cell in a water bath with controlled temperature. All values presented are averaged from triplicate measurements. Values of specific conductivity were plotted against concentration to obtain the degree of micelle ionization.

2.2.6- Electrophoretic light Scattering

The measurements were carried out with Nano-ZS Zetasizer (Malvern Instruments, UK). Zeta-Potential was obtained from electrophoretic mobility values using the Henri equation in the Smoluchowski approximation. Values presented are averaged from 45 measurements.

2.2.7- Isothermal titration calorimetry

Microcalorimetric titrations were performed in a Nano ITC, TA instruments – Waters LLC, New Castle, USA. The microcalorimeter consists of a sample cell and a reference cell (24K gold). The sample cell is connected to a 50 µL syringe. Samples were prepared with either MiliQ water or with the indicated concentration of salt (LiCl, NaCl, KCl or HCl). Samples were degassed before being injected. Different temperatures were used for demicellization experiments (4-60°C).

3- Research aims

The study of metallacarboranes, more precisely of cobalt bisdicarbollide (COSAN), has been ongoing at Prof. Pavel Matějíček laboratory for more than a decade. Several pioneering studies on COSAN solution behavior and its effect on polymers were originated in this laboratory. In more recent years, the interaction of COSAN with polymers in solution was studied in greater depth in search of applications such as drug delivery. Nonetheless, several questions remained unanswered about both topics and more detailed explanation were needed to further advance the field. Therefore, the research aims were focused on broadening the knowledge by studying in greater detail by combining thermodynamic and coarse-grained simulations to reach new conclusions. In summary, the research aims can be described as:

- The complete description of the COSAN micellization system by thermodynamic methods, focusing on the effect of counterions and co-solvents.

- The examination in detail on the effect that COSAN has on polymers and its use as a model particle for hydrophobic ions.

- The study of boron containing nanostructures through the self-assembly of carborane containing triblock terpolymers.

4- Results

The results section is organized with the scientific papers published during the duration of the PhD studies. In all of them I contributed as first author. The collaborations were done both locally (Charles University: Institute of Biology and Medical Genetics, First Faculty of Medicine, Faculty of Science; Institute of Macromolecular Chemistry) and internationally (University of Ljubljana, Slovenia, University of Lund, Sweden; Universitat Autonoma de Barcelona, Spain). The following list of publications is ordered chronologically:

1- Amphiphiles without Head-and-Tail Design: Nanostructures Based on the Self-Assembly of Anionic Boron Cluster Compounds.
Fernandez-Alvarez, R.; Ďorďovič, V.; Uchman, M.; Matějíček, P.
Langmuir 34 (2018) 3541-3554.

2- Total Description of Intrinsic Amphiphile Aggregation: Calorimetry Study and Molecular Probing **Fernandez-Alvarez, R.**; Medoš, Ž.; Tošner, Z.; Zhigunov, A.; Uchman, M.; Hervø-Hansen, S.; Lund, M.; Bešter-Rogač, M.; Matějíček, P.
Langmuir 34 (2018) 14448-14457.

3- Synthesis and self-assembly of a carborane-containing ABC triblock terpolymer: morphology control on a dual-stimuli responsive system
Fernandez-Alvarez, R.; Hlavatovičová, E.; Rodzeń, K.; Strachota, A.; Kereïche, S.; Matějíček, P.; Cabrera-González, J.; Núñez, R.; Uchman, M.
Polym. Chem. 10 (2019) 2774-2780.

4- Interactions of star-like polyelectrolyte micelles with hydrophobic counterions
Fernandez-Alvarez, R.; Nová, L.; Uhlík, F.; Kereïche, S.; Uchman, M.; Košovan, P.; Matějíček, P.
J. Colloid Interface Sci. 546 (2019) 371–380.

4.1- Publication I

Amphiphiles without Head-and-Tail Design: Nanostructures Based on the Self-Assembly of Anionic Boron Cluster Compounds*

Abstract

Anionic boron hydride cluster compounds (ABCCs) are intrinsically amphiphilic building blocks suitable for nanochemistry. ABCCs are involved in atypical weak interactions, notably dihydrogen bonding, due to their peculiar polyhedral structure, consisting of negatively charged B-H units. The most striking feature of ABCCs that differentiates them from typical surfactants is the lack of head-and-tail structure. Furthermore, their structure can be described as intrinsically amphiphilic or aquaneutral. Therefore, classical terms established to describe self-assembly of classical amphiphiles are insufficient and need to be reconsidered. The opinions and theories focused on the solution behavior of ABCCs are briefly discussed. Moreover, a comparison between ABCCs with other amphiphilic systems is made focusing on the explanation of enthalpy-driven micellization or relations between hydrophobic and chaotropic effects. Despite the unusual structure, ABCCs still show self- and co-assembly properties comparable to classical amphiphiles such as ionic surfactants. They self-assemble into micelles in water according to the closed association model. The most typical features of ABCCs solution behavior is demonstrated on calorimetry, NMR spectroscopy and tensiometry experiments. Altogether, the unique features of ABCCs makes them a valuable inclusion into the nanochemisty toolbox to develop novel nanostructures both alone and with other molecules.

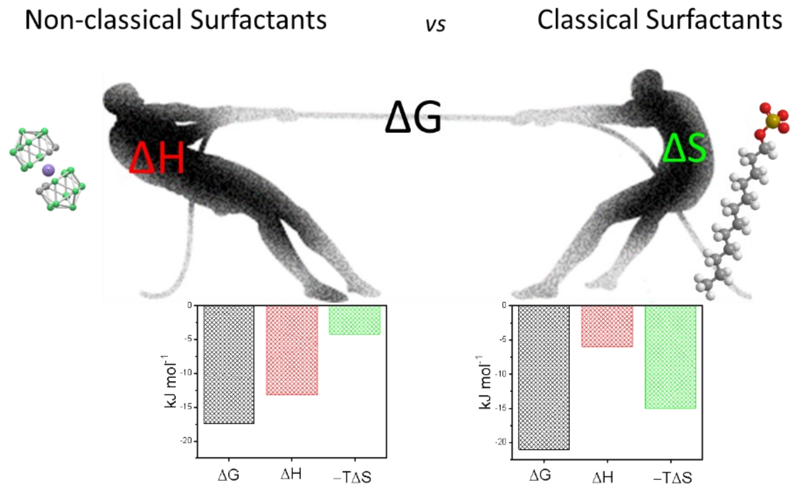

---

*Version presented here has small format modifications compared to the original form at: Amphiphiles without Head-and-Tail Design: Nanostructures Based on the Self-Assembly of Anionic Boron Cluster Compounds. Fernandez-Alvarez, R.; Ďorďovič, V.; Uchman, M.; Matějíček, P. Langmuir 34 (2018) 3541-3554

Introduction

Self-assembly is a well-known process and simultaneously one of the most useful principles in nanochemistry.[1] This bottom-up process is based on spontaneous association of building blocks leading to nanostructures with a different level of ordering. Self-assembly is crucial for preparing nanomaterials[2] using chemical patterning, nanolithography, and layer-by-layer methods. Moreover, self-assembly can create monolayer structures including self-assembly monolayers, nanoparticles of various shapes and sizes (nanoclusters, nanorods, nanotubes and nanosheets, among others), porous materials, photonic crystals and metal organic frameworks, for example. Five key principles should be considered when preparing nanostructures by self-assembling: (i) the shape, scale and surface structure of building blocks, (ii) attractive and repulsive interactions between building blocks, (iii) conformational changes in building blocks, (iv) interactions between building blocks and solvents, interfaces and templates, and (v) building block dynamics and transport.[2]

The *building block* is a cornerstone of self-assembly and a term common to all aforementioned principles. The adequate and careful choice of building blocks opens great opportunities for chemical designers. Even though the size of building blocks varies considerably, they usually consist of a single molecule. In addition to low molecular mass compounds, macromolecules[2] (usually hydrocarbon-based) play a key role in self-assembly due to the various architectures that are available thanks to recent advances in macromolecular chemistry.

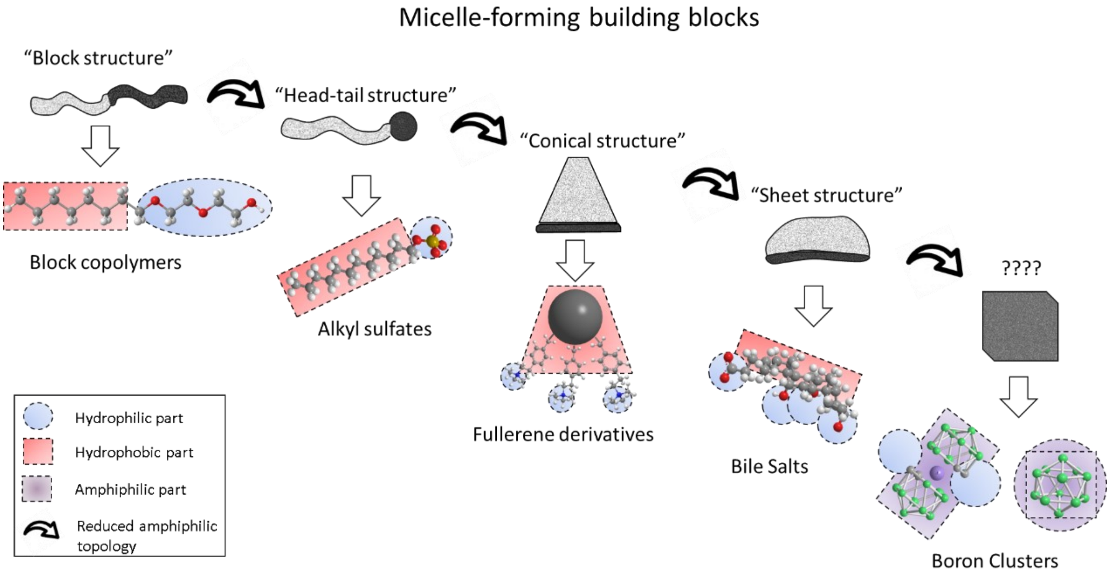

Figure 4.1.1 Schematic representation of molecular amphiphilic building blocks. The shape (top) and molecular structure (bottom) of hydrophobic (light grey) and hydrophilic (dark grey) parts of different types of micelle-forming blocks are shown from left to right in a decreasing order of amphiphilic topology. Classical surfactants may have a typical shape, including (i) amphiphilic block copolymers, which are commonly found in enthalpy-driven micellization

processes [Ref 6] and (ii) head-and-tail surfactants, such as alkyl sulfates (for example SDS), consisting of a long aliphatic tail and a small charged head and showing entropy-driven micellization in water,[Ref 74] or an atypical shape, including (iii) conical molecules with hydrophilic groups attached to fullerene.[Ref 11] (Interestingly, although these micelle-forming building blocks have a classical amphiphilic shape, they are surface-inactive because of their molecular design) and (iv) bile salts, which are biologically important amphiphiles that form a special class of surfactants.[Ref 7-10] Their micelles show a clear, although incomplete, separation of hydrophobic and hydrophilic parts. The driving force of the aggregation process is an intricate combination of the classical hydrophobic effect with hydrogen bonding between hydrophilic groups. Conversely, non-classical surfactants have undefined topologies, including (v) Anionic Boron Cluster Compounds, for example COSAN and dodecaborate, which are a new class of amphiphilic building blocks.

Amphiphilic building blocks are usually modelled by connecting the hydrophobic and hydrophilic moieties (Figure 4.1.1). The self-assembly, in this case termed micellization, of building blocks with classical block or head-and-tail structures is usually described using the (i) Pseudo Phase Model,[3, 4] when micellization occurs as a microphase separation, or (ii) the closed association model – also known as the Mass Action Model.[3, 4] In both cases, the micelles have defined core-shell structures in which the hydrophobic core is shielded by the hydrophilic shell.[5, 6] In addition to these typical structures, classical surfactants may also show atypical structures, which have been described in the literature as sheet[7-10] or conical-shaped[11] objects. However, all these structures follow the classical paradigm with clearly defined hydrophobic and hydrophilic parts in their molecules

In the present feature article, we aim to introduce anionic boron cluster compounds (ABCCs) as a class of building blocks suitable for nanochemistry. After introductory remarks on the structure, size and chemistry of boron hydrides (boranes, carboranes and metallacarboranes), we will focus on terminology because classical terms fail to accurately describe the behavior of ABCCs in solution. Before we outline the self-assembling potential of ABCCs in solution and in complexes with polymers, according to the aforementioned principles, the aggregation of classical and less classical surfactants will be discussed towards contextualizing our work. This Feature article will be focused on 10- and 12-vertex ABCCs, as well as metallacarboranes and their solution behavior. For information on their reactivity and structure please refer to the very thorough reviews on closo-borane clusters,[12,13] $C_2B_{10}H_{12}$,[14] $CB_9H_{11}^{-}$[15] and other carboranes.[16-18] Nanochemists should not be afraid of shifting their “theoretical” paradigms based on empirical evidence. Thus, we will also review the experimental methods that we have used to best understand the peculiar behavior of ABCCs in water solutions and dispersions.

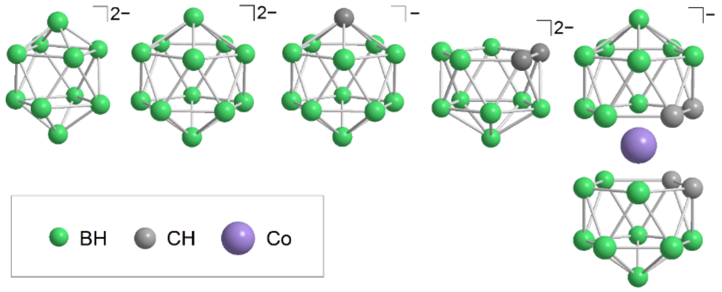

Figure 4.1.2 Structures of the most studied anionic boron cluster compounds (left to right): decaborate $[B_{10}H_{10}]^{2-}$; dodecaborate $[B_{12}H_{12}]^{2-}$; 1-carbadodecaborate $[CB_{11}H_{12}]^{-}$; 1,2-dicarbollide $[1,2\text{-}C_2B_9H_{11}]^{-}$; COSAN $\{3,3`\text{-}Co[1,2\text{-}C_2B_9H_{11}]_2\}^{-}$.

Boron Cluster Compounds

Boron is one of the few elements that form long-chain structures through a series of covalent bonds, in a process termed catenation. Boron catenation yields borohydrides, including boranes, carboranes and metallacarboranes (Figure 4.1.2) – boron cluster compounds, which are regarded as the boron equivalents of aliphatic and aromatic hydrocarbons, heterocycles and metallocenes, respectively. The shape of boron clusters is atypical due to their two-electron three-center bonds[19] with extensive electron delocalization over the cluster area, which is manifested as 3D aromaticity that can be successfully matched to their 2D carbon counterparts. Albeit, this aromaticity is fundamentally different since the electron delocalization occurs using sigma bonds instead of π-bonds as observed in 2D aromaticity.[20-22]

The electronegativity of boron is lower than that of hydrogen and carbon. This has important consequences for the discussion on bonding, weak interactions (Chapter 3) and reactions in boron chemistry. These properties also allow boron clusters to form the so-called dihydrogen bonds[23] that have been studied theoretically (quantum mechanics)[24] and experimentally (crystallography).[25]

Numerous neutral or anionic boranes have been prepared since they were first synthesized in 1912.[26] The most studied *closo*-boranes, decaborate $[B_{10}H_{10}]^{2-}$ and icosahedral dodecaborate $[B_{12}H_{12}]^{2-}$, are the parent units of large number of derivatives. Dodecaborate is arguably the most stable molecule known to chemistry, withstanding temperatures above 800°C.[19] Carboranes (in formal nomenclature carbaboranes) are boranes with one or more carbon atoms in the cluster framework. Most carboranes have two carbon atoms (three stable isomers, *ortho*-, *meta*- and *para*-carborane derived from their usual synthesis from alkynes. In carboranes, the C–H groups are more polar than the B–H. Thus, the hydrogens of C–H groups are weakly acidic.[27]

Closo-carboranes can be specifically degraded to *nido*-carboranes by removing the BH vertex next to the two CH vertices. The degradation leads to dicarbollides (Figure 4.1.2), including $[1,2\text{-}C_2B_9H_{11}]^{2-}$, which are suitable for metal complexation. This led to the discovery of metallacarboranes, which have become a specific subarea of boron chemistry. Since their first synthesis by Hawthorne in 1965,[28] carborane complexes of nearly all transition metals and many lanthanides have been synthesized and described.

Anion (*commo*-3,3'-Co(III)$(1,2\text{-}C_2B_9H_{11})_2)^-$ (Figure 4.1.2) was among the first metallacarborane synthesized,[28] and is the most studied carborane with hundreds of synthesized derivatives.[29] Several names of these compounds can be found in literature, such as cobalt bis(dicarbollide), cobaltabisdicarbollide, bis(dicarbollyl)cobaltate(–1) and the colloquial abbreviation COSAN (derived from CObalt SANdwich). Most COSAN salts are quite soluble in water and many organic solvents, excluding ammonium and alkylammonium salts, which have low solubility.[30]COSAN is exceptionally thermally and chemically stable and has all the key properties of carboranes, which makes it an interesting building block for self-assembly.

In summary, anionic and neutral boron clusters are fully artificial inorganic compounds[27] that have been mainly used as a "passive" source of boron atoms for boron neutron capture therapy in several types of cancer[31-33] and radionuclide extraction[34] Due to their unusual interaction potential, boron clusters and their derivatives are also intensively studied for more advanced biomedicine purposes (drug design)[32, 35,36] and other applications in different research areas and practical fields,[27, 37,38-40] including high temperature-resistant polymers, solid electrolytes, battery technology or catalysts.[41-46]

Weak Bonding of Boron Cluster Compounds Building Blocks

The current paradigm seeks to explain most physicochemical properties in terms of specific and locally acting interactions. The weak and non-covalent bonds underlying the assembling capability of boron cluster compoundss should be considered when analyzing ABCCs as building blocks. Due to the presence of B-H terminal hydrogens with a slightly negative partial charge, They are usually involved in non-classical types of bonding. Boron cluster compounds are poor H-bond acceptor and the partial negative charge of hydrogens also makes them bad H-bond donors. Therefore, classical hydrogen bonding has never been observed in boranes. The weak bonding interactions presented in this chapter play a key role on the interaction with RP-HPLC, which is a useful method that has been used to classify the hydrophobicity of boron clusters and its derivatives. [47-50]The hydrophobic effect, which can be considered a type of non-covalent interaction, is extensively discussed in Chapter 5.

Weak hydrogen bonds are considerably weaker than classical hydrogen bonds and are formed when the H-bond donor is C–H[51,52] (C–H···O, N, Cl, I) and/or the H-bond acceptor is the electron density of aromatic molecules (N, O, C–H···π). In carboranes, the presence of weak hydrogen bonding (such as C–H···O, N, S, halogen and P) has been observed in the crystal structures of carborane derivatives,[53,54] and C–H···π bonding has been found in carborane systems with benzene rings.[55] IR spectroscopy is a useful tool to identify this type of bonding in solid state.[56] Moreover, NMR has detected this weak hydrogen bonds in solution, entailing that they are strong enough to withstand solvation and not only existent in solid-state.[57]

Dihydrogen bonds are energetically weaker interactions than classical hydrogen bonds occurring between proton donors Y–H (Y = N, O, S, C) and the σ-bonding electron pair of M–H bonds in hydrides (M = electropositive atom, such as B, alkali or transition metals). Spectroscopic and structural evidence of dihydrogen bonds, including C-H···H-B, N-H···H-B, O-H···H-B, and S-H···H-B, has been found in heteroboranes, resulting from both electrostatic and dispersion interactions, and their energy increases with donor proton acidity. Studies have shown that they help to stabilize carborane structures in crystals,[58] materials,[25] biomolecules[24] and even water.[59]

B-H···π and π-hole contacts have been recently proposed as a new type of non-classical hydrogen bonding. The close contact between negatively charged terminal B-H hydrogens and the π-aromatic system was observed by X-ray diffraction in several carborane-based complexes.[60,61] The existence of such bonds was later questioned by refined quantum calculations and interpreted as a nonspecific dispersion-driven contact.[62,63] Therefore, the B-H...π contact is most likely enforced by steric circumstances in the solid state and does not exist as a "genuine" bond. This should not be confused with the bonding of π-systems with positively charged bridging protons (B-H_b) occurring in some types of boranes.[64-66]

σ-hole bonding is the interaction of halogen or chalcogen atom X in some molecules (R–X) with electron donor (Lewis basis). Depending on the type of X atom, this bonding is called halogen, chalcogen or pnictogen bonding. In halogen bonds (Cl, Br, I), the three pairs of unshared halogen electrons form a belt of negative electrostatic potential around its central region with a positive "σ-hole" on the outermost portion of its surface, centered around the R-X axis,[67] and this σ-hole interacts with negative regions of other molecules. Furthermore, studies have shown that this type of bonding is much stronger in carboranes than in organic architectures.[68-69]

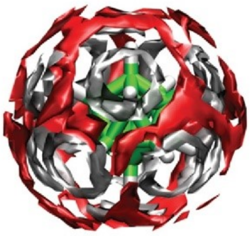

Figure 4.1.3 The spatial distribution function of the hydrogen (grey) and oxygen (red) atoms of water around dodecaborate anion, $[B_{12}H_{12}]^{2-}$, showing the first solvation shell. Reproduced from [Karki, K.; Gabel, D.; Roccatano, D. Structure and Dynamics of Dodecaborate Clusters in Water. *Inorg. Chem.* **2012,** *51* (9), 4894-4896]. Copyright (2012) American Chemical Society.

Terminology

Electroneutral boron cluster compounds, including *closo*-carboranes, are usually regarded as exceptionally hydrophobic (lipophilic) compounds.[27,48] However, the nature of ABCCs, is more controversial (Figure 4.1.2). ABCCs have a “non-classical” structure, due to the presence of B-H units and delocalized negative charge, which complicates the description of their behavior and self-assembling in solution using classical terminology. They show surface activity and are soluble in both water and oil,[70,71] but lack the head-and-tail structure of classical surfactants and amphiphiles. Thus, their hydrophobicity and hydrophilicity cannot be determined based on the length of the hydrophobic tail or the size of the hydrophilic head.[72] Self-assembly is driven by the hydrophobic effect in the case of COSAN,[71,73] but the entropy term has only a small contribution to the free energy of COSAN micellization. The entropy is otherwise the main driving force for surfactant micellization.[5,74] The hydration profile and bulkiness of ABCCs (Figure 4.1.3) are similar to those of chaotropes, whose concept has been established to clarify the Hofmeister series. However, typical chaotropes are not hydrophobic and do not aggregate in water.

Recent studies from our group have shown that the mechanism of COSAN self-assembling in water (Chapter 6 and 7.1) is fully comparable with classical surfactant micellization, obeying the closed association model.[3, 4] However, the structure of COSAN assemblies is hardly comparable with the stereotypical image of a micelle. The terminology of the self-assembling process and its associates has not been settled for ABCCs yet, and terms, such as micelles, aggregates or associates are simultaneously used in the literature.[71,75] According to the IUPAC definition, micelles are aggregates of colloidal dimensions, which exist in equilibrium with the molecules or ions from which they are formed. Therefore, ABCCs aggregates can be termed as micelles.

The classical terminology is somehow obsolete if applied to boron cluster compounds. There are two solutions: (i) modifying the definitions of previously established terms, or (ii) proposing new ones. To avoid confusions, we will briefly describe the classical terms first. Then, we will indicate all ABCCs similarities and peculiarities. Lastly, the ongoing discussion on terminology in the community of boron physical chemists will be addressed.

Classical terms related to ABCCs

Amphiphiles can be divided into two separate regions: (i) *hydrophobic* and (ii) *hydrophilic*. Hydrophobicity or amphiphilicity is quantified using the octanol-water partition coefficient, P_{ow}.[76] In general, amphiphilic molecules are surface-active and undergo self-assembly in water. However, the size, shape, structure and compactness of the associates are highly variable.

Surfactants (tensides or detergents) strongly decrease the surface tension of their solvents.[5] Such molecules typically have an amphiphilic structure, accumulate at air/water and oil/water interfaces and form multimolecular associates – micelles above the critical micelle concentration (CMC). The ratio of hydrophilic to hydrophobic parts is expressed using the empirical parameter hydrophile-lipophile balance.[77]

Hydrotropes increase the solubility of otherwise poorly soluble compounds in water. This shows that hydrotropes lack a common chemical motif. Alkyl-hydrotopes are specially related to the subject of interest because they are surfactants with a very short hydrophobic part[78-80] and surface-active yet usually fail to aggregate in water.

Pickering stabilizers are micro- or submicro-objects of various sizes, shapes and origins that keep oil-water dispersions stable over time (Pickering emulsions).[81] Their morphology, behavior and interface residence time are closer to macro- rather than to nano-objects and molecules. The stabilization energy is proportional to the particle size and surface tension between phases and peaks when both oil and water contact angles in respect to the particle are close to 90 degrees.

Chaotropes and kosmotropes. In recent decades, peculiar molecular effects on the structure of water molecules near the object of interest – ion, in our case – were commonly explained based on the stability of protein dispersions, that is, according to the well-known Hofmeister series. Subsequently, these effects were also related to the structure of the hydration shell around the corresponding ion considering that water molecules around chaotropes are less ordered than bulk water, conversely in kosmotropes water molecules have a more ordered “structure”. However, the “structure-of-water” paradigm has most recently shifted towards a “specific-interaction” concept.[82,83]

ABCCs as Intrinsic Amphiphiles or Aquaneutrals?

The unusual molecular structure of ABCCs prevents them from forming classical hydrogen bonds. Although dihydrogen bonds (Chapter 3.2.) between water molecules and boranes occurs (the hydration shell of dodecaborate in Figure 4.1.3),[59] this interaction is much weaker than classical hydrogen bonding and, therefore, boron cluster compounds tend to avoid contact with water, yet most ABCCs are very water soluble.[27] This clear contradiction has prompted several studies trying to explain the behavior of numerous ABCCs in solution, particularly COSAN. Initially, in 2001, Popov and Borisova assessed the surface activity of COSAN showing its amphiphilic behavior.[84] Later, computational studies conducted by Wipff group showed that COSAN accumulates at the water/organic solvent interface. Simultaneously, small COSAN aggregates were predicted by computer simulation.[70,85,86] Subsequently, experimental evidence of COSAN aggregation supported these self-assembly predictions (first reported by Matejicek *et al*).[75,87,88] However, COSAN hydrophobicity, amphiphilicity and surface activity remain controversial topics, as shown by the discrepant explanations that have been published in the literature.

The first concept was proposed by Teixidor and Zemb,[75,89,90] who described the solution behavior of H[COSAN] in water as a by labelling with a θ-shaped amphiphile assuming that COSAN consist of two bulky and highly hydrophobic dicarbollide clusters surrounding a cobalt (III) ion, which acts as the polar part of the amphiphile (Figure 4.1.2). However, such explanation is incorrect and overlooks the details of the molecular structure of a COSAN cluster.[23] This model has since been refined, proposing that the C-H…H-B dihydrogen bonds[88] of metallacarboranes account for their tendency to aggregate, albeit disregarding the hydrophobic effect as the driving force of self-assembly. Furthermore, the concept of inter-cluster dihydrogen bonding fails to explain the aggregation tendencies of ABCCs without C-H segments.[73]

ABCCs were classified as molecular-scale Pickering stabilizers due to the shape of these clusters and their surface activity.[71] However, this point of view is incoherent because clusters have a sub-nanometer size.[91] Therefore, the stabilization energy would be similar to the thermal motion (~1 *kT*). Moreover, it is impossible to define the contact angle of the clusters.

COSAN self-assembly has been recently compared with the SDS micellization, indicating the hydrophobic effect as the general driving force of aggregation for all amphiphiles. This thorough experimental study clearly showed that both SDS and COSAN micellization follows a mechanism of closed association.[71] However, the enthalpy term predominantly contributes to the free energy of COSAN aggregation. This behavior has been attributed to the nonclassical hydrophobic effect, in studies on protein-substrate interaction, or other host-guest processes, for example, the interaction of bile salts and carboranes with the cyclodextrin cavity.[10,49,92,93] Thus, COSAN aggregation is the only known example of an enthalpy-driven micellization.

Other ABCCs have also shown amphiphilicity, including hydrophilic and highly symmetric *closo*-boranes, according to evidence from the Gabel group, who introduced the term superchaotropicity to describe and understand the hydrophobic action of hydrophilic dodecaborate anions, (more comments in Chapter 5).[59,92] Generalizing this chaotropic behavior to other hydrophobic ABCCs such as COSAN is debatable, albeit more realistic than claiming that dodecaborate behaves similarly to SO_4^{2-} in aqueous media, which is a well-known kosmotropic anion.[88]

ABCCs differ in size, charge and hydrophobicity (Figure 4.1.2). This affects their surface activity and aggregation mechanism.[73] Tensiometry and chromatography experiments allow ordering ABCCs from small hydrophilic clusters, such as decaborate, to the fairly hydrophobic COSAN.[73] Based on the analogy of ABCCs with alkyl hydrotropes-surfactants, it seems plausible to assign dodecaborate to hydrotropes and COSAN to surfactants. However, our recent tensiometry measurements (Chapter 7.2.) showed that single COSAN clusters have values of surface pressure at the air/water interface as low as ~10 mN/m. The previously published data[71,73,94] are most likely affected by the presence of hydrophobic impurities of unknown origin. Therefore, the term surfactant should be used cautiously when referring to ABCCs.

Extensive studies conducted in our laboratory have shown that all ABCC form multimolecular aggregates and decrease the surface tension of water.[73] Thus, we have recently proposed the term “stealth amphiphiles” to describe ABCC based on the contrast between their “anti-amphiphilic” shape (dodecaborate resembles a Platonic solid) and their amphiphilic behavior. ABCCs presumably have an intrinsic amphiphilic nature, ranging from the rather hydrophilic decaborate to the bulky COSAN. Within the boron chemistry community, the classification of ABCCs as amphiphiles is controversial because they lack clearly hydrophilic and hydrophobic parts in their clusters. Therefore, he terms *aquaneutral* (Latin) or *hydrooudeteric* (Greek) have been proposed by Detlef Gabel because ABCCs are very water soluble yet only weakly hydrated.

Hydrophobic and Chaotropic Effects Induced by ABCCs

The hydrophobic effect is described as the arrangement of water molecules around a hydrophobic object leading to spontaneous aggregation processes. These water molecules are still debated among chemists, including some who describe them as an ice-like frozen structure with a more rigid hydrogen bond network than that of bulk water.[95] However, neutron scattering experiments have failed to account for the higher ordering of water molecules around hydrophobic groups.[95] This is supported by the experimental evidence of Brandeburgo *et al*, who observed slower hydrogen bond dynamics around hydrophobic groups by molecular dynamics and mid-infrared pump-probe spectroscopy.[96] However, results have consistently shown that water around hydrophobic groups has lower entropy and higher heat capacity than bulk water.[10] In micellization, the displacement of this “structured” water induces a large and positive ΔS_{mic} and is presumably the main reason for surfactant aggregation (Figure 4.1.4). In classical surfactants, the difference in entropy between the water molecules surrounding the hydrophobic group and bulk water decreases with temperature. The process becomes less entropy- and more enthalpy-driven. This is clearly observed in compensation plots (i.e., entropy-enthalpy compensation).[10,97]

Conversely, the nonclassical hydrophobic effect is considered as the presence of non-structured water molecules around a hydrophobic group.[10] As previously mentioned, it is observed in interactions between hydrophobic ligands and the hydrophobic pockets of proteins.[98-101] Although most of these interactions are entropy-driven because "structured" water molecules are released from the hydrophobic pocket, ΔH-driven interactions surprisingly occur in some cases. In these processes, the release of "non-structured" water molecules from the hydrophobic pocket will cause a small entropy change because they already have high degrees of freedom. The molecular interpretation of nonclassical hydrophobic effect is still debated, but the enthalpy-driven process in which two hydrophobic groups interact is regarded as its energetic signature. Similarly to its classical counterpart, it is characterized by negative heat capacity change, $\Delta C_p = \left(\frac{\partial \Delta H}{\partial T}\right)$, during micellization, which indicates that both processes are characterized by a rearrangement of solvent molecules.[10,101]

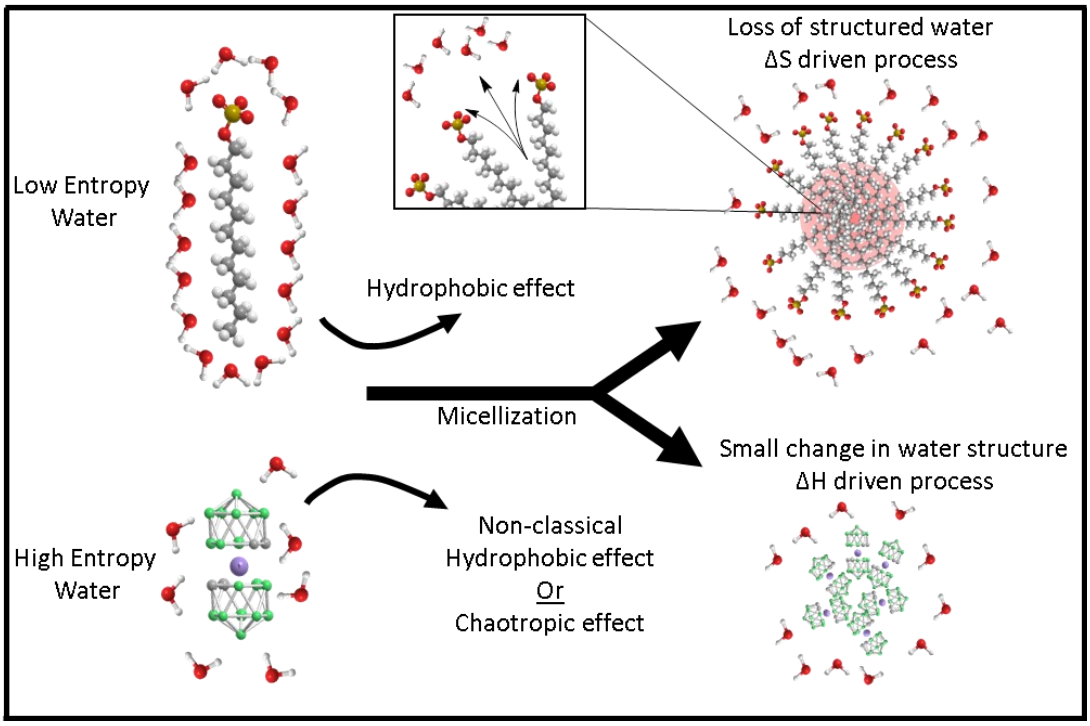

Figure 4.1.4 Molecular picture of micellization driven by classical and nonclassical hydrophobic effects with emphasized changes of hydration shells for classical surfactant SDS and intrinsic amphiphile COSAN.

Analyzing the arrangement of hydration water molecules around ABCCs is essential to understand the micellization process. Roccatano et al.[59] and our own group have recently focused their research efforts on hydration water around ABCCs. Specifically, the former have reported that hydration water around $[B_{12}H_{12}]^{2-}$ and its derivatives forms a different network with "hydrophobic" holes over B-H segments (Figure 4.1.3), identifying O-H···H-B dihydrogen bonds by molecular dynamics. This arrangement differs from the "structured" water model based on the hydrophobic effect, in which no direct interaction occurs between water molecules and the hydrophobic structure. In the case of COSAN, preliminary results of Molecular Dynamics and Monte Carlo simulations have shown a patchy pattern in the hydration shell similar to that of dodecaborate. However, the partly positively charged C-H groups of COSAN participate in weak hydrogen bonding with water molecules. Accordingly, the C-H units found in the "equatorial" region of COSAN are more hydrated than the rest of the cluster.

In here three different approaches will be described to justify the small value of ΔS_{mic} for COSAN micellization:

(i) Size-Dependent Hydration

According to this model,[102,103] the hydration of hydrophobic objects strongly depends on their size. The small oily molecules (smaller than the border-line 1 nm) fit into the network of water hydrogen bonds and they should be therefore considered "wet" with no distinct oil-water interface around them. The aggregation of such molecules into the larger objects results in destruction of the dense hydration shells and simultaneously in the creation of "soft" oil-water interface around the large aggregates. This is an entropy-driven process. Conversely, if the oily molecule is already sufficiently large, the interface is already formed and such molecules are "dry". The aggregation of such molecules results in the increase of this interface. Thus, the process is enthalpy-driven and the driving force is proportional to the area of the interface. The COSAN cluster can be imagined as prolonged object with long axis 1.1 nm and the short one 0.6 nm,[91] and it lies close to the border-line proposed by Chandler. Finally, the water density around objects of intermediate size, further calculated by Chandler, is noteworthy. Such molecules are neither wet, nor dry, and recall the term *aquaneutral* discussed in Chapter 4.2.

(ii) Nonclassical Hydrophobic Effect

Enthalpy-driven processes, such as COSAN micellization, are regarded as the hallmark of nonclassical hydrophobic effect , as previously discussed.[10] The small contribution of ΔS_{mic} to the ΔG_{mic} shows that the difference in degrees of freedom between bulk water and hydration water is insignificant (Figure 4.1.4). Additionally, the small negative value of ΔC_{p} suggests that only minor water restructuring occurs during micellization (for further explanation see Chapter 7.3.). This evidence clearly supports the nonclassical hydrophobic effect.

(iii) Chaotropic Effect

The notion of a disorganized water structure around ABCCs was introduced by Assaf *et al.* after preparing a set of cyclodextrin-ABCCs complexes and performing classic salting-in experiments.[92] They assessed that dodecaborate shows a very strong chaotropic behavior, which falls outside the scale of the Hofmeister series. Therefore, dodecaborate anion was considered a “superchaotrope”.[92] Concurrently, COSAN has a hydration shell similar to that of dodecaborate, thus suggesting “superchaotropic” behavior. Furthermore, COSAN is larger than dodecaborate and its charge is also distributed over a larger area, i.e., COSAN is more “hydrophobic” than dodecaborate.

In summary, although both size-dependent hydration model (i) and the nonclassical hydrophobic effect (ii) provide a possible explanation for the small value of ΔS_{mic} of COSAN, they both assume interactions between strictly hydrophobic surfaces. This is problematic because COSAN molecules are intrinsic amphiphiles with no clear differences between their hydrophobic and hydrophilic parts. Moreover, (ii) is apparently related to the chaotropic effect (iii), in the sense that (ii) may be a reaction to (iii). They both explain the small ΔS_{mic} of COSAN based on unstructured hydration water, but (ii) requires the presence of hydrophobic moieties (Figure 4.1.5). Therefore, the most comprehensive explanation for COSAN micellization is (iii). However, two questions remain unanswered: (1) to what extent do chaotropic and hydrophobic behaviors overlap and (2) how to differentiate them? (Figure 4.1.5)[104]

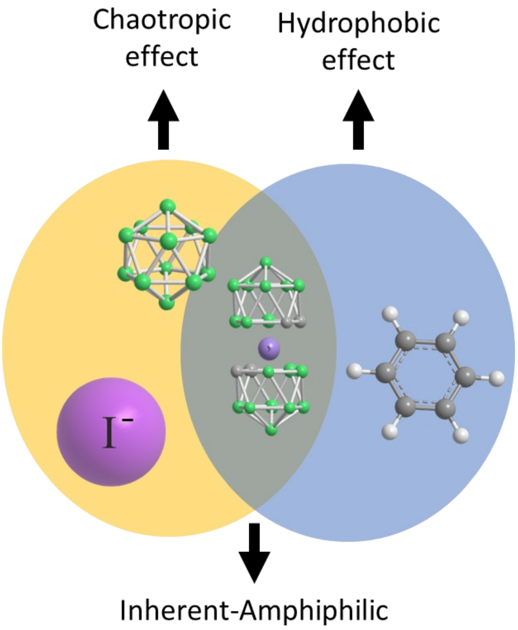

Figure 4.1.5 Schematic relation of chaotropic and hydrophobic effects of dodecaborate and COSAN as compared to typical chaotrope such as iodide and hydrophobic molecule of comparable size – benzene. For further discussion and related references see Chapter 5.

Micellization of Inherently Amphiphilic Building Blocks

ABCC building blocks are inherently amphiphilic. COSAN clusters contain slightly hydrophilic spots around the C-H groups (schematic representations of COSAN in Figures 4.1.1 and 4.1.2). However, these spots behave differently from the hydrophilic parts of classical surfactants, which are always exposed to bulk water. COSAN NMR data indicates that these C-H groups play a key role in micellization, specifically in intra-micellar dihydrogen bonds.[71] However, the main driving force of ABCCs micellization is not specific to dihydrogen bonding but rather to hydrophobic (COSAN) or chaotropic (dodecaborate) effects (Figure 4.1.5). This manifested as anion-anion attractions, as observed and calculated for COSAN and other ABCCs. The aggregation number of ABCCs micelles is given by the balance between the aforementioned cohesive forces and electrostatic repulsion.[71,73,75,89] Furthermore, short-range anion-cation repulsion accounts for very low values of N_{aag} in COSAN (~5-10).

The size and shape of COSAN aggregates have been highly debated in the literature. The first report of COSAN aggregates published by Matejicek *et al.* suggested large spherical particles (>100 nm) of unknown inner structure.[87] These were interpreted by Zemb and Teixidor as monolayer vesicles with parallel packing of COSAN clusters.[75,89] However, additional experiments (SAXS, NMR, ITC and cryo-TEM)[71,73] failed to confirm that these large structures were the most stable and dominant self-assemblies in solution, despite the theoretical predictions.[89]

NMR and ITC results have clearly shown that COSAN predominantly forms small micelles, which can be successfully described using the closed association model.[71,73] Currently, the exact inner structure of COSAN micelles remains unknown. Quantum calculations and computer simulations of COSAN pairs suggest strong dipole-dipole ordering and parallel cluster orientation within these micelles. Based on the low, albeit negative, ΔC_p value, these micelles have no core-shell structure. Instead, extensive parts of the amphiphilic COSAN surface remain exposed to bulk water after micelle formation (Figure 4.1.4).

Self-assembly is a typical feature of COSAN and other ABCCs. Nevertheless, an unambiguous molecular theory of micellization of clusters such as dodecaborate has not been proposed yet. COSAN association is enthalpy-driven, however, no study describing the thermodynamics and accurate aggregation mechanism of all ABCCs has been published in the literature thus far.

Experimental observations of ABCCs Self-Assemblies

Although scattering and microscopy methods are considered the “Gold Standards” in nanochemistry and colloidal chemistry, the specific features of ABCCs micelles (including their very low aggregation number) requires using other methods to accurately describe ABCCs self-assembly. As an example of boron cluster compounds, we chose sodium, lithium and potassium COSAN salts and COSAN acid, assigned as Na[COSAN], Li[COSAN], K[COSAN] and

H[COSAN], respectively, to show not only the specific features of COSAN solution behavior but also the influence of counterions on COSAN micellization.

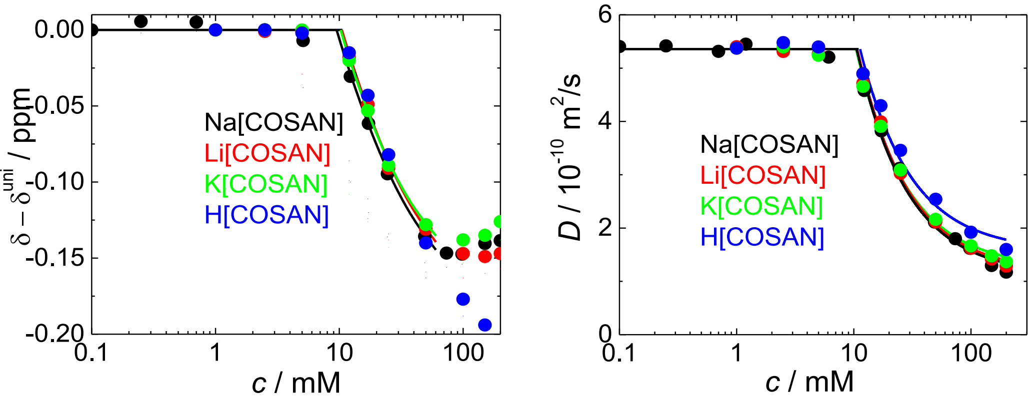

Figure 4.1.6 Relative chemical shift of C-H segments (**left**) and diffusion coefficient (**right**) as a function of the concentration of sodium, lithium and potassium COSAN salts and COSAN acid assessed by ^{1}H NMR and ^{1}H DOSY NMR.

NMR spectroscopy and Cryo-TEM Imaging

NMR spectroscopy is an excellent method to track the self-assembly process of small species from the molecular point of view.[71,73,105] The ^{1}H NMR spectra of ABCCs concentration series in water are particularly interesting because the electron clouds of peripheral hydrogen atoms are sensitive to inter-molecular contacts. In the case of COSAN, the C-H signals are the most affected. Figure 4.1.6 shows the abrupt change in the concentration as a function of chemical shifts that can be assigned to the value of CMC.[71] The suitable alternative to scattering methods, which overestimate large temporal agglomerates of unclear origin in ABCC solutions, is diffusion-ordered NMR spectroscopy (DOSY NMR) that provides the diffusion coefficients of small molecules and their still relatively small associates. As previously shown for Na[COSAN] and several other ABCCs, changes in the chemical shifts and diffusion coefficient of ABCC in water result from aggregation phenomena above the CMC. Although the fraction of aggregated molecules of small clusters such as dodecaborate is fairly low, micelles are prevalent in COSAN solutions above the CMC. Additionally, ^{11}B {^{1}H} NMR has been used to detect the transition of a [I_2COSAN]$^-$ lamellar phase from molten to frozen state.[90] Because of the strong spin-spin coupling of ^{11}B and ^{1}H nuclei, ^{1}H{^{11}B} decoupled spectra should be recorded to detect B-H units in both 1D and DOSY NMR experiments.

Figure 4.1.6 shows the comparison between the diffusion coefficients, *D*, of various COSAN salts, highlighting that (i) the nature of the counterion has a minor effect on COSAN micellization; (ii) the value of CMC is similar for all studied COSAN samples; (iii) *D* vs. *c* curves can be successfully fitted using the closed association model, which enables assessing the hydrodynamic radii, R_H, of COSAN micelles according to the following order Na ≈ Li ≥ K > H (1.78 nm, 1.71 nm, 1.60 nm, and 1.27 nm, respectively). These micelles have very similar sizes, inside the experimental margin of error, excluding COSAN acid micelles. This exception might be related to counterion condensation and ionic strength because the size and aggregation number of the micelles results from the balance between adhesive forces and electrostatic interactions

Cryo-TEM is the most suitable method for COSAN micelle visualization. Due to the small size of these micelles, the typical micrograph contains small round stains with low contrast.[73,75] These micrographs provide no information on the inner structure of COSAN micelles.

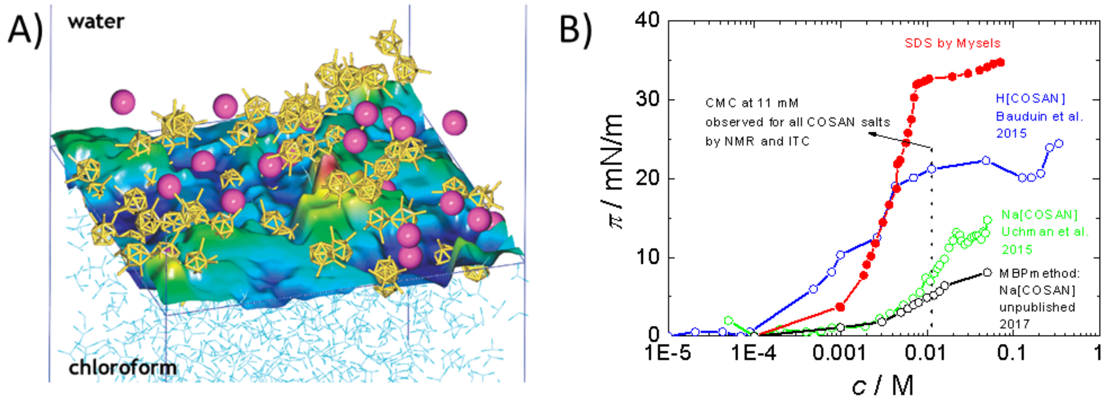

Figure 4.1.7 (**A**) Distribution of chlorinated COSAN anions and cesium cations within 10 Å from the interface. Reproduced from [Chevrot, G.; Schurhammer, R.; Wipff, G. Surfactant behavior of "ellipsoidal" dicarbollide anions: A molecular dynamics study. *J. Phys. Chem. B.* **2006,** *110* (19), 9488-9498]. Copyright (2006) American Chemical Society. (**B**) Surface pressure (π) as a function of the concentration of the classical surfactant SDS (red) [Mysels; Ref 106], COSAN acid (blue) [Bauduin et al.; Ref 94] and sodium COSAN measured using the pendant drop method (green) [Uchman et al. Ref 71] or the MBP method (black). (The dotted line represents the value of CMC determined by NMR and ITC).

Tensiometry

COSAN is commonly defined as a surfactant in the literature based on molecular dynamics simulations[70] and confirmed by tensiometry (for both water/air[71,73,84] and water/oil interfaces[84]). Furthermore, producing foam during electrolysis of COSAN solutions showed that COSAN behaves as a surfactant.[88] In 2001, the surface pressure, π, of various COSAN salts at the water/dichlorethane interface was compared by tensiometry.[84] The results showed that cation hydration partly affects COSAN/counterion stabilization at the interface, as assessed by changes in the magnitude of π, which reached relatively low values (20-25 mN/m) for divalent cations and even lower values (~15 mN/m) for monovalent alkaline salts of COSAN. The reported area per COSAN molecule at both water/oil and water/air interfaces is approximately 1 nm^2.[71,94,84] However, this has led to contradictory interpretations. On the one hand, Popov and Borisova[84] and Bauduin et al.[94] reported that COSAN forms compact structures. The former described close contacts between COSAN molecules parallel to the water/dichlorethane interface, whereas the latter claimed that COSAN forms monolayers with parallel contacts stabilized by dihydrogen bonds and with a longitudinal COSAN axis perpendicular to the water/air interface. On the other hand molecular dynamics simulations performed by Wipff et al. indicated loose structures unable to form a compact monolayer at the water/chloroform interface (Figure 4.1.7A).[70] However, recent tensiometry measurements suggest reviewing the classification of COSAN as a surfactant. Figure 4.1.7B shows the curves of surface pressure as a function of concentration of SDS as an example of a classical hydrophilic surfactant (Mysels),[106] H[COSAN] (Bauduin)[94] and Na[COSAN] (Uchman),[71] both measured using the pendant drop method, alongside preliminary results for Na[COSAN] measured by Maximum Bubble Pressure (MBP) (unpublished data from our group). Additional dynamic pendant-drop experiments assessing the surface tension, γ, of COSAN acid and salt solutions showed unusually long changes over time because the system only reached a steady-state after several hours (unpublished data from our group). According the Ward-Tordai equation, there is no physical meaning of such long-time periods for small molecules.[107] COSAN diffusion should be shorter than a second. Thus, the remaining process could be explained by hydrophobic impurities or surface-active aggregates. The pendant drop method precludes the short-term measurements. Therefore, we used the MBA method, which enables measurements at the shortest time response possible (tens of milliseconds), that is sufficient to obtain reliable data. The results from these experiments are shown in Figure 4.1.7B. The surface activity of single COSAN clusters is very low, with π values lower than 10mN/m. The surface area per COSAN molecule is estimated to be higher than 1-2 nm^2 from the MBP curve, thus suggesting that the predictions of Wipff[70] (Figure 4.1.7A) were realistic. Moreover, no clear “break” corresponding to the CMC (approximately 11 mM) is observed for any of the published data (Figure 4.1.7B), and the CMC has been corroborated by NMR and ITC measurements. These curves show that COSAN is only weakly surface-active and that the samples may contain undetectable amounts of unknown hydrophobic impurities. Alternatively, COSAN aggregates may be surface-active structures, thus explaining the lack of a “break” at the CMC.

In summary, tensiometry could provide valuable information on the amphiphilic nature of ABCCs and on the counterion effects on the air/water interface. However, the issue of sample purity must be addressed in order to ensure reliable data.

ITC in the study of ABCCs aggregation

Surfactant micellization is studied by Isothermal Titration Calorimetry (ITC) assessing the opposite process: demicellization.[3] A typical demicellization experiment consists of recording the heat released after injecting small aliquots of a concentrated surfactant solution into a reaction cell containing pure solvent. As the micelles dilute, they break up into individual surfactant molecules. When the surfactant concentration in the reaction cell exceeds the CMC, demicellization stops and, thus, only the heat of dilution is recorded. The data collected can be plotted into a thermogram (heat *vs* concentration), which typically has a sigmoidal shape (Figure 4.1.8). The transition between asymptotes corresponds to the concentration range where micelle formation occurs. Subsequently, the resulting thermogram can be used to calculate the ΔH_{mic} and the CMC directly, without requiring no model or complex analysis (Figure 4.1.8).[3]

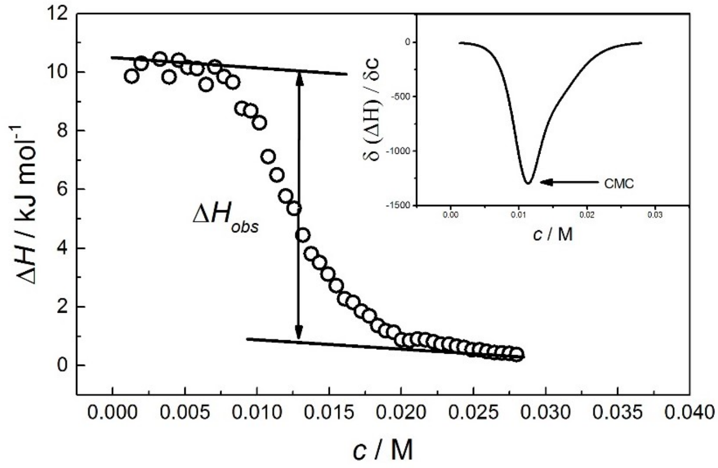

Figure 4.1.8 Typical enthalpogram of COSAN demicellization showing the ΔH and CMC calculations (Inset: the first derivative of the enthalpogram).

Several fitting procedures based on the Mass Action model have been developed in the past decades to determine all key thermodynamic parameters (N_{agg}, ΔG_{mic}, ΔS_{mic} and ΔH_{mic}) from a thermogram in a single experiment.[108-110] Alternatively, N_{agg} can be determined by SAXS. For example, preliminary SAXS measurements of Na[COSAN] micelles showed a very low N_{agg} (~5-10).[71] Furthermore, the Mass Action model has been successfully used to describe small surfactant molecules such as bile salts whose very small N_{agg} preclude their study using simpler models. This made us consider using this model to accurately describe COSAN micellization.

Thermograms of the four COSAN compounds (H, Li, Na and K) were acquired and showed the typical sigmoidal shape with a broad transition region (Figure 4.1.8). Broad transition regions have been previously attributed to low N_{agg}, as observed in bile salt micellization.

The degree of counterion condensation on the micelles (*β*) must be assessed to calculate the ΔG_{mic} and further analyze the micellization process. Very low values of *β*, ranging from 0.14 to 0.24, were calculated based on conductivity measurements for all COSAN salts, indicating the following order: $Li^+ \approx H^+ > Na^+ \approx K^+$ (opposite order to alkyl sulfates). The low *β* values match the simulations showing repulsion between COSAN and Na, which is the counterion.

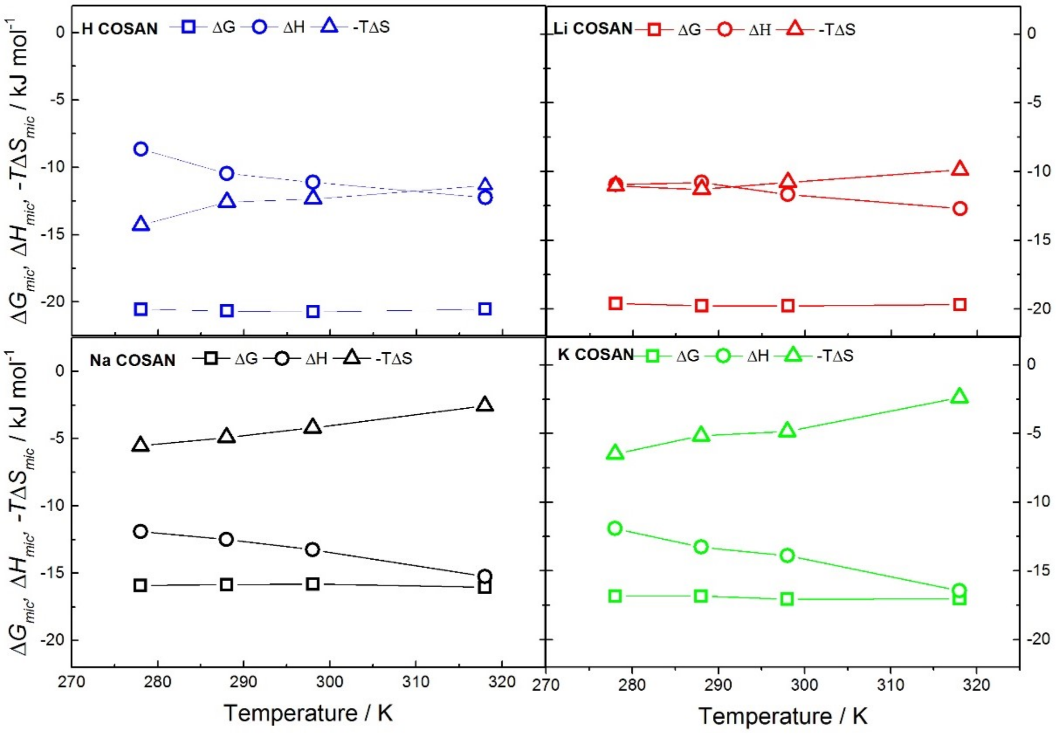

Figure 4.1.9 Thermodynamic parameters (ΔG_{mic}, ΔH_{mic}, and -TΔS_{mic}) of H[COSAN], Li[COSAN], Na[COSAN] and K[COSAN] calculated based on ITC data using the Mass Action model.

The thermodynamic potentials of all counterions were calculated according to the procedure by Uchman *et al.*[71] (Figure 4.1.9). The results show a smaller contribution of ΔS_{mic} to COSAN micellization than that observed in classical surfactants Furthermore, the driving force of micellization is apparently counterion-dependent. For Li^+ and H^+, the enthalpic contribution increases with temperature, although the process has similar enthalpic and entropic contributions at low temperatures. Conversely, Na^+ and K^+ showed enthalpy-driven micellization throughout the temperature range assessed. The magnitude of counterion condensation affects the ΔG_{mic}, and the presence of small cations, such as Li^+, within micelles enhances the entropic contribution to ΔG_{mic}.

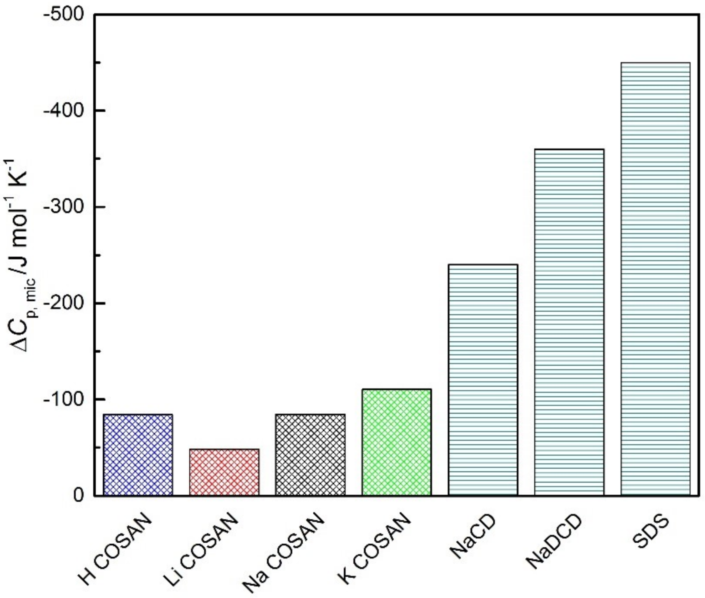

Figure 4.1.10 Comparison between the values of ΔC_p of various COSAN (H, Li, Na and K) and bile (sodium cholate, NaCD, and sodium deoxycholate, NaDCD) salts and SDS (Ref 108).

ΔC_p is the best measure of changes in hydrophobic parts exposed during micellization. Its values can be calculated from ITC measurements at different temperatures; ΔH vs temperature plots yield $\Delta C_p = \left(\frac{\partial \Delta H}{\partial T}\right)$. The ΔC_p values of COSAN salts are significantly smaller than those of bile salts and classical surfactants (SDS) (Figure 4.1.10).[108] Upon SDS micellization, most of the tail becomes shielded from bulk water (Figure 4.1.4). This creates a large rearrangement of water molecules leading to a large absolute value of ΔC_p, which indicates a core-shell micelle structure. The aggregates of bile salts (sodium cholate and sodium deoxycholate) display a distinct, though incomplete, separation of hydrophobic and hydrophilic parts. Therefore, the value of ΔC_p is still negative but relatively small compared with head-and-tail surfactants.

The counterion effects on ΔC_p were also studied in our group. In contrast to COSAN, this effect is negligible among classical surfactants (dodecyl sulfate, decyl sulfate),[111] because the ΔC_p contribution from the large hydrophobic tail masks that of the counterions Conversely, COSAN lacks a clearly defined and dominant hydrophobic moiety, thereby unmasking the contribution of counterions to the ΔC_p.

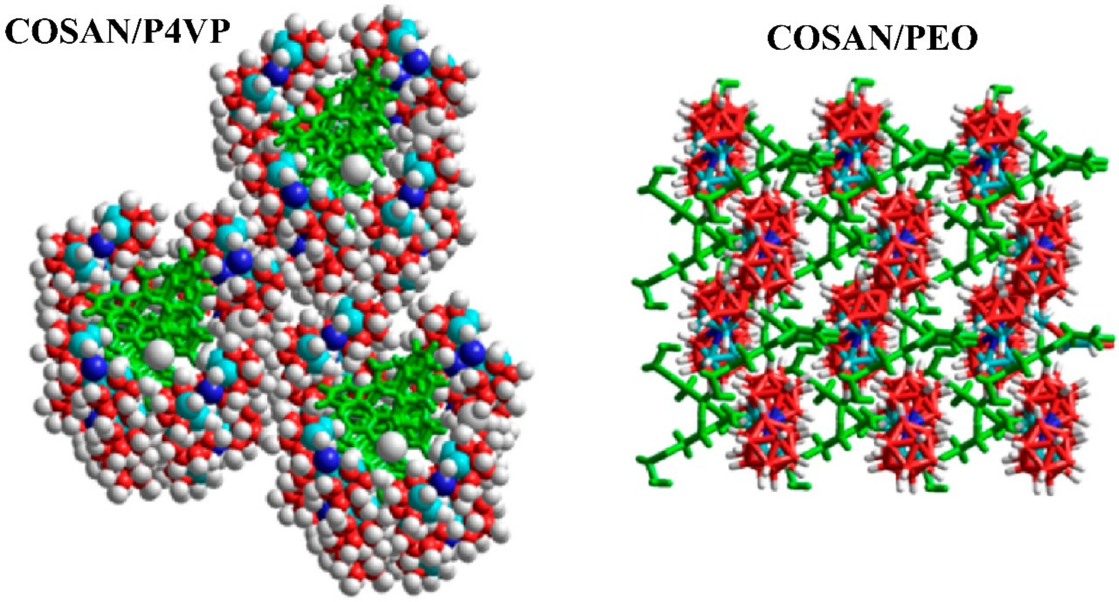

Figure 4.1.11 Idealized large-scale structures of COSAN$^-$/H$^+$/P4VP and COSAN$^-$/Na$^+$/PEO. Reproduced from [Brus, J.; Zhigunov, A.; Czernek, J.; Kobera, L.; Uchman, M.; Matejicek, P. Control over the Self-Assembly and Dynamics of Metallacarborane Nanorotors by the Nature of the Polymer Matrix: A Solid-State NMR Study. *Macromolecules* **2014,** *47* (18), 6343-6354] Copyright (2014) American Chemical Society.

ABCCs co-assembly with Polymers

To exemplify the properties of ABCCs as building blocks suitable for nanochemistry, this section summarizes key findings on the ability of COSAN to form nanostructured complexes with polymers. The co-assembly of classical ionic surfactants with oppositely charged polymers has been extensively published in the literature.[112-114] Similarly, non-classical surfactants, such as COSAN, interact with polycations forming nanostructured complexes.[91] Additionally, COSAN is able to form complexes with neutral polymers and proteins[23,24,35,36,115,116] through weak interactions (Chapter 3). The spontaneous precipitation of the COSAN/Poly(ethylene oxide) (PEO) complex is driven by dihydrogen bonding between the B-H segments of the cluster and the CH_2 segments of the polymer backbone.[91,117,118] Concurrently, this process is accompanied by the complexation of cations (counterions of COSAN) by PEO.[119] The resulting COSAN/PEO nanocomposite have a unique and highly ordered inner structure with evenly dispersed COSAN anions and alkaline cations within the amorphous PEO matrix (Figure 4.1.11). Even though the co-assembly of anionic COSAN with cationic poly(vinyl pyridine) provide amorphous nanocomposites COSAN/PVP, their short-range ordering as revealed by solid-state NMR is also noteworthy (Figure 4.1.11). The cluster orientation is controlled by the location of the positive charges on the polymer chain, which provides numerous opportunities for molecular design. In addition to the unique structure of COSAN nanocomposites, these clusters show a more dynamic motion than polymer segments. In other words, COSAN-containing nanomaterials are amphidynamic. Furthermore, ABCCs interact with conductive polymers such as polypyrroles protecting them against degradation and overoxidation, both of which are big obstacles for the inclusion of conductive polymers into everyday applications. Moreover, ABCCs add functionality to polypyrroles by converting them into sensitive cation exchangers.[120]

The self-assembly of ABCCs with polymers is still in its early research stages and needs further research to match the advances and breakthroughs found for systems with covalently bound ABCCs. Recent advances in the use of carboranes as liquid crystals highlight the importance of cluster dipolar moment on the formation of self-assembled monolayers.[121] Such insights, paired with the use of larger variety of polymers and ABCCs derivatives could be useful to design novel polymer-ABCCs complexes and tailor them to desired functionalities.

Summary and Challenges for Future Research

In this feature article, we have highlighted the importance of the shape and amphiphilic nature of ABCCs and how these properties set them apart from other building blocks that have been described thus far. These unique characteristics can result in new and better uses of ABCCs as building blocks for nanostructures, both alone and with other molecules. We have also reviewed the terms commonly used in the self-assembly field to pinpoint the need for a consensus on new terms describing compounds such as ABCCs. For example, the term aquaneutral or intrinsic amphiphile should be readily used for molecules with amphiphilic character but lacking a clear separation between hydrophobic and hydrophilic parts.

We have provided experimental evidence on the self-assembly process of ABCCs gathered by ITC, tensiometry and NMR. ITC is an essential method to calculate the thermodynamic properties of amphiphile micellization, including the ΔC_p, which shows the extent of hydration changes and the magnitude of the hydrophobic effect. In the case of COSAN, no model has been able to fit the data and indicate all thermodynamic variables thus far. Such a model would improve current data, particularly regarding the N_{agg}, although the main conclusions are expected to remain unchanged. However, determining the inner structure of COSAN micelles will most likely remain a challenge due to their small size, thus requiring tools such as computer simulation and quantum chemistry. This further underlines the need for reliable experimental thermodynamic data to develop realistic models based on Molecular Dynamics and Monte Carlo simulations.

Understanding the behavior of inherent amphiphiles at oil/water and air/water interfaces is another key challenge. Furthermore, the classical approach based on Gibbs adsorption isotherm of anionic surfactants assumes the presence of two species at the interface: the surface-active ion and its counterion Therefore, the depending on the value of the *n* factor used in the Gibbs adsorption isotherm, the effect of the counterions at the interface may be unintentionally disregarded. For example, the fact that COSAN shows short-range anion-cation repulsion forces generates uncertainty when assigning a value to *n*. This must be carefully considered to avoid misinterpreting key interactions at the interface.

Our group has described the molecular mechanism of COSAN self-assembly; however, this mechanism remains unknown for other ABCC. The C-H groups of COSAN and its higher hydrophobicity than that of other ABCC prevent generalizing conclusions from COSAN studies. Furthermore, the role of counterions in the micellization of COSAN is not yet clear and it apparently plays a key role in the thermodynamics of the process.

Moreover, the relationship between the nonclassical hydrophobic effect and the chaotropic effect should be clarified. Nevertheless, recent studies have added a new depth to the Hofmeister series by including and defining the hydrophobic-hydrophilic characteristics of such ions, in addition to analyzing their chaotropic-kosmotropic behavior. This could become a key contribution to the field of ABCCs chemistry.

Lastly, ABCCs co-assembly with polymers has great potential in the field of material chemistry because the ability of COSAN to form ordered co-assemblies with various polymers, both in aqueous media and in solid-state structures, may be use to add desirable properties to already known polymer composites.

Acknowledgment
The authors would like to acknowledge the financial support of the Czech Science Foundation 17-00648S. The authors thank Sami Kereïche (Charles University, Prague) for cryoTEM measurements, Josef Pleštil and Alexander Zhigunov (IMC CAS, Prague) for SAXS measurements and interpretation, Zdeněk Tošner (Charles University, Prague) for NMR experiments, Michael Gradzielski (TU Berlin, Germany) and Reinhard Miller (MPI Golm, Germany) for their help with surface tension experiments and valuable discussions, Martin Lepšík (IOCB CAS, Prague) and Mikael Lund (University of Lund) for quantum chemistry, Monte Carlo and molecular dynamics calculations, Detlef Gabel (Jacobs University Bremen, Germany) for discussions on terminology and Carlos V. Melo for editing the manuscript.

References

(1) Lee, Y. S. *Self-Assembly and Nanotechnology: A Force Balance Approach*. John Wiley & Sons, Inc.: New Jersey, 2008; p 344.
(2) Ozin, G. A.; Arsenault, A. C. *Nanochemistry: A Chemical Approach to Nanomaterials*. The Royal Society of Chemistry: Cambridge, 2005; p 628.
(3) Olofsson, G.; Loh, W. On the use of Titration Calorimetry to Study the Association of Surfactants in Aqueous Solutions. *J. Braz. Chem. Soc.* **2009,** *20* (4), 577-593.
(4) Loh, W.; Brinatti, C.; Tam, K. C. Use of isothermal titration calorimetry to study surfactant aggregation in colloidal systems. *Biochim. Biophys. Acta.* **2016,** *1860* (5), 999-1016.

(5) Wennerstrom, H.; Lindman, B. Micelles-Physical-Chemistry of Surfactant Association. *Phys. Rep.* **1979,** *52* (1), 1-86.

(6) Tuzar, Z. Copolymer micelles in aqueous media. In *Solvents and Self-Organization of Polymers*, first edition ed.; Webber, S. E.; Munk, P.; Tuzar, Z., Eds. Springer Netherlands: 1996; pp 309-318.

(7) Hildebrand, A.; Garidel, P.; Neubert, R.; Blume, A. Thermodynamics of demicellization of mixed micelles composed of sodium oleate and bile salts. *Langmuir* **2004,** *20* (2), 320-328.

(8) Madenci, D.; Egelhaaf, S. U. Self-assembly in aqueous bile salt solutions. *Curr. Opin. Colloid Interface Sci.* **2010,** *15* (1-2), 109-115.

(9) Olesen, N. E.; Westh, P.; Holm, R. Determination of thermodynamic potentials and the aggregation number for micelles with the mass-action model by isothermal titration calorimetry: A case study on bile salts. *J. Colloid Interface Sci.* **2015,** *453*, 79-89.

(10) Paul, B. K.; Ghosh, N.; Mukherjee, S. Interaction of Bile Salts with beta-Cyclodextrins Reveals Nonclassical Hydrophobic Effect and Enthalpy-Entropy Compensation. *J. Phys. Chem. B.* **2016,** *120* (16), 3963-3968.

(11) Nitta, H.; Harano, K.; Isomura, M.; Backus, E. H. G.; Bonn, M.; Nakamura, E. Conical Ionic Amphiphiles Endowed with Micellization Ability but Lacking Air-Water and Oil-Water Interfacial Activity. *J. Am. Chem. Soc.* **2017,** *139* (23), 7677-7680.

(12) Kaszynski, P. Four decades of organic chemistry of closo-boranes: A synthetic toolbox for constructing liquid crystal materials. A review. *Collect. Czech. Chem. Commun.* **1999,** *64* (6), 895-926.

(13) Sivaev, I. B.; Bregadze, V. I.; Sjoberg, S. Chemistry of closo-Dodecaborate Anion $[B_{12}H_{12}]^{2-}$: A Review. *Collect. Czech. Chem. Commun*. **2002,** *67*(6), 679-727.

(14) Jelínek, T.; Plešek, J.; Heřmánek, S.; Štíbr, B. Chemistry of compounds with the 1-carba-closo-dodecaborane (12) framework. *Collect. Czech. Chem. Commun*. **1986,** *51*(4), 819-829.

(15) Douvris, C.; Michl, J. Chemistry of the Carba-closo-dodecaborate(−) Anion, $CB_{11}H_{12}^{-}$. *Chem. Rev.* **2013**, *113* (10), pp PR179-PR233.

(16) Stibr, B. Carboranes other than $C_2B_{10}H_{12}$. *Chem. Rev.* **1992**, *92* (2), 225-250.

(17) Deng, L.; Xie, Z. Advances in the chemistry of carboranes and metallacarboranes with more than 12 vertices. *Coord. Chem. Rev.* **2007,** *251* (17-20), 2452-2476.

(18) Zhang, J.; Xie, Z. Synthesis, structure, and reactivity of 13-and 14-vertex carboranes. *Acc. Chem. Res.* **2014,** *47* (5), 1623-1633.

(19) Grimes, R. N. *Carboranes*. Third edition ed.; Academic Press: London, 2016.

(20) King, R. B. Three-dimensional aromaticity in polyhedral boranes and related molecules. *Chem. Rev.***2001,** *101* (5), 1119-1152.

(21) Poater, J.; Sola, M.; Vinas, C.; Teixidor, F. A simple link between hydrocarbon and borohydride chemistries. *Chem. Eur. J.***2013,** *19* (13), 4169-4175.

(22) Poater, J.; Sola, M.; Vinas, C.; Teixidor, F. pi Aromaticity and three-dimensional aromaticity: Two sides of the same coin? *Angew. Chem. Int. Ed.* **2014,** *53* (45), 12191-12195.

(23) Farras, P.; Juarez-Perez, E. J.; Lepsik, M.; Luque, R.; Nunez, R.; Teixidor, F. Metallacarboranes and their interactions: theoretical insights and their applicability. *Chem. Soc. Rev.* **2012,** *41* (9), 3445-3463.

(24) Fanfrlik, J.; Lepsik, M.; Horinek, D.; Havlas, Z.; Hobza, P. Interaction of carboranes with biomolecules: Formation of dihydrogen bonds. *ChemPhysChem* **2006,** *7* (5), 1100-1105.

(25) Planas, J. G.; Vinas, C.; Teixidor, F.; Comas-Vives, A.; Ujaque, G.; Lledos, A.; Light, M. E.; Hursthouse, M. B. Self-assembly of mercaptane-metallacarborane complexes by an unconventional cooperative effect: A C-H···S-H···H-B hydrogen/dihydrogen bond interaction. *J. Am. Chem. Soc.* **2005,** *127* (45), 15976-15982.

(26) Stock, A. *Hydrides of Boron and Silicon*. Cornell University Press: Ithaca, New York, 1933; 150.

(27) Plesek, J. Potential Applications of the Boron Cluster Compounds. *Chem. Rev.***1992,** *92* (2), 269-278.

(28) Hawthorne, M. F.; Young, D. C.; Wegner, P. A. Carbametallic boron hydride derivatives i. apparent analogs of ferrocene and ferricinium ion. *J. Am. Chem. Soc.* **1965,** *87* (8), 1818-1819.

(29) Sivaev, I. B.; Bregadze, V. I., Chemistry of cobalt bis(dicarbollides). A review. *Collect. Czech. Chem. Commun.* **1999,** *64* (5), 783-805.

(30) Plesek, J.; Base, K.; Mares, F.; Hanousek, F.; Stibr, B.; Hermanek, S. Potential Uses of Metallocarborane Sandwich Anions for Analysis, Characterization and Isolation of Various Cations and Organic-bases. *Collect. Czech. Chem. Commun.* **1984,** *49* (12), 2776-2789.

(31) Soloway, A. H.; Tjarks, W.; Barnum, B. A.; Rong, F. G.; Barth, R. F.; Codogni, I. M.; Wilson, J. G., The chemistry of neutron capture therapy. *Chem. Rev.***1998,** *98* (4), 1515-1562.

(32) Lesnikowski, Z. J. Boron units as pharmacophores - New applications and opportunities of boron cluster chemistry. *Collect. Czech. Chem. Commun.* **2007,** *72* (12), 1646-1658.

(33) Hawthorne, M. F.; Lee, M. W. A critical assessment of boron target compounds for boron neutron capture therapy. *J. Neurooncol.* **2003,** *62* (1), 33-45

(34) Gruner, B.; Rais, J.; Selucky, P.; Lucanikova, M. Recent progress in extraction agents based on cobalt bis(dicarbollides) for partitioning of radionuclides from high level nuclear waste. *Boron Science: New Technologies and Applications*, first edition ed.; Hosmane, N. S., Ed. CRC Press: New York, 2012; pp 463-490.

(35) Rezacova, P.; Cigler, P.; Matejicek, P.; Lepsik, M.; Gruner, B.; Konvalinka, J., Medicinal Application of Carboranes: Inhibition of HIV Protease. In *Boron Science: New Technologies and Applications*, First edition ed.; Hosmane, N. S., Ed. CRC Press: New York, 2012; pp 41-70.

(36) Cigler, P.; Kozisek, M.; Rezacova, P.; Brynda, J.; Otwinowski, Z.; Pokorna, J.; Plesek, J.; Gruner, B.; Doleckova-Maresova, L.; Masa, M.; Sedlacek, J.; Bodem, J.; Krausslich, H. G.; Kral, V.; Konvalinka, J. From nonpeptide toward noncarbon protease inhibitors: Metallacarboranes as specific and potent inhibitors of HIV protease. *Proc. Natl. Acad. Sci. U.S.A.* **2005,** *102* (43), 15394-15399.

(37) Qian, E. A.; Wixtrom, A. I.; Axtell, J. C.; Saebi, A.; Jung, D.; Rehak, P.; Han, Y.; Moully, E. H.; Mosallaei, D.; Chow, S.; Messina, M.; Wang, J.Y.; Royappa, A. T.; Rheingold, A. L.; Maynard, H. D.; Kral, P.; Spokoyny, A. M. Atomically Precise Organomimetic Cluster Nanomolecules Assembled via Perfluoroaryl-Thiol SNAr Chemistry. *Nature Chem.* **2017**, *9* (4), 333-340.

(38) Teixidor, F.; Vinas, C.; Demonceau, A.; Nunez, R. Boron clusters: Do they receive the deserved interest? *Pure Appl. Chem.* **2003,** *75* (9), 1305-1313.

(39) Lesnikowski, Z. J.; Shi, J. X.; Schinazi, R. F. Nucleic acids and nucleosides containing carboranes. *J. Organomet. Chem.* **1999,** *581* (1-2), 156-169.

(40) Grimes, R. N. Carboranes in the chemist's toolbox. *Dalton Trans.* **2015,** *44* (13), 5939-5956.

(41) McArthur, S. G.; Jay, R.; Geng, L.; Guo, J.; Lavallo, V. Below the 12-vertex: 10-vertex carborane anions as non-corrosive, halide free, electrolytes for rechargeable Mg batteries. *Chem. Commun.* **2017**, *53* (32), 4453-4456.

(42) Green, J.; Cohen, M. S.; Kotloby, A. P.; Mayes, N.; Obrien, E. L.; Fein, M. M. Carborane polymers. *J. Polym. Sci. B* **1964,** *2* (1PB), 109-&.

(43) Fox, M. A.; Wade, K. Model compounds and monomers for phenylene ether carboranylene ketone (PECK) polymer synthesis: preparation and characterization of boron-arylated ortho-carboranes bearing carboxyphenyl, phenoxyphenyl or benzoylphenyl substituents. *J. Mater. Chem.* **2002,** *12* (5), 1301-1306.

(44) Jakle, F. Borylated polyolefins and their applications. *J. Inorg. Organomet. Polymer Mater.* **2005,** *15* (3), 293-307.

(45) Wei, X. L.; Carroll, P. J.; Sneddon, L. G. Ruthenium-catalyzed ring-opening polymerization syntheses of poly(organodecaboranes): New single-source boron-carbide precursors. *Chem. Mater.* **2006,** *18* (5), 1113-1123.

(46) Crespo, E.; Gentil, S.; Vinas, C.; Teixidor, F. Post-overoxidation self-recovery of polypyrrole doped with a metallacarborane anion. *J. Phys. Chem. C* **2007,** *111* (49), 18381-18386.

(47) Lesnikowski, Z. J. Boron Clusters- A new entity for DNA-Oligonucleotide modification. *Eur. J. Org. Chem.* **2003,** *23*, 4489-4500.

(48) Matejicek, P.; Uchman, M.; Lepsik, M.; Srnec, M.; Zednik, J.; Kozlik, P. Preparation and Separation of Telechelic Carborane-Containing Poly(ethylene glycol)s *ChemPlusChem* **2013**, *78* (6), 528-535.

(49) Fan, P.; Neumann, J.; Stolte, S.; Arning, J.; Ferreira, D.; Edwards, K.; Gabel, D. Interaction of dodecaborate cluster compounds on hydrophilic column materials in water. *J. Chromatogr. A* **2012,** *1256*, 98-104.

(50) Horakova, H.; Gruner, B.; Vespalec, R. Emerging Subject for Chiral Separation Science: Cluster Boron Compounds. *Chirality* **2011,** *23* (4), 307-319.

(51) Taylor, R.; Kennard, O. Crystallographic evidence for the existence of C-H...O, C-H...N, and C-H...C1 hydrogen-bonds. *J. Am. Chem. Soc.* **1982,** *104* (19), 5063-5070.

(52) Barbera, G.; Vinas, C.; Teixidor, F.; Rosair, G. M.; Welch, A. J. Self-assembly of carborane molecules via C-H center dot center dot center dot I hydrogen bonding: the molecular and crystal structures of 3-I-1,2-closo-C2B10H11. *J. Chem. Soc., Dalton Trans.* **2002,** *19*, 3647-3648.

(53) Fox, M. A.; Hughes, A. K. Cage C-H···X interactions in solid-state structures of icosahedral carboranes. *Coordin. Chem. Rev.* **2004,** *248* (5-6), 457-476.

(54) Puga, A. V.; Teixidor, F.; Sillanpaa, R.; Kivekas, R.; Arca, M.; Barbera, G.; Vinas, C. Iodinated ortho-Carboranes as Versatile Building Blocks to Design Intermolecular Interactions in Crystal Lattices. *Chem. Eur. J.* **2009,** *15* (38), 9764-9772.

(55) Blanch, R. J.; Williams, M.; Fallon, G. D.; Gardiner, M. G.; Kaddour, R.; Raston, C. L. Supramolecular complexation of 1,2-dicarbadodecaborane(12). *Angew. Chem. Int. Ed.* **1997,** *36* (5), 504-506.

(56) Leites, L. A. Vibrational Spectroscopy of Carboranes and Parent Boranes and its Capabilities in Carborane Chemistry. *Chem. Rev.***1992,** *92* (2), 279-323.

(57) Puga, A. V.; Teixidor, F.; Sillanpaa, R.; Kivekas, R.; Vinas, C. From mono- to poly-substituted frameworks: A way of tuning the acidic character of C-c-H in o-Carborane derivatives. *Chem. Eur. J.* **2009,** *15* (38), 9755-9763.

(58) Campbell, J. P.; Hwang, J. W.; Young, V. G.; Von Dreele, R. B.; Cramer, C. J.; Gladfelter, W. L. Crystal engineering using the unconventional hydrogen bond. Synthesis, structure, and theoretical investigation of cyclotrigallazane. *J. Am. Chem. Soc.* **1998,** *120* (3), 521-531.

(59) Karki, K.; Gabel, D.; Roccatano, D. Structure and Dynamics of Dodecaborate Clusters in Water. *Inorg. Chem.* **2012,** *51* (9), 4894-4896.

(60) Zhang, X. L.; Dai, H. M.; Yan, H.; Zou, W. L.; Cremer, D. B-H center dot center dot center dot pi Interaction: A New Type of Nonclassical Hydrogen Bonding. *J. Am. Chem. Soc.* **2016,** *138* (13), 4334-4337.

(61) Ilie, A.; Crespo, O.; Gimeno, M. C.; Holthausen, M. C.; Laguna, A.; Diefenbach, M.; Silvestru, C. (N,Se) and (Se,N,Se) Ligands Based on Carborane and Pyridine Fragments - Reactivity of 2,6- (1'-Me-1',2'-closo-$C_2B_{10}H_{10}$)$SeCH_2$(2)C_5H_3N towards Copper and Silver. *Eur. J. Inorg. Chem.* **2017,** (20), 2643-2652.

(62) Fanfrlik, J.; Pecina, A.; Rezac, J.; Sedlak, R.; Hnyk, D.; Lepsik, M.; Hobza, P. B-H center dot center dot center dot pi: a nonclassical hydrogen bond or dispersion contact? *Phys. Chem. Chem. Phys.* **2017,** *19* (28), 18194-18200.

(63) Grunenberg, J. The Weakness of B-H...pi Interactions: Much Softer than a Hydrogen Bond. *Chem. Eur. J.***2016,** *22* (52), 18678-18681.

(64) Bhattacharyya, P. K. B-H_b···π interactions in benzene-borazine sandwich and multidecker complexes: a DFT study. *New J. Chem.***2017,** *41* (3), 1293-1302.

(65) Saha, B.; Bhattacharyya, P. K. B-H_b···π interaction in borane-graphene complexes: coronene as a case study. *New J. Chem.***2017,** *41* (12), 5040-5054.

(66) Anufriev, S. A.; Sivaev, I. B.; Suponitsky, K. Y.; Godovikov, I. A.; Bregadze, V. I. Synthesis of 10-Methylsulfide and 10-Alkylmethylsulfonium nido-Carborane Derivatives: B–H•••π Interactions between the B–H–B Hydrogen Atom and Alkyne Group in 10-RC≡CCH2S(Me)-7,8-C2B9H11. *Eur. J. Inorg. Chem.* **2017,** 4436-4443.

(67) Clark, T.; Hennemann, M.; Murray, J. S.; Politzer, P. Halogen bonding: the sigma-hole. *Journal of Molecular Modeling* **2007,** *13* (2), 291-296.

(68) Fanfrlik, J.; Prada, A.; Padelkova, Z.; Pecina, A.; Machacek, J.; Lepsik, M.; Holub, J.; Ruzicka, A.; Hnyk, D.; Hobza, P. The Dominant Role of Chalcogen Bonding in the Crystal Packing of 2D/3D Aromatics. *Angew. Chem. Int. Ed.* **2014,** *53* (38), 10139-10142.

(69) Fanfrlik, J.; Holub, J.; Ruzickova, Z.; Rezac, J.; Lane, P. D.; Wann, D. A.; Hnyk, D.; Ruzicka, A.; Hobza, P. Competition between halogen, hydrogen and dihydrogen bonding in brominated carboranes. *ChemPhysChem* **2016,** *17* (21), 3373-3376.

(70) Chevrot, G.; Schurhammer, R.; Wipff, G. Surfactant behavior of "ellipsoidal" dicarbollide anions: A molecular dynamics study. *J. Phys. Chem. B.* **2006,** *110* (19), 9488-9498.

(71) Uchman, M.; Dordovic, V.; Tosner, Z.; Matejicek, P. Classical Amphiphilic Behavior of Nonclassical Amphiphiles: A Comparison of Metallacarborane Self-Assembly with SDS Micellization. *Angew. Chem. Int. Ed.* **2015,** *54* (47), 14113-14117.

(72) Nagarajan, R. Molecular packing parameter and surfactant self-assembly: The neglected role of the surfactant tail. *Langmuir* **2002,** *18* (1), 31-38.

(73) Dordovic, V.; Tosner, Z.; Uchman, M.; Zhigunov, A.; Reza, M.; Ruokolainen, J.; Pramanik, G.; Cigler, P.; Kalikova, K.; Gradzielski, M.; Matejicek, P. Stealth Amphiphiles: Self-Assembly of Polyhedral Boron Clusters. *Langmuir* **2016,** *32* (26), 6713-6722.

(74) Medos, Z.; Bester-Rogac, M. Thermodynamics of the micellization process of carboxylates: A conductivity study. *J. Chem. Thermodyn.* **2015,** *83*, 117-122.

(75) Bauduin, P.; Prevost, S.; Farras, P.; Teixidor, F.; Diat, O.; Zemb, T. A Theta-Shaped Amphiphilic Cobaltabisdicarbollide Anion: Transition From Monolayer Vesicles to Micelles. *Angew. Chem. Int. Ed.* **2011,** *50* (23), 5298-5300.

(76) Rak, J.; Dejlova, B.; Lampova, H.; Kaplanek, R.; Matejicek, P.; Cigler, P.; Kral, V. On the Solubility and Lipophilicity of Metallacarborane Pharmacophores. *Mol. Pharm.* **2013,** *10* (5), 1751-1759.

(77) Ganguli, A. K.; Ganguly, A.; Vaidya, S. Microemulsion-based synthesis of nanocrystalline materials. *Chem. Soc. Rev.* **2010,** *39* (2), 474-485.

(78) Kunz, W.; Holmberg, K.; Zemb, T. Hydrotropes. *Curr. Opin. Colloid Interface Sci.* **2016,** *22*, 99-107.

(79) Eastoe, J.; Hatzopoulos, M. H.; Dowding, P. J. Action of hydrotropes and alkyl-hydrotropes. *Soft Matter* **2011,** *7* (13), 5917-5925.

(80) Hatzopoulos, M. H.; Eastoe, J.; Dowding, P. J.; Rogers, S. E.; Heenan, R.; Dyer, R. Are Hydrotropes Distinct from Surfactants? *Langmuir* **2011,** *27* (20), 12346-12353.

(81) Cui, X. H.; Mao, S. Z.; Liu, M. L.; Yuan, H. Z.; Du, Y. R. Mechanism of surfactant micelle formation. *Langmuir* **2008,** *24* (19), 10771-10775.

(82) Okur, H. I.; Hladilkova, J.; Rembert, K. B.; Cho, Y.; Heyda, J.; Dzubiella, J.; Cremer, P. S.; Jungwirth, P. Beyond the Hofmeister Series: Ion-Specific Effects on Proteins and Their Biological Functions. *J. Phys. Chem. B.* **2017,** *121* (9), 1997-2014.

(83) Salis, A.; Ninham, B. W. Models and mechanisms of Hofmeister effects in electrolyte solutions, and colloid and protein systems revisited. *Chem. Soc. Rev.* **2014,** *43* (21), 7358-7377.

(84) Popov, A.; Borisova, T. Adsorption of dicarbollylcobaltate(III) anion {(π-(3)-1,2-$B_9C_2H_{11}$)(2)Co(III)(-)} at the water/1,2-dichloroethane interface. Influence of counterions' nature. *J. Colloid Interface Sci.* **2001,** *236* (1), 20-27.

(85) Chevrot, G.; Schurhammer, R.; Wipff, G. Molecular dynamics study of dicarbollide anions in nitrobenzene solution and at its aqueous interface. Synergistic effect in the Eu(III) assisted extraction. *Phys. Chem. Chem. Phys.* **2007,** *9* (44), 5928-5938.

(86) Chevrot, G.; Schurhammer, R.; Wipff, G. Synergistic effect of dicarbollide anions in liquid-liquid extraction: a molecular dynamics study at the octanol-water interface. *Phys. Chem. Chem. Phys.* **2007,** *9* (16), 1991-2003.

(87) Matejicek, P.; Cigler, P.; Prochazka, K.; Kral, V. Molecular assembly of metallacarboranes in water: Light scattering and microscopy study. *Langmuir* **2006,** *22* (2), 575-581.

(88) Vinas, C.; Tarres, M.; Gonzalez-Cardoso, P.; Farras, P.; Bauduin, P.; Teixidor, F. Surfactant behaviour of metallacarboranes. A study based on the electrolysis of water. *Dalton Trans.* **2014,** *43* (13), 5062-5068.

(89) Bauduin, P.; Zemb, T. Perpendicular and lateral equations of state in layered systems of amphiphiles. *Curr. Opin. Colloid Interface Sci.* **2014,** *19* (1), 9-16.

(90) Brusselle, D.; Bauduin, P.; Girard, L.; Zaulet, A.; Vinas, C.; Teixidor, F.; Ly, I.; Diat, O. Lyotropic Lamellar Phase Formed from Monolayered theta-Shaped Carborane-Cage Amphiphiles. *Angew. Chem. Int. Ed.* **2013,** *52* (46), 12114-12118.

(91) Brus, J.; Zhigunov, A.; Czernek, J.; Kobera, L.; Uchman, M.; Matejicek, P. Control over the Self-Assembly and Dynamics of Metallacarborane Nanorotors by the Nature of the Polymer Matrix: A Solid-State NMR Study. *Macromolecules* **2014,** *47* (18), 6343-6354.

(92) Assaf, K. I.; Ural, M. S.; Pan, F. F.; Georgiev, T.; Simova, S.; Rissanen, K.; Gabel, D.; Nau, W. M. Water Structure Recovery in Chaotropic Anion Recognition: High-Affinity Binding of Dodecaborate Clusters to -Cyclodextrin. *Angew. Chem. Int. Ed.* **2015,** *54* (23), 6852-6856.

(93) Xiong, H. J.; Zhou, D. F.; Zheng, X. H.; Qi, Y. X.; Wang, Y. H.; Jing, X. B.; Huang, Y. B. Stable amphiphilic supramolecular self-assembly based on cyclodextrin and carborane for the efficient photodynamic therapy. *Chem. Commun.* **2017,** *53* (24), 3422-3425.

(94) Gassin, P. M.; Girard, L.; Martin-Gassin, G.; Brusselle, D.; Jonchere, A.; Diat, O.; Vinas, C.; Teixidor, F.; Bauduin, P. Surface Activity and Molecular Organization of Metallacarboranes at the Air-Water Interface Revealed by Nonlinear Optics. *Langmuir* **2015,** *31* (8), 2297-2303.

(95) Kronberg, B. The hydrophobic effect. *Curr. Opin. Colloid Interface Sci.* **2016,** *22*, 14-22.

(96) Brandeburgo, W. H.; van der Post, S. T.; Meijer, E. J.; Ensing, B. On the slowdown mechanism of water dynamics around small amphiphiles. *Phys. Chem. Chem. Phys.* **2015,** *17* (38), 24968-24977.

(97) Chen, L. J.; Lin, S. Y.; Huang, C. C. Effect of hydrophobic chain length of surfactants on enthalpy-entropy compensation of micellization. *J. Phys. Chem. B.* **1998,** *102* (22), 4350-4356.

(98) Syme, N. R.; Dennis, C.; Phillips, S. E. V.; Homans, S. W. Origin of heat capacity changes in a "Nonclassical" hydrophobic interaction. *ChemBioChem* **2007,** *8* (13), 1509-1511.

(99) Biela, A.; Sielaff, F.; Terwesten, F.; Heine, A.; Steinmetzer, T.; Klebe, G. Ligand Binding Stepwise Disrupts Water Network in Thrombin: Enthalpic and Entropic Changes Reveal Classical Hydrophobic Effect. *J. Med. Chem.* **2012,** *55* (13), 6094-6110.

(100) Biela, A.; Nasief, N. N.; Betz, M.; Heine, A.; Hangauer, D.; Klebe, G. Dissecting the Hydrophobic Effect on the Molecular Level: The Role of Water, Enthalpy, and Entropy in Ligand Binding to Thermolysin. *Angew. Chem. Int. Ed.* **2013,** *52* (6), 1822-1828.

(101) Rick, S. W. Heat capacity change of the hydrophobic interaction. *J. Phys. Chem. B.* **2003,** *107* (36), 9853-9857.

(102) Chandler, D. Interfaces and the driving force of hydrophobic assembly. *Nature* **2005,** *437* (7059), 640-647.

(103) Zangi, R. Driving Force for Hydrophobic Interaction at Different Length Scales. *J. Phys. Chem. B.* **2011,** *115* (10), 2303-2311.

(104) Morita, T.; Westh, P.; Nishikawa, K.; Koga, Y. How Much Weaker Are the Effects of Cations than Those of Anions? The Effects of K^+ and Cs^+ on the Molecular Organization of Liquid H2O. *J. Phys. Chem. B.* **2014,** *118* (29), 8744-8749.

(105) Lin, J. H.; Chen, W. S.; Hou, S. S. NMR Studies on Effects of Tetraalkylammonium Bromides on Micellization of Sodium Dodecylsulfate. *J. Phys. Chem. B.* **2013,** *117* (40), 12076-12085.

(106) Elworthy, P. H.; Mysels, K. J. Surface tension of sodium dodecylsulfate solutions and phase separation model of micelle formation. *J. Colloid Interface Sci.* **1966,** *21* (3), 331-347.

(107) Eastoe, J.; Dalton, J. S. Dynamic surface tension and adsorption mechanisms of surfactants at the air-water interface. *Adv. Colloid Interface Sci.* **2000,** *85* (2-3), 103-144.

(108) Paula, S.; Sus, W.; Tuchtenhagen, J.; Blume, A. Thermodynamics of micelle formation as a function of temperature - a high-sensitivity titration calorimetry study. *J. Phys. Chem.* **1995,** *99* (30), 11742-11751.

(109) Garidel, P.; Hildebrand, A.; Neubert, R.; Blume, A. Thermodynamic characterization of bile salt aggregation as a function of temperature and ionic strength using isothermal titration calorimetry. *Langmuir* **2000,** *16* (12), 5267-5275.

(110) Kroflic, A.; Sarac, B.; Cerkovnik, J.; Bester-Rogac, M. Hydrophobicity of counterions as a driving force in the self-assembly process: Dodecyltrimethylammonium chloride and parabens. *Colloids Surf., A* **2014,** *460*, 108-117.

(111) Ropers, M. H.; Czichocki, G.; Brezesinski, G. Counterion effect on the thermodynamics of micellization of alkyl sulfates. *J. Phys. Chem. B.* **2003,** *107* (22), 5281-5288.

(112) Ruokolainen, J.; ten Brinke, G.; Ikkala, O. Supramolecular polymeric materials with hierarchical structure-within-structure morphologies. *Adv.Mater.* **1999,** *11* (9), 777-780.

(113) Winnik, F. M.; Regismond, S. T. A. Fluorescence methods in the study of the interactions of surfactants with polymers. *Colloids Surf., A* **1996,** *118* (1-2), 1-39.

(114) Faul, C. F. J.; Antonietti, M. Ionic self-assembly: Facile synthesis of supramolecular materials. *Adv.Mater.* **2003,** *15* (9), 673-683.

(115) Fanfrlik, J.; Brynda, J.; Rezac, J.; Hobza, P.; Lepsik, M. Interpretation of Protein/Ligand Crystal Structure using QM/MM Calculations: Case of HIV-1 Protease/Metallacarborane Complex. *J. Phys. Chem. B.* **2008,** *112* (47), 15094-15102.

(116) Goszczynski, T. M.; Fink, K.; Kowalski, K.; Lesnikowski, Z. J. Interactions of Boron Clusters and their Derivatives with Serum Albumin. *Scientific Reports* **2017,** *7*, 9800.

(117) Matejicek, P.; Zednik, J.; Uselova, K.; Plestil, J.; Fanfrlik, J.; Nykanen, A.; Ruokolainen, J.; Hobza, P.; Prochazka, K. Stimuli-Responsive Nanoparticles Based on Interaction of Metallacarborane with Poly(ethylene oxide). *Macromolecules* **2009,** *42* (13), 4829-4837.

(118) Matejicek, P.; Brus, J.; Jigounov, A.; Plestil, J.; Uchman, M.; Prochazka, K.; Gradzielski, M. On the Structure of Polymeric Composite of Metallacarborane with Poly(ethylene oxide). *Macromolecules* **2011,** *44* (10), 3847-3855.

(119) Dordovic, V.; Uchman, M.; Reza, M.; Ruokolainen, J.; Zhigunov, A.; Ivankov, O. I.; Matejicek, P. Cation-sensitive compartmentalization in metallacarborane containing polymer nanoparticles. *RSC Adv.* **2016,** *6* (12), 9884-9892.

(120) Nunez, R.; Romero, I.; Teixidor, F.; Vinas, C. Icosahedral boron clusters: a perfect tool for the enhancement of polymer features. *Chem. Soc. Rev.* **2016,** *45* (19), 5147-5173.

(121) Schwartz, J. J.; Mendoza, A. M.; Wattanatorn, N.; Zhao, Y. X.; Nguyen, V. T.; Spokoyny, A. M.; Mirkin, C. A.; Base, T.; Weiss, P. S. Surface Dipole Control of Liquid Crystal Alignment. *J. Am. Chem. Soc.* **2016**, *138* (18), 5957-5967.

4.2- Publication II

Total Description of Intrinsic Amphiphile Aggregation: Calorimetry Study and Molecular Probing

Abstract

Isothermal Titration Calorimetry is an apt tool for a total thermodynamic description of self-assembly of atypical amphiphiles such as anionic boron cluster compounds (COSAN) in water. Global fitting of ITC enthalpograms reveal remarkably features that differentiate COSAN from classical amphiphiles: (i) strong enthalpy and weak entropy contribution to the free energy of aggregation, (ii) low degree of counterion binding, and (iii) deviation of concentration profiles of COSAN unimers and micelles from simple closed association model due to the low aggregation number. The counterion condensation obtained from the thermodynamic model was compared with results of 7Li DOSY NMR of Li[COSAN] micelles that allows direct tracking Li cations. The basic thermodynamic study of COSAN alkaline salts aggregation was complemented by NMR and ITC experiments in dilute Li/NaCl and acetonitrile aqueous solutions of COSAN. The strong affinity of acetonitrile molecules to COSAN clusters were microscopically investigated by all-atomic MD simulations. The impact of ionic strength on COSAN self-assembling was comparable to the behavior of classical amphiphiles, whereas even small amount of acetonitrile co-solvent pronounced non-classical character of COSAN aggregation. It demonstrates that large changes in self-assembling can be triggered by the presence of traces of organic solvents.

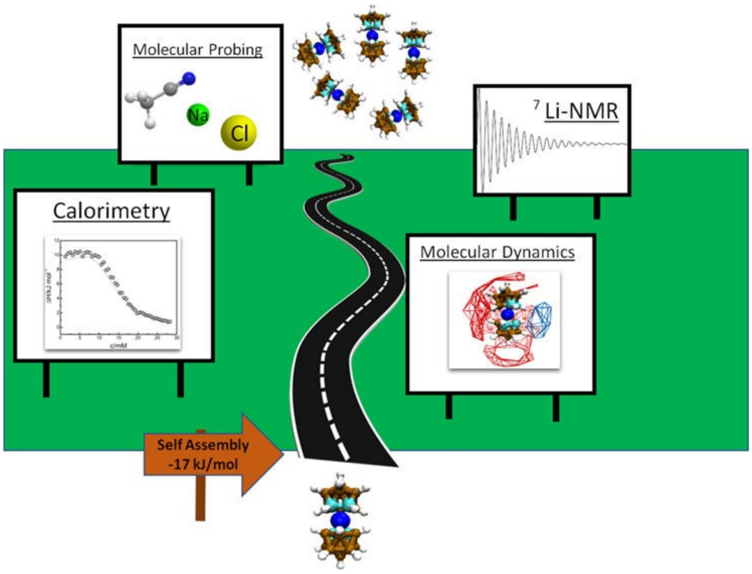

*Version presented here has small format modifications compared to the original form at: Total Description of Intrinsic Amphiphile Aggregation: Calorimetry Study and Molecular Probing Fernandez-Alvarez, R.; Medoš, Ž.; Tošner, Z.; Zhigunov, A.; Uchman, M.; Hervø-Hansen, S.; Lund, M.; Bešter-Rogač, M.; Matějíček, P. Langmuir 34 (2018) 14448-14457.

Introduction

New amphiphiles lacking traditional head-and-tail structure have recently been discovered and spawn great interest since they defy the general idea that specific molecular topologies induce self-assembly.[1] Micellization is not solely dependent on the molecular topology and the presence of separated hydrophobic and hydrophilic parts. Molecules with atypical shapes such as bile salts and some borane clusters also aggregate, despite the lack of a traditional head-and-tail structure.[2-6] The growing list of non-classical amphiphiles reveals added factors that need consideration when predicting self-assembly.[1] Hence, there is a general need for models capable of providing a total description of the self-assembly for both classical and non-classical amphiphiles.

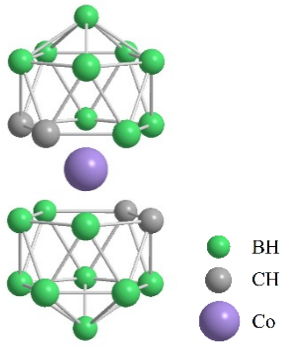

Scheme 4.2.1. Molecular structure of cobalt bis-dicarbollide (COSAN)

The metallocarborane [3,3'-cobalt(III) bis(1,2-dicarbollide)](1-) anion (COSAN) is classified as an intrinsic amphiphile[1,7] and shares many characteristics with the recently described superchaotropes.[1, 8, 9] It is composed of two dicarbollide *nido*-clusters facing each other with a cobalt(III) ion sandwiched in between (Scheme 4.2.1), resembling the well-known ferrocene[10] Its chemistry is diverse[11, 12] and with a broad range of applications.[13-15] The molecular structure is incapable of forming classical hydrogen bonds with water, yet it is able to form dihydrogen bonds.[16-18] The latter are considerably weaker, leading to a patchy structure of hydration water around COSAN molecules, as recently determined through molecular dynamic simulations.[19] Nonetheless, most COSAN salts are readily soluble in water and common polar organic solvents.[20] The negative charge (-1) is delocalized across its entire structure and presents a decreased electron density around the C-H bonds creating a dipole moment in the *cisoid* and *gauche* conformations (the last of three COSAN rotamers – *transoid* has negligible dipole moment; shown in Scheme 4.2.1).[21]

The properties of boron cluster aggregates have previously been studied in detail by SAXS, SANS, cryo-TEM and ITC.[1, 7, 22] Nanostructures such as vesicles,[22] large spherical aggregates,[6] lamellar structures,[23] and small micelles,[22, 24] with the latter being the predominant form have been observed.[7, 25] ITC and DOSY NMR studies determined that, in water, COSAN micellization follows the closed association model with a critical micelle concentration (CMC) at ~11 mM, self-assembling into small micelles with hydrodynamic radii, R_H, around 1.5 nm.[25]

Our previous experimental and theoretical results showed that COSAN micellization is predominantly an enthalpically driven process with only a minor effect of counterions (H, Li, Na, K).[1] Conversely, most surfactants are characterized by entropy-driven micellization.[26] In case of COSAN there is no hydrophobic tail which leads to aggregation driven by nonclassical hydrophobic effect characterized by small entropy changes upon micellization.[19] To our knowledge, COSAN aggregation is the only enthalpy driven micellization process in water found in literature, and it can be categorized as an example where an intricate combination of non-classical hydrophobic effect[27] and superchaotropic effect[8, 28] takes place. Computer simulations rationalized the COSAN association by counterintuitive anion-anion attraction due to hydrophobic, solvent mediated interactions, and anion-cation repulsion in aqueous media.[19] Besides strong impact of solvent redistribution, intermicellar dihydrogen bonding stabilizes the COSAN micelles in aqueous solutions and may contribute to the enthalpy of micellization. [19, 23]

We previously calculated the free energy of micellization, $\Delta_M G$, for COSAN using literature models that include fixed parameters such as aggregation number (n) and the degree of counterion binding on the micelles (β).[25] The values of n and β were obtained from scattering and conductivity experiments under very different conditions as compared to ITC demicellization. The n parameter is usually neglected in the formula for $\Delta_M G$ for classical surfactants that form micelles with $n > 50$. However, this is invalid in the case of COSAN due to small aggregation numbers. So far SAXS and SANS have been used to determine n of COSAN micelles, but have disadvantages. SAXS and SANS yield n values with high experimental error and at concentrations much higher than CMC. The value of β is commonly estimated from conductivity experiments that also have limitations.[29] COSAN being an unusual example for micellization, a more thorough determination of thermodynamic parameters is therefore needed.

In this work, we applied a combination of various techniques in order to fully understand the self-assembly process of COSAN. First, we applied an association model to globally fit experimental data from ITC and estimated all the parameters describing the micellization process from one set of ITC curves. It provided standard thermodynamic parameters of micellization (enthalpy ($\Delta_M H^\theta$), entropy ($\Delta_M S^\theta$), Gibbs free energy ($\Delta_M G^\theta$)), and heat capacity of micellization ($\Delta_M C_p^\theta$)), as well as parameters CMC, n and β for several COSAN salts: X[COSAN], where X = H, Li, Na, K (the model introduced in Supporting Information, SI). The model describes the micellization as a one-step process and is based on the mass action model. The large aggregates observed in previous reports[6, 22-24] have not been included to the model because of their negligible fraction as compared to unimers and small micelles in the given concentration range.[25] By using n as a fitting parameter, we circumvented the aforementioned problems with *n* determination through SAXS/SANS. A similar mass action model has previously been used to describe the micellization of dodecyltrimethylammonium chloride (DTAC)[30, 31], imidazolium-based surface active ionic liquids[32], and a non-classical amphiphile CHAPS[3]. The model was recently improved by taking into account the state of the titrant and titrated solution during the ITC experiment and it successfully described the micellization of sodium dodecanoate[33] and surface active ionic liquids[34]. The data obtained from the fitting procedure was critically compared to data obtained from complementing techniques (SAXS, NMR).

Additionally, micellization of COSAN in the presence of water-acetonitrile mixtures with increased ionic strength was also assessed. We used acetonitrile molecules (MeCN) and counterions (Li^+) as NMR-probes to investigate the solvation shell of COSAN cluster and its surroundings. In water-acetonitrile mixtures, the balance of solvophobic/solvophilic interactions is altered. Under such conditions, micellization experiments provide information about the solute-solvent interactions behind the hydrophobic and superchaotropic effects.[1, 19] Moreover, salt addition to COSAN solutions probes the role of electrostatic balance within the COSAN micelles, and also kosmotropic/chatropic effect of corresponding counterions.[35]

Experimental section

Materials

Cesium Cobalt bis(dicarbollide), Cs[COSAN], was purchased from KatChem Ltd., Czech Republic. It was subsequently transformed to the other salts and acid, Li[COSAN], Na[COSAN], K[COSAN], and H[COSAN], using an extraction procedure previously described (purity confirmed by NMR, and the water content in M[COSAN] for M = H, Li, Na, K was determined by TGA to be 7%, 13%, 16%, and 0% (wt%), respectively).[36] No traces of cationic impurities were evident in electropherograms from capillary electrophoresis (shown in Figure S4.2.1 in Supporting Information, S.I.). LiCl, NaCl, KCl, HCl and Acetonitrile were acquired from Sigma-Aldrich and used as received. All COSAN solutions were prepared by weighting and dissolving in Milli-Q water. Salted COSAN solutions were prepared by dissolving a weighted amount in the corresponding LiCl/NaCl solution.

Isothermal Titration Calorimetry (ITC)

Microcalorimetric titrations were performed in a Nano ITC, TA instruments – Waters LLC, New Castle, USA. The microcalorimeter consists of a sample cell and a reference cell (24K gold). The sample cell is connected to a 50 µL syringe. The syringe is equipped with a flattened, twisted paddle at the tip which ensures continuous mixing of the solutions in the cell rotating at 250 rpm. The reaction cell was filled with Milli Q water or with the corresponding LiCl/NaCl solution. Aliquots of COSAN were subsequently injected into the filled reaction cell. Concentration of the COSAN salts in the syringe variated depending on temperature in the following way: 90, 120, 120, 200 mM for temperatures of 278, 288, 298 and 318 K, respectively (for exact concentrations please refer to Table S4). For salted solutions all measurements were conducted at 298 K and COSAN syringe concentration variated depending on the salt concentration in the following way: 120, 120, 120, 40 and 30 mM for salt concentrations of 0, 0.01, 0.1, 0.5 and 1 M.

Different acetonitrile (MeCN) solutions were prepared (0.2, 0.5, 0.85 and 1% (mol%)) and used to directly prepare solution of COSAN 120 mM. Percentage values refer to mol percentage of MeCN in solution (for exact concentrations please refer to Table S5).

Fitting of ITC curve and model equation described in detail in Supporting Information, SI.

Small Angle X-ray scattering (SAXS). The SAXS experiments were performed using a pinhole camera (Molecular Metrology SAXS System) attached to a microfocused X-ray beam generator (Osmic Micro-Max 002) operating at 45 kV and 0.66 mA (30 W). The camera was equipped with a multiwire gas-filled detector with an active area diameter of 20 cm (Gabriel design). Two experimental setups were used to cover the q range of 0.04−11 nm^{-1}. Scattering vector $q = (4\pi/\lambda)\sin\vartheta$, where $\lambda = 0.154$ nm is the wavelength, and ϑ is the angle between the incident X-ray beam and the detector measuring the scattered intensity.

NMR spectroscopy.

All NMR data were recorded using Bruker Avance III spectrometer operating at proton Larmor frequency of 600 MHz. ^{1}H, ^{13}C and ^{15}N experiments were measured using a cold probe while for ^{7}Li a broadband probe was used. ^{15}N chemical shift was observed indirectly by measuring ^{1}H-^{15}N HMBC correlation spectrum employing the long-range coupling constant of 5 Hz. The carbon T_1 relaxation of COSAN and acetonitrile was estimated in two separate inversion recovery experiments using 9-12 values of variable delay adapted to the short (about 1 s) and very long (about 30 s) relaxation times. The double stimulated echo experiment with bipolar pulse field gradients was used to monitor translational diffusion for both ^{1}H and ^{7}Li signals. The diffusion time and the duration of gradients were optimized to follow signal decays down to at least 10% of the initial value in all cases. The diffusion coefficients were calibrated using a standard sample of 1% H_2O in D_2O (doped with $GdCl_3$) assuming the diffusion coefficient 1.9×10^{-9} m^2s^{-1} for the HDO signal at 25 °C. For lithium, the effect of the magnetic field gradients was recalculated using the corresponding gyromagnetic ratio. Data were processed using the spectrometer software (Topspin 3.5, Bruker).

Molecular Dynamics.

All atomic molecular dynamics have been conducted using the optimized geometries for the three COSAN isomers utilizing the same force field parameters from our previous study.[1930] Acetonitrile force field parameters were obtained from the DFT (B3LYP/6-31G*) optimized geometry with partial charges evaluated utilizing the Merz-Singh-Kollman scheme,[37] while LJ and bonded parameters were assigned from the universal force field using the OBGMX server.[38, 39] One COSAN molecule in a specific isomer was initially packed with 150 acetonitrile (~5 mol-% by amount) and solvated with 3020 water molecules in a 5×5×5 nm^3 periodic cubic box. All simulations were conducted using the OpenMM 7 simulation package[40] with long range electrostatic interactions handled by particle mesh Ewald summation with an 8 Å cutoff for the direct space interactions, Lorentz-Berthelot mixing rules for LJ interactions, and with frozen COSAN atoms in the center of the box. The systems were first minimized and next equilibrated first in terms of temperature to 298 Kelvin by a linear gradient in temperature from 10 to 298 Kelvin over 50000 steps utilizing Langevin dynamics with a friction coefficient of 1.0 ps^{-1} and second in terms of density to 1 bar pressure using an isotropic Monte Carlo barostat with attempts of volume change every 25 steps for a total of 50000 steps with all simulations using a time step of 2 fs. The equilibration was followed by a production run in the *NPT* ensemble, where configurations were gathered every 4 ps for statistical evaluation over the course of 100 ns of simulation.

The saved configurations for the three molecular dynamics run, were used to generate spatial distribution functions with a bin size of 0.1 nm using the GROMACS 2016.3 software package[41] and visualized using visual MD.[42] Radial distributions functions were generated using MDTraj.[43]

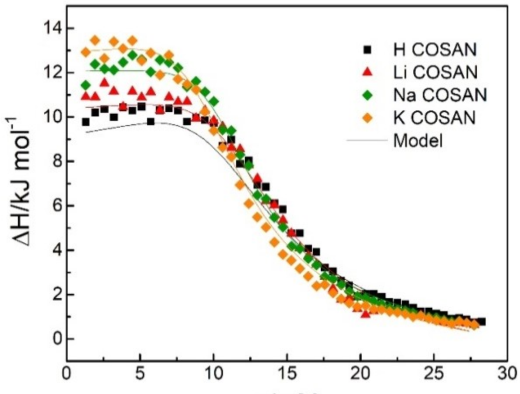

Figure 4.2.1. Enthalpograms of COSAN salts in water at 298.15 K. Solid lines represent the fit according to the Equation xviii in SI.

Thermodynamics of COSAN aggregation

Isothermal Titration Calorimetry (ITC) demicellization experiments were carried out for X[COSAN] salts (X = Li, Na, K and H) at four different temperatures (278, 288, 298 and 318 K). Figure 4.2.1 shows the enthalpograms of all four salts at 298 K. Counterions give rise only to small variations in $\Delta_M H^\theta$, indicating that the mechanism of aggregation and CMC values for the different salts are similar, in agreement with previous DOSY NMR experiments.[25]

The titration curves adopt a characteristic sigmoidal shape of demicellization processes[44] (Figure S4.2.2). This is characterized by an initial linear region where the measured heat effect corresponds to the combination of breaking up of added micelles and changes in the concentration of monomers. This is followed by a transition region in which the concentration inside the reaction cell is close to the CMC. The broadness of this region seen here for COSAN is characteristic of amphiphiles with small aggregation numbers (from previous scattering experiments: $n \approx$ 5-15).[7, 22, 25] In the final region the measured heat affects are the sum of many contributions, primarily the dilution of the titrated solution fallowed by small changes in amounts of aggregates and monomers.

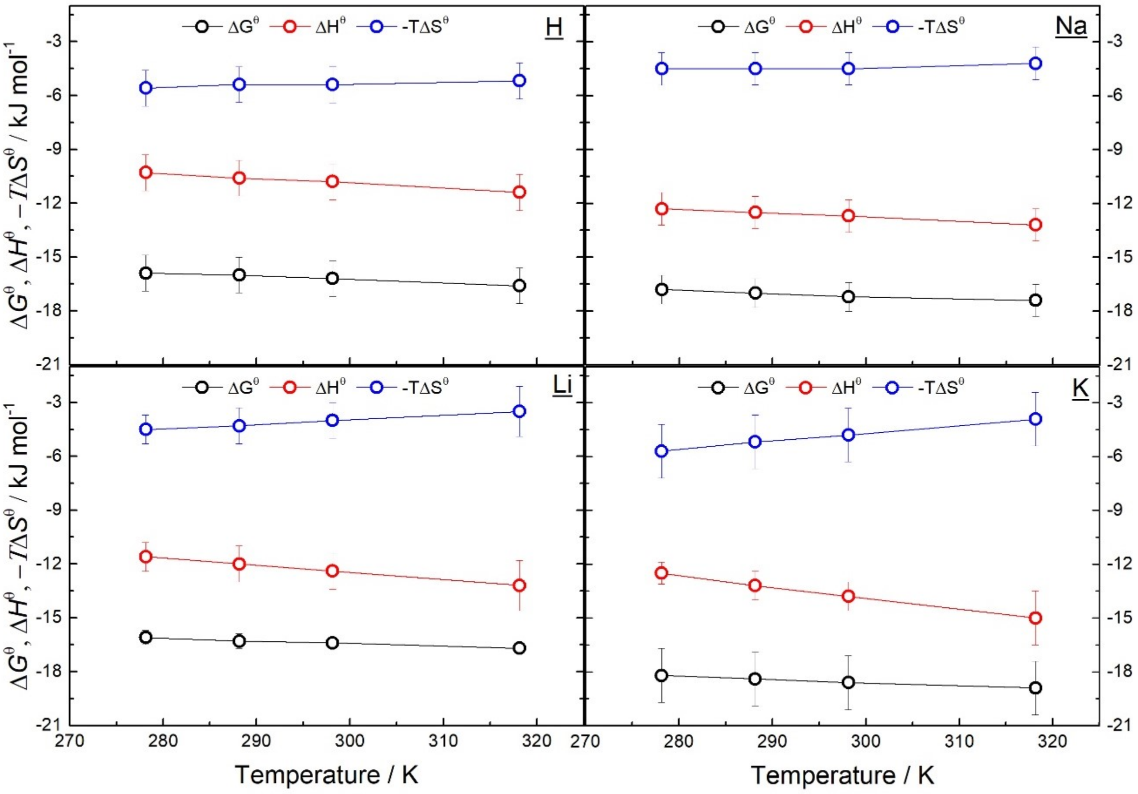

Figure 4.2.2. Temperature dependences of thermodynamic parameters of aggregation for X[COSAN] (X = H, Li, Na, K) in water: standard enthalpy, $\Delta_M H^\theta$, Gibbs free energy, $\Delta_M G^\theta$, and

entropy contributions, $-T\Delta_M S^\theta$, as obtained by the fitting procedure according to the model equation (corresponding values given in Table S1 in SI).

The fitting procedure of Equation (equation xviii in SI) directly yields $\Delta_M G^\theta$ and $\Delta_M H^\theta$, while the Gibbs-Helmholtz equation was used to obtain $T\Delta_M S^\theta$. Figure 4.2.2 compares these thermodynamic parameters of aggregation for all alkali COSAN salts. The results are very similar, with only small differences in the $\Delta_M H^\theta$ as expected from inspection of Figure 4.2.1. Overall, H[COSAN] shows slightly larger entropic contribution to $\Delta_M G^\theta$ and K[COSAN] has the most negative $\Delta_M G^\theta$ among the COSAN salts. The general trend agrees with previously published results,[1] albeit the thermodynamic values differ slightly. Contrary to classical amphiphiles, the micellization of COSAN is enthalpy driven even at low temperature (5°C) and the entropy contribution to $\Delta_M G^\theta$ remains unusually low across the studied temperature range (5-45°C).

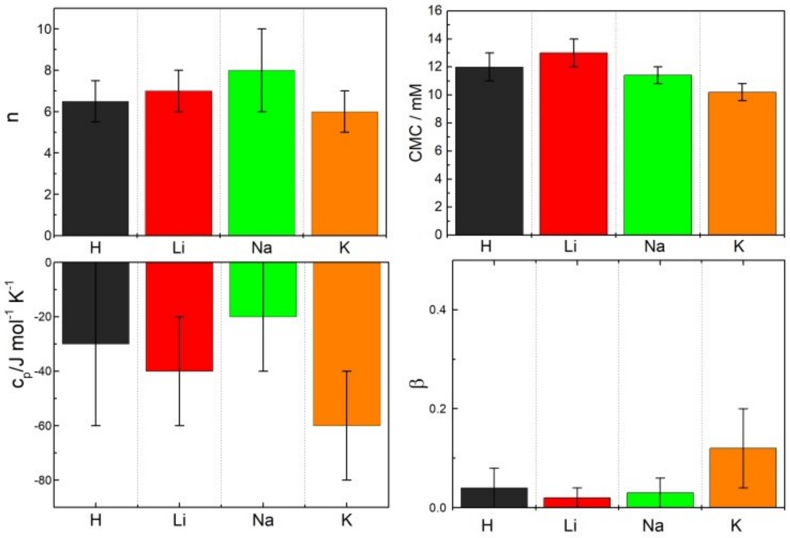

Figure 4.2.3. Parameters of global fitting of enthalpograms temperature series aggregation number (*n*), degree of counterion binding on micelles (*β*) and heat capacity change of micellization ($\Delta_M C_p^\theta$), and values of critical micelle concentration (CMC) at 298.15 K for various COSAN salts (marked by counterions).

Temperature affects the shape of enthalpograms for the micellization of all X[COSAN]. There is an increase in the absolute value of ΔH and cmc with raising temperature (Tables S1 and S2 in SI). In most surfactants, cmc *vs* temperature reveals a typical U-shaped plot with a minimum cmc around room temperature where $\Delta_M H^\theta = 0$.[43, 45] However Figure S4.2.3 in SI shows otherwise for COSAN.[46] Similar behavior has been observed recently at micellization of 1-

dodecyl-3-methylimidazolim iodide and salicylate, where the process was also exothermic in the studied temperature range without any minimum in cmc.[32]

The temperature change of enthalpy of micellization is related to the heat capacity change of micellization, $\Delta_M C_p^\theta$. This parameter can be used as a measure of the hydrophobic effect.[47] For COSAN salts, it gives the values in range between -20 and -60 $J \cdot K^{-1} \cdot mol^{-1}$ with only small impact of cation selectivity, where K[COSAN] has slightly higher contribution of hydrophobic effect than other COSAN salts (Figure 4.2.3 and Table S4.2.2). The absolute values are significantly lower than for classical surfactants and also other non-classical ones (bile salts) pointing to only minor rearrangement of water molecules during the COSAN micellization [details in ref 6]. These results correlate well with recently published results in which $^1H\{^{11}B\}$ and $^{11}B\{^1H\}$ NMR were used to study the micellization process.[48]

Comparison of obtained degree of counterion binding, β, and aggregation number, n: ITC versus other methods

In previous papers, *β* was estimated based on experimental and simulation evidences to be close to zero for all COSAN salts.[1] The same picture was obtained from ITC data (Figure 4.2.3). In all cases, the counterion binding on the micelles is close to zero and on the edge of the experimental error. The value of *β* can also be related to cation-anion pairing.[49] The noticeably low values agree with previous MD simulations which show a short-range $COSAN^-$-Na^+ repulsion, current results indicate that such counterintuitive behavior is extended for COSAN when paired with any alkaline counterion.[19] Moreover, the simulations were carried out for single molecules but experimental results imply the repulsion is maintained in the micelles bearing multiple charges. The mild contact of counterions with COSAN micelles is also consistent with The Law of Matching Water Affinities and the so-called “volcano plot” describing contact ion pairs of chaotropic and kosmotropic ions.[35] The *β* value for the potassium salt is slightly higher than for other salts, agreeing with the aforementioned theory that ion pairing of K^+ with COSAN should be strongest among the studied salts.

The aggregation number, *n*, is used as a fitting parameter in the applied model, allowing us to estimate a COSAN aggregation number in micelles, independent from scattering data (Figure 4.2.3). Values obtained from the model are small (<10) as expected from previous results. As a comparison the SAXS/WAXS section in SI shows curves for all COSAN salts (Figures S4.2.4A, B in SI). The Guinier region was used to estimate the forward scattering (proportional to *n*), yielding a broad range of *n* for the different COSAN salts: 4-20 depending on the *q*-range used (see data in SI). Due to the negligible impact of cation on COSAN aggregation, we find this result questionable. Further, Zemb *et al.* obtained $n = 12$ for H[COSAN] by SANS proposing that aggregation number of 12-14 is the upper limit for packing of the charged clusters to the globular aggregate without compensation of charge by counterions.[50]

Mobility of COSAN counterions

^{7}Li DOSY NMR was used to track the self-diffusion of lithium in Li[COSAN] solutions. Figure 4.2.4 shows that the diffusion of Li^+ is identical for LiCl and Li[COSAN] below CMC, while above a fraction of the Li^+ ions are slowed-down by COSAN micelles as reflected by a decrease in the average diffusion coefficient. The relative decrease for lithium diffusion follows the trend of COSAN micellization (Figure S4.2.5 in SI).

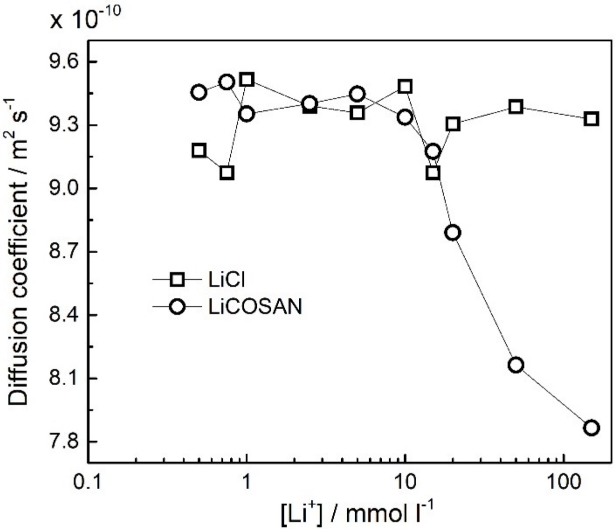

Figure 4.2.4. Apparent diffusion coefficient of Li^+ obtained by ^{7}Li DOSY NMR in LiCl and Li[COSAN] solutions.

The apparent value of lithium diffusion, D_{Li}(mean), is given as a number average between free lithium diffusion (D_{Li} obtained by ^{7}Li DOSY NMR for LiCl) and of lithium diffusion slowed-down by COSAN micelles (D_{MIC} obtain by fitting of ^{1}H DOSY NMR for Li[COSAN] concentration series by the closed association model).[25] The value of β^{NMR} was estimated from ^{1}H and ^{7}Li DOSY NMR data as described in Scheme 4.2.2. Resulting equation gives β^{NMR} ~0.15-0.20 that is higher than from the global fitting of ITC curves, yet still in the range of rough estimate based on preliminary predictions ($\beta < 0.25$).[170] This value was further corrected by taking into account deviations of COSAN micellization from "ideal" closed association model proposed for classical surfactants (details in SI).

The difference raised the question whether the same β was being monitored by calorimetry and by DOSY NMR. It is questionable if counterion binding is strictly binary as assumed by the thermodynamic model expressed by Equation (i) in SI. In contrast, the mobility of Li^+ can be affected by the electrostatic potential of COSAN micelles, especially for cations located within the diffuse layer. The shape of the potential of mean force for $COSAN^-…Na^+$ shows shallow minimum at cation-anion separations ~1 nm,[19] implying that more distant counterions in the double layer are affected, thus $\beta^{\mathrm{ITC}} < \beta^{\mathrm{NMR}}$.

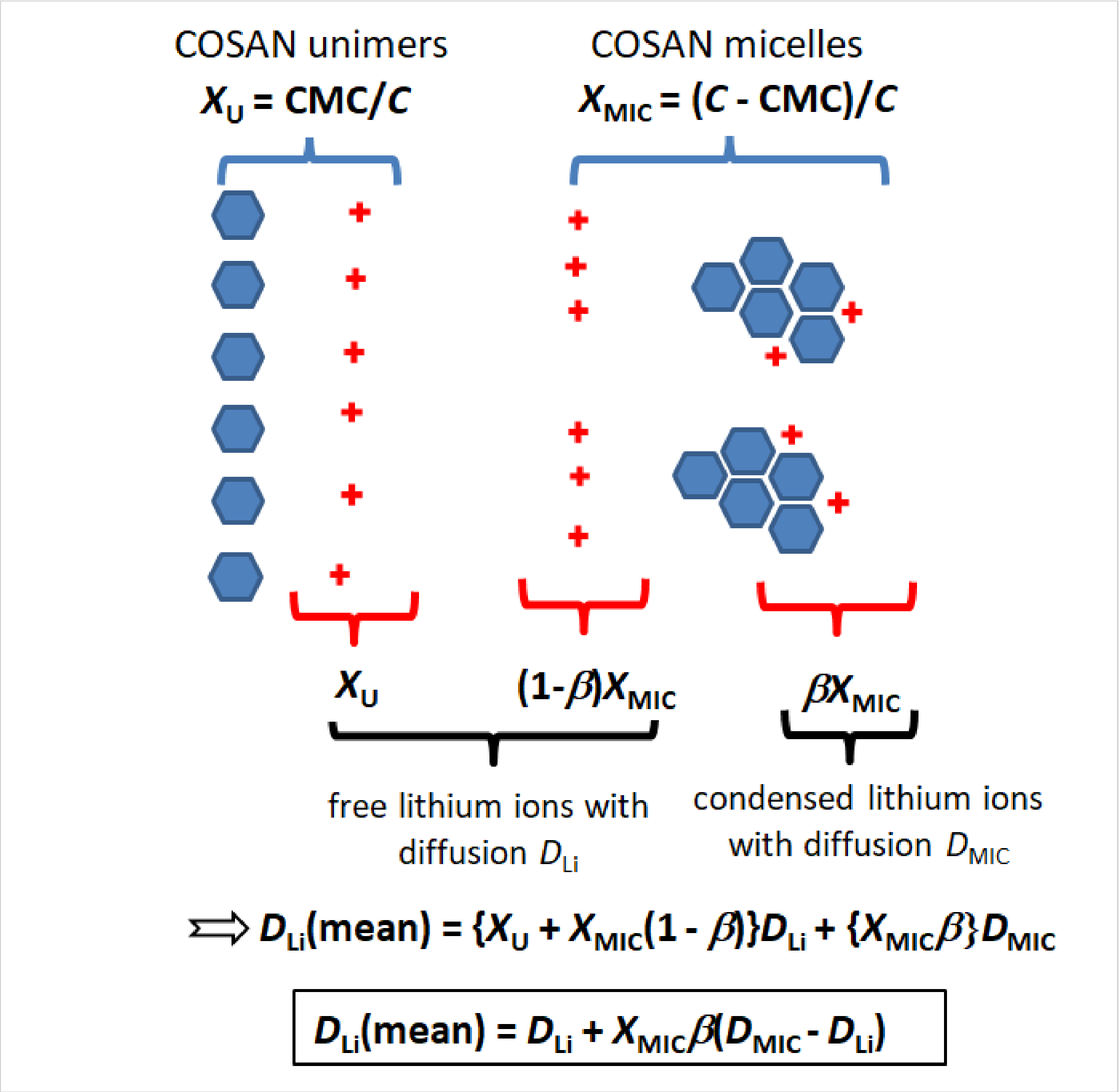

Scheme 4.2.2. Schematic contribution of free and condensed lithium ions to mean diffusion D_{Li}(mean) (measured by ^{7}Li DOSY NMR for concentration series of COSAN), where $D_{\mathrm{Li}} = 9.3 \times 10^{-10}$ m^2/s was obtained from ^{7}Li DOSY NMR of LiCl, $D_{\mathrm{MIC}} = 1.17 \times 10^{-10}$ m^2/s was obtained from fitting of ^{1}H DOSY NMR concentration series of COSAN by closed association model, and $X_{\mathrm{MIC}} = (C\text{-CMC})/C$ is based on simplified assumptions of the closed association model.

Impact of ionic strength

Li and Na[COSAN] were selected for experiments with added salt to study the effect of cation and ionic strength on COSAN micellization. Chloride salts with cations matching the COSAN salts were used to increase ionic strength, while avoiding the heat from cation exchange to interfere in the data collection. Figure S4.2.7 and Table S4.2.3 in SI show the effect of salt addition on enthalpograms in ITC experiments. The large decrease in CMC suggests that electrostatic repulsion between COSAN anions is an important barrier for the micellization process. The increase in salt concentration generates a screening effect allowing COSAN molecules to come into close proximity where the short-range COSAN-COSAN attraction acts to form the micelles (as predicted by MD simulations).[29] The promoting effect of ionic strength on micellization is significant, however, yet weaker compared to classical surfactants, SDS for example (Figure S4.2.8 in SI). SDS undergoes a more pronounced drop in CMC with increasing salt concentration,[51] which can be explained by a higher charge density on the surface of the classical micelles as compared to the surface of intrinsically amphiphilic COSAN. This makes classical amphiphiles more sensitive to electrostatic screening.

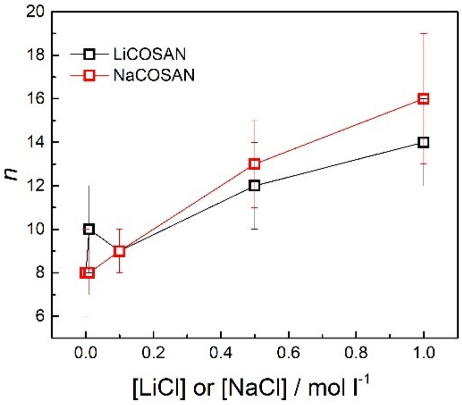

Figure 4.2.5. Dependence of COSAN aggregation number for Li and Na[COSAN] on corresponding salt concentration (LiCl and NaCl, respectively) as obtained from fitting of ITC data.

An increase in salt concentration also enables more COSAN molecules to form part of the same aggregate as reflected in the increase of *n* up to 16 (Figure 5). Even though this puts *n* over the proposed theoretical limit,[50] the theory neglects condensation of counterions. This ensures an electrostatic balance within the micelles even with $n \geq 12$.

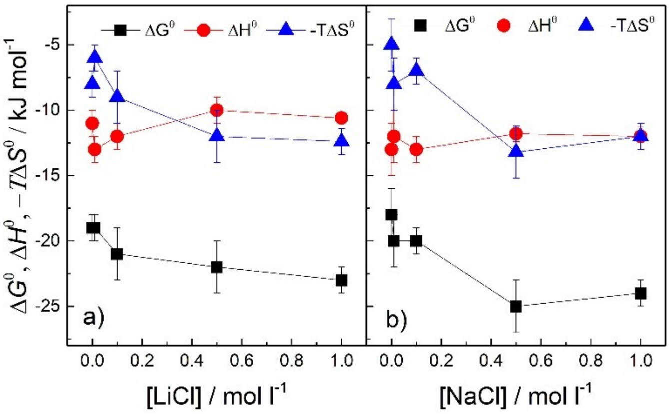

Figure 4.2.6. Dependences of thermodynamic parameters of aggregation for Li and Na[COSAN] on LiCl and NaCl concentration respectively, where standard enthalpy, $\Delta_M H^\theta$, Gibbs free energy, $\Delta_M G^\theta$, and entropy contributions, $-T\Delta_M S^\theta$, was obtained by the fitting procedure according to the model equation (corresponding values given in Table S3 in SI).

The dependence of thermodynamic parameters on the salt concentration (Figure 4.2.6) revealed the growing contribution of entropy to the free energy of micellization with increasing salt concentrations, while the enthalpy term remains constant. It implies that the hydration shell of COSAN micelles is altered in the salt solutions, and the driving force of micellization is shifted from the non-classical to more classical regime. Speculating, it may be caused by hydration of cations condensed on the micelles, or by morphological changes of COSAN micelles upon increase of ionic strength which carries a larger water displacement from the COSAN monomers upon self-assembly.

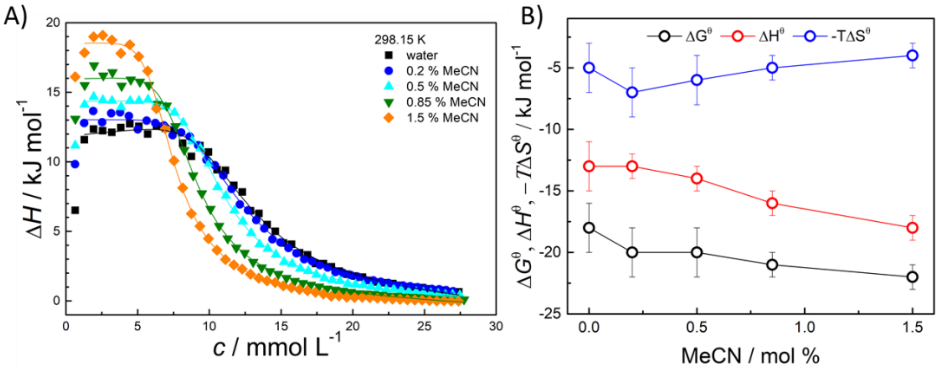

Figure 4.2.7. (A) Enthalpograms of Na[COSAN] demicellization in acetonitrile/water mixtures (molar fractions of MeCN in % within the graph). Solid lines represent the fit according to the model (equation xviii). (B) Corresponding values of thermodynamic parameters of micellization for Na[COSAN] as functions of acetonitrile molar fraction, where standard enthalpy, $\Delta_M H^\theta$, Gibbs free energy, $\Delta_M G^\theta$, and entropy contributions, $-T\Delta_M S^\theta$, was obtained by the fitting procedure according to the model equation (corresponding values given in Table S3 in SI).

Probing of COSAN micellization by MeCN

Co-solvents like acetonitrile (MeCN) have been used for changing the solvation of surfactants and thus alter the micellization equilibrium.[52-54]

We used low amounts of MeCN (x < 1.5% (mol%)) as probes in calorimetry and NMR experiments. Enthalpograms and the resulting fitting parameters are shown in Figure 4.2.7 and Table S3. Similar to classical amphiphiles, even small amounts of MeCN lead to an increase of the exothermic character of COSAN micellization (up to ~5 kJ/mol). In contrast with classical amphiphiles, micelle formation is promoted as demonstrated by a decrease of CMC and an increase of $\Delta_M G^\theta$. The sought effect, the tempering of the hydration water around COSAN, was evident in change of thermodynamic parameters. It is noteworthy that such levels of MeCN do not considerably alter the solvent polarity or dielectric constant (static dielectric constant of water decreases at 5 mol % MeCN from 78 to 75).[55] Furthermore, COSAN salts are readily soluble in both water and polar organic solvents, thus, there is no nanoprecipitation of COSAN (aggregation number and counterion binding almost are unchanged upon MeCN addition, Table S3).

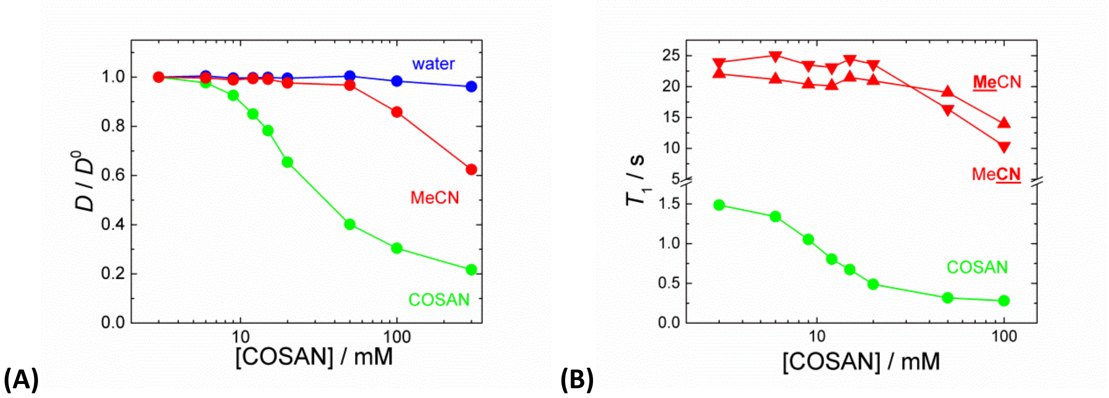

Figure 4.2.8. Dependence of (A) relative diffusion coefficients from 1H DOSY NMR (related to diffusion at low compound concentration or free compound), and (B) T_1 relaxation times from 13C NMR on COSAN concentration of COSAN clusters and parts of acetonitrile (MeCN) molecules. The molar fraction of acetonitrile in all solutions was set x = 0.5%.

NMR experiments show a significant decrease in D and changes in chemical shifts of MeCN signals. These are only observed for concentrations much higher than CMC. This raised the question whether MeCN was interacting with monomers or exclusively with micelles. However, both hydration shell and surface charge density should be the same for single COSAN cluster and COSAN micelle, and this feature differentiates intrinsic amphiphiles such as COSAN from classical surfactants. We can consider that at low COSAN concentrations the amount of MeCN molecules in solution is overwhelmingly larger than COSAN molecules. This causes

MeCN-COSAN interactions to be lost in the average of the signal of non-interacting MeCN molecules. As COSAN concentration grows, the signal of MeCN affected by COSAN becomes detectable. Spin-lattice relaxation times (T_1) of carbon nuclei (Figure 4.2.8B) are used to estimate the extent of molecular tumbling. The dependence for COSAN (green curve) follows the COSAN micellization and the slight decrease of T_1 for MeCN (red curves) reflects the restricted rotation of acetonitrile in the solvation shell.

Further details on MeCN affinity to all three rotamers of single COSAN cluster were revealed by all atomic molecular dynamics simulations in a periodic box packed with water and MeCN (5 mol%). As seen in Figure 4.2.9 (further details in SI), the spatial distribution functions reveal a strong association between COSAN and MeCN, with acetonitrile having predominant affinity for the B-H vertices of COSAN. In contrast, water preferentially associates to the carbon rich sites. These results compare well with Uchman *et al*,[1, 19] and reveals that the observed interaction between water and COSAN has been replaced by COSAN-MeCN, with the only exception of carbon-rich sites of COSAN. To gain further understanding of this phenomenon, radial distribution functions (RDF), $g(r)$, from the methyl and nitrile functional groups of MeCN to boron or carbon atoms of COSAN has been generated from the MD trajectories. The RDF between the methyl group and the boron atoms have distinct peaks with the distance between the peaks correlating to the B-B atom distances. The RDF between the nitrile group and the boron vertices of COSAN has a much broader distribution. These two observations show that the methyl group is the main site of interaction with COSAN, while the nitrile group possesses more rotational freedom. This correlates well with conclusions extracted from chemical shifts observed in ^{1}H, ^{13}C and ^{1}H-^{15}N HMBC NMR experiments (Figure S4.2.9 and more details in SI).

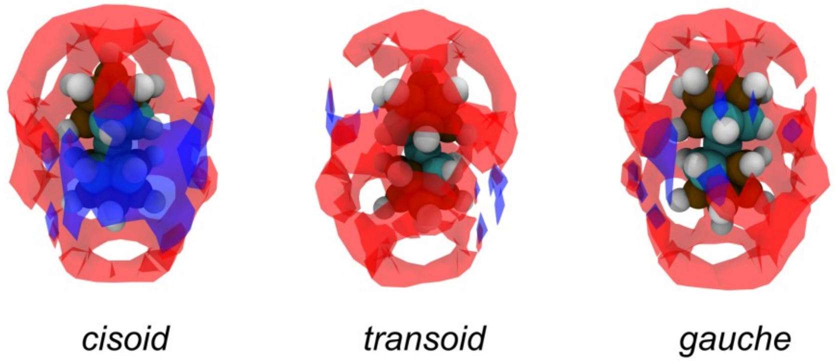

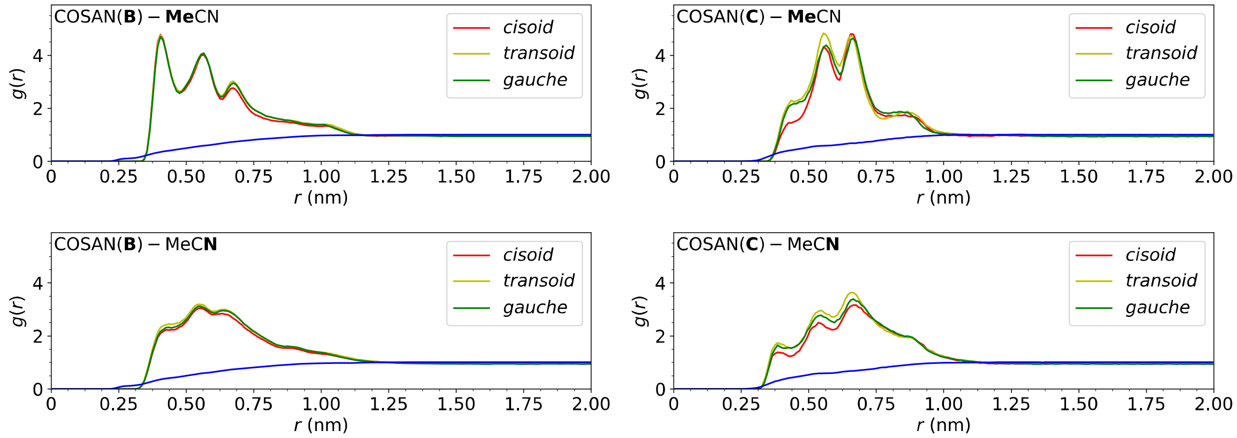

Figure 4.2.9. (**top**) Spatial distribution function of acetonitrile (red) and water (blue) surrounding COSAN in the three isomers (*cisoid*, *transoid*, and *gauche*); (**bottom**) Radial distribution function, $g(r)$, between COSAN in the *cisoid*, *transoid* and *gauche* isomer and acetonitrile or water with the functional group marked in bold, using the boron atoms of COSAN to the methyl carbon of acetonitrile (*top-left*), the boron atoms of COSAN to the nitrile nitrogen of acetonitrile (*bottom-left*), the carbon atoms of COSAN to the methyl carbon of acetonitrile (*top-right*), and the carbon atoms of COSAN to the nitrile nitrogen of acetonitrile (*bottom-right*) and oxygen of water.

To summarize, MeCN affects micellization by altering the COSAN solvation shell. We find a preferential binding of acetonitrile to COSAN over water. MeCN interacts with COSAN through the methyl group to the boron-rich areas, while water still shows elevated affinity for the carbon-rich areas. Experimentally, the free energy of COSAN micellization in water-MeCN mixtures increased over pure water with the process being dominantly enthalpic driven. Additionally, there is no evidence of bonding or permanent contact of MeCN with COSAN (no cross-peaks in 2D NOESY NMR, and the exchange rate is beyond the NMR limit). One plausible mechanism to explain such an effect is the stabilization of the aggregated state by acetonitrile solvation as visualized in Figure 4.2.10. The proposed mechanism can explain the aggregation if COSAN-COSAN interacts stronger compared to COSAN-MeCN and agrees with experimental finding of acetonitrile not being trapped inside the micelle. MeCN molecules bearing strong dipole moment act as "chaperones" by facilitating the approach of different COSAN molecules through alteration of its hydration shell. Moreover, the biggest contribution to $\Delta_M S^\theta$ are due to changes in hydration water, by doing these experiments in acetonitrile we managed to preemptively displace water from COSAN hydration shell except for that around the C-H bonds. As a result, $\Delta_M S^\theta$ remains virtually unchanged upon addition of acetonitrile (Figure 4.2.7) hence it is safe to assume that the same water displacement is taking place whereas acetonitrile is present or not. Consequently, we can deduce that the C-H bonds in COSAN micelles face towards the “inside” of the micelle and that the hydrophilic “spot” close to the C-H segments of COSAN disappeared.

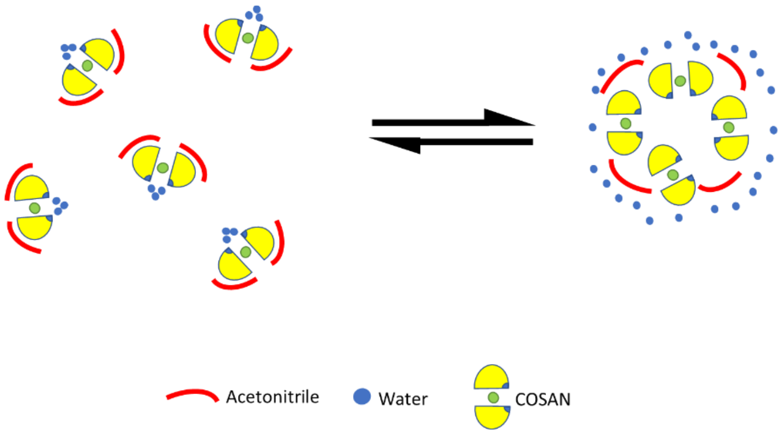

Figure 4.2.10. Proposed mechanism for the stabilization of the aggregated state of COSAN in an acetonitrile-water mixture.

Conclusions

Enthalpy ($\Delta_M H^\theta$), entropy ($\Delta_M S^\theta$), Gibbs free energy ($\Delta_M G^\theta$), heat capacity of micellization ($\Delta_M C_p^\theta$) as well as the critical micellization concentration, CMC, aggregation number, *n*, and degree of counterion binding, β, of COSAN micellization have been obtained from fitting a one-step mass action model to the ITC enthalpograms. This provided, for the first time, a full thermodynamic description of COSAN micellization as well as parameters describing the micellization mechanism. The results from ITC were compared to data from other experimental techniques. The aggregation numbers of COSAN micelles obtained from modeling of ITC experimental data are reliable in the concentration range just above and near CMC, and more realistic than values obtained from SAXS/SANS experiments where relatively high concentrations are required, whereby the aggregation numbers obtained are higher. Furthermore, a fraction of counterions affected by COSAN micelles was obtained for the first time from NMR data for Li[COSAN] (~0.2-0.25), although this should be taken as an upper limit of degree of counterion binding, because it reflects a dynamic process rather than the state postulated in the thermodynamic model.

The effect of increase in ionic strength on CMC further reveals that the behavior of COSAN is comparable to that of classical amphiphiles albeit with different degree due to charge delocalization in COSAN. The use of MeCN as a probe on COSAN micellization provided in-depth sight on the aggregation process as well as on the solvation shell of COSAN clusters. From detailed ITC, NMR and all-atom Molecular Dynamics simulation studies it can be concluded that MeCN molecules enhance the aggregation of COSAN through dipole-dipole interactions and solvation shell modification but do not co-micellize with COSAN.

Supporting Information

(1) Thermodynamics of micellization: A model equation and Fitting of ITC enthalpograms

-Calculating amounts of species at given total concentration of surfactant

The simplest micellization model of an anionic surfactant can be represented with equilibria

$$n\,\mathrm{A}^{-} + \beta n\mathrm{C}^{+} \overset{K_\mathrm{M}}{\rightleftarrows} \mathrm{C}_{\beta n}\mathrm{A}_{n}^{(1\text{-}\beta)n-} \tag{i}$$

where A^- represents the monomeric state of surfactant, C^+ the corresponding counterions, β is the degree of counterion binding, n aggregation number and the micellar aggregate (M) with $\mathrm{C}_{\beta n}\mathrm{A}_n^{(1\text{-}\beta)n-}$ an effective charge $(1\text{-}\beta)n$. The equilibrium between species can be expressed by apparent equilibrium constant, K_M,

$$K_\mathrm{M} = \frac{x_\mathrm{M}}{x_\mathrm{C}^{\beta n}\,x_\mathrm{A}^{n}} \tag{ii}$$

where activities are approximated to be equal to molar fraction of species.

K_M determines composition of each species at given total concentration of surfactant, c, and can be obtained from standard Gibbs free energy of micellization, $\Delta_\mathrm{M}G^\theta$,

$$\Delta_\mathrm{M}G^{\theta} = -\frac{RT}{n}\ln K_\mathrm{M} \tag{iii}$$

On the assumption that the density of the solution is always approximately 1 g mL^{-1} the total mass of solution, m, is approximated and by taking into account the molar mass of solvent and surfactant, the amount of solvent, n_sol, and the total amount of surfactant, n_S, are calculated. Introducing the sum of amounts of species, $\sum n_\mathrm{i}$,

$$\sum n_\mathrm{i} = n_\mathrm{sol} + 2\,n_\mathrm{S} + \left(1 - \left(1+\beta\right)n\right)n_\mathrm{M} \tag{iv}$$

the amounts of free monomers, n_A,

$$n_\mathrm{A} = n_\mathrm{S} - n_\mathrm{M}n \tag{v}$$

and free counterion, n_C,

$$n_\mathrm{C} = n_\mathrm{S} - \beta n_\mathrm{M}n \tag{vi}$$

enables the transformation of eq ii into expression

$$K_\mathrm{M} = \frac{n_\mathrm{M}\left(n_\mathrm{sol} + 2n_\mathrm{S} + \left(1 - \left(1+\beta\right)n\right)n_\mathrm{M}\right)^{(1+\beta)n-1}}{\left(n_\mathrm{S} - \beta n_\mathrm{M}n\right)^{\beta n}\left(n_\mathrm{S} - n_\mathrm{M}n\right)^{n}} \tag{vii}$$

with only one unknown variable, the amount of micelles, n_{M}. This equation cannot be solved analytically therefore tangent method is used to find solution numerically.

-Enthalpy of solution

Knowing all the amounts of species in added titrant and cell before and after its addition theoretical enthalpy of solution is calculated. Enthalpy of solution can be defined in two ways: with enthalpies of ions

$$H = n_{\mathrm{sol}}\overline{H}_{\mathrm{sol}} + n_{\mathrm{C}}\overline{H}_{\mathrm{C}} + n_{\mathrm{A}}\overline{H}_{\mathrm{A}} + n_{\mathrm{M}}\overline{H}_{\mathrm{M}} \tag{viii}$$

and enthalpies of ion pairs

$$H = n_{\mathrm{sol}}\overline{H}_{\mathrm{sol}} + n_{\mathrm{CA}}\overline{H}_{\mathrm{CA}} + n_{\mathrm{M}}\overline{H}_{\mathrm{CM}} \tag{ix}$$

where indexes “sol”, “CA” and “CM” represents solvent, surfactant monomers in form of ion pairs (amount equal to free anions) and micelle/counterion pairs (amount equal to micelles), respectively. For ion pairs simplified Guggenheim approximation is used to calculate standard enthalpies

$$\overline{H}_{\mathrm{S}} = \overline{H}_{\mathrm{CA}}^{\theta} + 2RT^2B_{\mathrm{CA}}^{'}b_{\mathrm{CA}} \tag{x}$$

$$\overline{H}_{\mathrm{CM}} = \overline{H}_{\mathrm{CM}}^{\theta} + \left(1+(1-\beta)n\right)RT^2B_{\mathrm{CM}}^{'}b_{\mathrm{CM}} \tag{xi}$$

where B_{CA}', and B_{CM}' are the temperature derivatives of Guggenheim’s coefficients B_{CA}, and B_{CM}. By combining standard enthalpy of micellization, $\Delta_{\mathrm{M}}H^{\theta}$,

$$\Delta_{\mathrm{M}}H^{\theta} = \frac{1}{n}\overline{H}_{\mathrm{CM}}^{\theta} - \overline{H}_{\mathrm{CA}}^{\theta} \tag{xii}$$

with eqs ix-xi, the enthalpy of solution is obtained

$$H = n_{\mathrm{sol}}\overline{H}_{\mathrm{sol}} + n_{\mathrm{S}}\overline{H}_{\mathrm{CA}}^{\theta} + n_{\mathrm{M}}n\Delta_{\mathrm{M,1}}H^{\theta} + 2RT^2B_{\mathrm{CA}}^{'}b_{\mathrm{A}}n_{\mathrm{A}} + RT^2\left[\left(1+(1-\beta)n\right)B_{\mathrm{CM}}^{'}b_{\mathrm{M}}n_{\mathrm{M}}\right] \tag{xiii}$$

which applies to any experimental method.

-ITC enthalpy change

Heat changes measured with ITC are contributions of three enthalpies, divided by total surfactant amount added, $n_{\mathrm{S,stock}}$;

$$\Delta H = \frac{q}{n_{\mathrm{S,stock}}} = \frac{H - H_0 - H_{\mathrm{stock}}}{n_{\mathrm{S,stock}}} \tag{xiv}$$

enthalpy of stock solution, H_{stock}, and enthalpies of solution in cell before, H_0, and after addition, H. By using eq xiii for each enthalpy and combining it with eq xiv, heat change after an addition of stock solution can be expressed as

$$\Delta H = \frac{n_{\mathrm{sol}} - n_{\mathrm{sol,0}} - n_{\mathrm{sol,stock}}}{n_{\mathrm{S,stock}}} \overline{H}^{\theta}_{\mathrm{sol}} + \frac{n_{\mathrm{S}} - n_{\mathrm{S,0}} - n_{\mathrm{S,stock}}}{n_{\mathrm{S,stock}}} \overline{H}^{\theta}_{\mathrm{CA}} + n \frac{n_{\mathrm{M}} - n_{\mathrm{M,0}} - n_{\mathrm{M,stock}}}{n_{\mathrm{S,stock}}} \Delta_{\mathrm{M}} H^{\theta} +$$

$$RT^2 \left(2B'_{\mathrm{CA}} \frac{b_{\mathrm{A}} n_{\mathrm{A}} - b_{\mathrm{A,0}} n_{\mathrm{A,0}} - b_{\mathrm{A,stock}} n_{\mathrm{A,stock}}}{n_{\mathrm{S,stock}}} + \left(1 + (1-\beta) n\right) B'_{\mathrm{CM}} \frac{b_{\mathrm{M}} n_{\mathrm{M}} - b_{\mathrm{M,0}} n_{\mathrm{M,0}} - b_{\mathrm{M,stock}} n_{\mathrm{M,stock}}}{n_{\mathrm{S,stock}}} \right)$$

(xv)

Due to the experimental design of Nano-ITC calorimeter (TA Instruments), which assumes the volume of the titration cell is constant by "ignoring" the excess solution in the neck above the titration cell, the first two terms in eq xv are not zero because solvent and surfactant outside of the titration cell are presumed to no longer contribute to the experiment. To overcome this design deficiency we assumed the total amount of surfactant before the addition, $n_{\mathrm{S,0}}$, was approximately equal to the value after the addition, n_{S}, reduced by the amount of the added surfactant, $n_{\mathrm{S,stock}}$. The same was assumed for water as solvent. Thus, the first two terms in the eq xv are now equal to zero, but eqs iv-vii and numerical calculations of all of the amounts for the (approximated) state before the addition are not the same as the previous experimental point, consequently doubling the time of calculations. Replacing molalities, b_{i}, by

$$b_{\mathrm{i}} = \frac{n_{\mathrm{i}}}{m_{\mathrm{sol}}} \qquad \text{(xvi)}$$

and defining the change in amount of micelles, $\Delta n_{\mathrm{M}}/\Delta n$, as

$$\frac{\Delta n_{\mathrm{M}}}{\Delta n} = n \frac{n_{\mathrm{M}} - n_{\mathrm{M,0}} - n_{\mathrm{M,stock}}}{n_{\mathrm{S,stock}}} \qquad \text{(xvii)}$$

eq xv reduces into its final form

$$\Delta H = \frac{\Delta n_{\mathrm{M}}}{\Delta n} \Delta_{\mathrm{M}} H^{\theta} + \frac{RT^2}{n_{\mathrm{S,stock}}} 2B'_{\mathrm{CA}} \left(\frac{n_{\mathrm{A}}^2}{m_{\mathrm{sol}}} - \frac{n_{\mathrm{A,0}}^2}{m_{\mathrm{sol,0}}} - \frac{n_{\mathrm{A,stock}}^2}{m_{\mathrm{sol,stock}}} \right) +$$

$$\frac{RT^2}{n_{\mathrm{S,stock}}} B'_{\mathrm{CM}} \left(1 + (1-\beta) n\right) \left(\frac{n_{\mathrm{M}}^2}{m_{\mathrm{sol}}} - \frac{n_{\mathrm{M,0}}^2}{m_{\mathrm{sol,0}}} - \frac{n_{\mathrm{M,stock}}^2}{m_{\mathrm{sol,stock}}} \right) \qquad \text{(xviii)}$$

From the eqs iii, and xviii it is evident, that the ITC model equation for a given temperature may be described in terms of n, β, $\Delta_{\mathrm{M}} G^{\theta}$, $\Delta_{\mathrm{M}} H^{\theta}$, and the coefficients B_{CA}' and B_{CM}' at any surfactant concentration, c.

-Global analysis

In the global analysis of ITC experimental data the Kirchoff's law

$$\Delta_{\mathrm{M}}H^{\theta} = \Delta_{\mathrm{M}}H^{\theta}_{T_{\mathrm{r}}} + \Delta_{\mathrm{M}}c^{\theta}_{\mathrm{p}}\left(T\text{-}T_{\mathrm{r}}\right) \tag{xix}$$

and the integrated Gibbs-Helmholtz equation

$$\Delta_{\mathrm{M}}G^{\theta} = T\left[\Delta_{\mathrm{M}}G^{\theta}_{T_{\mathrm{r}}}/T_{\mathrm{r}} + \Delta_{\mathrm{M}}H^{\theta}_{T_{\mathrm{r}}}\left(1/T - 1/T_{\mathrm{r}}\right) + \Delta_{\mathrm{M}}c^{\theta}_{\mathrm{p}}\left(1 - T_{\mathrm{r}}/T - \ln\left(T/T_{\mathrm{r}}\right)\right)\right] \tag{xx}$$

are used, where $\Delta_{\mathrm{M}}G_{Tr}^{\theta}$ is the standard Gibbs free energy and $\Delta_{\mathrm{M}}H_{Tr}^{\theta}$ is the standard enthalpy of micellization at reference temperature T_{r}. Heat capacity of micellization, $\Delta_{\mathrm{M}}c_{\mathrm{p}}^{\theta}$, was taken as temperature independent in the examined temperature range and also coefficient B_{S}' and B_{CM}' were assumed to be temperature independent.

From the eqs iii, xviii, xix, and xx it is evident that the ITC model equations may be described in terms of n, β, $\Delta_{\mathrm{M}}G_{Tr}^{\theta}$, $\Delta_{\mathrm{M}}H_{Tr}^{\theta}$, $\Delta_{\mathrm{M}}c_{\mathrm{p}}^{\theta}$, and the coefficients B_{CA}' and B_{CM}' at any surfactant concentration, c, and temperature, T.[Ref. S1]

-Fitting procedure

The values of the fitting parameters, either at one temperature or in global analysis at multiple temperatures, were obtained by fitting of the model equation to the experimental data points in the following manner. The model equation was compared to the experimental curves via the χ^2 function defined as

$$\chi^2 = \sum_{\mathrm{T}} f_T \sum_{\mathrm{i}}\left(\Delta H_{\mathrm{i}} - \Delta H_{\mathrm{i}}^{\mathrm{mod}}\right)^2 \tag{xxi}$$

where ΔH_{i} and $\Delta H_{\mathrm{i}}^{\mathrm{mod}}$ represent the experimental and the model enthalpy, whereas f_T represents the correction factor which differs from 1 if error of experimental points at temperature T is significantly greater. By minimization of χ^2 function best-fit values of the above-mentioned global parameters were calculated using modified Simplex method which was ran at least 100 times each time from randomly generated starting set of parameters. Values of global parameters were further used to calculate corresponding parameters for each temperature. The entropy of micellization, $\Delta_{\mathrm{M}}S^{\theta}$, associated with the examined process was obtained from the Gibbs-Helmholtz equation.

$$\Delta_{\mathrm{M}}S^{\theta} = \frac{\Delta_{\mathrm{M}}H^{\theta} - \Delta_{\mathrm{M}}G^{\theta}}{T} \tag{xxii}$$

Table S1. Thermodynamic parameters of micellization for alkali COSAN in water at all the investigated temperatures as obtained by the global fitting procedure: Gibbs free energy, $\Delta_{\mathrm{M}}G^{\theta}$, enthalpy, $\Delta_{\mathrm{M}}H^{\theta}$, entropy, $\Delta_{\mathrm{M}}S^{\theta}$, of micellization, and critical micelle concentration, cmc.[a]

T	$\Delta_M G^\theta$	$\Delta_M H^\theta$	$\Delta_M S^\theta$	cmc
H[COSAN]				
278.15	-15.9 ± 1	-10.3 ± 1	20.1	8 ± 1
288.15	-16.0 ± 1	-10.6 ± 1	18.7	10 ± 1
298.15	-16.2 ± 1	-10.8 ± 1	18.1	12 ± 1
318.15	-16.6 ± 1	-11.4 ± 1	16.3	16 ± 2
Li[COSAN]				
278.15	-16.1 ± 0.4	-11.6 ± 0.8	16.2	9 ± 1
288.15	-16.3 ± 0.4	-12.0 ± 1	14.9	10 ± 1
298.15	-16.4 ± 0.3	-12.4 ± 1	13.4	13 ± 1
318.15	-16.7 ± 0.3	-13.2 ± 1.4	11.0	18 ± 1
Na[COSAN]				
278.15	-16.8 ± 0.8	-12.3 ± 0.9	16.2	7.7 ± 0.4
288.15	-17.0 ± 0.8	-12.5 ± 0.9	15.6	9.7 ± 0.5
298.15	-17.2 ± 0.8	-12.7 ± 0.9	15.1	11.4 ± 0.6
318.15	-17.4 ± 0.9	-13.2 ± 0.9	13.2	17.0 ± 1.5
K[COSAN]				
278.15	-18.2 ± 1.5	-12.5 ± 0.6	20.5	7.2 ± 0.5
288.15	-18.4 ± 1.5	-13.2 ± 0.8	18.0	8.5 ± 0.6
298.15	-18.6 ± 1.5	-13.8 ± 0.8	16.1	10.2 ± 0.6
318.15	-18.9 ± 1.5	-15.0 ± 1.5	12.3	15 ± 1

[a] Units: T, K; $\Delta_M G^\theta$, $\Delta_M H^\theta$, kJ·mol^{-1}; $\Delta_M S^\theta$, J·K^{-1}·mol^{-1}; cmc, mmol·L^{-1}

Table S2. Degree of counterion binding, β, aggregation number, n, heat capacity of micellization, $\Delta_M c_p^\theta$, coefficients B_{CA}' and B_{CM}' (eqs x and xi) for alkali and acid COSAN in water as obtained by the global fitting procedure.[a]

	β	n	$\Delta_M c_p^\theta$	B_{CA}'	B_{CM}'
H[COSAN]	0.04 ± 0.04	6.5 ± 1	-30 ± 30	0.04 ± 0.03	-0.05 ± 0.01
Li[COSAN]	0.02 ± 0.02	7 ± 1	-40 ± 20	0.02 ± 0.02	-0.04 ± 0.03
Na[COSAN]	0.03 ± 0.03	8 ± 2	-20 ± 20	0.01 ± 0.01	-0.16 ± 0.06
K[COSAN]	0.12 ± 0.08	6 ± 1	-60 ± 20	0.03 ± 0.03	-0.09 ± 0.03

[a] Units: $\Delta_M c_p^\theta$, J·K^{-1}·mol^{-1}; B_{CA}', B_{CM}', kg·K^{-1}·mol^{-1}

Table S3. Thermodynamic parameters of micellization for alkali COSAN in solutions of salts and mixture of acetonitrile in water at 298.15 K as obtained by the fitting procedure: Gibbs free energy, $\Delta_M G^\theta$, enthalpy, $\Delta_M H^\theta$, entropy, $\Delta_M S^\theta$, of micellization, and critical micelle concentration, cmc, degree of counterion binding, β, aggregation number, *n*, coefficients B_{CA}' and B_{CM}' (eqs x and xi).[a]

	$\Delta_M G^\theta$	$\Delta_M H^\theta$	$\Delta_M S^\theta$	cmc	β	*N*	B_{CA}'	B_{CM}'
% acetonitrile	Na[COSAN] in mixture of acetonitrile and water							
0	-18 ± 2	-13 ± 2	16.8	11.4 ± 0.5	0.04 ± 0.04	8 ± 2	0.03 ± 0.03	-0.10 ± 0.05
0.2	-20 ± 2	-13 ± 1	23.5	10.7 ± 0.5	0.12 ± 0.06	7 ± 1	0.01 ± 0.01	-0.16 ± 0.05
0.5	-20 ± 2	-14 ± 1	20.1	9.7 ± 0.5	0.10 ± 0.10	8 ± 2	0.01 ± 0.01	-0.17 ± 0.04
0.85	-21 ± 1	-16 ± 1	16.8	8.0 ± 0.5	0.15 ± 0.08	8 ± 1	0.01 ± 0.01	-0.13 ± 0.04
1.5	-22 ± 1	-18 ± 1	13.4	6.6 ± 0.5	0.18 ± 0.08	7 ± 2	0.01 ± 0.01	-0.14 ± 0.04
c(NaCl)	Na[COSAN] in solution of NaCl							
0	-18 ± 2	-13 ± 2	16.8	11.4 ± 0.5	0.04 ± 0.04	8 ± 2	0.03 ± 0.03	-0.10 ± 0.05
0.01	-20 ± 2	-12 ± 2	26.8	10.5 ± 0.5	0.12 ± 0.05	8 ± 1	0.05 ± 0.05	-0.20 ± 0.06
0.1	-20 ± 1	-13 ± 1	23.5	5.9 ± 0.5	0.04 ± 0.04	9 ± 1	0.1 ± 0.1	-0.15 ± 0.03
0.5	-25 ± 2	-11.8 ± 0.6	44.3	3.0 ± 0.5	0.28 ± 0.2	13 ± 2	0.09 ± 0.06	-1.0 ± 0.3
1.0	-24 ± 1	-12.0 ± 0.7	40.2	2.0 ± 0.5	0.1 ± 0.1	16 ± 3	0.08 ± 0.08	-1.2 ± 0.3
c(LiCl)	Li[COSAN] in solution of LiCl							
0	-19 ± 1	-11 ± 1	26.8	12.5 ± 0.5	0.13 ± 0.06	8 ± 1	0.005 ± 0.005	-0.14 ± 0.04
0.01	-19 ± 1	-13 ± 1	20.1	9.3 ± 0.5	0.05 ± 0.05	10 ± 2	0.005 ± 0.005	-0.11 ± 0.03
0.1	-21 ± 2	-12 ± 1	30.2	6.0 ± 0.5	0.15 ± 0.15	9 ± 1	0.01 ± 0.01	-0.13 ± 0.02

0.5	-22 ± 2	-10 ± 1	40.2	3.0 ± 0.5	0.1 ± 0.1	12 ± 2	0.02 ± 0.02	-0.5 ± 0.3
1.0	-23 ± 1	-10.6 ± 0.4	41.6	2.3 ± 0.5	0.1 ± 0.1	14 ± 2	0.08 ± 0.04	-1.0 ± 0.3

[a]Units: $\Delta_{M}G^{\theta}$, $\Delta_{M}H^{\theta}$, kJ·mol^{-1}; $\Delta_{M}S^{\theta}$, J·K^{-1}·mol^{-1}; cmc, mmol·L^{-1}; B_{CA}', B_{CM}', kg·K^{-1}·mol^{-1}

Table S4. Exact syringe concentration of COSAN solutions during ITC experiments at various temperatures.

Temperature (K)	[COSAN] (mol·L^{-1})
H [COSAN]	
278.15	0.090
288.15	0.118
298.15	0.118
318.15	0.200
Li [COSAN]	
278.15	0.0936
288.15	0.1196
298.15	0.1196
318.15	0.1984
Na [COSAN]	
278.15	0.0900
288.15	0.1200
298.15	0.1200
318.15	0.1808
K [COSAN]	
278.15	0.0893
288.15	0.1200
298.15	0.1200
318.15	0.1984

Table S5. Exact syringe concentration of COSAN solutions during ITC experiments at variating concentrations of acetonitrile, NaCl, and LiCl.

% acetonitrile	[COSAN] (mol·L^{-1})	[NaCl] (mol·L^{-1})	[COSAN] (mol·L^{-1})	[LiCl] (mol·L^{-1})	[COSAN] (mol·L^{-1})
0	0.1200	0	0.1200	0	0.1196
0.2	0.1183	0.01	0.1161	0.01	0.1151
0.5	0.1203	0.1	0.1171	0.1	0.1188
0.85	0.1216	0.5	0.0394	0.5	0.0403
1.5	0.1199	1	0.0308	1	0.0305

(2) Characterization of X[COSAN] samples

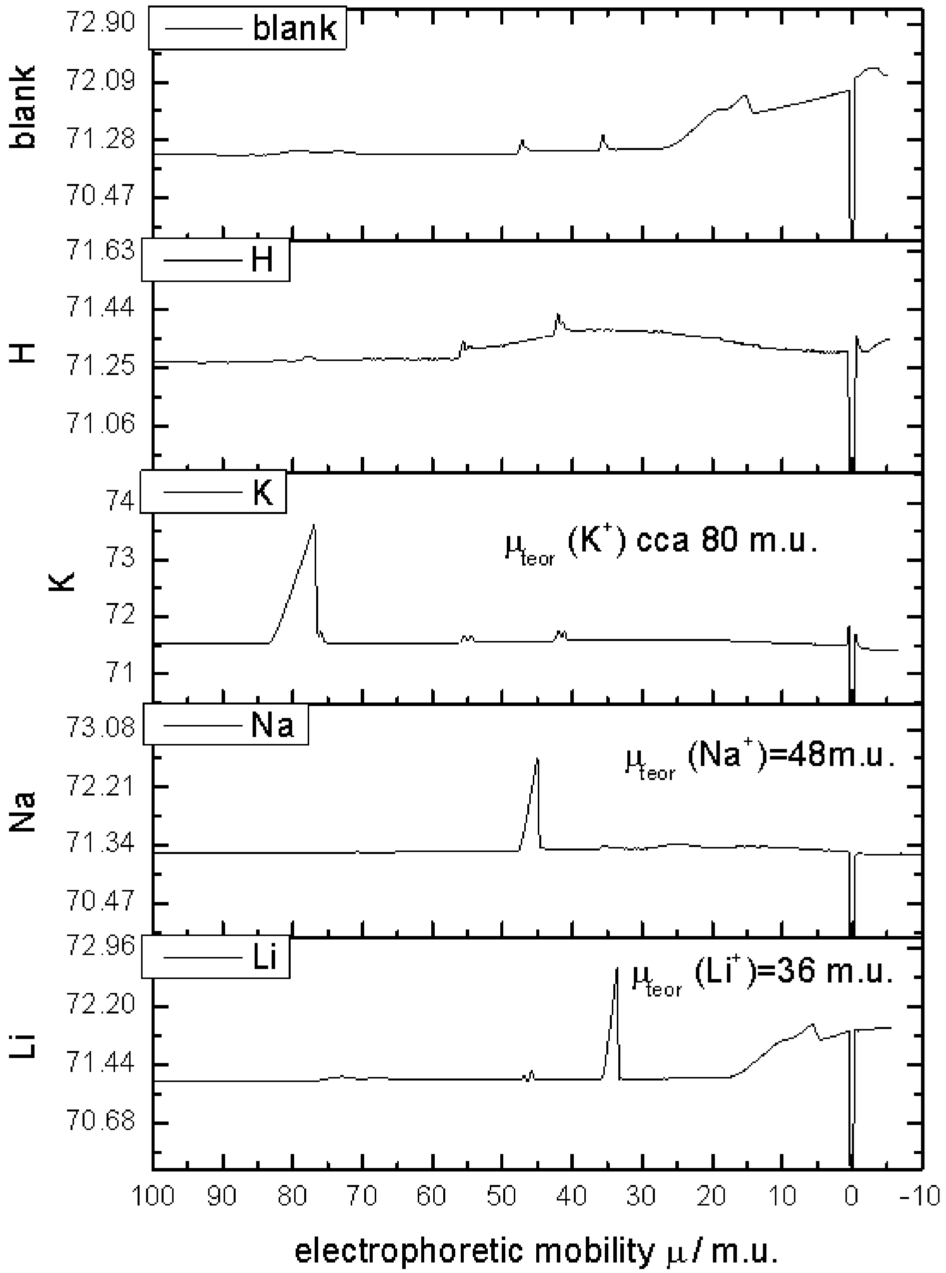

Figure S4.2.1. Electropherogramms of H, Li, Na and K COSAN proving the cationic purity of the samples

(3) Results of ITC fitting for X[COSAN]

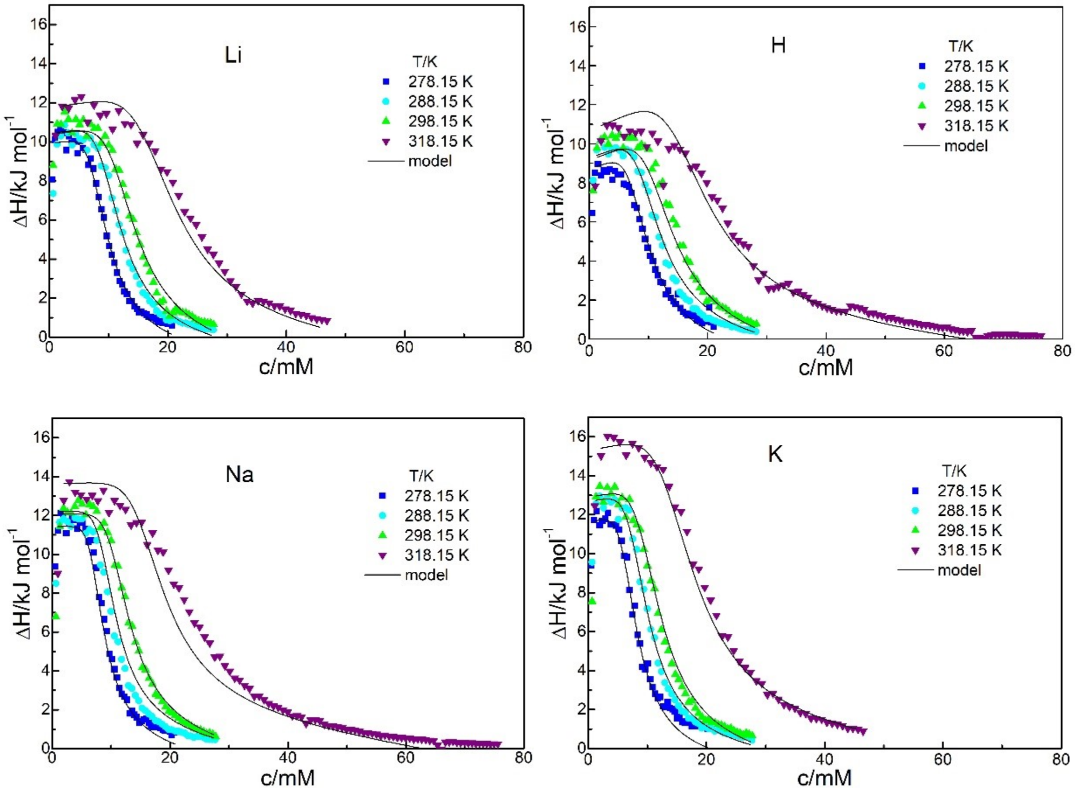

Figure S4.2.2. Enthalpograms of alkali COSAN in water in temperature range between 278.15 and 318.15 K. Solid lines represent the fit according to the model (equation xviii).

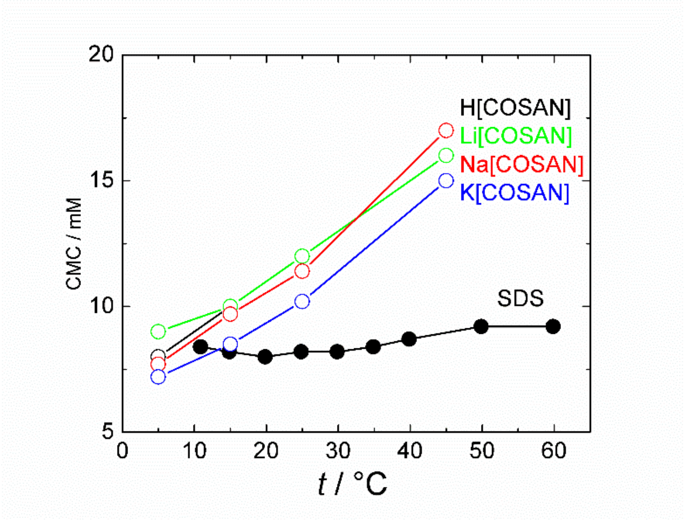

Figure S4.2.3. Temperature dependence of CMC of COSAN salts (from fitting of ITC enthalpograms) and SDS [Ref. S2].

(4) SAXS and WAXS results: Data evaluation

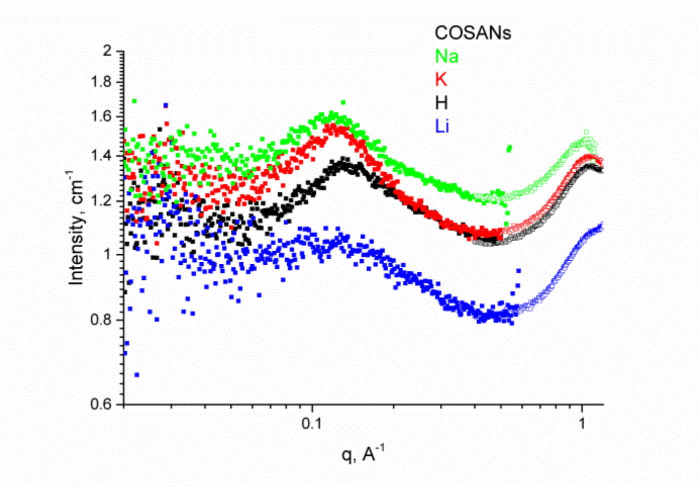

Figure S4.2.4A. Typical SAXS/WAXS curves for X[COSAN], X = H, Li, Na, K; evaluation explained as follows:

Li[COSAN], the sample with weakest interactions, was chosen for analysis. Assuming that data are on absolute scale (were scaled using GlassyCarbon), *I*(0) could be calculated using equation:

$$I(0) = \left(\frac{4}{3}\pi R^3 \Delta\eta\right)^2 \qquad \text{(xxiii)}$$

where Δη is the scattering length density difference between particle and matrix.

Sphere + hard sphere structure factors were used for fitting. Sphere radius is 9.1 Å. Hard sphere repulsion radius = 19.1 Å with volume fraction ~0.09.

Experimental curve of COSAN with Li ions gives $\Delta\eta$ equal to $1.66\cdot10^{-4}$ Å^{-2}. We have scale in I(0)/c cm^2/g. Calculating extrapolation to $q = 0$ using equation above will give us $I(0)/c = 0.274$ cm^2/g.

$$M_w = \frac{I_0}{c}\cdot\frac{N_a}{\Delta b^2} \qquad \text{(xxiv)}$$

where N_{av} – Avogadro’s number, Δb^2 – scattering contrast.

Assuming COSAN density to be 1.2 g/cm^3, we can calculate scattering contrast and then molecular weight of the spherical particle:

$\Delta b^2 = 4.48\cdot10^{19}$

$M_w = 0.274 * 6.022 \cdot 10^{23} / 4.48 \cdot 10^{19} = 3683$ g/mol

Molecular weight of Li-COSAN is 330.7 g/mol. Aggregation number can be calculated as a ratio of these two molecular weights, which will give **Nagg(Li*COSAN) = 11.1.**

All other samples exhibit very strong interparticle interactions (strong correlation peak), which complicates radius determination. Water subtraction will influence mainly higher angles, but peak intensity remains the same. The two correlation peaks can be assigned to the direct COSAN-COSAN contact in parallel orientation ($q \sim 1$ Å^{-1}), and to the correlation of COSAN micelles in solution ($q \sim 0.1$ Å^{-1}) that is concentration dependent.

The results for other COSAN salts:

Nagg(K*COSAN) = 19.9

Nagg(H*COSAN) = 11.61

Nagg(Na*COSAN) = 4.58

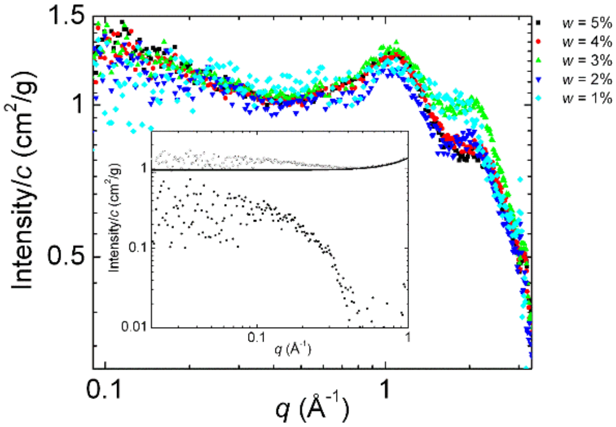

Figure S4.2.4B. SAXS curve for Na[COSAN] used in our previous studies giving **Nagg ~ 5**:

Combined SAXS and WAXS curves of Na[COSAN] aqueous solutions with subtracted water contribution in WAXS region for several concentrations as indicated in graph. **Inset:** Averaged SAXS curves of Na[COSAN] aqueous solutions (hollow points), background (line) and SAXS from the Na[COSAN] associates (filled points); evaluation explained as follows:

The micelles of Na[COSAN] (concentrations 1 – 5 weight-%) were characterized by combined SAXS and WAXS. The background contribution in SAXS region was subtracted from the experimental data as follows: The averaged scattering intensity for five measured concentrations (hollow points in Inset of Figure) was fitted with the empirical function $I(q) = A + B \cdot q^3$ in the q-range of (0.8 – 1.0 Å^{-1}) and extrapolated to low q-part of the spectrum (line in Inset of Figure). The curve resulting from the subtraction (filled points in Inset of Figure) is ascribed to the scattering from Na[COSAN] micelles. Using the Guinier analysis, we estimate that the mass-averaged association number of [COSAN]-anions is in the range of 2.5 – 5.0 with corresponding radius of gyration 0.8 – 1.1 nm.

(5) Ion mobility in Li[COSAN]

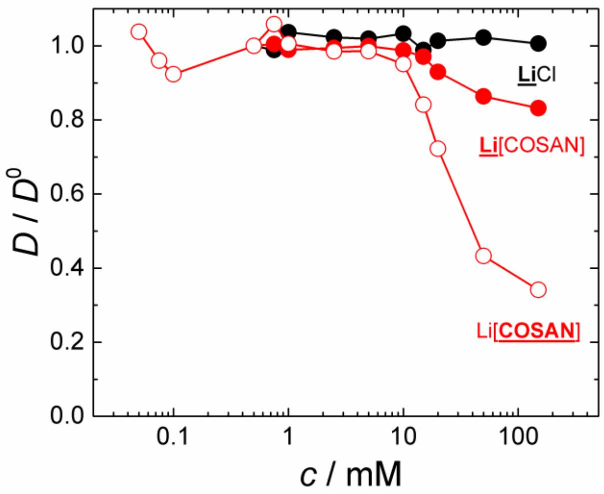

Figure S4.2.5. Relative diffusion (related to low concentration of solute) of lithium in LiCl and Li[COSAN] solutions from 7Li DOSY NMR and COSAN clusters from 1H DOSY NMR as a function of concentration; the diffusions of Li and COSAN were "normalized" in order to better visualize and compare the trends in ion mobilities.

(6) Estimation of the fraction of COSAN micelles

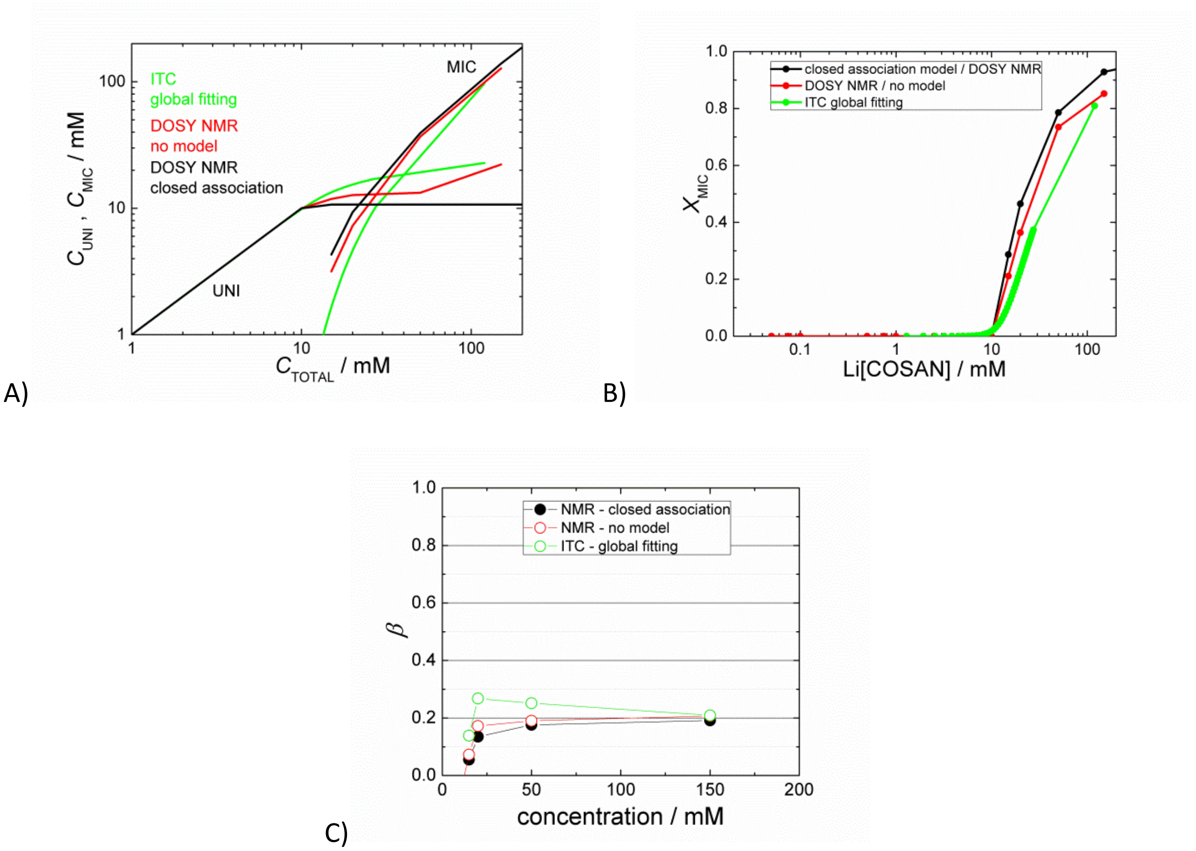

Figure S4.2.6. (**A**) Concentration profiles of micelles and unimers, (**B**) Fraction of micelles, and (**C**) Values of counterion binding, *β*, calculated according equation shown in Scheme 4.2.2 in the main text for 3 different approaches (i) DOSY NMR data fitted by closed association model, (ii) DOSY NMR data without using any model, and (iii) global fitting of ITC data; Another limitation of the concept described in Scheme 4.2.2 (Main Text) comes from the estimation of parameters X_{MIC} and D_{MIC}, because we implemented the simple closed association model developed for micellization of classical surfactants with $n > 50$. The model was used with certain success for the description of COSAN micellization in our previous studies.[Ref S3] However, the thermodynamic model proposed here should be more realistic. For example, it does not put restrictions on the unimer concentration above CMC (the fraction of micelles estimated from ITC global fitting is lower as compared to simple closed association model – comparison in Figures S6A,B). Furthermore, it has been noted previously that experimental values of D_{COSAN} slightly deviates from the simple model toward lower values. After corrections based on X_{MIC} estimation, it leads to higher estimate of $\beta^{NMR,corr}$ ~ 0.20-0.25 (Figure S4.2.6C).

(7) Results of ITC fitting for X[COSAN] in salt solutions

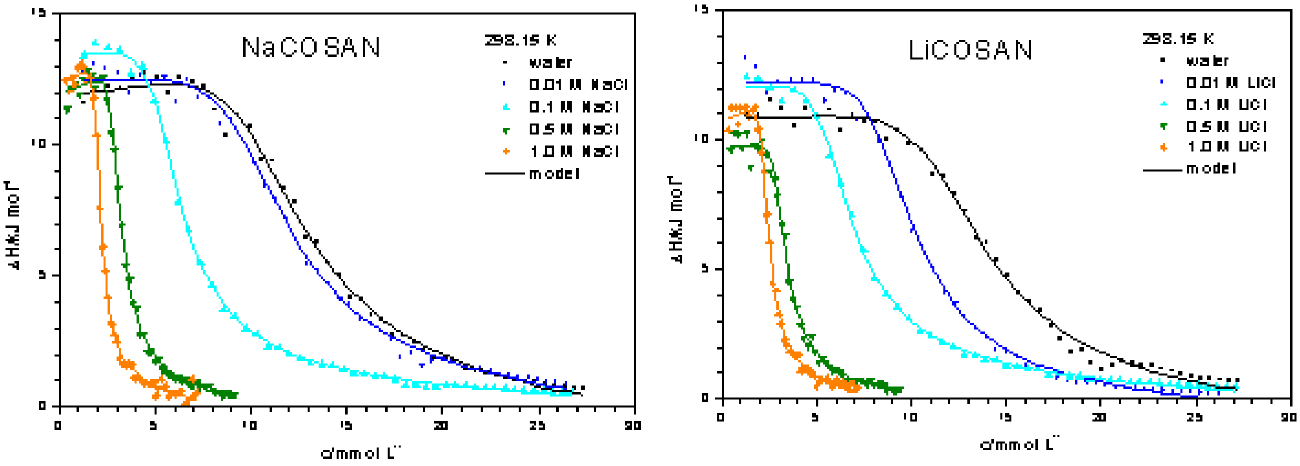

Figure S4.2.7. Enthalpograms of NaCOSAN and LiCOSAN in NaCl and LiCl solutions (respectively) at 298.15 K. Solid lines represent the fit according to the model (equation xviii).

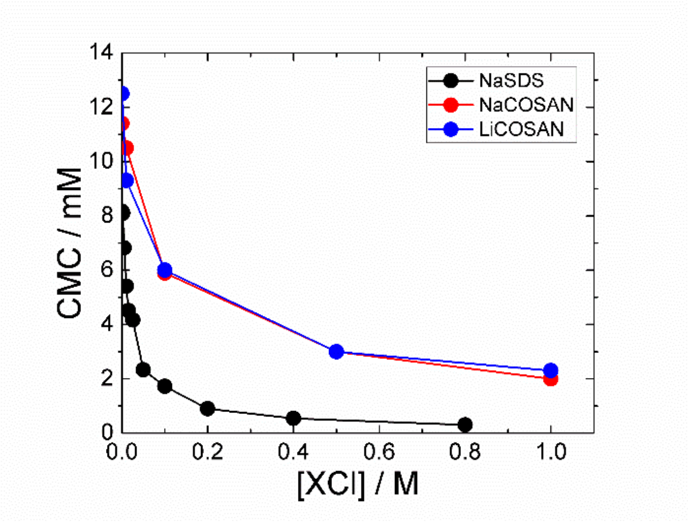

Figure S4.2.8. Dependence of CMC of COSAN salts (from fitting of ITC enthalpograms) and SDS on salt concentration [Ref. S4].

(8) NMR data for Na[COSAN] with MeCN

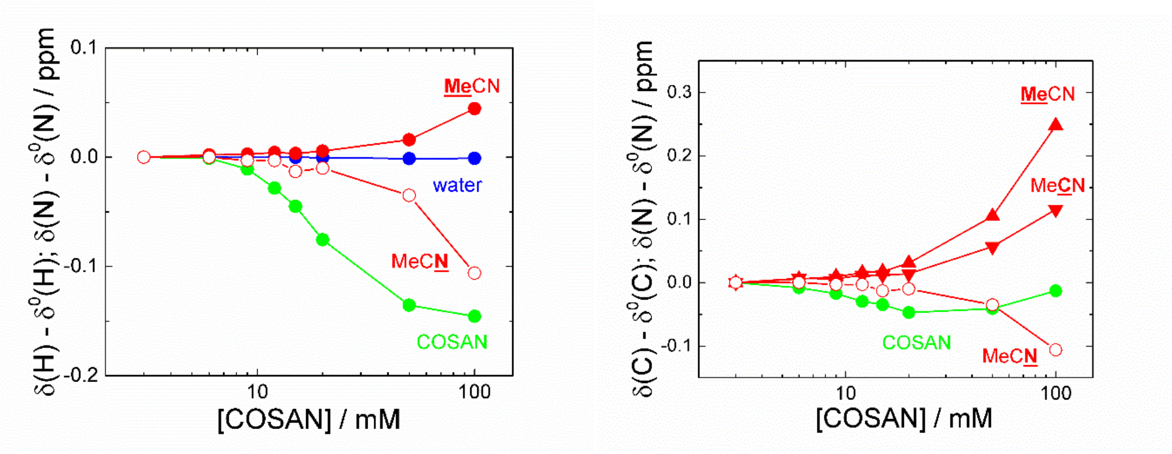

Figure S4.2.9. Relative chemical shifts of water, COSAN and acetonitrile signals as a function of Na[COSAN] concentration with fixed molar fraction of MeCN (*x* = 0.5%) from 1H NMR, 13C NMR and 1H-15N HMBC NMR experiments.

The localization, orientation and dynamics of MeCN molecule in respect to COSAN cluster were further studied by NMR. Changes in chemical shift of MeCN have been observed in all ^{1}H, ^{13}C and ^{1}H-^{15}N HMBC NMR experiments at high COSAN concentrations, revealing an impact of COSAN on all parts of MeCN molecule especially the peripheral atoms (**Me**CN and MeC**N** signals in Figure S4.2.9). Analogue to water the hydration shell, we consider dipole-dipole interaction between COSAN (*cisoid* is the most stable rotamer of COSAN in water)[30] and its solvation shell; the values of dipole moment of water and MeCN is 1.85 D and 3.92 D, respectively. In this sense, the N≡ group should be oriented towards C-H groups of COSAN, and $–CH_3$ groups towards B-H vertices of COSAN cluster.

(9) Molecular dynamics

Molecular dynamics simulations have been conducted to investigate the binding of acetonitrile and water to COSAN. As seen in Figure 4.2.9 in the main text, with the given choice of parameters, the spatial distribution functions reveal a strong association between COSAN and MeCN, with acetonitrile having predominant affinity for the boron-hydrogen vertices of COSAN. In contrast, water preferentially associates to the carbon rich sites. These results compare well with our previous results and reveals that the observed interaction between water and COSAN has been replaced by COSAN-MeCN, with the only exception of carbon-rich sites of COSAN still revealing preferential binding with water. To gain further understanding of the association of MeCN and water to COSAN, radial distribution functions (RDF), $g(r)$, from the methyl and nitrile functional to boron or carbon atoms has been generated from the MD trajectories. The RDF between the methyl group the boron atoms of COSAN have distinct peaks with the distance between the peaks correlating to the B-B atom distances. The RDF between the nitrile group and the boron vertices of COSAN has a much broader distribution. These two observations show that the methyl group is the main site of interaction with the boron atoms, while the nitrile group possesses more rotational freedom. Water is excluded from COSAN in agreement with the SDFs, however from the RDF between the carbon atoms of COSAN and the nitrile group of acetonitrile there is a decreasing RDF at low distances (r<0.75 nm) depending on the isomers in specific $g(r)_{transoid} > g(r)_{gauche} > g(r)_{cisoid}$. This tendency correlates with the dipole moment of COSAN (*cisoid* ~6.1 D, *gauche* ~3.6 D, and *transoid* ~0 D), in particular water increasingly binds to carbon of COSAN with increasing dipole moment. Oppositely, the preferential binding of acetonitrile increases with *decreasing* dipole moment as also hinted by the SDFs and the radial distribution function between COSAN water (Figure S4.2.10).

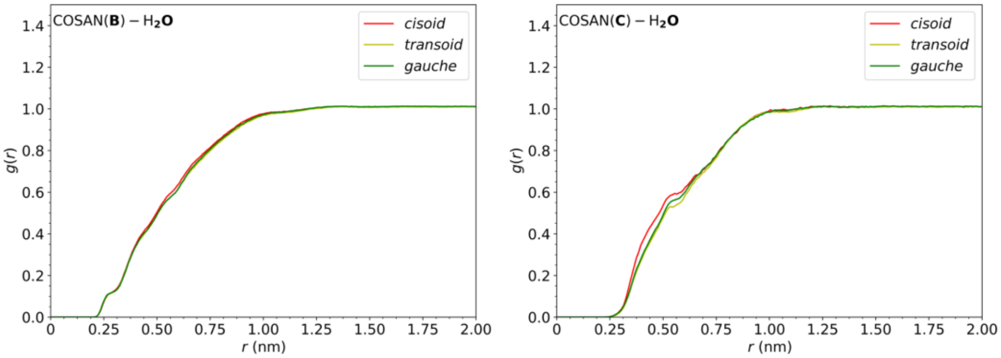

Figure S4.2.10. Radial distribution function between COSAN in the *cisoid*, *transoid* and *gauche* isomer and water with the selected atom for the RDF marked in bold.

We have addressed the binding of acetonitrile and water to the structural isomers of COSAN and find a preferential binding of acetonitrile to COSAN over water, despite COSAN being fully soluble in water [S3]. Where water interacts with COSAN through dihydrogen binds, observe acetonitrile interacts with COSAN through the methyl group to the boron-rich areas of COSAN, while water still shows elevated affinity for the carbon-rich areas of COSAN. Radial distribution functions show that the affinity for water near carbon deceases with the inherent dipole moment of COSAN in its specific geometrical isomers. Due to water and acetonitrile being miscible, the solvation of COSAN by acetonitrile could increase the solubility of COSAN in water as also found experimentally by cosolvent-induced solubilization enhancement [S5]. While these results address solvation of COSAN in a mixture of acetonitrile and water at infinite dilution, the resulting contribution to two-body COSAN-COSAN interactions at finite concentrations is left unanswered. Experimentally, increased the free energy of micellization in a water-acetonitrile mixture over water with the process being dominantly enthalpic driven. One plausible mechanism to explain such an effect is the stabilization of the aggregated state by acetonitrile solvation. The proposed mechanism can explain the aggregation if COSAN-COSAN interacts stronger compared to COSAN-acetonitrile and agrees with experimental finding of acetonitrile not actively participating in the aggregation of COSAN.

Acknowledgment

PM, ZT and RFA would like to acknowledge the financial support of the Czech Science Foundation 17-00648S. SHH and ML thanks the Swedish Research Council and the Marie Cure Actions Network, PIPPI for financial support.

References

(1) Stock, A. *Hydrides of Boron and Silicon*; Cornell University Press: Ithaca, New York, 1933.

(2) Dickerson, R. E.; Lipscomb, W. N. Semitopological Approach to Boron-Hydride Structures. *J. Chem. Phys.* **1957**, *27* (1), 212–217. https://doi.org/10.1063/1.1743672.

(3) Lipscomb, W. N. *Boron Hydrides*; Courier Corporation: New York, 2012.

(4) Muetterties, E. L. *Boron Hydride Chemistry*; Academic Press, Inc: London, 1975.

(5) Hoffmann, R.; Lipscomb, W. N. Theory of Polyhedral Molecules. I. Physical Factorizations of the Secular Equation. *J. Chem. Phys.* **1962**, *36* (8), 2179–2189. https://doi.org/10.1063/1.1732849.

(6) Hoffmann, R.; Lipscomb, W. N. Theory of Polyhedral Molecules. III. Population Analyses and Reactivities for the Carboranes. *J. Chem. Phys.* **1962**, *36* (12), 3489–3493. https://doi.org/10.1063/1.1732484.

(7) Hoffmann, R.; Lipscomb, W. N. Boron Hydrides: LCAO—MO and Resonance Studies. *J. Chem. Phys.* **1962**, *37* (12), 2872–2883. https://doi.org/10.1063/1.1733113.

(8) Hawthorne, M. F.; Young, D. C.; Andrews, T. D.; Howe, D. V; Pilling, R. L.; Pitts, A. D.; Reintjes, M.; Warren, L. F.; Wegner, P. A. π-Dicarbollyl Derivatives of the Transition Metals. Metallocene Analogs. *J. Am. Chem. Soc.* **1968**, *90* (4), 879–896. https://doi.org/10.1021/ja01006a008.

(9) Teixidor, F.; Viñas, C. Boron and Carbon: Antagonistic or Complementary? Proposal for a Simple Prototype of a Molecular Clutch or Molecular Switch. *Pure Appl. Chem.* **2012**, *84* (11), 2457–2465. https://doi.org/10.1351/PAC-CON-12-05-02.

(10) Bühl, M.; Hnyk, D.; Machácek, J. Computational Study of Structures and Properties of Metallaboranes: Cobalt Bis(Dicarbollide). *Chem. - A Eur. J.* **2005**, *11* (14), 4109–4120. https://doi.org/10.1002/chem.200401202.

(11) Juárez-Pérez, E. J.; Núñez, R.; Viñas, C.; Sillanpää, R.; Teixidor, F. The Role of C-H···H-B Interactions in Establishing Rotamer Configurations in Metallabis(Dicarbollide) Systems. *Eur. J. Inorg. Chem.* **2010**, No. 16, 2385–2392. https://doi.org/10.1002/ejic.201000157.

(12) Malaspina, D. C.; Viñas, C.; Teixidor, F.; Faraudo, J. Atomistic Simulations of COSAN: Amphiphiles

without a Head-and-Tail Design Display “Head and Tail” Surfactant Behavior. *Angew. Chemie - Int. Ed.* **2020**, *59* (8), 3088–3092. https://doi.org/10.1002/anie.201913257.

(13) Hawthorne, M. F.; Zink, J. I.; Skelton, J. M.; Bayer, M. J.; Liu, C.; Livshits, E.; Baer, R.; Neuhauser, D. Electrical or Photocontrol of the Rotary Motion of a Metallacarborane. *Science (80-.).* **2004**, *303* (5665), 1849–1851. https://doi.org/10.1126/science.1093846.

(14) Lipscomb, W. N.; Pitochelli, A. R.; Hawthorne, M. F. PROBABLE STRUCTURE OF THE B 10 H 10 -2 ION. *J. Am. Chem. Soc.* **1959**, *81* (21), 5833–5834. https://doi.org/10.1021/ja01530a073.

(15) King, R. B.; Rouvray, D. H. Chemical Applications of Group Theory and Topology. 7. A Graph-Theoretical Interpretation of the Bonding Topology in Polyhedral Boranes, Carboranes, and Metal Clusters. *J. Am. Chem. Soc.* **1977**, *99* (24), 7834–7840. https://doi.org/10.1021/ja00466a014.

(16) King, R. B. Three-Dimensional Aromaticity in Polyhedral Boranes and Related Molecules. *Chem. Rev.* **2001**, *101* (5), 1119–1152. https://doi.org/10.1021/cr000442t.

(17) Schleyer, P. von R.; Najafian, K. Stability and Three-Dimensional Aromaticity of Closo - Monocarbaborane Anions, CB n - 1 H n - , and Closo -Dicarboranes, C 2 B n - 2 H N. *Inorg. Chem.* **1998**, *37* (14), 3454–3470. https://doi.org/10.1021/ic980110v.

(18) Gershoni-Poranne, R.; Stanger, A. Magnetic Criteria of Aromaticity. *Chemical Society Reviews*. Royal Society of Chemistry 2015, pp 6597–6615. https://doi.org/10.1039/c5cs00114e.

(19) Poater, J.; Solà, M.; Viñas, C.; Teixidor, F. π Aromaticity and Three-Dimensional Aromaticity: Two Sides of the Same Coin. *Angew. Chemie - Int. Ed.* **2014**, *53* (45), 12191–12195. https://doi.org/10.1002/anie.201407359.

(20) Núñez, R.; Tarrés, M.; Ferrer-Ugalde, A.; De Biani, F. F.; Teixidor, F. Electrochemistry and Photoluminescence of Icosahedral Carboranes, Boranes, Metallacarboranes, and Their Derivatives. *Chem. Rev.* **2016**, *116* (23), 14307–14378. https://doi.org/10.1021/acs.chemrev.6b00198.

(21) Núñez, R.; Tarrés, M.; Ferrer-Ugalde, A.; De Biani, F. F.; Teixidor, F. Electrochemistry and Photoluminescence of Icosahedral Carboranes, Boranes, Metallacarboranes, and Their Derivatives. *Chem. Rev.* **2016**, *116* (23), 14307–14378. https://doi.org/10.1021/acs.chemrev.6b00198.

(22) Knoth, W. H.; Sauer, J. C.; England, D. C.; Hertler, W. R.; Mtjetterties, E. L. Chemistry of Boranes. XIX.1 Derivative Chemistry of B10H10-2 and B12H12-. *J. Am. Chem. Soc.* **1964**, *86* (19), 3973–3983. https://doi.org/10.1021/ja01073a015.

(23) Keener, M.; Hunt, C.; Carroll, T. G.; Kampel, V.; Dobrovetsky, R.; Hayton, T. W.; Ménard, G. Redox-Switchable Carboranes for Uranium Capture and Release. *Nature* **2020**, *577* (7792), 652–655. https://doi.org/10.1038/s41586-019-1926-4.

(24) Jones, G.; Dole, M. The Viscosity of Aqueous Solutions of Strong Electrolytes with Special Reference to Barium Chloride. *J. Am. Chem. Soc.* **1929**, *51* (10), 2950–2964. https://doi.org/10.1021/ja01385a012.

(25) Okur, H. I.; Hladílková, J.; Rembert, K. B.; Cho, Y.; Heyda, J.; Dzubiella, J.; Cremer, P. S.; Jungwirth, P. Beyond the Hofmeister Series: Ion-Specific Effects on Proteins and Their Biological Functions. *J. Phys. Chem. B* **2017**, *121* (9), 1997–2014. https://doi.org/10.1021/acs.jpcb.6b10797.

(26) Salis, A.; Ninham, B. W. Models and Mechanisms of Hofmeister Effects in Electrolyte Solutions, and Colloid and Protein Systems Revisited. *Chem. Soc. Rev.* **2014**, *43* (21), 7358–7377. https://doi.org/10.1039/C4CS00144C.

(27) Assaf, K. I.; Nau, W. M. The Chaotropic Effect as an Assembly Motif in Chemistry. *Angew. Chemie - Int. Ed.* **2018**, *57* (43), 13968–13981. https://doi.org/10.1002/anie.201804597.

(28) Nau, W. M.; Assaf, K. The Chaotropic Effect as an Assembly Motif in Chemistry. *Angew. Chemie Int. Ed.* **2018**. https://doi.org/10.1002/anie.201804597.

(29) Karki, K.; Gabel, D.; Roccatano, D. Structure and Dynamics of Dodecaborate Clusters in Water. *Inorg. Chem.* **2012**, *51* (9), 4894–4896. https://doi.org/10.1021/ic300223z.

(30) Uchman, M.; Abrikosov, A. I.; Lepšík, M.; Lund, M.; Matějíček, P. Nonclassical Hydrophobic Effect in Micellization: Molecular Arrangement of Non-Amphiphilic Structures. *Adv. Theory Simulations* **2017**, *1700002*, 1700002. https://doi.org/10.1002/adts.201700002.

(31) Uchman, M.; ɰorŋovič, V.; Tošner, Z.; Matějíček, P. Classical Amphiphilic Behavior of Nonclassical Amphiphiles: A Comparison of Metallacarborane Self-Assembly with SDS Micellization. *Angew. Chemie - Int. Ed.* **2015**, *54* (47), 14113–14117. https://doi.org/10.1002/anie.201506545.

(32) Assaf, K. I.; Holub, J.; Bernhardt, E.; Oliva-Enrich, J. M.; Fernández Pérez, M. I.; Canle, M.; Santaballa, J. A.; Fanfrlík, J.; Hnyk, D.; Nau, W. M. Face-Fusion of Icosahedral Boron Hydride Increases Affinity to γ-Cyclodextrin: Closo,Closo-[B21H18]− as an Anion with Very Low Free Energy of Dehydration. *ChemPhysChem* **2020**, 1–7. https://doi.org/10.1002/cphc.201901225.

(33) Ďorďovič, V.; Tošner, Z.; Uchman, M.; Zhigunov, A.; Reza, M.; Ruokolainen, J.; Pramanik, G.; Cígler, P.; Kalíková, K.; Gradzielski, M.; et al. Stealth Amphiphiles: Self-Assembly of Polyhedral Boron Clusters. *Langmuir* **2016**, *32* (26), 6713–6722. https://doi.org/10.1021/acs.langmuir.6b01995.

(34) Sivaev, I. B.; Bregadze, V. I.; Sjöberg, S. Chemistry of Closo-Dodecaborate Anion [B12H12]2-: A Review. *Collect. Czechoslov. Chem. Commun.* **2002**, *67* (6), 679–727. https://doi.org/10.1135/cccc20020679.

(35) Knoth, W. H.; Miller, H. C.; Sauer, J. C.; Balthis, J. H.; Chia, Y. T.; Muetterties, E. L. Chemistry of Boranes. IX. Halogenation of B10H10−2 and B12H12−2. *Inorg. Chem.* **1964**, *3* (2), 159–167. https://doi.org/10.1021/ic50012a002.

(36) Knoth, W. H.; Miller, H. C.; Muetterties, E. L.; England, D. C.; Parshall, G. W. Derivative Chemistry of B10H10- and B12H12-. *J. Am. Chem. Soc.* **1962**, *84* (6), 1056–1057. https://doi.org/10.1021/ja00865a040.

(37) Peymann, T.; Herzog, A.; Knobler, C. B.; Hawthorne, M. F. Aromatic Polyhedral Hydroxyborates: Bridging Boron Oxides and Boron Hydrides. *Angew. Chemie Int. Ed.* **1999**, *38* (8), 1061–1064. https://doi.org/10.1002/(SICI)1521-3773(19990419)38:8<1061::AID-ANIE1061>3.0.CO;2-B.

(38) Maderna, A.; Knobler, C. B.; Hawthorne, M. F. Twelvefold Functionalization of an Icosahedral Surface by Total Esterification of [B12(OH)12]2−: 12(12)-Closomers. *Angew. Chemie Int. Ed.* **2001**, *40* (9), 1661–1664. https://doi.org/10.1002/1521-3773(20010504)40:9<1661::AID-ANIE16610>3.0.CO;2-U.

(39) Peymann, T.; Knobler, C. B.; Khan, S. I.; Hawthorne, M. F. Dodeca(Benzyloxy)Dodecaborane, B12(OCH2Ph)12: A Stable Derivative Ofhypercloso-B12H12. *Angew. Chemie Int. Ed.* **2001**, *40* (9), 1664–1667. https://doi.org/10.1002/1521-3773(20010504)40:9<1664::AID-ANIE16640>3.0.CO;2-O.

(40) Wixtrom, A. I.; Shao, Y.; Jung, D.; Machan, C. W.; Kevork, S. N.; Qian, E. A.; Axtell, J. C.; Khan, S. I.; Kubiak, C. P.; Spokoyny, A. M. Rapid Synthesis of Redox-Active Dodecaborane B12(OR)12 Clusters under Ambient Conditions. *Inorg. Chem. Front.* **2016**, *3* (5), 711–717. https://doi.org/10.1039/c5qi00263j.

(41) Jalisatgi, S. S.; Kulkarni, V. S.; Tang, B.; Houston, Z. H.; Lee, M. W.; Hawthorne, M. F. A Convenient Route to Diversely Substituted Icosahedral Closomer Nanoscaffolds. *J. Am. Chem. Soc.* **2011**, *133* (32), 12382–12385. https://doi.org/10.1021/ja204488p.

(42) Qian, E. A.; Wixtrom, A. I.; Axtell, J. C.; Saebi, A.; Jung, D.; Rehak, P.; Han, Y.; Moully, E. H.; Mosallaei, D.; Chow, S.; et al. Atomically Precise Organomimetic Cluster Nanomolecules Assembled via Perfluoroaryl-Thiol SNAr Chemistry. *Nat. Chem.* **2017**, *9* (4), 333–340. https://doi.org/10.1038/nchem.2686.

(43) Sivaev, I. B.; Semioshkin, A. A.; Brellochs, B.; Sjöberg, S.; Bregadze, V. I. Synthesis of Oxonium Derivatives of the Dodecahydro-Closo-Dodecaborate Anion [B12H12]2-. Tetramethylene Oxonium Derivative of [B12H12]2- as a Convenient Precursor for the Synthesis of Functional Compounds for Boron Neutron Capture Therapy. *Polyhedron* **2000**, *19* (6), 627–632. https://doi.org/10.1016/S0277-5387(00)00293-X.

(44) Sivaev, I. B.; Kulikova, N. Y.; Nizhnik, E. A.; Vichuzhanin, M. V.; Starikova, Z. A.; Semioshkin, A. A.; Bregadze, V. I. Practical Synthesis of 1,4-Dioxane Derivative of the Closo-Dodecaborate Anion and Its Ring Opening with Acetylenic Alkoxides. *J. Organomet. Chem.* **2008**, *693* (3), 519–525. https://doi.org/10.1016/j.jorganchem.2007.11.027.

(45) Körbe, S.; Schreiber, P. J.; Michl, J. Chemistry of the Carba-Closo-Dodecaborate(-) Anion, CB11H12-. *Chem. Rev.* **2006**, *106* (12), 5208–5249. https://doi.org/10.1021/cr050548u.

(46) Grimes, R. N. *Carboranes*, 3rd editio.; Academic Press, Inc: London.

(47) Quan, Y.; Qiu, Z.; Xie, Z. Transition-Metal-Catalyzed Selective Cage B−H Functionalization of o-Carboranes. *Chem. - A Eur. J.* **2018**, *24* (12), 2795–2805. https://doi.org/10.1002/chem.201704937.

(48) Olid, D.; Núñez, R.; Viñas, C.; Teixidor, F. Methods to Produce B-C, B-P, B-N and B-S Bonds in Boron Clusters. *Chem. Soc. Rev.* **2013**, *42* (8), 3318–3336. https://doi.org/10.1039/c2cs35441a.

(49) Lyu, H.; Quan, Y.; Xie, Z. Rhodium-Catalyzed Regioselective Hydroxylation of Cage B−H Bonds of o-Carboranes with O2or Air. *Angew. Chemie - Int. Ed.* **2016**, *55* (39), 11840–11844. https://doi.org/10.1002/anie.201605880.

(50) Lyu, H.; Quan, Y.; Xie, Z. Transition Metal Catalyzed Direct Amination of the Cage B(4)-H Bond in o-Carboranes: Synthesis of Tertiary, Secondary, and Primary o-Carboranyl Amines. *J. Am. Chem. Soc.* **2016**, *138* (39), 12727–12730. https://doi.org/10.1021/jacs.6b07086.

(51) Hawthorne, M. F.; Young, D. C.; Garrett, P. M.; Owen, D. A.; Schwerin, S. G.; Tebbe, F. N.; Wegner, P. A. The Preparation and Characterization of the (3)-1,2- and (3) -1,7-Dicarbadodecahydroundecaborate (–1) Ions. *J. Am. Chem. Soc.* **1968**, *90* (4), 862–868.

https://doi.org/10.1021/ja01006a006.

(52) Yoo, J.; Hwang, J. W.; Do, Y. Facile and Mild Deboronation of O-Carboranes Using Cesium Fluoride. *Inorg. Chem.* **2001**, *40* (3), 568–570. https://doi.org/10.1021/ic000768k.

(53) Mortimer, M. D.; Knobler, C. B.; Hawthorne, M. F. Methylation of Boron Vertices of the Cobalt Dicarbollide Anion. *Inorg. Chem.* **1996**, *35* (19), 5750–5751. https://doi.org/10.1021/ic960353s.

(54) Plešek, J.; Heřmánek, S.; Franken, A.; Císařová, I.; Nachtigal, C. Dimethyl Sulfate Induced Nucleophilic Substitution of the [Bis(1,2-Dicarbollido)-3-Cobalt(1-)]Ate Ion. Syntheses, Properties and Structures of Its 8,8′-μ-Sulfato, 8-Phenyl and 8-Dioxane Derivatives. *Collect. Czechoslov. Chem. Commun.* **1997**, *62* (1), 47–56. https://doi.org/10.1135/cccc19970047.

(55) Wojtczak, B. A.; Andrysiak, A.; Grüner, B.; Lesnikowski, Z. J. “Chemical Ligation”: A Versatile Method for Nucleoside Modification with Boron Clusters. *Chem. - A Eur. J.* **2008**, *14* (34), 10675–10682. https://doi.org/10.1002/chem.200801053.

(56) Stockmann, P.; Gozzi, M.; Kuhnert, R.; Sárosi, M. B.; Hey-Hawkins, E. New Keys for Old Locks: Carborane-Containing Drugs as Platforms for Mechanism-Based Therapies. *Chem. Soc. Rev.* **2019**, *48* (13), 3497–3512. https://doi.org/10.1039/c9cs00197b.

(57) Sivaev, I. B.; Bregadze, V. V. Polyhedral Boranes for Medical Applications: Current Status and Perspectives. *Eur. J. Inorg. Chem.* **2009**, No. 11, 1433–1450. https://doi.org/10.1002/ejic.200900003.

(58) Scholz, M.; Hey-Hawkins, E. Carbaboranes as Pharmacophores: Properties, Synthesis, and Application Strategies. *Chem. Rev.* **2011**, *111* (11), 7035–7062. https://doi.org/10.1021/cr200038x.

(59) Brynda, J.; Mader, P.; Šícha, V.; Fábry, M.; Poncová, K.; Bakardiev, M.; Grüner, B.; Cígler, P.; Řezáčová, P. Carborane-Based Carbonic Anhydrase Inhibitors. *Angew. Chemie - Int. Ed.* **2013**, *52* (51), 13760–13763. https://doi.org/10.1002/anie.201307583.

(60) Cígler, P.; Kožíšek, M.; Řezáčová, P.; Brynda, J.; Otwinowski, Z.; Pokorná, J.; Plešek, J.; Grüner, B.; Dolečková-Marešová, L.; Máša, M.; et al. From Nonpeptide toward Noncarbon Protease Inhibitors: Metallacarboranes as Specific and Potent Inhibitors of HIV Protease. *Proc. Natl. Acad. Sci. U. S. A.* **2005**, *102* (43), 15394–15399. https://doi.org/10.1073/pnas.0507577102.

(61) Hosmane, N. S. *Boron Science: New Technologies and Applications*; CRC Press: Boca Raton, 2012.

(62) Řezáčová, P.; Pokorná, J.; Brynda, J.; Kožíšek, M.; Cígler, P.; Lepšík, M.; Fanfrlík, J.; Řezáč, J.; Šašková, K. G.; Sieglová, I.; et al. Design of HIV Protease Inhibitors Based on Inorganic Polyhedral Metallacarboranes. *J. Med. Chem.* **2009**, *52* (22), 7132–7141. https://doi.org/10.1021/jm9011388.

(63) Popescu, A. R.; Teixidor, F.; Viñas, C. Metal Promoted Charge and Hapticities of Phosphines: The Uniqueness of Carboranylphosphines. *Coord. Chem. Rev.* **2014**, *269* (1), 54–84. https://doi.org/10.1016/j.ccr.2014.02.016.

(64) Guerrero, I.; Kelemen, Z.; Viñas, C.; Romero, I.; Teixidor, F. Metallacarboranes as Photoredox Catalysts in Water. *Chem. - A Eur. J.* **2020**, *26* (22), 5027–5036. https://doi.org/10.1002/chem.201905395.

(65) Eo, M.; Park, M. H.; Kim, T.; Do, Y.; Lee, M. H. Polynorbornene Copolymers with Pendent O-Carborane and Carbazole Groups: Novel Side-Chain Donor-Acceptor Copolymers for Turn-on Sensing of Nucleophilic Anions. *Polym. (United Kingdom)* **2013**, *54* (23), 6321–6328. https://doi.org/10.1016/j.polymer.2013.09.031.

(66) Vohlídal, J.; Vangani, V. H.; Plešek, J.; Rajabi, F. H.; Blechta, V.; Němec, I. Synthesis of New Polymers Involving Deltahedral Carborane Units. *Macromol. Chem. Phys.* **1997**, *198* (1), 193–218. https://doi.org/10.1002/macp.1997.021980115.

(67) Pichaandi, K. R.; Safronov, A. V.; Sevryugina, Y. V.; Everett, T. A.; Jalisatgi, S. S.; Hawthorne, M. F. Rodlike Polymers Containing Nickel and Cobalt Metal Bis(Dicarbollide) Anions: Synthesis and Characterization. *Organometallics* **2017**, *36* (19), 3823–3829. https://doi.org/10.1021/acs.organomet.7b00578.

(68) Gigante, A.; Duchêne, L.; Moury, R.; Pupier, M.; Remhof, A.; Hagemann, H. Direct Solution-Based Synthesis of Na4(B12H12)(B10H10) Solid Electrolyte. *ChemSusChem* **2019**, *12* (21), 4832–4837. https://doi.org/10.1002/cssc.201902152.

(69) Bennour, I.; Cioran, A. M.; Teixidor, F.; Viñas, C. 3,2,1 and Stop! An Innovative, Straightforward and Clean Route for the Flash Synthesis of Metallacarboranes. *Green Chem.* **2019**, *21* (8), 1925–1928. https://doi.org/10.1039/c8gc03943g.

(70) Fernandez-Alvarez, R.; Ďorďovič, V.; Uchman, M.; Matějíček, P. Amphiphiles without Head-and-Tail Design: Nanostructures Based on the Self-Assembly of Anionic Boron Cluster Compounds. *Langmuir* **2018**, *34* (12), 3541–3554. https://doi.org/10.1021/acs.langmuir.7b03306.

References for supporting information

[S1] Woolley, E. M.; Burchfield, T. E. Model for thermodynamics of ionic surfactant solutions. 2. Enthalpies, heat capacities, and volumes. *J. Phys. Chem.* 1984, *88*, 2155–2163.

[S2] Marcolongo, J. P.; Mirenda, M. Thermodynamics of Sodium Dodecyl Sulfate (SDS) Micellization: An Undergraduate Laboratory Experiment. *J. Chem. Educ.* **2011**, *88* (5), 629–633.

[S3] Uchman, M.; Dordovič, V.; Tošner, Z.; Matějíček, P. Classical Amphiphilic Behavior of Nonclassical Amphiphiles: A Comparison of Metallacarborane Self-Assembly with SDS Micellization. *Angew. Chemie - Int. Ed.* **2015**, *54* (47), 14113–14117.

[S4] Dutkiewicz, E.; Jakubowska, A. Effect of Electrolytes on the Physicochemical Behaviour of Sodium Dodecyl Sulphate Micelles. *Colloid Polym. Sci.* **2002**, *280* (11), 1009–1014.

[S5] Banerjee, S., & Yalkowsky, S. (1988). Cosolvent-induced solubilization of hydrophobic compounds into water. *Analytical Chemistry, 60*(19), 2153-2155.

4.3- Publication III

Synthesis and self-assembly of carborane-containing ABC triblock terpolymer: morphology control on a dual-stimuli responsive system

Abstract

Amphiphilic triblock terpolymers offer an attractive application in the field of preparation of nanoparticles with controlled morphology. An additional level of morphology control can be provided by reactive blocks which change interaction with the solvent upon different stimuli. In this work, we synthesized a triblock terpolymer (poly(acrylicacid)-*b*-poly(4-hydroxystyrene)-*b*-poly{1-[4-(1-methyl-1,2-dicarba-*closo*-dodecaborane-2-yl methyl)-phenyl] ethylene})), (PAA-*b*-PHS-*b*-PSC), containing carboranes as pendant groups by reversible addition fragmentation chain transfer (RAFT) polymerization and we subsequently studied its behavior in aqueous solution. The solubility of the second and third block was changed after the nanoparticles were already formed. This was done via pH and CsF reaction, respectively. The obtained micelles formed work as ON/OFF system making use of changes in fluorescence intensity at different pH.

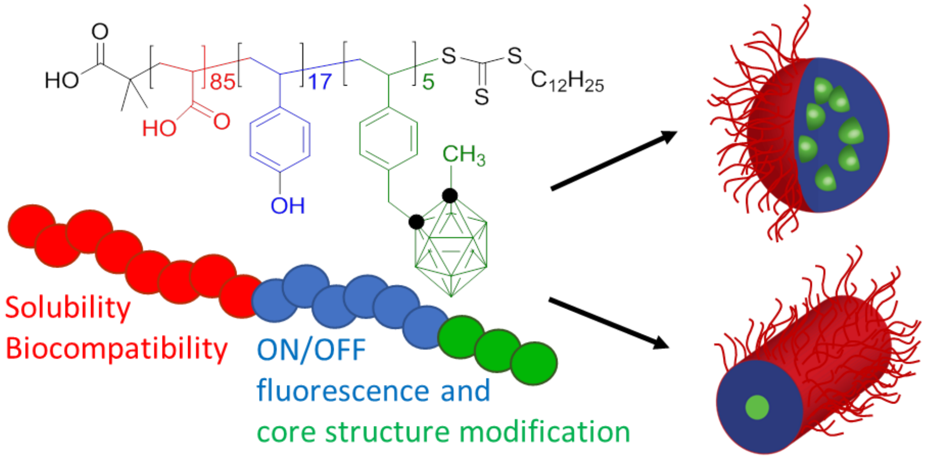

*Version presented here has small format modifications compared to the original form at: Synthesis and self-assembly of a carborane-containing ABC triblock terpolymer: morphology control on a dual-stimuli responsive system. Fernandez-Alvarez, R.; Hlavatovičová, E.; Rodzeń, K.; Strachota, A.; Kereïche, S.; Matějíček, P.; Cabrera-González, J.; Núñez, R.; Uchman, M. Polym. Chem. 10 (2019) 2774-2780.

Main body

Triblock terpolymer synthesis continuously broadens the possibilities and the product range in the field of solution-prepared nanoparticle architectures,[1] thanks to the high potential of terpolymers for new functional designs.[2,3] Linear terpolymers are frequently designed to ensure different interactions between each block and the solvent and among the blocks (e.g.: hydrophilic, lipophilic, fluorophilic), thereby facilitating microphase separation of polymer chains in solution. Block order plays a key role in the formation of complex nanostructures and can lead to multi-compartment micelles.[4,5] A powerful method for triblock terpolymer preparation is reversible addition fragmentation chain transfer (RAFT) polymerization.[6,7] This living polymerization is compatible with various substrates and solvents, thus enhancing block length and polydispersity control.[6,8,9] RAFT has also been used to prepare triblock terpolymers with different block orders and complex micellar structures. Therefore, RAFT is an excellent tool to introduce architectural flexibility into terpolymer nanostructures and to incorporate novel functional blocks.

Boron clusters are among the most resistant functional moieties incorporated into polymers to protect them from oxidation,[10] heat[11,12] and other degradation factors. Carboranes are commonly used in polymer chemistry,[13] luminescent materials,[14–19] and drug design[20] thanks to their versatile and unique properties. Specifically, in polymer chemistry, carboranes have been recently incorporated into vinyl-type polymers and transformed from *closo* to *nido* carboranes to modify the photoluminescent properties of these polymers.[21,22] Despite these advances in carborane incorporation into linear polymers, their behavior and self-assembly in aqueous solution remains mostly unexplored limiting their possible application to thin film coatings. In contrast, non-cluster boron compounds are routinely incorporated into polymers and studied in solution.[23–25] Hence, understanding their solution behavior is crucial for their use as stimuli-responsive blocks or in biomedical applications as agents in boron neutron cancer therapy treatment (BNCT).

The combination of incompatible blocks with different stimuli-responsive properties is a powerful tool for nanostructure manipulation.[26] The availability of powerful polymerization techniques is widening the range of stimuli-responsive polymers based on creative designs.[27,28] For example, *closo*-carboranes can undergo deboronation into *nido*-carboranes in the presence of strong nucleophiles, which improves the water solubility.[29] Thus, carboranes are excellent candidates for adding nucleophile-responsiveness to block copolymers.

Despite the progress in triblock terpolymer synthesis, in carborane incorporation into polymers and in stimuli-responsive nanostructure design, no stimuli-responsive triblock terpolymer with a caborane block has ever been prepared and studied in solution. Thus far, studies in solution have been limited to carborane dendrimers[30,31], and carborane copolymers have only been analyzed in solid state. Therefore, combining the structural flexibility of triblock terpolymers with the photoluminescent and protective properties of carboranes, through a simple synthetic approach such as RAFT, may enable us to study the self-assembly of these carborane nanostructures in solution.

Thus, in this study, we used RAFT polymerization to prepare poly(acrylic acid)-*b*-poly(4-hydroxystyrene)-*b*-poly{1-[4-(1-methyl-1,2-dicarba-*closo*-dodecaborane-2-yl methyl)-phenyl] ethylene)}, (PAA-*b*-PHS-*b*-PSC) an amphiphilic triblock terpolymer. To our knowledge, this is the first study of a carborane-containing terpolymer in solution. This terpolymer was designed to have a charged block (PAA) which provides water solubility and micelle stability via electrostatic repulsion. The middle block (PHS) is hydrophobic and forms intermolecular hydrogen bonds. Lastly, a short third block (PSC) with high hydrophobicity due to its *ortho*-carborane moiety. Furthermore, in our system, both hydrophobic blocks, PHS and PSC, can become hydrophilic under different stimuli, namely pH and CsF, respectively. Thus, their interactions with the solvent can be individually controlled. For example, at pH > 11, the phenolic group of PHS is deprotonated, adding a delocalized charge, which increases hydrophilicity. When adding CsF and heating the solution, PSC block undergoes deboronation, losing one B-H unit, and the resulting *nido*-cluster has an overall -1 charge. The preparation of such terpolymer is outlined in **Figure 4.3.1a**.

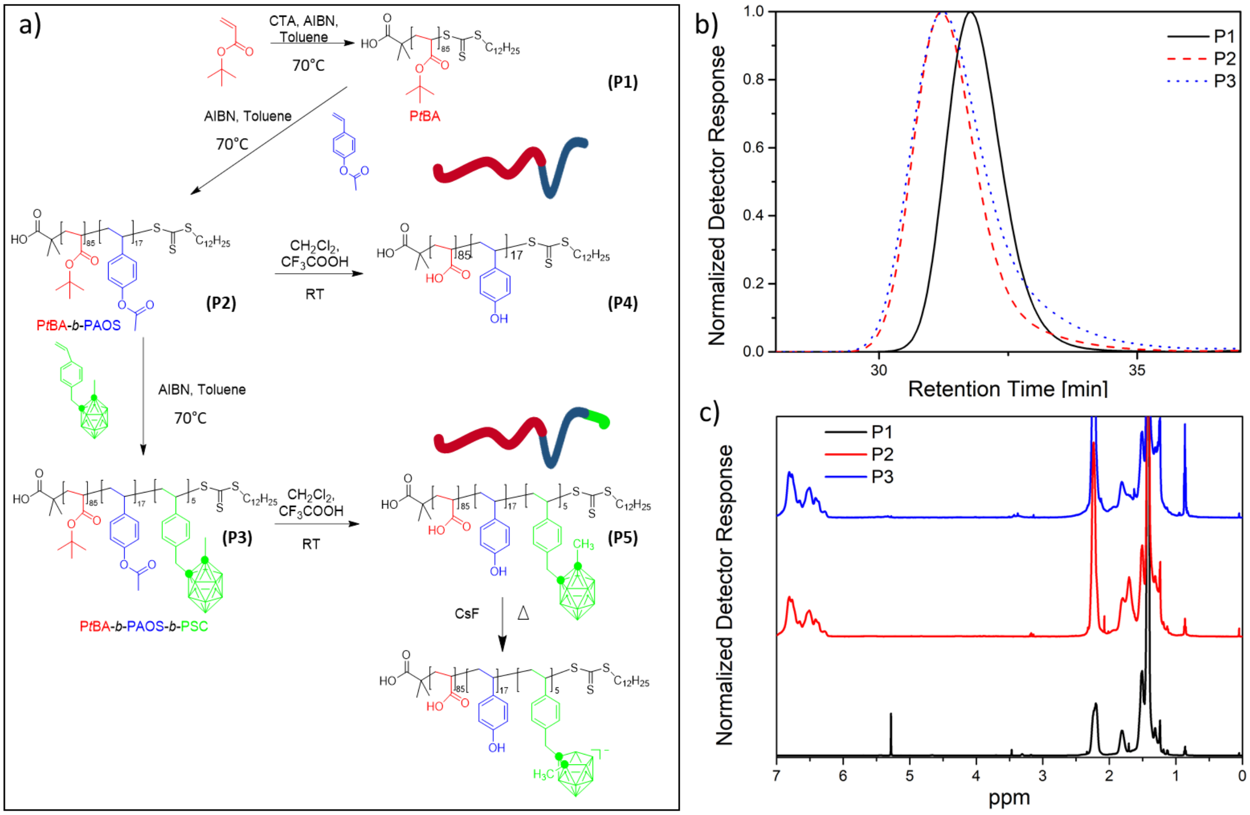

Figure 4.3.1. **(a)** Synthesis route to di- and tri-block amphiphilic copolymers, via RAFT polymerization followed by acidolysis. **(b)** SEC traces of P*t*BA (P**1**), P*t*BA-*b*-PAOS (P**2**) and of P*t*BA-*b*-PAOS-*b*-PSC (P**3**). ^{1}H NMR spectra of **P1** (bottom), **P2** (middle) and **P3** (top) in CDCl$_3$.

Poly(*tert*-butyl acrylate) **P1** was synthesized as the first block of the future copolymers using AIBN as initiator and the trithiocarbonate compound as chain transfer agent (CTA) (**Figura 1a**). Toluene was used as solvent to avoid an excessive increase in viscosity during polymerization, which resulted in relatively high monomer conversions without solidification. After removing the monomer residues, **P1** (P*t*BA) was used as the macrotransfer agent for chain extension with 4-acetoxystyrene, yielding the diblock copolymer P**2**. After isolating **P2**, the carborane-containing monomer (SC) was added to the chain, thereby generating the triblock terpolymer **P3**. Lastly, acidolysis of the pendant ester groups of **P3** yielded the amphiphilic P**5**, which was purified by dialysis. Similarly, the carborane-free diblock copolymer **P2** was converted into the copolymer **P4** by acidolysis, for comparative studies.

The final products of each synthesis step were analyzed by ^{1}H NMR and by SEC to assess their structure and molecular mass. **Figure 4.3.1b** and **Table S4.3.1** show SEC results with monomodal distribution and relatively narrow molecular mass distributions in all polymers. Nevertheless, their polydispersity increased with the successive addition of blocks. Additionally, a small tail was observed in the region of low molecular mass, which commonly occurs in RAFT copolymerization products. Both the apparent decrease in the M_n of **P5** and the discrepancies between M_n(SEC) and M_n(^{1}H NMR) can be explained by differences in chain conformation between di- or triblock and polystyrene standards used for SEC calibration.

In turn, M_n(NMR) were obtained from the ^{1}H NMR spectra (**Figure 4.3.1c, details in Figure S4.3.1**), using the ratios of suitable signal integrals from repeating units. The signal from the ω-methyl group of the CTA at 0.86 ppm was used as "end-group-signal". The following signals were used: for PAA, the methine protons on the main chain at 2.2 ppm; for PHS, the signals of the aromatic protons near 6.6 ppm; lastly, the length of PSC was calculated using the wide signal around 3.3 ppm, which corresponds to the methylene bridge between styrene and the carborane cage in SC. The aromatic signals of the PHS block fully overlap with the aromatic signals of the PSC block. To evaluate the PHS block length of P**3**, the expected aromatic signal intensity (integral) from PSC was calculated as the double value of the signal integral at 3.3 ppm. This value was then subtracted from the integral of the signals near 6.6 ppm, thus yielding the remaining aromatic signal intensity from the PHS.

After the synthesis, we assessed differences in self-assembly behavior between **P4** and **P5** in various THF-water mixtures. The chain composition of **P4** and **P5** has a large portion of PAA (0.72 and 0.62 mass fraction, respectively), which indicates that spherical micelles should be the predominant shape in aqueous solution. The degree of swelling in the core can be controlled using different solvent mixtures, which changes the packing parameter (*P*) and, therefore, the resulting nanostructures.[32,33] Accordingly, water was chosen as a selective solvent for the PAA block and as a non-solvent for the PHS and PSC blocks, whereas THF was used as a good solvent for PHS and PSC. **P4** and **P5** were solubilized in solvent mixtures ranging from 10-90% v/v THF-water. Unexpectedly, **P4** was only soluble in a 90% THF mixture, despite having a shorter hydrophobic part (no PSC block), whereas **P5** was soluble in the entire range of mixtures. Apparently, the PSC block facilitates the microphase separation in low THF mixtures. The results from dynamic light scattering (DLS) indicate that both **P4** and **P5** form micelles in THF-H_2O mixtures and that their size and dispersity increase with THF v/v % (**Figure S4.3.4**). Therefore, the resulting micelles consisted of one or two blocks (PHS and PSC) nanoconfined in a core surrounded by a PAA corona.

To understand the behavior of the linear polymers in water, the initial micellar solutions (THF-H_2O mixtures) were added dropwise to a large excess of water to preserve the micellar structures formed in the organic solvent mixture.[34] Subsequently, samples were dialyzed against water. One (90% THF, henceforth **P4-90**) and three (10, 50 and 90% v/v THF-water; **P5-10**, **P5-50**, **P5-90**) solvent mixtures were chosen to further study **P4** and **P5** self-assembly in water, respectively. When micelles in a solvent mixture are added to a large excess of water, THF quickly migrates from the core to the outside of the micelle.[35] Moreover, micelles become kinetically trapped if their core has a high Tg (as PHS has).[34] Thus, to further analyze the resulting micelles and their structure, we used DLS, cryo-TEM and SAXS.

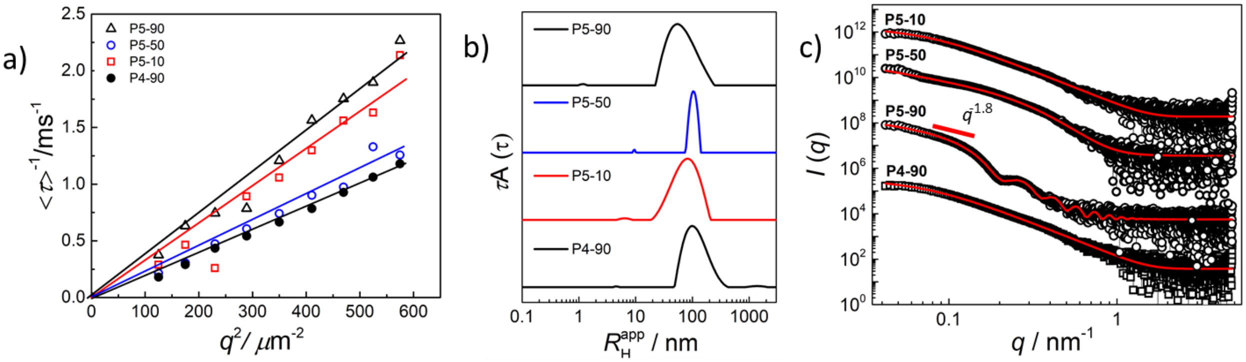

Figure 4.3.2. **(a)** Mean relaxation rates as a function of q^2, **(b)** DLS CONTIN distributions of apparent hydrodynamic radii (scattering angle, $\vartheta = 90^\circ$) and **(c)** SAXS curves for the different micellar preparations of PAA-*b*-PHS (**P4**) and PAA-*b*-PHS-*b*-PSC (**P5**) in water. SAXS curves were independently fitted to their specific model (red line, details in SI). All SAXS curves, except **P4**, are artificially offset on the Y axis for clarity.

DLS measurements show monomodal distributions in all samples, with no large aggregates (**Figure 4.3.2b**, **Table S4.3.6**). P4-90 produces larger micelles than all **P5** preparations, which indicates the formation of a less compact and partly swelled PHS micellar core. Micelle stability in water is determined by the charged PAA corona, as shown by ζ-potential measurements (> -35 mV). Although some deviations were observed in **P5-90**, which could be attributed to the inner motion of long cylindrical micelles (**Figure 4.3.2a**), the linear correlation between the mean relaxation rates (τ) and q^2 confirms that τ corresponds to the diffusive motion of micelles.

Cryo-TEM confirmed the presence of spherical micelles, as expected for both **P4** and **P5** (**Figure 4.3.3**). However, P5 showed variations in shape caused by the solvent mixture. Both **P5-10** and **P5-50** form spherical micelles, whereas **P5-90** formed cylindrical micelles due to increased core swelling. This volumetric increase in the core reduces the curvature of the micelles at the interface and allows them to acquire a cylindrical shape. Comparatively, in the same solvent system, **P4-90** forms only spherical micelles, thus indicating that the bulky carborane block significantly contributes to the hydrophobic volume, despite its short extension. Thus, SAXS was used to further study the structure of the micelles (**Figure 4.3.2c**), and the models used for fitting SAXS curves are shown in SI.

The SAXS curves of **P4-90** micelles were fitted with a Pedersen-Gertenberg form factor consisting of hard spherical core and a corona of gaussian chains attached to the core. These estimated values of core radius were very similar to those assessed by cryo-TEM (R_{core} ≈7.8 nm), which indicates an adequate choice of fitting model (**Table S4.3.5**). In conclusion, **P4-90** micelles are predominantly spherical.

The SAXS curves of P5-90 were fitted using a combination of long cylinder and sphere form factors, resulting in a good fit. These SAXS curves clearly indicate cylindrical micelles because, at low q values, the power law exponent has a value of -1.8, thus suggesting an elongated structure followed by a higher power law exponent after q=1.2 nm^{-1}. Although the power law exponent of cylindrical micelles is typically ≈-1 at low q, the higher power law exponent of P5-90 may be explained by the concomitant presence of spherical and cylindrical micelles. The results from the models show cylinders with a cross section radius of 20 nm and spherical micelles with a radius of 17 nm. Both results are in in excellent agreement with the cryo-TEM results (**Table S4.3.3**), thus showing that **P5-90** micellar solutions contain a mixture of spherical and cylindrical micelles, as shown by DLS and Cryo-TEM (**Figure 4.3.2b**, and **3**).

Conversely, our initial attempts to fit **P5-10** and **P5-50** to the form factor used for **P4-90** or to simple spherical models failed. We expected PSC to form multi-compartments due to incompatibility with the PHS core. To explore this possibility, we fitted the **P5-10** SAXS curve to a model consisting of small scattering objects (representing multi-compartments or carborane clusters) with attractive forces (simulated by a mass fractal structure factor). The model yields spherical scattering units of 0.4 nm in size and fractal aggregate of 13 nm (**Table S4.3.4**). The small extension of the PSC block could correspond to the spherical scatterers. Therefore, the PSC block may form multi-compartments inside the PHS core. However, the fit was not entirely satisfactory at high q values. In contrast, the Fisher-Burford cluster model provided good fits. The apparent shapeless nature of **P5-10** and **P5-50** micelles (in SAXS) derives from their polydispersity, most likely because the M_{w} distribution of **P5** was broader than that of **P4** (**Table S4.3.1**). Nonetheless, the values from the Fisher-Burford model agree well with the results from cryo-TEM and DLS. R_{g} values obtained from the SAXS fit were in the range of $R_{\mathrm{core}}<R_{\mathrm{g}}<R_{\mathrm{H}}$ (**Table S4.3.2**). In addition, the power law exponent values of both **P5-10** and **P5-50** indicate that these micelles have a rough surface. In summary, although the polydispersity of **P5-10** and **P5-50** precludes the determination of their shape by SAXS, these micelles are spherical, based on the Cryo-TEM results.

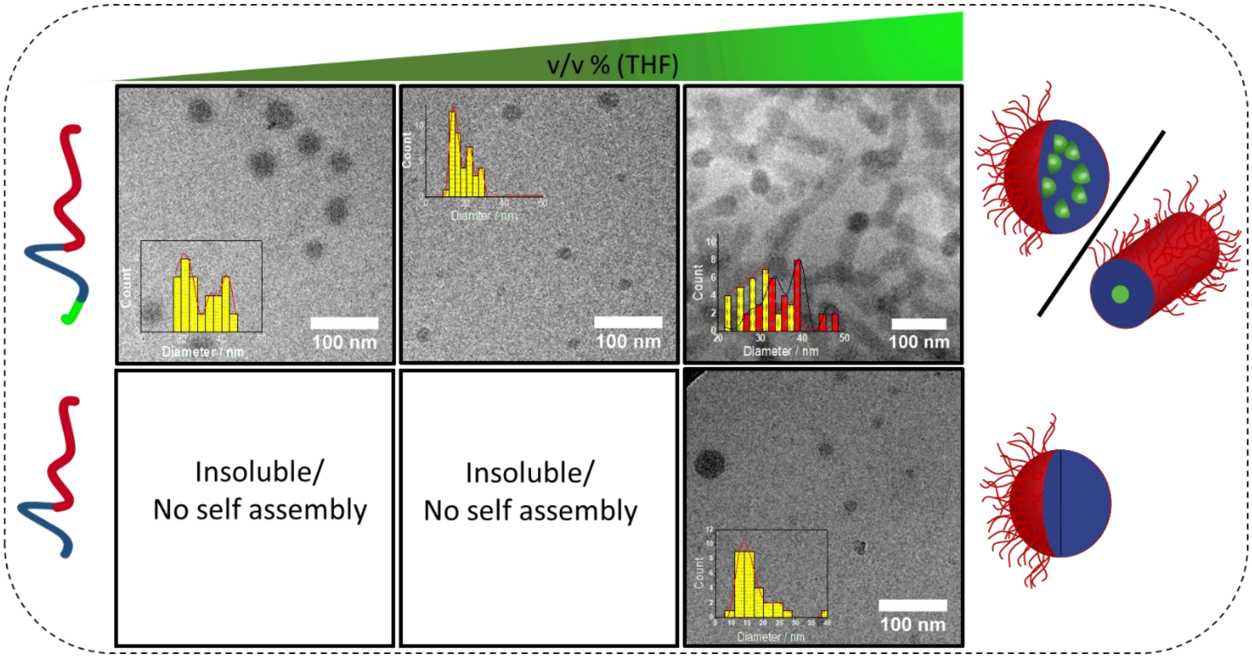

Figure 4.3.3. Cryo-*TEM* pictures depicting self-assembly structures of PAA-*b*-PHS (**P4**) (bottom) and PAA-*b*-PHS-*b*-PSC (**P5**) (top) in water. The volume percentage of THF refers to the percentage used to prepare the micelles (THF-water v/v %). *Inset*: Histogram depicting the size distribution of spherical micelles (yellow) and the cross-section diameter of cylindrical micelles (red).

Lastly, we modified the solvophobic interactions of the PHS and PSC blocks in **P5-10** micelles by changing the pH or alternatively by treating them with CsF, thus increasing their hydrophilicity, to assess the resulting structural changes. These changes were analyzed by TEM, DLS and fluorescence, and the results showed that pH influences the core size of the micelles while fluoride changes the inner structure of the core (**Figure 4.3.4**).

When increasing the pH to 12 ($pKa_{(PHS)} = 9 - 11.5$)[36], to ensure a high degree of deprotonation, the PHS block became charged, but not PSC, thus increasing the hydrophilic character of PHS without altering the carborane block. DLS measurements showed that R_H^{app} increased from 74nm to 114nm because the corona extended due to chain repulsion. In addition, TEM images were acquired to track changes in the micelle core, and the samples were treated with a standard negative staining method to improve visualization (**Figure 4.3.4a**, top panel). The TEM images show a clear reduction in core size after the increase in pH, thereby indicating that PHS is deprotonated and becomes part of the corona (**Figure 4.3.4a**, histogram). In the fluorescence measurements, observed spectra comes from PHS block. P5-10 showed two distinctive fluorescence bands, one around 308 nm attributed to emission from single repetitive units and a broad band around 350 nm resulting from excimer emission of PHS.[37] However, the increase in pH to $pH>pKa_{PHS}$ causes an abrupt loss of fluorescence, which indicates that PHS is the main contributor to the observed fluorescence. This fluorescence was restored by decreasing the pH to $pH<pKa_{PHS}$ (**Figure 4.3.4c**). Moreover, this ON/OFF process can be repeated while micelles conserve their spherical shape

thanks to the PSC. Therefore, we determined that changes in pH can work as an OFF/ON switch for fluorescence in **P5** micelles.

When adding CsF for the deboronation of the *closo*-carborane pendant groups, the PSC block became charged. Furthermore, this reaction allowed us to selectively change the solvophobic character of this block without affecting the PHS block. After 24h, DLS measurements showed a small decrease in R_H^{app} (8 nm). Deboronation was confirmed via B{H} NMR, and the quadruplet signal at 0.6 ppm is a known side product of deboronation when using CsF. Post-deboronation TEM images revealed that the micellar shape and the core size remained almost unchanged (**Figure 4.3.4a**), thus indicating that the PSC block remains in the core, despite the improvement in its water solubility. In addition, we observed a 27% increase in fluorescence intensity. We speculate that carborane moieties are distributed in the PHS core and that they disrupt the hydrogen-bonding network of the PHS block before deboronation. After deboronation, PHS and PSC undergo a micro-phase separation in the core, which allows a more extensive hydrogen bond network among PHS chains, thus increasing core rigidity and fluorescence intensity.[37] Accordingly, we added a small amount of THF to the reaction mixture to increase core plasticity and to promote rearrangement of PSC. In this case, fluorescence intensity increased by 84% (after removal of THF) (**Figure 4.3.4c** and **Figure S4.3.2**). A control sample containing both **P4** and **P5** micelles was prepared to ensure that the observed fluorescence effect resulted from deboronation and not from other effects (**Figure S4.3.3**). Therefore, **P5** micelles can act as a responsive system capable of lowering (high pH), restoring (neutral pH) or increasing (CsF) the fluorescence intensity in response to external stimuli, while maintaining their stability.

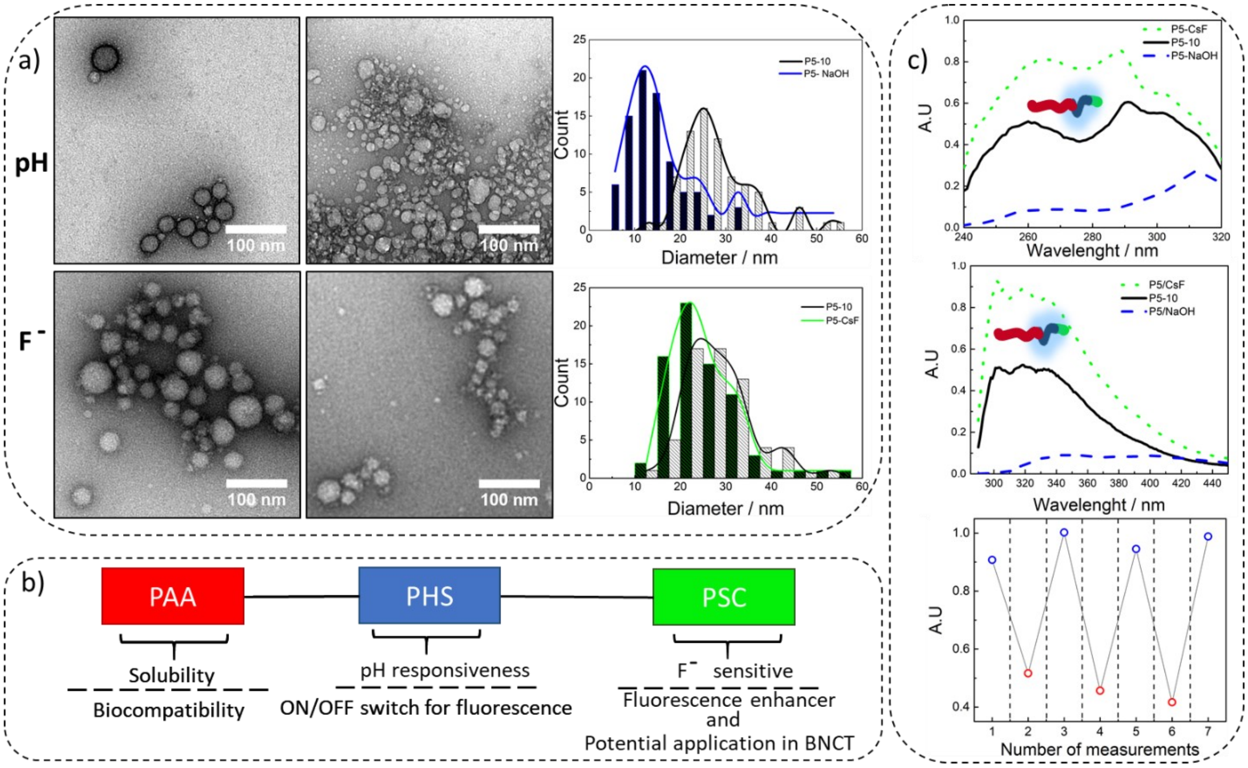

Figure 4.3.4. (**a**) *Upper panel:* TEM micrograph of **P5-10** at neutral pH (left) and at basic pH (center), (right) histogram depicting the number size distribution of the core diameter. *Bottom panel*: TEM micrograph before (left) and after (center) reaction with CsF, (right) histogram depicting the number size distribution of the core diameter. (**b**) Schematic representation of triblock terpolymer and function of individual blocks. (**c**) Excitation spectra (λ_{em}= 350 nm) (top), fluorescence spectra (λ_{ex}= 274 nm) (middle) of **P5-10** micelles demonstrating fluorescence response to different stimuli. Fluorescence intensity of **P5-10** micelles at pH 11.8 (red) and 8 (blue) working as an ON/OFF switch (bottom).

In conclusion, we used RAFT polymerization to synthesize a novel triblock terpolymer containing carboranes (poly(acrylic acid) -*b*- poly(4-hydroxystyrene) -*b*- poly{1-[4-(1-methyl-1,2-dicarba-*closo*-dodecaborane-2-yl methyl)-phenyl] ethylene}), (PAA_{85}-*b*-PHS_{17}-*b*-PSC_5). The amphiphilic terpolymer self-assembles in water/THF mixtures and the micelles maintain stability when subsequently transferred into water. The morphology of the resulting micelles was controlled by core swelling with THF during the first preparation step achieving a transition from spherical to cylindrical micelles. Moreover, the inclusion of PHS and PSC blocks into the terpolymer granted control over the photophysical properties of the micelles and their use as a dual responsive system to both pH and fluoride anions. Specifically, we were able to use the pH stimulus as an OFF/ON fluorescence switch in P5 micelles and the fluoride sensitivity amplified the fluorescence through modification of the micellar core structure. Therefore, we developed a new method to incorporate carboranes into a terpolymer system capable of self-assembling into stable nanoparticles with a biocompatible stabilizing corona suitable for future applications in the design of boron nanocarriers for boron neutron capture therapy.

Acknowledgments

The authors acknowledge the financial support from the Czech Science Foundation Grant No. 17-00289Y. Authors would like to thank Prof. Miroslav Štěpánek for his counseling in SAXS fitting and interpretation, Prof. Jiří Vohlídal for his assistance in polymer nomenclature and Carlos V. Melo for editing the manuscript. The group from ICMAb thanks to Spanish Ministerio de Economía y Competitividad, MINEICO (CTQ2016-75150-R9 and and Generalitat de Catalunya (2017/SGR/1720) for the financial support.

Supporting Information

Experimental Section

Materials

Tert-butyl acrylate (*t*BA, 98%) and 4-Acetoxystyrene (AOS, 96%) were obtained from Sigma-Aldrich and purified by distillation under reduced pressure from CaH_2 followed by filtration over a column with silica gel and were subsequently stored at -20°C under N_2 in dark. 2,2′-Azobis(2-methylpropionitrile) (98%, AIBN) was recrystallized from ethanol. Toluene (p.a., Lachner) was dried by distillation under reduced pressure from P_2O_5. Trifluoroacetic acid (TFA, 99%, Sigma-Aldrich), 2-(Dodecylthiocarbonothioylthio)-2-methylpropionic acid (CTA, 98%, Sigma-Aldrich), dichloromethane (HPLC grade, Lachner), CsF (Sigma-Aldrich) and methanol (HPLC grade, Lachner) were used as received. Styrene with attached carborane cage ("Styrene carborane", or "SC") was delivered by Núñez group and reported in article.[i] Dialysis tubes used in this work (supplied by Spectrum Laboratories, Inc., CA USA) had a nominal molar mass cutoff of 3.5 kDa.

Syntheses

<u>Synthesis of Poly(*tert*-butyl acrylate), P*t*BA, **P1**.</u>

A 50 ml Schlenk flask, equipped with a Teflon-coated stir bar was filled with 5 g (39.01 mmol, 200 eq.) of *t*BA, 71.1 mg (0.195 mmol, 1.00 eq.) of CTA, 6.4 mg (39 µmol, 0.20 eq.) of AIBN and 1 g of toluene, in this order of sequence. The mixture was deoxygenated by purging with Ar for 30 min under intense stirring, after which the flask with the yellow solution was capped by a rubber septum and degassed by 3 – 5 cycles of freezing / evacuation / thawing. The Schlenk flask was subsequently filled with Ar. A small aliquot of the well-mixed starting mixture was removed for conversion analysis (using a syringe with a long needle piercing the rubber septum). Thereafter, the Schlenk flask was immersed in an oil bath pre-heated to 70°C. After 3.5 h, another small sample was taken for conversion determination and the reaction was stopped by quenching it with a liquid nitrogen bath. Subsequently, the mixture was allowed to reach room temperature. Most of the residual monomer was removed by vacuum distillation. Next, the crude polymer was dissolved in a small amount of dichloromethane and precipitated by adding its solution to an ice-cold 1:1 water/methanol mixture. The pale yellow (solid) precipitate was separated by decantation and dissolved again in dichloromethane. This solution was evaporated and dried overnight under vacuum at RT. The final product was obtained as a yellow sticky rubber.

Yield: 3.2 g, monomer (*t*BA) conversion 76%.

Characterization: SEC: M_n=18001 Da, M_w=20548 Da, PDI=1.11; 1H-NMR ($CDCl_3$): M_n=11259 Da; δ=0.86 (trip, CH_3CH_2-), 1.20-1.98 (br, -CH_2CH- methylene backbone, alkyl chain and HOOCC$(CH_3)_2$- from CTA), 1.25-1.65 (br, $(CH_3)_3$C-), 2.05-2.50 (br, -CHCH_2- methine backbone), 3.10–3.25 (br,-SCSCH_2-), 4.62–4.72 (br, -CH_2CHS) ppm.

Synthesis of Poly(*tert*-butyl acrylate)-*block*-Poly(4-acetoxystyrene), P*t*BA-*b*-PAOS, **P2**.

A 50 ml Schlenk flask, equipped with a Teflon-coated stir bar was filled with 2g (0.17 mmol, 1 eq.) of the macrotransfer agent (**P1**), 3g (18.49 mmol, 100 eq.) of AOS, 9.11 mg (56.16 µmol, 0.30 eq.) of AIBN and 1 g of toluene. The mixture was deoxygenated by purging with Ar for 30 min under simultaneous intense stirring (important also for the dissolution of (**P1**)), after which the flask with the transparent yellow solution was capped by a rubber septum and degassed by 3 – 5 cycles of freezing / evacuation / thawing. The Schlenk flask was subsequently filled with Ar. A small aliquot of the well-mixed starting mixture was removed for conversion analysis (using a syringe with a long needle piercing the rubber septum). Thereafter, the Schlenk flask was immersed in an oil bath pre-heated to 70°C. After 16 h, another small sample was taken for conversion determination and thereafter the reaction was stopped by quenching it with a liquid nitrogen bath. Subsequently, the mixture was allowed to reach room temperature. Most of the residual monomer was removed by vacuum distillation. Next, the crude polymer was dissolved in a small amount of dichloromethane and precipitated by adding its solution to an ice-cold 1:1 water/methanol mixture. The pale yellow (solid) precipitate was separated by decantation and dissolved again in dichloromethane. This solution was evaporated and dried overnight under vacuum at RT. The final product was obtained as a light-yellow solid.

Yield: 2.23 g, second-block-monomer (AOS) conversion 26%.

Characterization: SEC: M_n=22177 Da, M_w=28711 Da, PDI=1.29; 1H-NMR ($CDCl_3$): M_n=14016 Da; δ=0.86 (trip, CH_3CH_2-), 1.20-1.98 (br, -CH_2CH- methylene backbone, alkyl chain and HOOCC$(CH_3)_2$- from CTA), 1.25-1.65 (br, $(CH_3)_3$C-), 2.05-2.50 (br, -CHCH_2- methine backbone and -OCOCH_3), 3.10–3.25 (br,-SCSCH_2-), 4.62–4.72 (br, -CH_2CHS), 6.2-7 (br, Ar-*H*) ppm.

Synthesis of Poly(*tert*-butyl acrylate)-*block*-Poly(4-acetoxystyrene)-*block*- poly{1-[4-(1-methyl-1,2-dicarba-*closo*-dodecaborane-2-yl methyl)-phenyl] ethylene}), P*t*BA-*b*-PAOS-*b*-PSC, **P3**.

A 50 ml Schlenk flask, equipped with a Teflon-coated stir bar was filled with 1.0 g (71.35 µmol, 1 eq.) of macrotransfer agent (**P2**), 1.0 g (3.63 mmol, 50 eq.) of SC, 1.7 mg (0.29 µmol, 0.50 eq.) of AIBN and 1.5 g of toluene. The mixture was deoxygenated by purging with Ar for 30 min under simultaneous intense stirring (important also for the dissolution of (**P2**)), after which the flask with the transparent yellow solution was capped by a rubber septum and degassed by 3 – 5 cycles of freezing / evacuation / thawing. The Schlenk flask was subsequently filled with Ar. A small aliquot of the well-mixed starting mixture was removed for conversion analysis (using a syringe with a long needle piercing the rubber septum). Thereafter, the Schlenk flask was immersed in an oil bath pre-heated to 70°C. After 27 h, another small sample was taken for conversion determination and thereafter the reaction was stopped by quenching it with a liquid nitrogen bath. Subsequently, the mixture was allowed to reach room temperature. Most of the residual monomer was removed by vacuum distillation. Next, the crude polymer was dissolved in a small amount of dichloromethane and precipitated by adding its solution to an ice-cold 1:1 water/methanol mixture. The amber-colored solid precipitate was separated by decantation and dissolved again in dichloromethane. This solution was evaporated and dried overnight under vacuum at RT. The final product was obtained as an amber solid.

Yield: 1.11g, third-block-monomer (SC). corresponding to 27% conversion of the

Characterization: SEC: M_n=22177 Da, M_w=28711 Da, PDI=1.29; 1H-NMR ($CDCl_3$): M_n=14016 Da; δ=0.86 (trip, CH_3CH_2-), 1.20-1.98 (br, -CH_2CH- methylene backbone, alkyl chain and HOOCC(CH_3)$_2$- from CTA), 1.25-1.65 (br, (CH_3)$_3$C-), 2.05-2.50 (br, -CHCH$_2$- methine backbone, -OCOCH$_3$ and -CCH$_3$), 3.10–3.25 (br,-SCSCH$_2$-), 3.27-3.50 (br, -CCH$_2$C-), 4.62–4.72 (br, -CH$_2$CHS), 6.20-7.00 (br, Ar-*H*) ppm.

Preparation of amphiphilic block copolymers Poly(acrylic acid)-*block*-Poly(4-hydroxystyrene), PAA-*b*-PHS, **P4** and Poly(acrylic acid)-*block*-Poly(4-hydroxystyrene)-*block*- poly{1-[4-(1-methyl-1,2-dicarba-*closo*-dodecaborane-2-yl methyl)-phenyl] ethylene}), PAA-*b*-PHS-*b*-PSC, **P5**.

The simultaneous acidolysis of the ester pendant groups in the poly(*t*BA) and poly(AOS) blocks similar to [ii,iii], which yielded poly(Acrylic acid) and poly(4-Hydroxystyrene) blocks in the final product, was carried out in a 100 ml one-neck round bottom flask equipped with a Teflon-coated stir bar. Diblock and triblock copolymers (which both contained poly(*t*BA) as well as poly(AOS) blocks) were processed in an identical way: **P2** (0.7 g, 50 µmol) or **P3** (0.7 g, 45 µmol) was put into the reaction flask together with 15 ml of dichloromethane and the flask was capped by a rubber septum. The respective copolymer was dissolved by 30 min of intense stirring. Thereafter, 5 ml of 99% TFA were injected through the septum and the reaction mixture was stirred for 24 h, at room temperature. In the next step, the solvent, TFA, as well as the volatile by-products were removed under vacuum. The crude product was dissolved in 15 ml of THF and transferred into a dialysis tube with nominal molar mass cutoff of 3.5 kDa. It was dialyzed against water for 3 days to remove remaining low-molecular impurities. The purified solution of the acidolysis product was evaporated and dried overnight under vacuum at RT. **P4** was obtained as a light-yellow solid, and **P5** as an amber solid.

Yield: **P4**: 0.377 g (92%); **P5**: 0.411 g (93%).

Self-assembly

General procedure for preparation of core-shell micelles from P4 and P5

Each polymer was initially dissolved in a mixture of THF/H_2O (ranging from 10 to 90% v/v THF) to a final concentration of 2mg/ml in a total volume of 2 ml. The mixtures that resulted soluble were then added dropwise into 2 ml of deionized water under vigorous agitation. After 30 min of agitation the samples were moved to dialysis membranes (MWCO= 3.5 kDa) and dialyzed against deionized water for 1 day with several changes of outer water bath to ensure complete removal of organic solvent.

General procedure for deboronation of Carborane in P5 micelles

An aqueous solution of P5 micelles (1 mg/ml) and CsF (0.2 mg/ml) were heated to 80°C in a closed vial for 24h. Blank solutions were prepared following an identical procedure with the exception of CsF addition, this was added after the solution was cooled down to room temperature.

Characterization Techniques

Dynamic Light Scattering

For most samples the light scattering setup (ALV, Langen, Germany) consisted of a 22 mW He-Ne laser (λ= 632.8 nm), an ALV-CGS/8F goniometer, an ALV High QE APD detector, and an ALV 50004, multibit, multitau autocorrelator. The measurements were carried out at 296 K for scattering angles ranging from 30° to 150° corresponding in aqueous solutions to scattering vector magnitudes ranging from 6.8 to 25.6 μm^{-1}. The normalized time autocorrelation function of the scattered light intensity was fitted by the constrained regularization algorithm (CONTIN), which provides the distribution of relaxation times τ. Effective angle dependent hydrodynamic radii, $R_H(q)$, were obtained from the mean values of relaxation times, τ(q), of individual diffusive modes using the Stokes-Einstein equation. R_H values correspond to apparent hydrodynamic radii.

Electrophoretic Light Scattering

The measurements were carried out with Nano-ZS Zetasizer (Malvern Instruments, UK). Zeta-Potential was obtained from electrophoretic mobility values using the Henri equation in the Smoluchowski approximation. Values presented are averaged from 45 measurements. For comparison of zeta potential values samples were measured at matching ionic strength. NaCl was used to increase ionic strength when required.

Fluorescence

All steady-state fluorescence spectra were acquired at a polymer concentration of 0.5 mg ml^{-1} using a Fluorolog FL- 3-22 (Horiba Jobin Yvon, France) equipped with an excitation and emission double monochromators and a 450 W xenon lamp. For both P4 and P5 micelles λ_{ex}= 274 nm, λ_{em}= 350 nm. After changes in pH samples were allowd to equilibrate for 30 min before measuring.

Cryo -Transmission Electron Microscopy (Cryo-TEM)

Cryo-Tem measurements were carried out using a Tecnai G^2 Sphera 20 electron microscope (FEI Company, Hillsboro, OR, USA) equipped with a Gatan 626 cryo-specimen holder (Gatan, Pleasanton, CA, USA) and a LaB_6 gun. The samples for cryo-TEM were prepared by plunge-freezing.*(J. Dubochet, M. Adrian, J.-J. Chang, J.-C. Homo, J. Lepault, A. W. McDowall and P. Schultz, Q. Rev. Biophys., 1988, 21, 129–228).* Briefly, 3 µL of the sample solution was applied to a copper electron microscopy grid covered with a perforated carbon film forming woven-mesh-like openings of different sizes and shapes (the lacey carbon grids #LC-200 Cu, Electron Microscopy Sciences, Hatfield, PA, USA) and then glow discharged for 40 s with 5 mA current. Most of the sample was removed by blotting (Whatman No. 1 filter paper) for approximately 1 s, and the grid was immediately plunged in liquid ethane held at −183 °C. The grid was then transferred without rewarming to the microscope. In both cases, images were recorded at an accelerating voltage of 120 kV and magnifications ranging from 11 500× to 50 000× using a Gatan UltraScan 1000 slow scan CCD camera in the low-dose imaging mode, with an electron dose not exceeding 1500 electrons per nm^2. The magnifications resulted in final pixel sizes ranging from 1 to 0.2 nm, and the typical value of the applied under focus ranged from 0.5 to 2.5 µm. The applied blotting conditions resulted in specimen thicknesses varying between 100 and ca. 300 nm. Brightness and contrast corrections of the acquired images were performed using the ImageJ software.

Negative stained technics

5 µL of the sample solutions were applied to a glow discharged carbon-coated copper grids. The excess of solution were blotted, samples were stained with 2% uranyl acetate.

Small Angle X-ray Scattering (SAXS)

SAXS experiments were carried out on the P12 BioSAXS beamline (PETRA III storage ring, EMBL/DESY, Hamburg, Germany), equipped with a Pilatus 2M detector. The measurement was carried out at 20 °C and the sample-detector distance 3 m, allowing for covering the q-range interval from 0.07 to 4.4 nm^{-1} for the X-ray wavelength lambda = 0.1 nm. The q range was calibrated using the diffraction patterns of silver behenate. The experimental data were normalized to the transmitted beam intensity and corrected for nonhomogeneous detector response, and the background scattering of the solvent was subtracted. The solvent scattering was measured before and after the sample scattering to control for possible sample holder contamination. 20 consecutive frames with 0.05 s exposures comprising the measurement of the solvent, sample, and solvent were performed. Data have been checked for radiation damage. The final scattering curves were processed by automated data acquisition software and recalculated to absolute scattering intensities. The data were fitted to different models as described in the Supporting Information using the SASfit 0.94.7 software.

Table S4.3.1. Molecular masses and polydispersity of the prepared polymers, as determined by SEC and ^{1}H NMR spectroscopy; ratios monomer/chain-transfer-agent/initiator are also listed.

	Polymer[c]	[M]/[CTA]/[I][a]	M_n (SEC)[b] Da	M_w (SEC)[b] Da	M_w/M_n (SEC)[b]	M_n (^{1}H NMR)[c] Da
P1	$(tBA)_{85}$	200/1/0.2	18 001	20 548	1.11	11 259
P2	$(tBA)_{85}$-b-$(AOS)_{17}$	100/1/0.3	22 177	28 711	1.29	14 016
P3	$(tBA)_{85}$-b-$(AOS)_{17}$-b-$(SC)_5$	50/1/0.5	21 173	31 066	1.46	15 383
P4	$(AA)_{85}$-b-$(HS)_{17}$	-	-	-	-	8 532
P5	$(AA)_{85}$-b-$(HS)_{17}$-b-$(SC)_5$	-	-	-	-	9 899

[a] [M]/[CTA]/[I] eq. of monomer, chain transfer agent or macrotransfer agent and initiator.

[b] Measured by SEC calibrated with PS standards in THF as eluent.

[c] Determined by ^{1}H NMR spectroscopy.

H-NMR and B-NMR details from triblock terpolymer

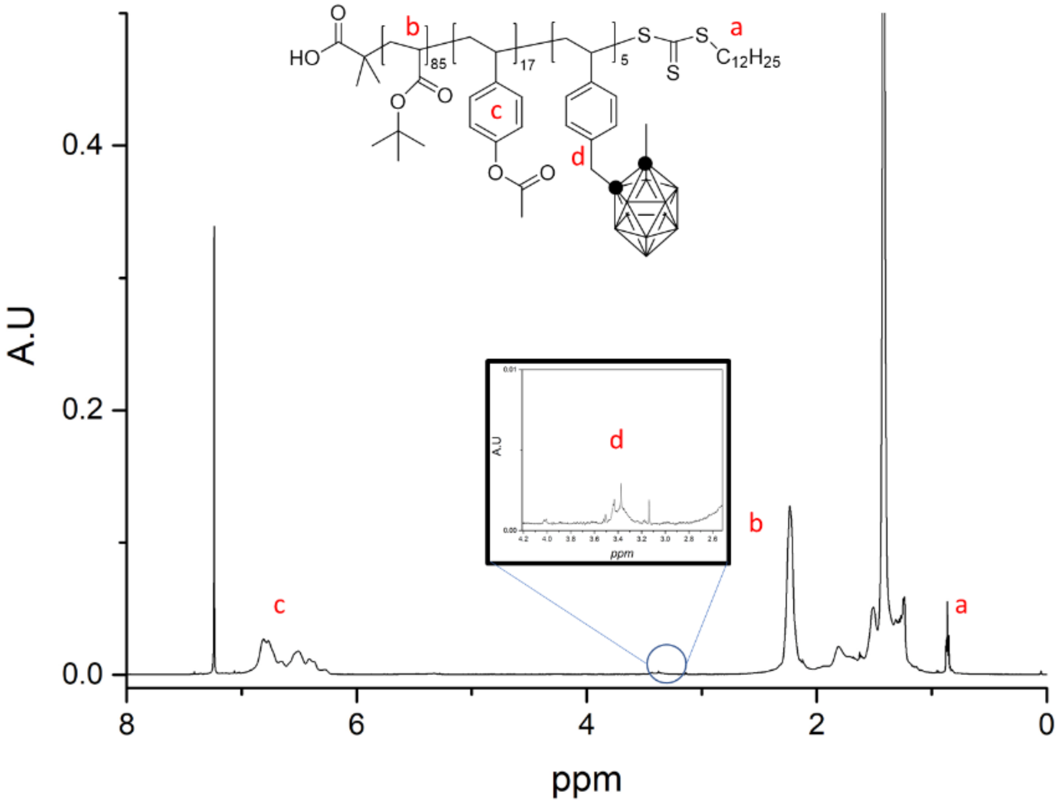

Figure S4.3.1. H-NMR spectra of triblock terpolymer P3 indicating signals used for quantification of segments.

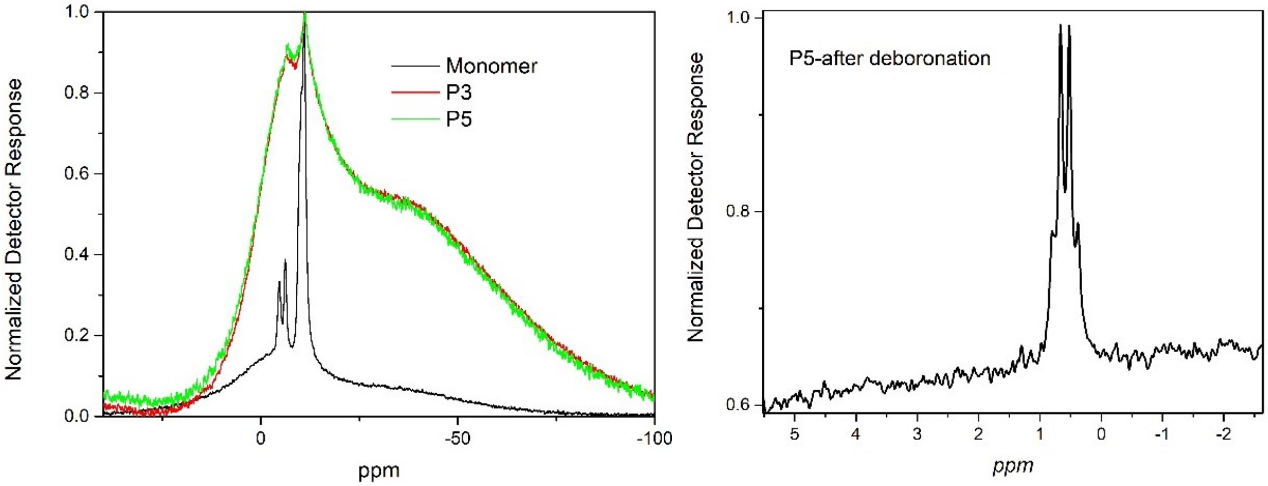

Figure S4.3.2. (*left*) B-NMR spectra of monomer before polymerization, triblock terpolymer before deprotection (P3) and final triblock terpolylmer (P5). (*right*) B-NMR of P5 after deboronation, spectra is zoomed to peak at 0.6 ppm.

Evaluation of SAXS data for P4, P5-10, P5-50 and P5-90 micelles in water

a) The SAXS curves of **P5-10** and **P5-50** were fitted by the Fisher-Burford model.

$$I(q, D, R_g) = \left(1 + \frac{2}{3D} q^2 R_g^2\right)^{-\frac{D}{2}} \qquad \textbf{(S1)}$$

Where D is the fractal dimension and R_g is the radius of gyration of the aggregate. Results obtained from the fitting process are presented in Table SI.

Table S4.3.2. Results obtained from fit of equation S1 to SAXS curves for P5-10 and P5-50.

Sample	***R_g (nm)***	***R_{core} (nm) (TEM)***	***R_H (nm) (DLS)***	***I_0***	***Power law exponent***
P5-10	29.2	18	58	3.3×10^5	3.0
P5-50	57.3	9	101	2.6×10^6	3.1

Both P5-10 and P5-50 were also fitted with a form factor of simple sphere to simulate small scattering units and the adhesion between scatterers was simulated by a mass fractal structure factor.

(b) The SAXS curves from **P5-90** were fitted by a combination of a sphere and a long cylinder form factor.

$$I(R, q, r, \Delta\eta) =$$

$$(\Delta\eta\pi R^2 L)^2 \frac{2q}{L} \left\{ Si_{\frac{\pi}{2}}(qL) \Lambda_1^2(qR) - \frac{\omega(2qR)}{qL} - \frac{\sin(qL)}{(qL)^2} \right\} + \left(\frac{4}{3}\pi r^3 \Delta\eta 3 \frac{\sin(qr) - qr * \cos(qr)}{(qr)^3} \right)^2$$

(S2)

Where Δη is the scattering length density difference between particle and matrix, R is the radius of cylinder, L is the length of the cylinder, and r is the radius of sphere

The functions Si and Λ_1 are defined as

$$Si_{\frac{\pi}{2}}(x) = \left(Si(x) + \frac{\cos x}{x} + \frac{\sin x}{x} \right) \qquad \textbf{(S3)}$$

$$\Lambda_1 = \frac{2}{x} J_1(x) \tag{S4}$$

Where J_1 is the regular cylindrical Bessel function of order 1. Porod's approximations for long cylinders was taken because previous analysis of cryo-TEM images confirmed the condition of L > 2R was satisfied.

Table S4.3.3. Results obtained from fit of equation S2 to SAXS curves of P5-90.

$R_{cylinder}$ (nm)	***$R_{cylinder}$ (nm) (TEM)***	***$L_{cylinder}$ (nm)***	***R_{sphere} (nm)***	***R_{sphere} (nm) (TEM)***
20	18	215	17.3	15

(c) Second fitting of **P5-10** by sphere model and mass fractal structure factor. The Sphere model was described above (right part of equation **S2**).

$$I(\xi, q, r, \Delta\eta, D, r_0) =$$

$$I_0\left\{1 + \frac{D\Gamma(D-1)\sin\left[(D-1)\arctan(q\xi)\right]}{(qr_0)^D(1+q^{-2}\xi^{-2})}\right\} x \left(\frac{4}{3}\pi r^3 \Delta\eta 3 \frac{\sin(qr) - qr * \cos(qr)}{(qr)^3}\right)^2 \tag{S5}$$

Where ξ is the correlation length of the fractal cluster, I_0 is the forward scattering, D is the mass fractal dimension and r_0 is the characteristic dimension of a particle forming part of the cluster. The gamma function Γ is defined as

$$\Gamma(a, x) = \int_x^\infty t^{-a} \exp(-t)\,\mathrm{d}t \tag{S6}$$

Table S4.3.4. Results obtained from best fit of equation S5 to SAXS curves of P5-10

r_0 (nm)	**ξ (nm)**	***D***
0.4	13.4	2.6

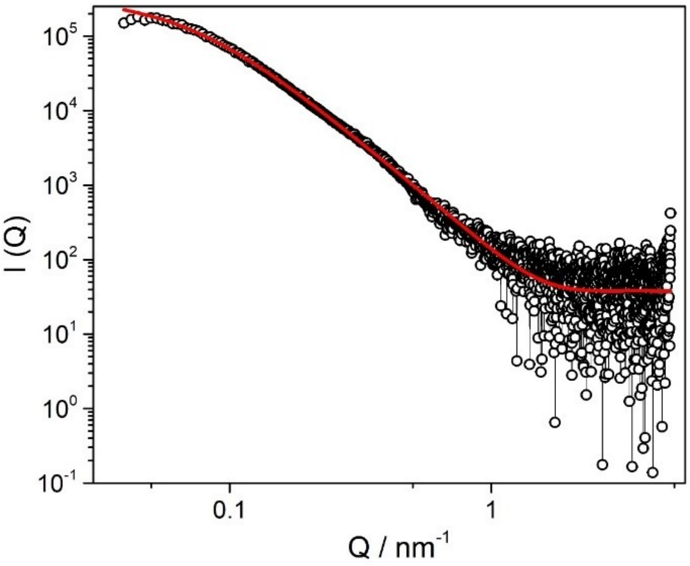

Figure S4.3.3. SAXS curve of P5-10 fitted with a sphere model form factor and a mass fractal structure factor.

(d) The SAXS curves for **P4-90** were fitted to the Pedersen-Gertenberg form factor. To account for the dispersity of the sample a Gaussian distribution model was used.

$$I\left(q, r_0, k, \rho_s, \rho_c, N_{agg}\right) = \int_0^\infty f(R, r_0, k)\, P_{mic}(q, R, R_g, \rho_s, \rho_c, N_{agg}, d)dR \tag{S7}$$

Where r_0 is the radius of the core, r_g is the radius of gyration of the chains, ρ_s is the excess scattering of the length of a block in the core, ρ_c is the excess scattering length of a block in the chains, N_{agg} is the aggregation number, and d is a parameter describing the penetration of chains into the core (no penetration is expressed as d≈1). Parameter d was not fixed due to the possibility of PAA chains penetrating the PHS core via hydrogen bond interactions. The form factor consists of a hard sphere with the scattering length of $\rho_s N_{agg}$ surrounded by N_{agg} Gaussian chains with an R_g. And it takes the following form

$$P_{mic}\left(q, R, r_g, \rho_s, \rho_c, N_{agg}, d\right) = N_{agg}^2 \rho_s^2 F_s(q, R) + N_{agg} \rho_c^2 F_c\left(q, r_g\right) +$$
$$N_{agg}\left(N_{agg} - 1\right)\rho_c^2 S_{cc}\left(q, R, r_g, d\right) + 2N_{agg}^2 \rho_s \rho_c S_{sc}\left(q, R, r_g, d\right) \tag{S8}$$

Functions stated in the form factor stand for self-correlation of the sphere (F_s (q, R)), self-correlation of the chains (F_c(q, r_g)), cross-correlation between the chains (S_{cc}(q, R, r_g, d)), and cross correlation between the sphere and the chains (S_{sc}(q, R, r_g, d)). They are given by the following equations

$$F_s(q,R) = 9\left[\frac{\sin(qR) - qR\cos(qR)}{(qR)^3}\right]^2 \tag{S9}$$

$$F_c(q,r_g) = 2\,\frac{\exp(-r_g^2 q^2) - 1 + r_g^2 q^2}{r_g^4 q^4} \tag{S10}$$

$$S_{cc}(q,R,R_g,d) = \left[\frac{1-\exp(-r_g^2 q^2)}{r_g^2 q^2}\right]^2 \left[\frac{\sin(qR+qdr_g)}{qR+qdr_g}\right]^2 \tag{S11}$$

$$S_{sc}(q,R,R_g,d) = 3\left[\frac{1-\exp(-r_g^2 q^2)}{r_g^2 q^2}\right]\left[\frac{\sin(qR)-qR\cos(qR)}{(qR)^3}\right]\left[\frac{\sin(qR+qdr_g)}{qR+qdr_g}\right] \tag{S12}$$

And the Gaussian distribution is given by

$$f(R,N,\sigma,R_0) = \frac{N}{c_{Gauss}}\,e^{-\frac{(R-R_0)^2}{2\sigma^2}} \tag{S13}$$

$$c_{Gauss} = \sqrt{\frac{\pi}{2}}\,\sigma\left(1 + erf\left(\frac{R_0}{\sqrt{2}\sigma}\right)\right) \tag{S14}$$

Table S4.3.5. Results obtained from fit of equation S5 to SAXS curves for P5-90

N_{agg}	***R_{core} (nm)***	***R_{core} (nm) (TEM)***	***R_g (nm)***	***d***	***σ***
504	7.8	7	27	0.95	10.5

Information obtained from dynamic light scattering

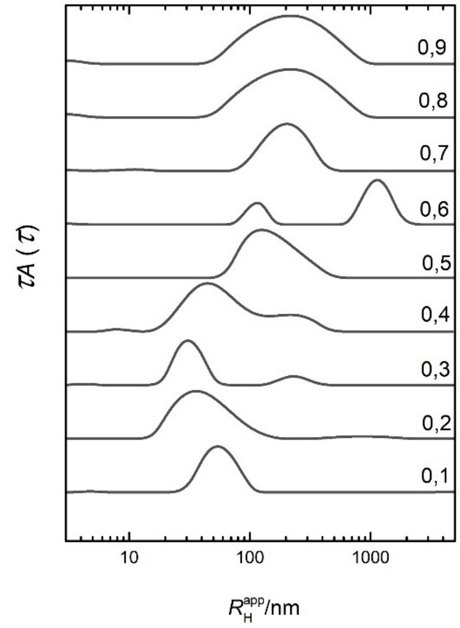

Figure S4.3.4. Hydrodynamic radii distribution of P5 polymer in THF-H_2O mixtures. Numbers to the right indicate the volumetric fraction of THF.

Table S4.3.6. Data obtained from DLS for polymer samples in aqueous solution.

Sample	R_H	PDI
PAA-b-PHS-b-PSC-10	58	0.110
PAA-b-PHS-b-PSC-50	101	0.113
PAA-b-PHS-b-PSC-90	73	0.207
PAA-b-PHS -90	116	0.120

Fluorescence

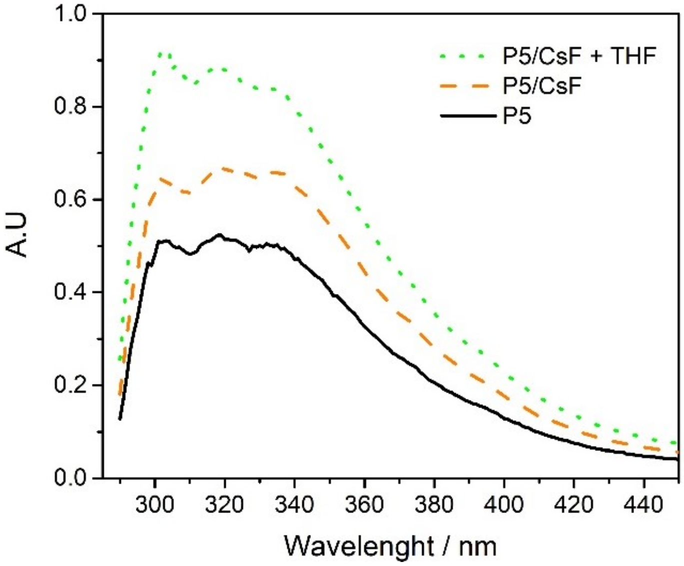

Figure S4.3.5. Fluorescence spectra of P5 micelles under different stimuli.

Cs^+ is an effective fluorescence quencher due to the heavy atom effect. Nonetheless it is necessary for it to come in close contact with the fluorescent compound, in our specific case the PHS block. Dynamic quenching experiments with heavy ions have shown that a polyelectrolyte shell around the micelles makes it is difficult for the quenching ions to access the core.[1,2]

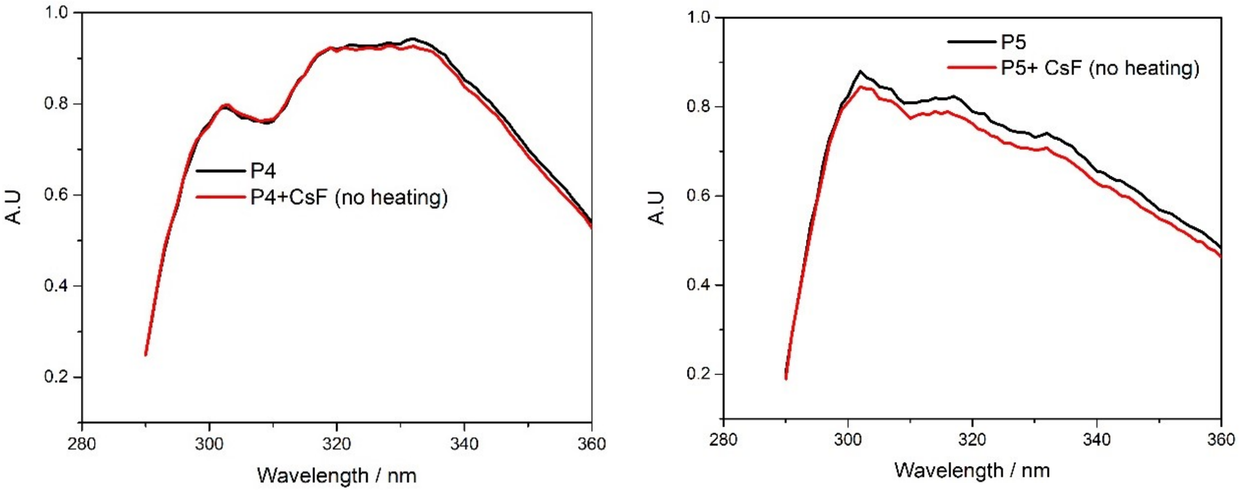

Figure S4.3.6. Fluorescence spectra of P5 micelles after exposure to CsF without heating (control experiments).

Extra images of Cryo-TEM

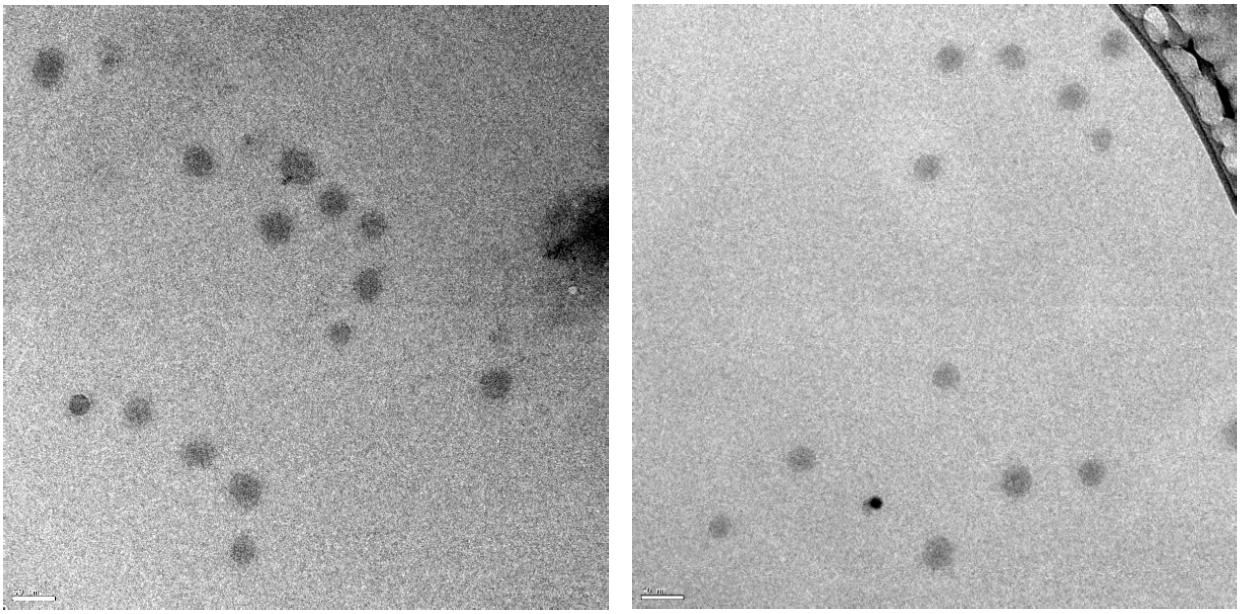

Figure S4.3.7. Cryo-TEM images of P5-10 micelles. Scale bar 100 nm.

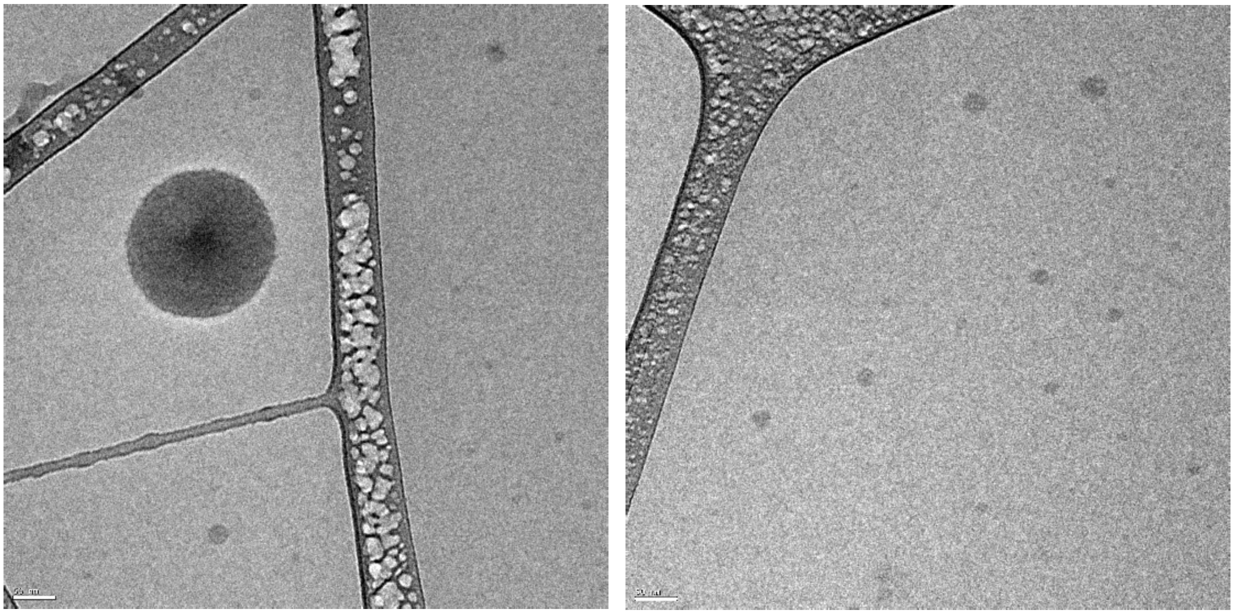

Figure S4.3.8. Cryo-TEM images of P5-50 micelles. Scale bar 100 nm.

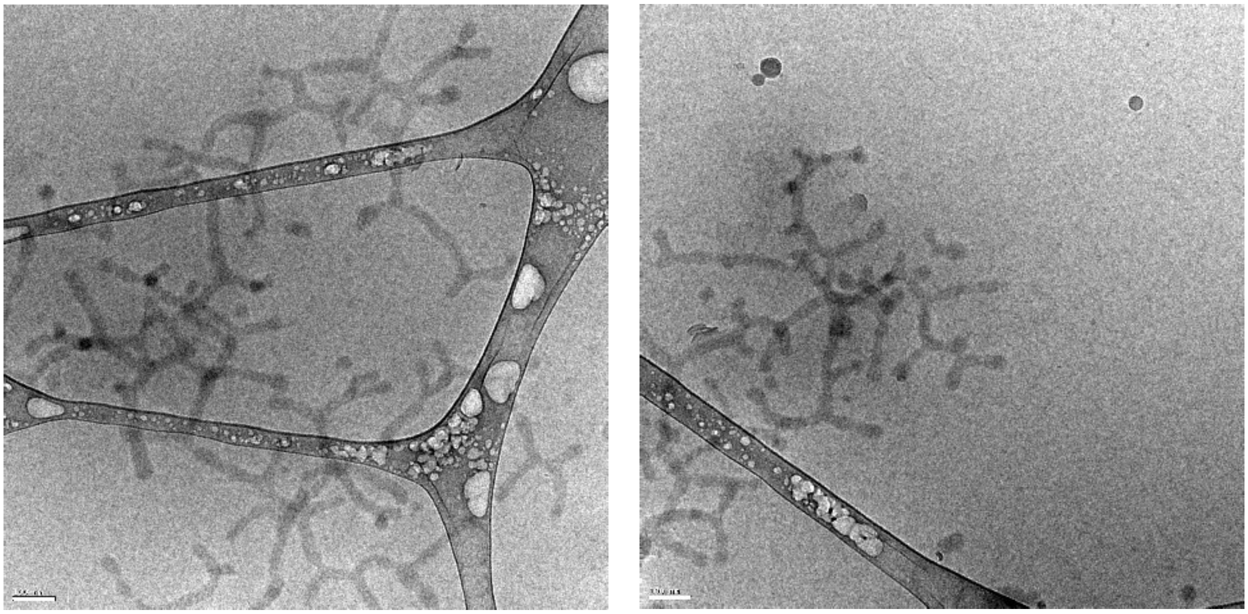

Figure S4.3.9. Cryo-TEM images of P5-90 micelles. Scale bar 100 nm.

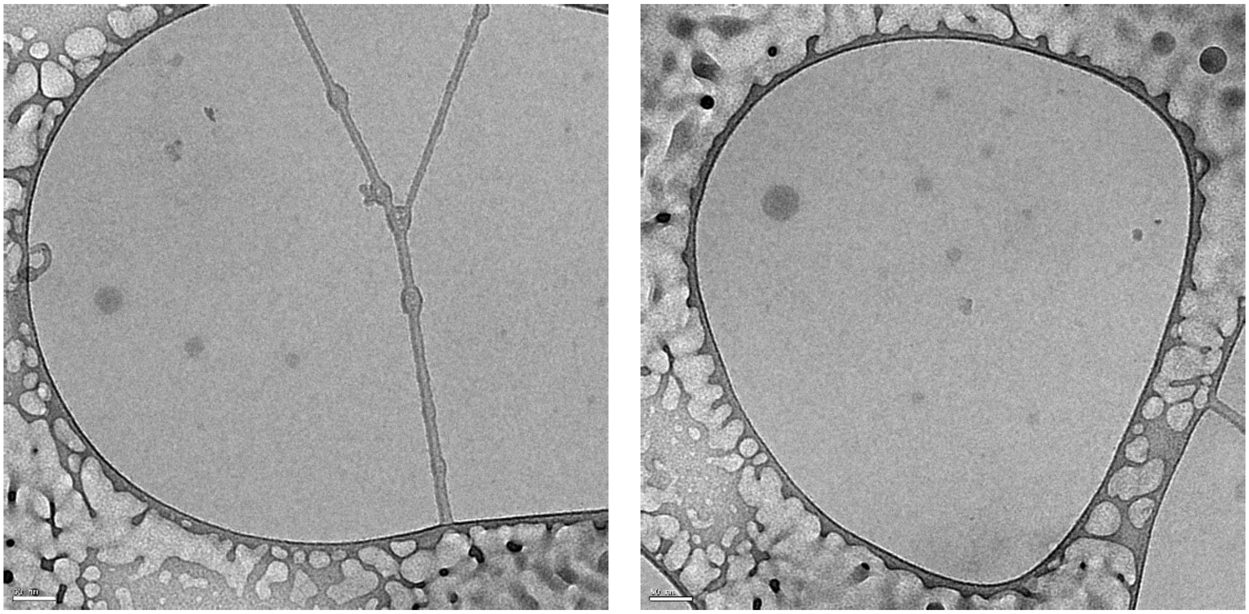

Figure S4.3.10. Cryo-TEM images of P4-90 micelles. Scale bar 100 nm.

References

(1) Blanazs, A.; Armes, S. P.; Ryan, A. J. Self-Assembled Block Copolymer Aggregates: From Micelles to Vesicles and Their Biological Applications. *Macromol. Rapid Commun.* **2009**, *30*, 267–277.

(2) Ludwigs, S.; Böker, A.; Voronov, A.; Rehse, N.; Magerle, R.; Krausch, G. Self-Assembly of Functional Nanostructures from ABC Triblock Copolymers. *Nat. Mater.* **2003**, *2*, 744–747.

(3) Cao, X.; Mao, W.; Mai, Y.; Han, L.; Che, S. Formation of Diverse Ordered Structures in ABC Triblock Terpolymer Templated Macroporous Silicas. *Macromolecules.* **2018**, *51*, 4381–4396.

(4) Verheyen, L.; Timmermans, B.; Koeckelberghs, G. Influence of the Sequence in Conjugated Triblock Copolymers on Their Aggregation Behavior. *Macromolecules.* **2018**, *51*, 6421–6429.

(5) Moughton, A. O.; Hillmyer, M. A.; Lodge, T. P. Multicompartment Block Polymer Micelles. *Macromolecules.* **2012**, *45*, 2–19.

(6) Moad, G.; Rizzardo, E.; Thang, S. H. Radical Addition-Fragmentation Chemistry in Polymer Synthesis. *Polymer.* **2008**, *49*, 1079–1131.

(7) Perrier, S. 50th Anniversary Perspective: RAFT Polymerization - A User Guide. *Macromolecules.* **2017**, *50*, 7433–7447.

(8) Skandalis, A.; Pispas, S. pH- and Thermo-Responsive Solution Behavior of Amphiphilic, Linear Triblock Terpolymers. *Polymer.* **2018**, *157*, 9–18.

(9) Skandalis, A.; Pispas, S. PDMAEMA-*b*-PLMA-*b*-POEGMA Triblock Terpolymers via RAFT Polymerization and Their Self-Assembly in Aqueous Solutions. *Polym. Chem.* **2017**, *8*, 4538–4547.

(10) Masalles, C.; Borrós, S.; Viñas, C.; Teixidor, F. Are Low-Coordinating Anions of Interest as Doping

Agents in Organic Conducting Polymers? *Adv. Mater.* **2000**, *12*, 1199–1202.

(11) Delman, A. D.; Kellyt, J. J.; Simms, B. B.; Naval, U. S. Thermal Stability of Structurally Related Polymers Containing Carborane and Phthalocyanine Groups. *J. Polym. Sci. Part A* **1970**, *8*, 111–123.

(12) Fox, M. A.; Wade, K. Model Compounds and Monomers for Phenylene Ether Carboranylene Ketone (PECK) Polymer Synthesis: Preparation and Characterization of Boron-Arylated Ortho-Carboranes Bearing Carboxyphenyl, Phenoxyphenyl or Benzoylphenyl Substituents. *J. Mater. Chem.* **2002**, *12*, 1301–1306.

(13) Yisgedu, T. B.; Chen, X.; Schricker, S.; Parquette, J.; Meyers, E. A.; Shore, S. G. Synthesis and Characterization of Homopolymers and Copolymers Containing *Closo*-$[B_{12}H_{12}]^{2-}$ Boron Cage Derivatives. *Chem. Eur. J.* **2009**, *15*, 2190–2199.

(14) Wee, K. R.; Cho, Y. J.; Jeong, S.; Kwon, S.; Lee, J. D.; Suh, I. H.; Kang, S. O. Carborane-Based Optoelectronically Active Organic Molecules: Wide Band Gap Host Materials for Blue Phosphorescence. *J. Am. Chem. Soc.* **2012**, *134*, 17982–17990.

(15) Ferrer-Ugalde, A.; González-Campo, A.; Viñas, C.; Rodríguez-Romero, J.; Santillan, R.; Farfán, N.; Sillanpää, R.; Sousa-Pedrares, A.; Núñez, R.; Teixidor, F. Fluorescence of New O-Carborane Compounds with Different Fluorophores: Can It Be Tuned? *Chem. Eur. J.* **2014**, *20* , 9940–9951.

(16) Núñez, R.; Romero, I.; Teixidor, F.; Viñas, C. Icosahedral Boron Clusters: A Perfect Tool for the Enhancement of Polymer Features. *Chem. Soc. Rev.* **2016**, *45*, 5147–5173.

(17) Bellomo, C.; Chaari, M.; Cabrera-González, J.; Blangetti, M.; Lombardi, C.; Deagostino, A.; Viñas, C.; Nerea Gaztelumendi, N.; Nogués, C.; Nuñez, R.; Prandi, C. Carborane-BODIPY Dyads: New Photoluminescent Materials Through an Efficient Heck Coupling. *Chem. Eur. J.* **2018**, *24*, 15622–15630.

(18) Chaari, M.; Kelemen, Z.; Planas, J. G.; Teixidor, F.; Choquesillo-Lazarte, D.; Ben Salah, A.; Viñas, C.; Núñez, R. Photoluminescence in *m* -Carborane–anthracene Triads: A Combined Experimental and Computational Study. *J. Mater. Chem. C.* **2018**, *6*, 11336–11347.

(19) Mukherjee, S.; Thilagar, P. Boron Clusters in Luminescent Materials. *Chem. Commun.* **2016**, *52*, 1070–1093.

(20) Valliant, J. F.; Guenther, K. J.; King, A. S.; Morel, P.; Schaffer, P.; Sogbein, O. O.; Stephenson, K. A. The Medicinal Chemistry of Carboranes. *Coord. Chem. Rev.* **2002**, *232*, 173–230.

(21) Park, M. H.; Lee, K. M.; Kim, T.; Do, Y.; Lee, M. H. Ortho-Carborane-Functionalized Luminescent Polyethylene: Potential Chemodosimeter for the Sensing of Nucleophilic Anions. *Chem. Asian J.* **2011**, *6*, 1362–1366.

(22) Eo, M.; Park, M. H.; Kim, T.; Do, Y.; Lee, M. H. Polynorbornene Copolymers with Pendent O-Carborane and Carbazole Groups: Novel Side-Chain Donor-Acceptor Copolymers for Turn-on Sensing of Nucleophilic Anions. *Polymer.* **2013**, *54*, 6321–6328.

(23) Vancoillie, G.; Hoogenboom, R. Synthesis and Polymerization of Boronic Acid Containing Monomers. *Polymer Chemistry*. **2016**, *7*, 5484–5495.

(24) Yin, X.; Guo, F.; Lalancette, R. A.; Jäkle, F. Luminescent Main-Chain Organoborane Polymers: Highly Robust, Electron-Deficient Poly(Oligothiophene Borane)s via Stille Coupling Polymerization. *Macromolecules* **2016**, *49*, 537–546.

(25) Adachi, Y.; Ooyama, Y.; Ren, Y.; Yin, X.; Jäkle, F.; Ohshita, J. Hybrid Conjugated Polymers with Alternating Dithienosilole or Dithienogermole and Tricoordinate Boron Units. *Polym. Chem.* **2018**, *9*, 291–299.

(26) Sun, G.; Cui, H.; Lin, L. Y.; Lee, N. S.; Yang, C.; Neumann, W. L.; Freskos, J. N.; Shieh, J. J.; Dorshow, R. B.; Wooley, K. L. Multicompartment Polymer Nanostructures with Ratiometric Dual-Emission PH-Sensitivity. *J. Am. Chem. Soc.* **2011**, *133*, 8534–8543.

(27) Grimm, O.; Schacher, F. H. Dual Stimuli-Responsive P(NIPAAm-Co-SPA) Copolymers: Synthesis and Response in Solution and in Films. *Polymers.* **2018**, *10*, 645..

(28) Salgarella, A. R.; Zahoranová, A.; Šrámková, P.; Majerčíková, M.; Pavlova, E.; Luxenhofer, R.; Kronek, J.; Lacík, I.; Ricotti, L. Investigation of Drug Release Modulation from Poly(2-Oxazoline) Micelles through Ultrasound. *Sci. Rep.* **2018**, *8*, 1–13.

(29) Yinghuai, Z.; Peng, A. T.; Carpenter, K.; Maguire, J. A.; Hosmane, N. S.; Takagaki, M. Substituted Carborane-Appended Water-Soluble Single-Wall Carbon Nanotubes: New Approach to Boron Neutron Capture Therapy Drug Delivery. *J. Am. Chem. Soc.* **2005**, *127*, 9875–9880.

(30) González-Campo, A.; Ferrer-Ugalde, A.; Viñas, C.; Teixidor, F.; Sillanpää, R.; Rodríguez-Romero, J.; Santillan, R.; Farfán, N.; Núñez, R. A Versatile Methodology for the Controlled Synthesis of Photoluminescent High-Boron-Content Dendrimers. *Chem. Eur. J.* **2013**, *19*, 6299–6312.

(31) Cabrera-González, J.; Ferrer-Ugalde, A.; Bhattacharyya, S.; Chaari, M.; Teixidor, F.; Gierschner, J.; Núñez, R. Fluorescent Carborane-Vinylstilbene Functionalised Octasilsesquioxanes: Synthesis, Structural, Thermal and Photophysical Properties. *J. Mater. Chem. C.* **2017**, *5*, 10211–10219.

(32) Löbling, T. I.; Ikkala, O.; Gröschel, A. H.; Müller, A. H. E. Controlling Multicompartment Morphologies Using Solvent Conditions and Chemical Modification. *ACS Macro Lett.* **2016**, *5*, 1044–1048.

(33) Walther, A.; Goldmann, A. S.; Yelamanchili, R. S.; Drechsler, M.; Schmalz, H.; Eisenberg, A.; Müller, A. H. E. Multiple Morphologies, Phase Transitions, and Cross-Linking of Crew-Cut Aggregates of Polybutadiene-Block-Poly(2-Vinylpyridine) Diblock Copolymers. *Macromolecules* **2008**, *41*, 3254–3260.

(34) Mai, Y.; Eisenberg, A. Self-Assembly of Block Copolymers. *Chem. Soc. Rev.* **2012**, *41*, 5969–5985.

(35) Meng, F. T.; Ma, G. H.; Qiu, W.; Su, Z. G. W/O/W Double Emulsion Technique Using Ethyl Acetate as Organic Solvent: Effects of Its Diffusion Rate on the Characteristics of Microparticles. *J. Control. Release* **2003**, *91*, 407–416.

(36) Flanagin, L. W.; McAdams, C. L.; Hinsberg, W. D.; Sanchez, I. C.; Willson, C. G. Mechanism of Phenolic Polymer Dissolution: Importance of Acid-Base Equilibria. *Macromolecules* **1999**, *32*, 5337–5343.

(37) Himuro, S. Fluorescence and Viscometry Studies of Poly(4-Hydroxystyrene) in Solution. *Polym. J.* **1993**, *25*, 1223–1228.

References for supporting information

(1) Štépanek, M.; Procházka, K. Fluorometric Studies of the Polyelectrolyte Shell of Block Copolymer Micelles in Aqueous Media. *Langmuir* **1999,** *15,* 8800-8806.

(2) Krijtová, K.; Štépanek, M.; Procházka, K.; Webber, S. E. Fluorescence Study of the Core/Shell Interface in Polyelectrolyte Micelles. Binding of Fluorescent Surfactants in the Interfacial Region. *J Fluoresc.* **1998,** *8,* 21-25.

4.4- Publication IV

Interactions of star-like polyelectrolyte micelles with hydrophobic Counterions*

Abstract

Hydrophobicity of a counterion has a profound effect on the interaction with polyelectrolytes similar to that of multivalency. Specifically, understanding this interaction in weak polyelectrolyte micelles might assist in developing nanocarriers for pH-controlled encapsulation and release. We used star-like weak polyelectrolyte micelles of polystyrene-block-poly(2-vinyl pyridine) (PS-P2VP) with fixed aggregation number as a model polyelectrolyte, and cobalt bis(1,2-dicarbollide) (COSAN) as a model hydrophobic anion. We used NMR to assess the mobility of the polymer segments in the presence of varying amounts of COSAN, and at varying protonation degrees of the polyelectrolyte. Same experiments with indifferent electrolyte (NaCl) were used as a control. Furthermore, we used coarse-grained simulations to obtain a detailed picture of the effect of hydrophobic counterions on the conformation of the micelles. A small amount of hydrophobic counterions causes morphological changes within the micelles, whereas a bigger amount causes precipitation. This was confirmed both in simulations and in experiments. Furthermore, adsorption of the counterions induces ionization of the collapsed segments of the polyelectrolyte. Although the COSAN/P2VP system is rather specific, the generic model used in the coarse-grained simulations shows that the observed behavior is a consequence of synergy of hydrophobic and electrostatic attraction between polyelectrolytes and hydrophobic counterions. Our study provides general insights into the molecular mechanisms of these interactions.

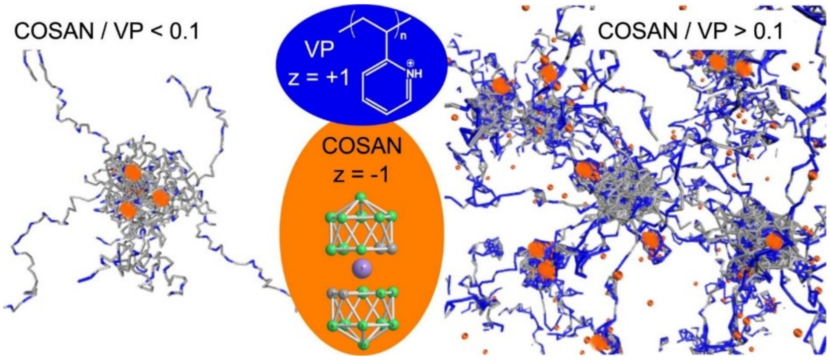

*Version presented here has small format modifications compared to the original form at: Interactions of star-like polyelectrolyte micelles with hydrophobic counterions. Fernandez-Alvarez, R.; Nová, L.; Uhlík, F.; Kereïche, S.; Uchman, M.; Košovan, P.; Matějíček, P. J. Colloid Interface Sci. 546 (2019) 371–380.

Introduction

Hydrophobic interactions play an important role in self organization behavior of soft matter systems. Most synthetic polymers are hydrophobic, and the role of polymer hydrophobicity in the self-organization process can be considered well understood. However, much less attention has been paid to the hydrophobicity of low-molecular solutes [1], despite its importance in targeted drug delivery and controlled release applications. Even though the total amount of solute may be rather low, it can significantly alter the polymer solubility. In this work we specifically address the interaction of a charged hydrophobic solute with an oppositely charged polymer (polyelectrolyte). The influence of combined electrostatic and hydrophobic interaction on the overall behavior can be assessed using an analogy with the properties of hydrophobic polyelectrolytes, amphiphilic and hydrophobic ions, and multivalent counterions.

The interplay of hydrophobicity and electrostatic interactions in polyelectrolytes leads to the formation of intra-molecular nanostructures, such as pearl-necklaces in linear polymers [2–6], core-shell structures in star-like polyelectrolytes [7,8], or bundles of chains in polyelectrolyte brushes [9,10]. The short-ranged hydrophobic attraction between the repetitive units favors dense collapsed structures, whereas the long-ranged electrostatic repulsion favors expanded conformations. The role of counter-ions (small ions with opposite charge to that of the polyelectrolyte) is often neglected in this qualitative description. In the absence of specific interactions, indifferent monovalent counterions are preferentially located near the polyelectrolyte [11–13].

Multivalent cations have a stronger tendency to associate with polyelectrolytes because they lose the same amount of entropy but gain several times the electrostatic energy as compared to the monovalent ones [14–18]. Therefore, the addition of multivalent counterions triggers collapse of polyelectrolytes, and this effect is particularly strong in star-like polyelectrolytes, polyelectrolyte brushes or polyelectrolyte hydrogels [14–18]. In addition to causing the brush collapse, the adsorption of multivalent cations induces further ionization of the weak acid groups of the polyelectrolyte [18,19].

If the counterions are hydrophobic, then their interaction with polyelectrolytes is affected by hydrophobicity in a similar manner as it is affected by valency. For example, self-assembly of miktoarm star polyelectrolytes can be modified by replacing iodide counterions with triiodide [20]. Although both are monovalent, the hydrophobic triiodide triggers morphological transitions in the self-assembly that are not observed with iodide. The same effect was successfully used to trigger and govern the resulting assembled structure of block copolymers due to the addition of organic counterions with varying degree of hydrophobicity, and in combination with solvent mixing [21–25]. Although there is a clear experimental evidence that hydrophobic counterions strongly affect behavior of polyelectrolytes, a systematic investigation of this effect, similar to what has been done for hydrophobic solutes in neutral hydrogels [26], still seems to be lacking.

The interaction of hydrophobic counterions with polyelectrolytes should qualitatively resemble the effect of multivalent counterions because both hydrophobicity and multivalency provide an additional polymer-solute attraction, although by different mechanisms. It can be seen on the example of trivalent counterions causing a partial collapse and bundling of chains in spherical polyelectrolyte brushes [27]. Similar morphologies have been observed in hydrophobic star-like polyelectrolytes and polyelectrolyte brushes [28,9]. Understanding these effects is necessary to maximize drug loading into nanostructures containing polyelectrolytes and to potentiate their use as drug delivery vectors [29].

However, there is a lack of understanding of the specific effect of hydrophobic counterions on the structure. The synergistic use of experiments and simulations provides a means to obtain such understanding.

Charged surfactants introduce another function to the library of aforementioned interactions: due to the asymmetry in molecular structure, these amphiphilic ions self-assemble to micelles. Hydrophobic tails are hidden inside the micelle, and the charged heads are exposed on its surface, such that overall the micelle appears as a hydrophilic charged sphere. Therefore, micelles were called colloidal ions in the early days of polymer science [30]. Micellization occurs not only in water but also inside the polyelectrolyte-surfactant complexes leading to hierarchical self-assembly [31–33]. Diverse morphologies and nanostructures such as pearl-necklaces, spheres-in-spheres, etc. have been obtained by mixing of polyelectrolytes with oppositely charged surfactants [32,34–36]. This diversity of structures is due to the unique combination of multivalency, hydrophobicity and amphiphilicity of the surfactant micelles.

The hydrophobic counterion used in our experiments, is the [3,30-cobalt(III) bis(1,2-dicarbollide)](-1) anion, COSAN. It belongs to metallacarboranes [37–40] and consists of two nido-clusters that complex the cobalt cation between them, as an analogy to ferrocene [41]. In contrast with metallocenes, COSAN is chemically stable and water soluble [38]. Despite its solubility, water molecules form patchy network around the COSAN cluster, pointing to a rather hydrophobic character of boron cluster compounds [42]. The peculiar structure of COSAN is expressed by intrinsically amphiphilic and superchaotropic behavior in water [43,44]. However, in contrast with ionic surfactants which consist of a charged hydrophilic head and a hydrophobic tail, the amphiphilicity of COSAN does not stem from strong asymmetry in distribution of charge and polarity within the molecule. COSAN, its derivatives and analogs are used in applications as viral enzymes inhibitors [45,46] or agents in radioactive ion extraction [47,48].

COSAN combines both electrostatic and hydrophobic solute-polymer interactions and seems to be a suitable model to investigate generic features of such a system. It possesses peculiar interactions with both charged and neutral polymers. The presence of slightly hydridic B-H vertices in COSAN clusters enables them to form so-called dihydrogen bonds with C-H units of biomolecules and other compounds such as poly(ethylene oxide), PEO [49,50,43,51–53]. Electrostatic interactions of COSAN with polymers have been previously studied in our group in systems containing poly(4-vinylpyridine) and poly(2-

vinylpyridine) [52,54]. In this work we decided to omit peculiarities of COSAN, generalize its specific interactions by an effective attraction, and consider COSAN as a suitable prototype of a hydrophobic anion.

It is noteworthy that in theory and simulations, the term hydrophobicity is used as a generic term that describes an effective (non-electrostatic) attraction which favors monomer-monomer or monomer-solute interactions over interactions with solvent. In a real system, this effective attraction may be caused by various mechanisms, such as the formation of hydrogen bonds or unfavorable interactions with water molecules which disrupt the local water structure. Depending on the actual mechanism of the interaction, one can distinguish hydrophobic, superhydrophobic, kosmotropic and chaotropic molecules. In here, we will use the term hydrophobicity in the generic sense, irrespective of the detailed mechanism of the interaction with solvent.

In the current study, we investigated the interaction of COSAN with P2VP as a model system of a hydrophobic counterion interacting with a weak, moderately hydrophobic polyelectrolyte. We used polystyrene-block-poly(2-vinyl pyridine), PS-P2VP, block copolymer that forms star-like micelles with a kinetically frozen PS core and a P2VP shell in HCl solutions. Combining experiments and simulations, we showed that the hydrophobic interactions between the polymer and its counterions lead to non-trivial and unexpected effects. We used a generic simulation model of a hydrophobic weak polyelectrolyte interacting with hydrophobic counterions to show that the observed effects are not specific to the COSAN-P2VP system but they are more generic, and should be observed in any system of a polyelectrolyte with hydrophobic counterions. The advantage of using PS-P2VP micelles is that well-defined PS-P2VP copolymers are readily available, and we have experience with these systems from our previous studies on polycationic micelles. The advantage of using COSAN as a model hydrophobic anion stems from its evenly distributed charge and hydrophobicity, and compact shape. Unlike asymmetric ionic surfactants, its interaction with polyelectrolytes does not compete with self-association, and its hydrophobicity is directly exposed to the polyelectrolyte. In addition, encapsulation of the COSAN anion is interesting for its potential applications in extraction and drug-delivery.

Materials and methods

2.1. Materials

Polystyrene-block-poly(2-vinylpyridine), PS-P2VP, block copolymer was purchased from Polymer source, Inc. (Dorval, Quebec, Canada). The copolymer characterization provided by manufacturer is as follows: PS245-P2VP224, M_w(PS-P2VP) = 49000 g/mol, w_{PS} = 0.52, Đ = 1.05. Caesium [cobalt(III) bis(1,2-dicarbollide)], Cs[COSAN], was purchased from KatChem Ltd., Czech Republic. It was subsequently transformed to sodium salt, $NaCOSAN \cdot 4H_2O$, using an extraction procedure previously described [55]. NaCl was acquired from Sigma-Aldrich and used as received. All experiments involving polymer solutions were performed at polymer concentration 2 mg/ml unless indicated otherwise. All COSAN solutions were prepared by weighting and dissolving in Milli-Q water. Deuterium chloride (DCl 20% in D_2O) was purchased from Chemotrade (Leipzig, Germany).

2.2. Methods

2.2.1. Dynamic and Static Light Scattering (DLS, SLS)

The light scattering setup (ALV, Langen, Germany) consisted of a 22 mW He-Ne laser (λ= 632.8 nm), an ALV-CGS/8F goniometer, an ALV High QE APD detector, and an ALV 50004, multibit, multitau autocorrelator. The measurements were carried out at 296 K for scattering angles ranging from 30° to 150° corresponding in aqueous solutions to scattering vector magnitudes ranging from 6.8 to 25.6 µm. DLS data analysis was performed by fitting the measured normalized time autocorrelation function of the scattered light intensity using the constrained regularization algorithm (CONTIN), which provides the distribution of relaxation times $\tau(A)\tau$. Effective angle- and concentration-dependent hydrodynamic radii, R_H (c, q), were obtained from the mean values of relaxation times, τ_m(q, c), of individual diffusive modes using the Stokes-Einstein equation. To obtain the true hydrodynamic radii, the data has been extrapolated to a zero scattering angle and diminishing concentration.

2.2.2. Electrophoretic light scattering

The measurements were carried out with Nano-ZS Zetasizer (Malvern Instruments, UK). Zeta-Potential values were calculated from electrophoretic mobilities (averages of 15–100 measurements) using the Henri equation in the Smoluchowski approximation.

2.2.3. ^{1}H NMR characterization

^{1}H NMR spectra were measured on a Varian UNITYINOVA 400 in deuterium chloride (99.5%, Chemotrade, Leipzig, Germany). Spectra were referenced to the solvent signal (4.80 ppm).

2.2.4. Cryo-Transmission Electron Microscopy (Cryo-TEM)

Cryo-TEM was used to characterize the structure of the nanoparticle in solution. The samples for Cryo-TEM were prepared as described earlier [56]. A 3 µl drop of the sample solution was applied to an electron microscopy grid with carbon-covered polymer supporting film (lacey-carbon grids LC200-CuC, Electron Microscopy Sciences), glow discharged for 30 s with 5 mA current. Most of the sample was removed by blotting (Whatman No. 1 Filter paper) for 1 s, and the grid was immediately plunged into liquid ethane held at -183 °C. The sample was then transferred without rewarming into a Tecnai Sphera G20 electron microscope (FEI, Hillsboro, OR) using a Gatan 626 cryo-specimen holder (Gatan Inc., Pleasanton, CA). Images were recorded at 120 kV accelerating voltage and microscope magnifications ranging from 5000x to 14500x using a Gatan UltrScan 1000 slow scan CCD camera (giving a final pixel size from 2 to 0:7 nm). The applied underfocus typically ranged between 1.5 and 2.7 nm. The applied blotting conditions resulted in the specimen thickness varying between 100 and 300 nm.

2.3. Coarse-grained simulations

Here, we provide just a brief description of the simulated systems. For additional technical details of the simulation setup and the simulation protocol, please refer to ESI. We used coarse-grained bead-spring model of a polymer in implicit solvent which is treated as structureless continuum characterized by the dielectric constant. Unless stated otherwise, we represented the star-like P2VP micelles as star-like polyelectrolytes with f= 20 arms, each N= 50 segments long, abbreviated as 20 x 50. We simulated smaller stars than those used in experiments because simulating stars of the same size would be unfeasible. For similar reasons, we set the monomer concentration c_{pol} = 0:01 mol/L, which is slightly lower than in the experiments. In addition to the polyelectrolyte, small ions were present, same as in the experiment: OH^- ions generated by the polymer ionization reaction, salt ions Na^+; Cl^-, and $COSAN^-$. The amount of additional salt ions is characterized by the ratio of salt ion pairs (Na^+Cl^- or Na^+COSAN^-) to the number of monomers of the polymer, denoted by n. For simplicity, all particles (monomer units of the polymer and all small ions) were represented as spheres of the same effective radius. However, they differ by charge, hydrophobicity, and chemical identity which determines their participation in the ionization reaction. Polymer connectivity is represented using the harmonic potential. Steric repulsion between all pairs of particles is represented by the same soft potential, as we used in previous publications [57]. Hydrophobic interactions are represented by adding an attractive potential of the same functional form as the steric repulsion, but with other set of parameters, same as we used in the model of hydrophobic star-like polyelectrolytes [7]. We quantify hydrophobicity by the parameter, τ, where the value of τ_p = 0:07 for the polymer corresponds to theta state. In the current simulation we make the polymer moderately hydrophobic by setting τ_p= 0:1. To represent the hydrophobic COSAN, we set τ_s= 0:3 solute-solute interactions. To represent indifferent (hydrophilic) solutes and small ions, we set τ_s= 0 which is equivalent to completely removing the attractive part of the potential. For polymer-solute interactions we apply the Lorentz-Berthelot combination rules by setting $\tau_{sp} = \sqrt{\tau_s \tau_p}$. We represent electrostatic interactions by the Coulomb potential, and evaluate it using the Ewald summation. To represent aqueous solutions at ambient conditions, we set the Bjerrum length to l_B= 0:7 nm.

All segments of the simulated polyelectrolyte are treated as weak bases, characterized by the basicity constant KB, i.e., equilibrium constant of the dissociation reaction

$M + (H_2O) \leftrightarrow MH^+ + OH^-$

where M stands for the monomer unit of the polymer, and (H2O) denotes the water molecule which is not explicitly simulated because we used implicit solvent. The reaction was simulated using the reaction ensemble method [58]. We varied the polymer basicity constant KB such that we obtained the whole range of the available ionization degrees of the polymer, $0 < \alpha < 1$. Note that both degree of ionization and pH are outputs of the reaction ensemble simulation, whereas the ionization constant, KB is the input. We calculate the pH by measuring the concentration of OH^- ions, and using the relation pH= pK_w - pOH. In further discussion, we use the acidity constant of conjugate acid, pKA= pK_w - pK_B, in order to conveniently express the ionization of the polyelectrolyte as a function of pH - pKA. For a more detailed discussion of the ionization reaction, please refer to ESI, and to the recent review by Landsgesell et al. [59].

Results

3.1. Stability of PS-P2VP micelles in the presence of COSAN

The PS-P2VP micelles formed a core-shell structure with a frozen PS core, and a corona composed of protonated and nonprotonated P2VP segments (see full characterization in Experimental section and in ESI: Fig. S1 and Table S1). The micellar core is kinetically frozen and relatively small because the core-forming PS block has high glass transition temperature [60]. Therefore, we describe the PS-P2VP block copolymer micelles in aqueous HCl solutions as star-like micelles with a fixed number of arms. The degree of protonation of the P2VP chain varies with pH and affects the size and the stability of the micelles in solution. At low pH (pH≤2) the electrostatic repulsion between the highly charged P2VP chains leads to the swelling of the micellar shell that prevents the aggregation of the micelles. As pH increases, the degree of protonation decreases, and a part of P2VP chains collapses, forming an inner layer around the PS-core. In addition to this, the hydrophobicity of non-protonated P2VP in water causes precipitation of the micelles at pH above 4.8 [61,62]. The addition of an indifferent salt, such as NaCl, to the micellar dispersion leads to a slight decrease of the hydrodynamic radius and zeta potential of the micelles. This decrease is a consequence of electrostatic screening by the added salt and it is well understood [63,64].

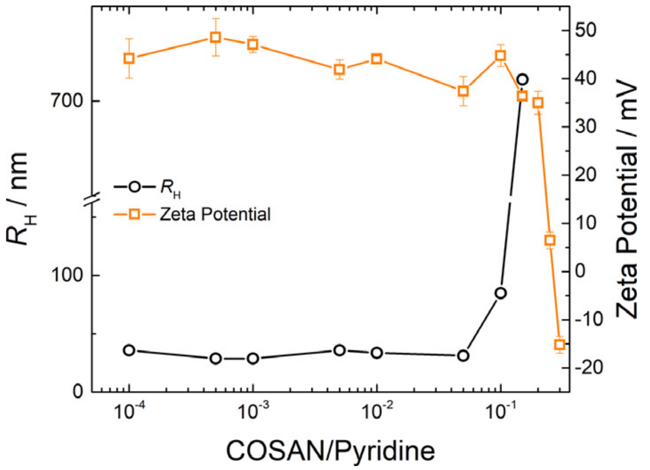

Fig. 4.4.1. The dependence of Zeta potential and hydrodynamic radius, R_H, of PS-P2VP micelles on COSAN/pyridine ratio (ξ) at p*H* 2.

In contrast to the negligible effect of indifferent NaCl, the stepwise addition of Na[COSAN] to the PS-P2VP star-like micelles resulted in aggregation at the molar ratio of COSAN to P2VP segments $\xi > 0.1$. Orange color of the precipitate evidenced complex formation between COSAN and PS-P2VP micelles. Due to kinetically frozen PS cores, the aggregation number of micelles did not change upon COSAN addition. The precipitate consists of individual micelles with collapsed P2VP/COSAN shells. This effect was observed both, at high protonation state of the micelles (p*H* = 0.3), and at low protonation state (p*H* = 2). Fig. 4.4.1 shows that up to $\xi \approx 0.1$, the addition of COSAN has almost no effect on both hydrodynamic radius of the micelles, R_H, and their zeta potential, ζ, in the low ionic strength regime (p*H* = 2). The high value of $\zeta \approx +50$ mV at $\xi < 0.1$ confirms that high surface charge of the micelles provides the electrostatic repulsion which prevents precipitation. The zeta potential could not be measured at p*H* = 0.3 because of high ionic strength which resulted in electrolysis. At $\xi \approx 0.1$ an abrupt increase of R_H, and concomitant decrease of ζ to -10 mV, indicates aggregation. We observed a similar behavior with several types of micelles with PS-core and PVP corona differing in size and architecture of block copolymer (linear and starlike). Always, R_H remained constant within the experimental uncertainty up to a specific value of ξ. Then the sample became turbid and R_H increased abruptly.

The intriguing question is what makes the interaction of PS-P2VP micelles with COSAN anion so much different from their interaction with indifferent chloride anions. In here, features of COSAN, such as amphiphilic nature and B-H dihydrogen bonding with C-H of polymers, might be the cause of the specific effects. Regardless of pH, these interactions might cause binding of COSAN to all monomer units of the micelle, including neutral and charged P2VP, as we schematically illustrate in Fig. 4.4.2. This type of interaction was observed in COSAN complexes with uncharged poly(ethylene oxide) [43,51–53] and poly(2-alkyl-2-oxazolines) [65,66]. Nevertheless, it remains an open question whether the amphiphilic nature of COSAN can explain the abrupt aggregation of the star-like micelles with increasing amount of COSAN at various levels of initial P2VP ionization, determined by the solution pH.

In order to study the impact of kinetics on the precipitation process, we changed the type of mixing experiment from direct stepwise addition to dialysis of COSAN through the dialysis bag filled with the PS-P2VP dispersion. This guaranteed a slow formation of the COSAN-P2VP complex, and suppressed the influence of kinetics on the complex formation. COSAN was added to the dialysis bath in the amount exceeding the precipitation threshold ($\xi = 1$). In the low ionization regime (pH = 2), we obtained surprisingly stable PS-P2VP/COSAN dispersions. The sample produced a completely flat NMR spectrum suggesting that all P2VP segments are in contact with COSAN and the entire micelle is in a kinetically frozen state. In contrast, a precipitant was produced in the high ionization regime ($\xi = 1$, pH = 0.3). As we demonstrate in the next sections, this occurred because highly ionized P2VP arms are prone to formation of interconnected structures that eventually lead to precipitation in the presence of COSAN. In contrast, the micelles with partly ionized shell accumulate COSAN inside the compact particles that are most likely in kinetically frozen state, and they are prevented from precipitation by kinetic and surface effects.

The morphology of PS-P2VP and PS-P2VP/COSAN micelles is further evidenced by cryo-TEM micrographs in Fig. 4.4.3. They show that individual spherical micelles exist in solution before addition of COSAN (Fig. .4.3, $\xi = 0$), and the micelle size is nearly unchanged upon COSAN addition close to the aggregation limit (Fig. 4.4.3, $\xi = 0.08$). Due to the low contrast of ionized parts of P2VP shell, only compact compartments such as PS core and collapsed P2VP domains are visualized. Thus, regular distances between PS cores of pure PS-P2VP micelles indicate hindrance between highly ionized P2VP arms. In contrast, the PS-P2VP/COSAN particles are located close to each other because the P2VP shell is collapsed, and direct contact of particles is not hindered. The cryo-TEM micrographs of the kinetically frozen nanoparticles above the aggregation limit (Fig. 4.4.3, $\xi = 1$, pH = 2) showed compact spherical particles similar to those at other n values, but with the presence of fused micelles. Their structure and COSAN loading should be almost the same, since they differ only in procedure of preparation. The fused micelles with partly merged P2VP/COSAN domains but with separated PS cores can be seen as prolonged particles, for example in the bottom-left part of Fig. 4.4.3c.

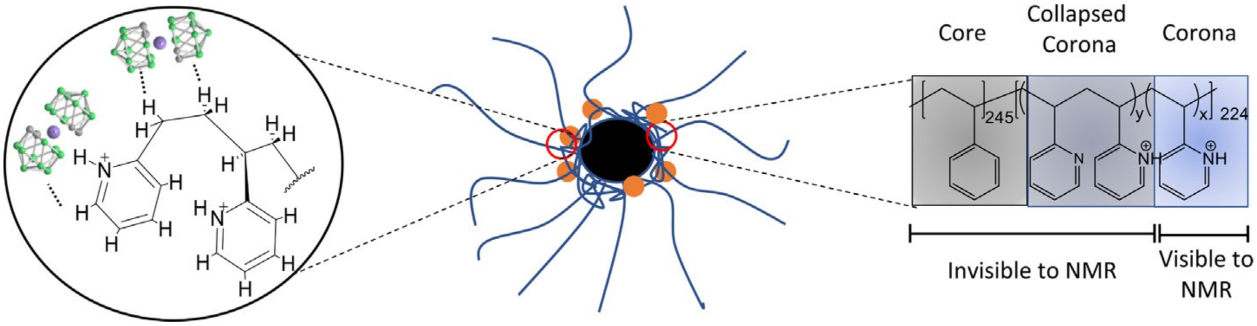

Fig. 4.4.2. Schematic representation of PS-P2VP micelles (PS-core in black, and P2VP shell in blue) and their interaction with COSAN (points in orange). Possible interaction of COSAN clusters with polymer backbone via dihydrogen bonding and with positive charge via electrostatic interaction is shown on left. Chemical structures of PS-P2VP segments in core, collapsed corona and corona as well as segments that are detectable and non-detectable in NMR spectrum is shown on right.

3.2. Simulations of weak PE stars with hydrophobic counterions

To better understand the role of hydrophobic interactions of COSAN with PS-P2VP star-like micelles we performed coarse grained simulations of a generic model of a weak star polyelectrolyte interacting with hydrophobic counterions. In Fig. 4.4.4a we show that the addition of a hydrophobic counterion to the star has little effect on the radius of gyration, R_g, at $\xi << 1$. Further addition of the hydrophobic counterion induces collapse of the star at $\xi \approx 0.1$. With single star in our simulation this collapse is seen as a decrease of R_g whereas in a macroscopic system it would lead to aggregation. Therefore, precipitation an increase in Rg were observed upon the addition of COSAN to the PS-P2VP stars. In contrast, Fig. 4.4.4b shows that the addition of indifferent counterions has very weak effect on Rg of the star in the same range of n, similar to the weak effect of NaCl on PS-P2VP star-like micelles.

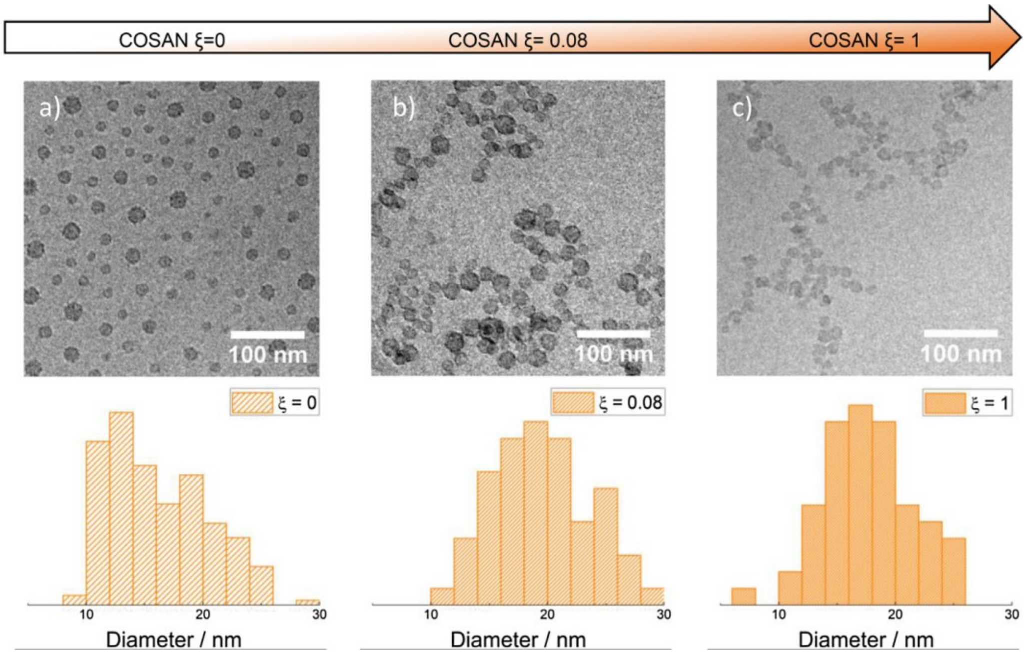

Fig. 4.4.3. Cryo-TEM images of PS-P2VP micelles (a) without COSAN, (b) after COSAN addition (ξ = 0.08), and (c) after dialysis with COSAN (ξ = 1.00) at pH 2. Scale bar 100 nm. Only PS core and collapsed P2VP domains are visible because the ionized P2VP shell swollen by water has low contrast. Size distribution of corresponding individual micelles shown below micrographs. Fused micelles were not included to analysis.

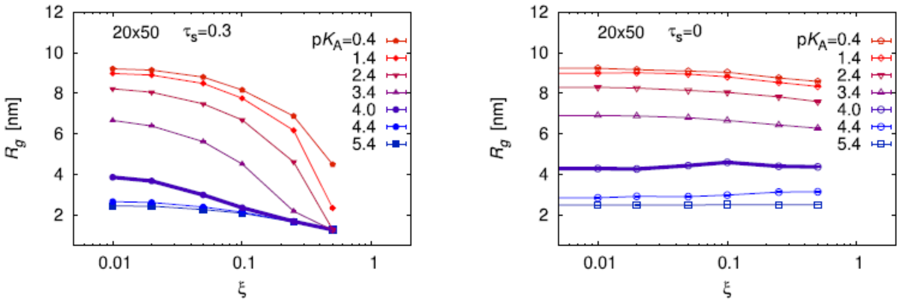

(a) Hydrophobic counterions, $\tau_s = 0.3$ (b) Indifferent counterions, $\tau_s = 0$

Fig. 4.4.4. Radius of gyration of the star, R_g , as a function of the charge ratio n for various ionization constants of the polymer, pK_A, comparing the indifferent counterions with τ_s = 0.0 and hydrophobic counterions with τ_s = 0.3 for stars with *f* = 20 arms and *N* = 50 segments per arm (20 x 50). Corresponding data for smaller stars 10 x 20 and abroader range of hydrophobicities are shown in Fig. S4.4.12.

Fig. 4.4.4a also shows that the highly ionized stars undergo a more abrupt collapse than the low-ionized ones. These changes can be observed also in simulation snapshots in Figs. S4.4.3 and S4.4.4 in ESI. This demonstrates that additional effects show up when ionization equilibrium of the polymer is considered.

In simulations, the ionization is conveniently controlled by varying pK_A, whereas in experiments it is more conveniently controlled by varying the pH. Although the 2-vinyl pyridine monomer is a rather strong base with $pK_A° = 4.92$ ($pK_B° = 9.02$), the star-like P2VP may not be fully ionized even at pH ≤ $pK_A°$. This is evidenced by titration curves of our model stars (Figs. S9 and S15 in ESI), showing that the effective pK_A is shifted by almost two units with respect to $pK_A°$ of the monomer. This effect has been reported in our earlier studies [67] and is also known from self-consistent field calculations [13] and from experiments [68].

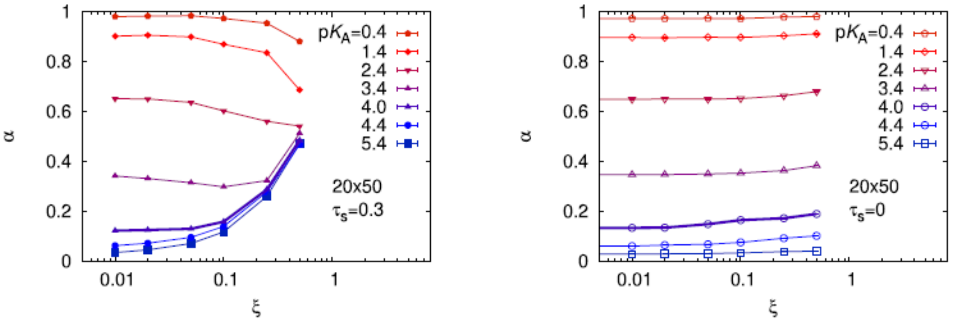

(a) Hydrophobic counterions, $\tau_s = 0.3$ (b) Indifferent counterions, $\tau_s = 0$

Fig. 4.4.5. Degree of ionization, α, as a function of the charge ratio n for various ionization constants of the polymer, pK_A, comparing the indifferent counterions with $\tau_s = 0.0$ and hydrophobic counterions with $\tau_s = 0.3$ for stars with *f* = 20 arms and *N* = 50 segments per arm (20 x 50). Corresponding data for smaller stars 10 x 20 and a broader range of hydrophobicities are provided in Fig. S4.4.13.

In addition to the shift in pK_A, the titration curves (Figs. S4.4.9 and S15 in the ESI) reveal that the addition of indifferent electrolyte, such as NaCl, has only marginal effect on polymer ionization, whereas the addition of hydrophobic counterions, such as COSAN, leads to a much more complex behavior. This is best seen in Fig. 4.4.5 where we plot the degree of ionization as a function of ξ. In Fig. 4.4.5a we observe that the addition of hydrophobic counterions decreases the polymer ionization at $pK_A° \le 4$, when the pure polymer is highly ionized. In contrast, the addition of hydrophobic counterions increases the polymer ionization at $pK_A° \ge 4$, when ionization degree of the pure polymer is a $\alpha \le 0.5$.

The effect of hydrophobic counterions on the polyelectrolyte morphology and ionization can be inferred from simulation snapshots in Fig. 4.4.6, showing the star with $pK_A = 4$. With indifferent counterions, the star forms a core-shell morphology, similar to the morphology observed in simulations of hydrophobic weak polyelectrolyte stars [7,8]. Some arms form the collapsed nonionized hydrophobic core, the others form the stretched and fully ionized shell. The core-shell morphology is rather insensitive to the amount of indifferent counterions. When hydrophobic counterions are added to the star, they accumulate in the core. At low ξ = 0:01, the core-shell structure is almost unaffected. At a higher ξ = 0:05, more arms are absorbed in the core while the others still remain stretched. Eventually, at ξ = 0:5 all arms collapse, forming a single globule.

As soon as the globule loses its ionized shell, it is no longer protected against aggregation with other globules. Such situation leads to aggregation of stars and macroscopic precipitation. The transition from the stretched arms through core-shell structure to collapsed globule can be quantified by the probability distribution of end-to-end distances of individual star arms, shown in ESI, Fig. S4.4.7. The bimodal distribution of R_e at low ξ = 0.01 has one peak at short distances, which correspond to collapsed arms, and second peak at long distances, which correspond to the stretched arms. With increasing ξ, the second peak gradually disappears as hydrophobic counterions accumulate near the core and induce collapse of additional arms. In contrast, the R_e distribution with indifferent counterions remains bimodal at any value of ξ.

The distribution of counterions depends on their hydrophobicity and is quantified in radial density profiles, shown Figs. S5 and S6 in ESI. We observe that the hydrophobic counterions are found almost exclusively in the core, and their density drops to zero in the region of stretched arms. Conversely, the density profile of indifferent counterions mirrors that of the charged segments and extends beyond the length of the arms. Comparing the density profiles of hydrophobic counterions and charged P2VP segments, we note that the counterions neutralize the charge in the core. In addition, in Figs. S5 and S6 we observe that the hydrophobic counterions induce higher ionization in the core, while they have very weak effect on ionization of the stretched parts of the arms.

Interestingly, the addition of hydrophobic counterions leads to different structure in the highly ionized stars than in the less ionized ones. While the highly ionized stars shrink with increasing ξ (Fig. 4.4.4), their degree of ionization decreases (Fig. 4.4.5). Here, the high charge of the star prevents the collapse of the core because the hydrophobic counterions cannot neutralize it sufficiently. A decrease in ionization decreases the energetic barrier to the collapse. However, at a certain n the star stops accumulating counterions in the core, and forms pearls at arm ends instead, as seen in Fig. 4.4.7. It is noteworthy that similar pearls appear as intermediate structures during equilibration also in systems with lower ionization. It cannot be ruled out that the pearls correspond to metastable structures, and they would eventually disappear also in systems with high ionization. But they are certainly more stable and persist over much longer time scales than in other cases.

The pearls at arm ends, seen in Fig. 4.4.7, could be stabilized if several stars come into contact. In such case, the other star provides additional polymer segments, such that a bigger and more stable pearl can be formed. Eventually, this should lead to aggregation of the stars, precipitation, and formation of a loose gel-like network.

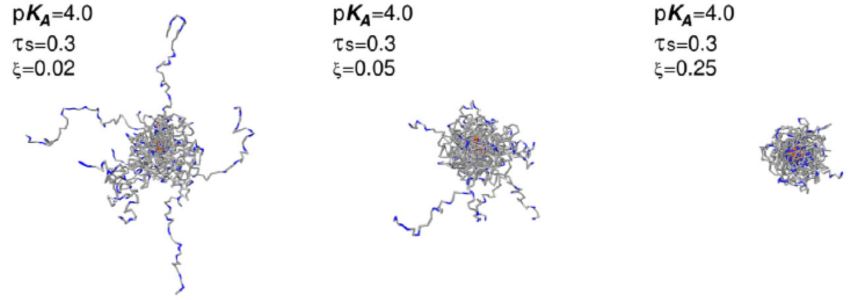

(a) Hydrophobic counterions, $\tau_\mathrm{s} = 0.3$

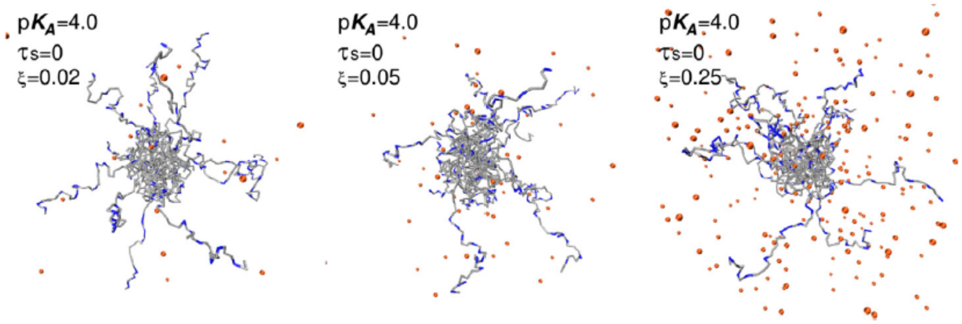

(b) Indifferent counterions, $\tau_\mathrm{s} = 0$

Fig. 4.4.6. Simulation snapshots of 20 x 50 stars with hydrophobic counterions (τ_s = 0.3, top) and hydrophilic counterions (τ_s = 0, bottom) at pK= = 4 and $\xi \in \{0.02, 0.05, 0.25\}$ from left to right. Additional data corresponding to smaller stars (10 x 20) and a broader range of pK_A values is shown in Figs. S4.4.10 and S4.4.11. Color code: grey = neutral polymer segments; blue = ionized segments; orange = solute anions with adjustable hydrophobicity τ_s; H^+ and Na^+ cations are not displayed for the sake of simplicity.

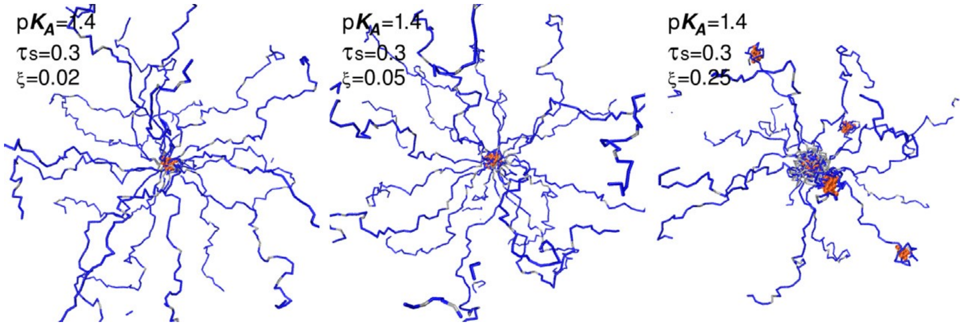

Fig. 4.4.7. Simulation snapshots of 20 50 stars with hydrophobic counterions (τ_s = 0.3, bottom) at pK_A = 1.4 at high values of $\xi \in \{0.02, 0.05, 0.25\}$ from left to right. Color code: grey = neutral polymer segments; blue = ionized segments; orange = solute anions with adjustable hydrophobicity τ_s; H^+ and Na^+ cations are not displayed for the sake of simplicity. Density profiles corresponding to the snapshots are shown in Figs. S4.4.5 and S4.4.6.

To investigate this possibility, we performed a series of simulations with five stars in the simulation box. Indeed, we observed that arms from different stars merge into one pearl. However, the simulations of such a big system became prohibitively slow and it is difficult to tell whether we observed equilibrium or just a metastable transition regime.

The presented simulations hint towards two possible mechanisms of precipitation of weak star-like polyelectrolytes upon addition of hydrophobic counterions. Both mechanisms undergo a similar process at low n where the counterions accumulate in the center of the star, trigger the collapse of its central part, and induce higher ionization of segments in this region. At higher ξ, the pathways differ depending on the ionization degree of the star. If the star is not fully ionized, then a sufficient amount of hydrophobic counterions make it collapse to a globule which is nearly charge neutral, and therefore it becomes insoluble. If the star is fully ionized, then the high ionization prevents further collapse of the star with increasing ξ, causing that the additional counterions accumulate in pearls at arm ends. These pearls then merge with arm ends of other stars, forming an interconnected network. Unfortunately, simulations of sufficiently big systems to study the aggregation mechanism are prohibitively slow and computationally expensive. Therefore, we can only extrapolate the information obtained from simulations of several stars in the box.

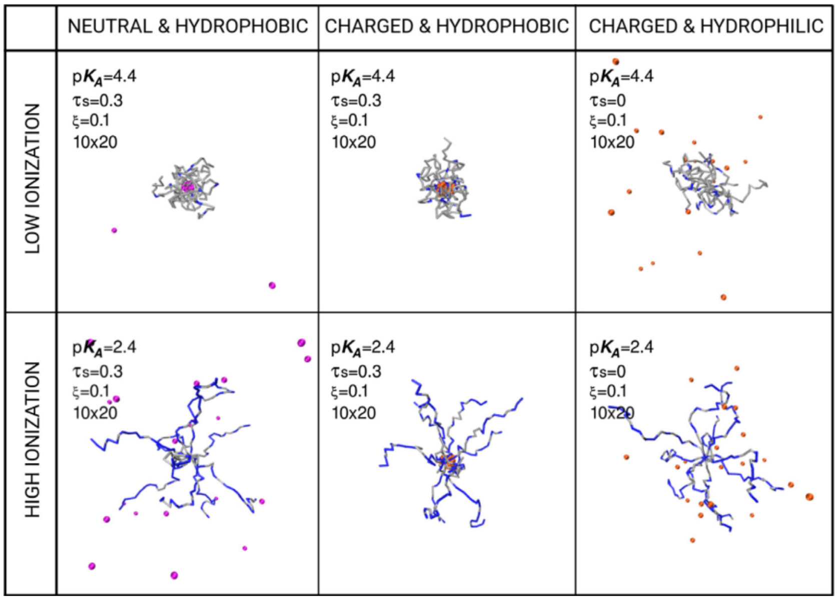

Fig. 4.4.8. Simulation snapshots of 10 x 20 stars with various solutes at low ionization degrees, α ≈ 0.1 (top), and at high ionization degrees, α ≈ 0.5 (bottom). Left: neutral hydrophobic solutes, middle: charged hydrophobic solutes (counterions), right: charged hydrophilic solutes (counterions). Color code: grey = neutral polymer segments; blue = ionized segments; orange = hydrophilic or hydrophobic counterions with hydrophobicity determined by ss; magenta = hydrophobic neutral solutes; H^+ and Na^+cations are not displayed for the sake of simplicity.

Finally, it is important to recognize that the peculiar interaction of hydrophobic counterions with polyelectrolytes is a synergistic effect of hydrophobic and electrostatic attraction. Absence of one of these interactions results in a qualitatively different behavior. To demonstrate this, we performed an additional set of simulations of 10 x 20 stars at high and low ionization degrees, interacting with neutral hydrophobic solutes. We compared them with charged hydrophobic solutes (counterions), and with charged hydrophilic solutes (counterions). In the simulation snapshots in Fig. 4.4.8 we observe that only charged hydrophobic solutes adsorb in the stars at any ionization of the polymer. The neutral hydrophobic solutes adsorb in the stars only at low ionization, when collapsed polymer domains are already present. A similar effect was observed in experiments with hydrophobic pyrene probes interacting with polyelectrolyte micelles with PS core: the pyrene accumulates in the hydrophobic domains (collapsed core and polyelectrolyte shell) irrespective of the ionization degree of the polymer [69]. Because the simulated star polymer lacks the collapsed PS core, neutral hydrophobic solutes do not adsorb at high polymer ionization because the hydrophobic attraction alone is not sufficient to trigger a collapse of the central part of the star. On the other hand, charged hydrophilic counterions accumulate inside the star much less than the hydrophobic ones. Also the electrostatic interaction alone is not sufficient to trigger a collapse of the central part of the star, as it is in the case of charged hydrophobic solutes (counterions), as we have seen in the experiments where COSAN was replaced by NaCl. This demonstrates that the synergy of hydrophobic and electrostatic attraction between the polymer and counterions leads to qualitatively new effects which are not observed if one of these interactions is absent.

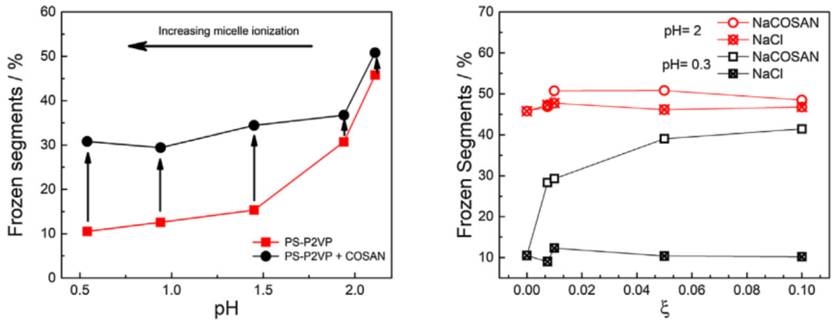

(a) (b)

Fig. 4.4.9. (a) Fraction of frozen P2VP-segments in the PS-P2VP micelles at various pH before and after the addition of COSAN. (b) Control experiment assessing the effect of NaCl on frozen P2VP-segments in comparison to COSAN at pH = 2 and pH = 0.3. Frozen segment percentage was obtained via H NMR.

3.3. Experimental evidence of varying ionization and domain formation

NMR spectra of the PS-P2VP micelles, shown in ESI, Fig. S4.4.2, revealed information about the amount of protonated P2VP segments, and about the amount of mobile P2VP segments. The signal from the protons in P2VP aromatic ring was used to track changes in the mobility of polymer segments (see Experimental Section in ESI for details of the analysis). Fig. 4.4.9a shows changes in frozen segments with addition of COSAN at different p*H*. Above p*H* ≈ 1.5 the fraction of frozen segments in the pure polymer increases significantly, corroborating the core-shell picture of the partly ionized hydrophobic star obtained from the simulations. In such case, the addition of COSAN has no effect on the fraction of frozen segments because it can adsorb in the already collapsed, hydrophobic P2VP domains. In contrast, the addition of hydrophobic counterions to the highly ionized stars causes large changes in the number of frozen segments that presumably form collapsed domains observed in the simulations. Furthermore, no signal of COSAN was detected, confirming the assumption that all COSAN clusters are embedded within the PS-P2VP micelles.

Finally, to support the findings of simulations we used the NMR measurements to compare the effect of COSAN to that of NaCl (Fig. 4.4.9b). At pH = 0.3 the number of frozen segments increases upon addition of COSAN from 10% to about 40%, indicating that the hydrophobic counterion induces the formation of collapsed domains in the P2VP stars. In contrast, the addition of NaCl has no effect on the number of frozen segments at neither of the tested pH values (0.3 or 2.0). Therefore, we conclude that the variation of ionic strength cannot induce the collapse, and the counterion induced collapse is indeed due to hydrophobicity of COSAN. Presumably, segments in the collapsed parts of shell get ionized to compensate the accumulated charge, similar to what we observed in simulations of less ionized stars with hydrophobic counterions. It is noteworthy that even though the amount of added COSAN corresponds to only 5% of the total P2VP segments, yet it immobilizes many more segments, hinting to a COSAN:P2VP segment ratio greater than 1:1, as we demonstrated in previous work [52].

Conclusions

Hydrophobic ions combine two fundamental features: electrostatic interaction and hydrophobic attraction of diverse origin. We studied and described on molecular level the impact of hydrophobic counterions on star-like polyelectrolyte micelles with fixed number of arms that has been hardly explored [1,70]. In contrast to previous studies, where the focus of the work was only to trigger morphology changes [20] or to prepare hybrid nanostructures via specific solute/polymer interaction [32,43,71], here we focused on generalizing the microphase behavior of star-like polyelectrolytes in the presence of hydrophobic counterions with respect to polyelectrolyte ionization. This was achieved using a concerted combination of computer simulations and experiments. As a model system, we chose the cobalt sandwich (COSAN) anions, as hydrophobic anion, and polycationic star-like micelles with kinetically frozen cores formed by poly(styrene)-b-poly(2-vinylpyridine) (PS-P2VP) [43,52].We observed that a gradual addition of COSAN causes precipitation of star-like micelles above COSAN-to-P2VP segment ratio $\xi > 0{:}05$, independent of the level of ionization of the micelle. Conversely, the addition of indifferent electrolyte (NaCl) did not cause such changes. Therefore, we ascribed the effect to the hydrophobic character of COSAN leading to its affinity to P2VP. Coarse grained simulations determined that hydrophobic counterions change the ionization profile of star-like micelles and induce the formation of compact domains within the stars. Furthermore, by studying the model system at both low and high ionization regime we determined differences in the precipitation mechanism. When the star is less ionized, hydrophobic counterions accumulate near the core and induce further ionization of the collapsed polymer segments. Increasing accumulation of counterions causes the collapse of the star to a single globule. In contrast, when the star is fully ionized, the accumulation in the core is followed by the formation of pearls which connect different stars to form an infinite gel network. The formation of collapsed domains due to hydrophobic counterions was confirmed by analyzing the fraction of immobilized segments through NMR. Interestingly, the maximum capacity of loading the micelles with COSAN was almost the same, independent of the mechanism which ultimately leads to destabilization of the corona, and to precipitation of the micelles. This is presumably a consequence of charge regulation in the polyelectrolyte corona, induced by the COSAN accumulation. The insights provided by our investigations extend beyond the model system that we have used. A similar effect of synergy between electrostatic and hydrophobic attraction should be seen in various systems for pH controlled targeted drug delivery and controlled release applications, which employ solubilization of hydrophobic ionic solutes in polyelectrolyte-based nanostructures.

Acknowledgment

We would like to thank Jani Seitonen and Janne Ruokolainen for preliminary cryo-TEM micrographs. PM and RFA acknowledge financial support of the Czech Science Foundation, grant 17-00648S; PK and LN acknowledge the Czech Science Foundation, grant 17-02411Y; MU and SK acknowledge the Czech Science Foundation, grant 17-00289Y. This research was supported by the Ministry of Education, Youth and Sports (CUCAM CZ.02.1.01/0.0/0.0/15_003/0000417). LN acknowledges the support by Charles University Research Centre program No. UNCE/SCI/014. Computational resources were provided by the CESNET LM2015042 and the CERIT Scientific Cloud LM2015085, provided under the program ‘‘Projects of Large Research, Development, and Innovations Infrastructures”.

Supporting Information

I. DETAILED EXPERIMENTAL CHARACTERIZATION

A. Micelles preparation and characterization

PS-b-P2VP self-assembled micelles were obtained by dissolving a carefully weighted amount of solid PS245-P2VP224 (10 mg, in 1,4-Dixoane (5 ml)). Afterwards, methanol was added dropwise until 90% v/v of Dioxane was obtained. All samples had a final concentration of 2 mg ml^{-1}. These solutions were further modified by adding HCl solution (0.01 M, 2.5 ml) dropwise (0.5 ml min^{-1}) with automatic injector under constant agitation. After 10 min the samples were dialyzed against HCl solution (0.01 M) for 30 h changing dialysis bath several times to ensure the complete removal of organic solvents. The PS-PVP/COSAN was prepared by step-wise addition of Na[COSAN] stock solution into PS-PVP solution in HCl. The amount of

COSAN was expressed as COSAN to PVP segment ratio ξ. The refractive index increment, *dn*/*dc* = 0.260 mL/g was calculated from literature data from PS and PVP. The SLS data for PS-PVP in 0.01 M HCL were treated by the standard Zimm method. It provides the following molar mass for PS-PVP micelles M_w(mic) = 25x10^6g/mol).

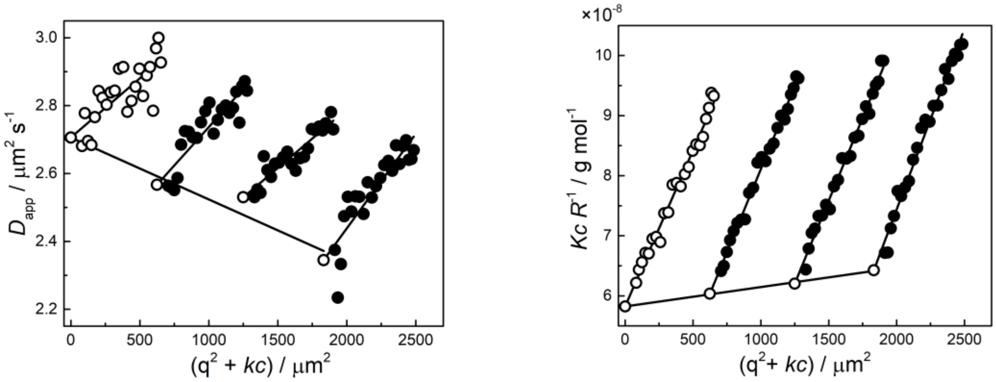

(a) Dynamic Zimm plot (b) Zimm plot

FIG. S4.4.1: Dynamic and static Zimm plots of PS-PVP micelles in HCl aqueous solution at pH=2.

TABLE S4.4.1: Properties of the PS-PVP micelles obtained from dynamic and static Zimm plots in Fig. S4.4.1a

Sample	R_H (nm)	R_g (nm)	M_w^{mic} (g/mol)	N_{agg}
PS-PVP	84	52	25 x 10^6	510

B. NMR characterization of PS-PVP and PS-PVP/COSAN

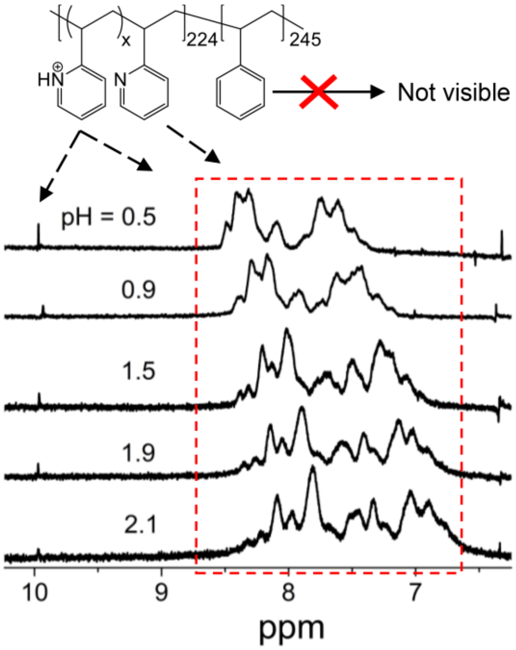

FIG. S4.4.2: NMR spectra of PS-P2VP micelles (without COSAN) at various pH. The peak around 9.8 ppm corresponds to H^+ on the protonated NH^+ group of the pyridine, and the peak around 8.5ppm corresponds to the aromatic ring of the protonated form. Both these peaks vanish with increasing pH. The peaks around 7.8 ppm and 7.0 ppm correspond to the deprotonated form. These peaks are absent at low pH and increase in intensity with increasing pH. In addition, the last two peaks slightly drift with varying pH.

1. NMR visible signal analysis

First, a known volume of PS-P2VP micellar solution with a known concentration was added into a NMR tube. A known amount of internal standard (*t*-butanol), was added and all signals normalized to its value. With the internal standard, a theoretical signal intensity for PS-P2VP was determined using the polymer concentration and the units of PVP per polymer chain. The number of visible segments refers to the parts of PVP that are not collapsed. This experiment was carried out for different pH values (0.2-2).

2. Frozen segment analysis

Frozen segment percentage was calculated by comparing ^{1}H-NMR signals before and after COSAN addition. NMR signal is decreased and broadened if the mobility of the corresponding moiety is reduced due complex formation, in this case with COSAN. Measurements were done as following, ^{1}H-NMR spectra was acquired for a solution of pure micelles in DCl at high polymer concentration (> 4mg ml^{-1}) with an internal standard (t-butanol). Afterwards, a determined amount of COSAN was added and left to rest for 1h before acquiring the new spectra. Signals were normalized to *t*-BuOH signal, and ratios before and after COSAN addition were used to calculate the frozen segment. The ^{1}H-NMR signals analyzed for the PS-PVP micelles were “Backbone" (2.8 and 2.1 ppm) and “Aromatic" (8.6 - 6.6 ppm). The later corresponds to both the protonated and non-protonated PVP segments of the micellar shell. The spectrum is too fuzzy to assign individual peaks due to the atactic character of PS-PVP block copolymer. However, the integral of signal intensity in this ppm range can be used to quantify the fraction of "frozen" PVP segments.

II. SIMULATION MODEL AND METHOD

A. Details of the coarse grained model

All particles are represented as spheres of the same effective radius, σ= 0.41 nm. By choosing the simulation box size L = 22.43nm and σ= 0:41nm we fix the molar concentration of polymer segments in our model. The concentration of P2VP used in the experiment, c_{pol}= 2 mg/mL, corresponds to c_{pol} = 0.02 mol/L concentration of monomer units. Such concentration would be too close to overlap concentration for the smaller stars used in the simulation. Therefore, we simulated them at a slightly lower concentration c_{pol} = 0.01 mol/L.

Polymer connectivity is represented using the harmonic potential with the spring constant k= $10k_{\mathrm{B}}T\sigma^2$, and the minimum at r= 1.0σ. Steric repulsion between all pairs of particles is represented by a soft repulsive potential:

$$U_{steric}(r;\ \epsilon, c) = \epsilon k_B T \frac{(r-c)^2}{r^2} for\ r < c \tag{S1}$$

and $U_{\mathrm{steric}}(r;\ \epsilon;\ c)$= 0 for $r > c$, where we set ϵ= 1.5, c = 2. Hydrophobic interactions are represented by adding the potential U_{phobic}= $-U_{\mathrm{steric}}(r;\ \epsilon;\ 2c)$. The hydrophobicity parameter τ defines the strength of hydrophobic attraction. The value τ= 0 (no hydrophobicity) is used for all small ions except COSAN. The value of τ_{p} = 0.07 for polymer-polymer interactions corresponds to the theta state. In the current simulation we make the polymer moderately hydrophobic by setting τ_{p}= 0.1. For solute-solute interactions we set τ_{s} = 0.3 for hydrophobic solute representing COSAN. For polymer-solute interactions we apply the Lorentz-Berthelot combination rules by setting $\tau_{\mathrm{sp}} = \sqrt{\tau_s\, \tau_p}$.

Electrostatic interactions are represented by the Coulomb potential

$$U_{coulomb\ i,j} = k_B T z_i z_j e^2 \frac{l_B}{r} \tag{S2}$$

Where l_{B} = 0.715nm is the Bjerrum length in water at ambient conditions, e is the elementary charge, and z_{i} is the valency of ion i. We evaluated the electrostatic interactions using the Ewald summation.

B. Simulation method and simulation protocol

We used our in-house implementation of Hamiltonian Monte Carlo (HMC) in the reaction ensemble, same as in our previous studies [1, 2]. In each HMC step we randomly select to perform a conformational move or a reaction move. In the conformational move we combine Monte Carlo (MC) with molecular dynamics

(MD) in the following way: We let the system evolve according to Newton equations of motion for 50-time steps. The time-step-length varies during one HMC step, which ensures higher Monte Carlo acceptance rate. In the beginning of each HMC step, the time-step-length is set 0.05. Then, the actual time-step-length value is divided by 2 in randomly selected MD steps.

The final configuration of the MD evolution is accepted or rejected using the Metropolis criterion. In the reaction move we choose with equal probabilities the forward or reverse direction of the reaction

$$\mathrm{M} + (\mathrm{H_2O}) \leftrightarrow \mathrm{MH}^{+} + \mathrm{OH}^{-} \tag{S3}$$

In the forward direction, the chemical identity of the monomer M is to M^{+}, and an oppositely charged counterion OH^{-} is created. In the reverse direction, the counterion is deleted, and the monomer chemical identity is changed from M^{-} back to M. Because we use the implicit solvent representation, no explicit water molecules are created or deleted in the actual reaction move. The reaction is accepted or rejected using the criterion due to Smith and Tříska [3].

First 20% of the simulation was discarded as equilibration. The productive run typically produced about 103 uncorrelated samples of R_{g}, which was the slowest evolving quantity. We used the method of Wolff [4] to estimate the statistical error of the simulated quantities, corrected for correlation between individual samples.

III. SIMULATION RESULTS FOR THE 20X50 STAR ARCHITECTURE

A. Simulation snapshots for the 20x50 star architecture

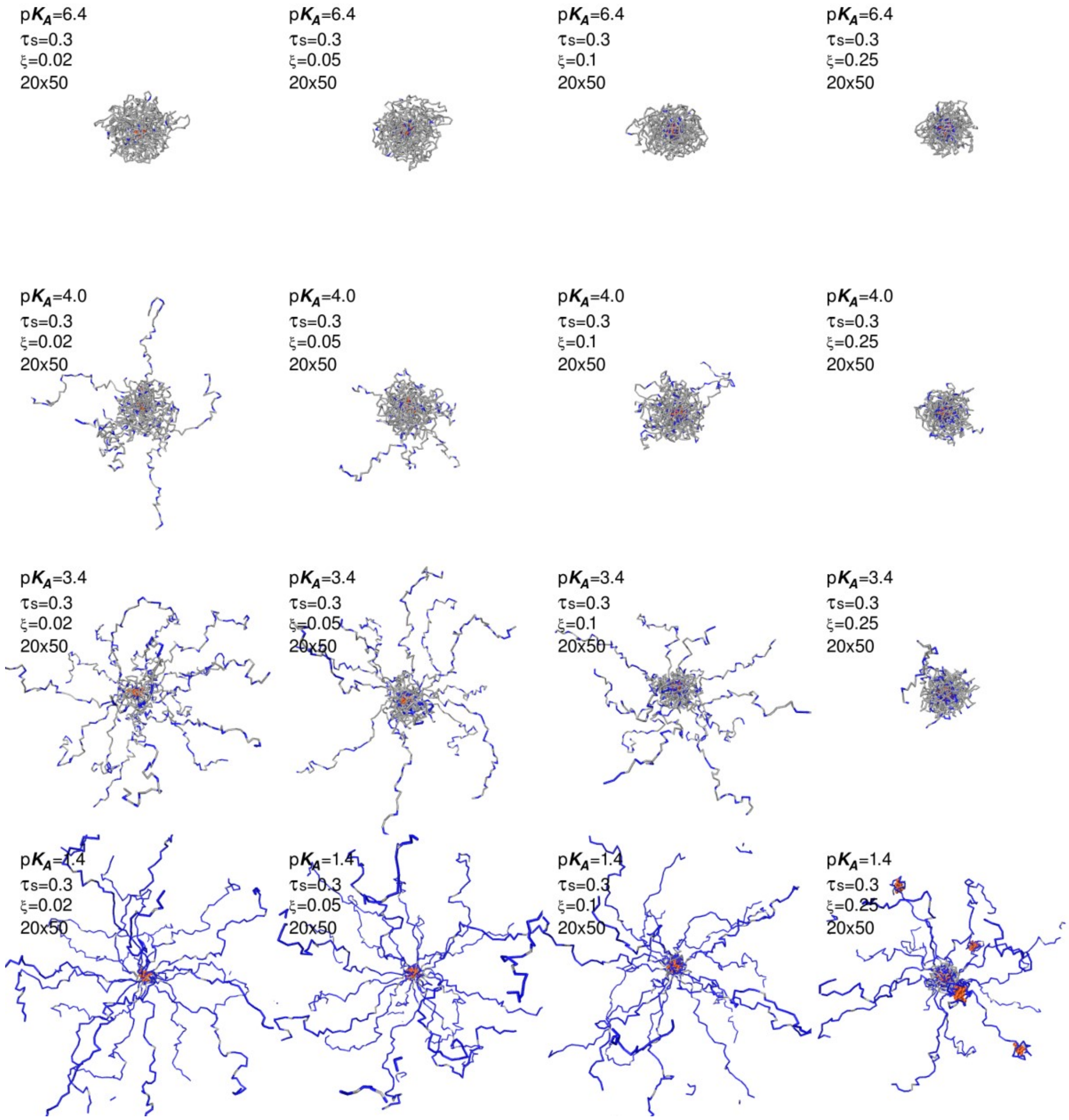

FIG. S4.4.3: Simulation snapshots for 20x50 star with hydrophobic salt counterions, τ_s = 0.3. Increasing ξ from left to right; increasing ionization from top to bottom. Colour code: blue ionized segments, gray non-ionized segments, orange salt counterions.

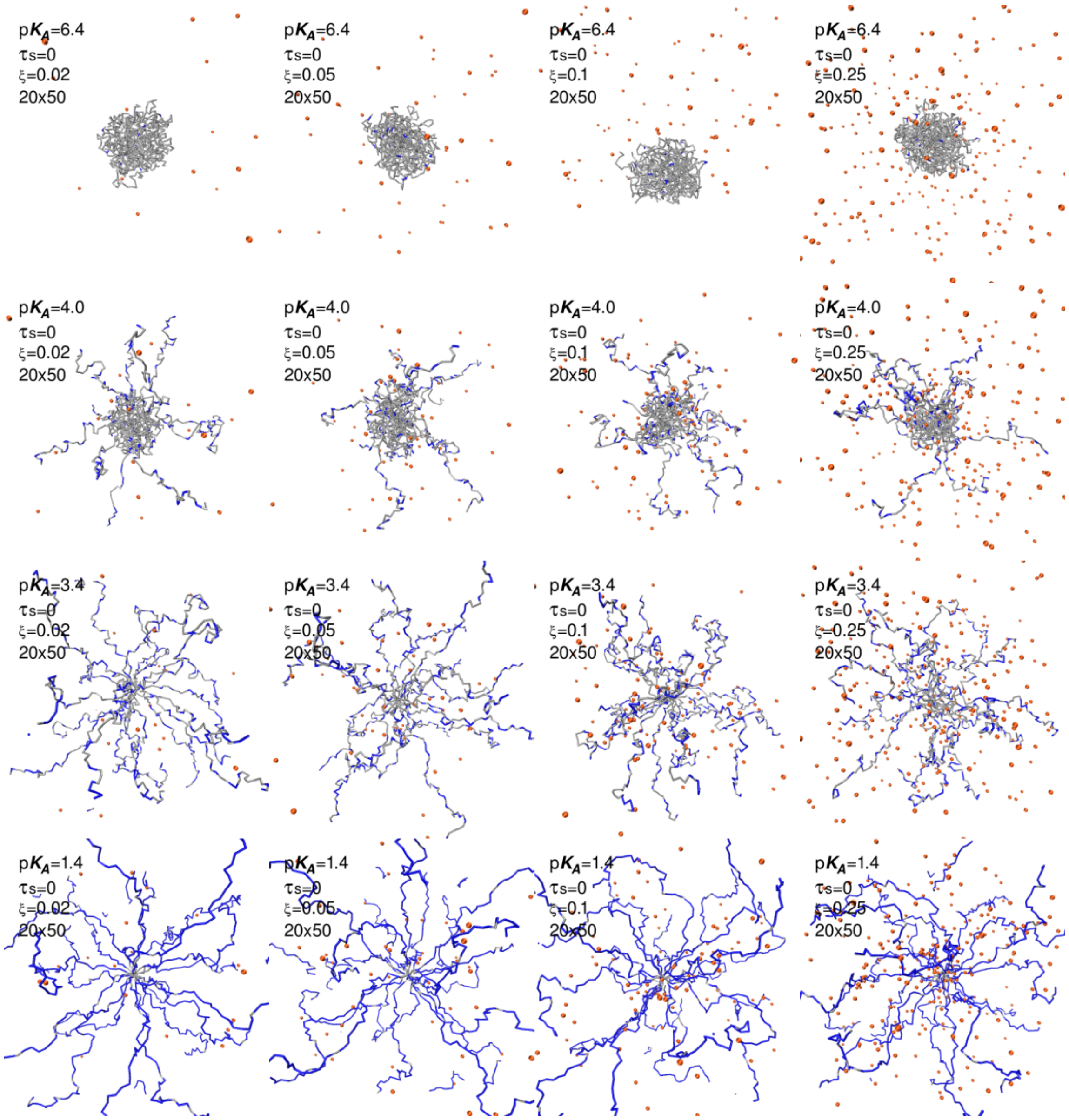

FIG. S4.4.4: Simulation snapshots for 20x50 star with hydrophilic salt counterions, τs = 0. Increasing ξ from left to right; increasing ionization from top to bottom. Colour code: blue ionized segments, grey non-ionized segments, orange salt counterions.

B. Radial distribution functions for individual particle types for the 20x50 star architecture

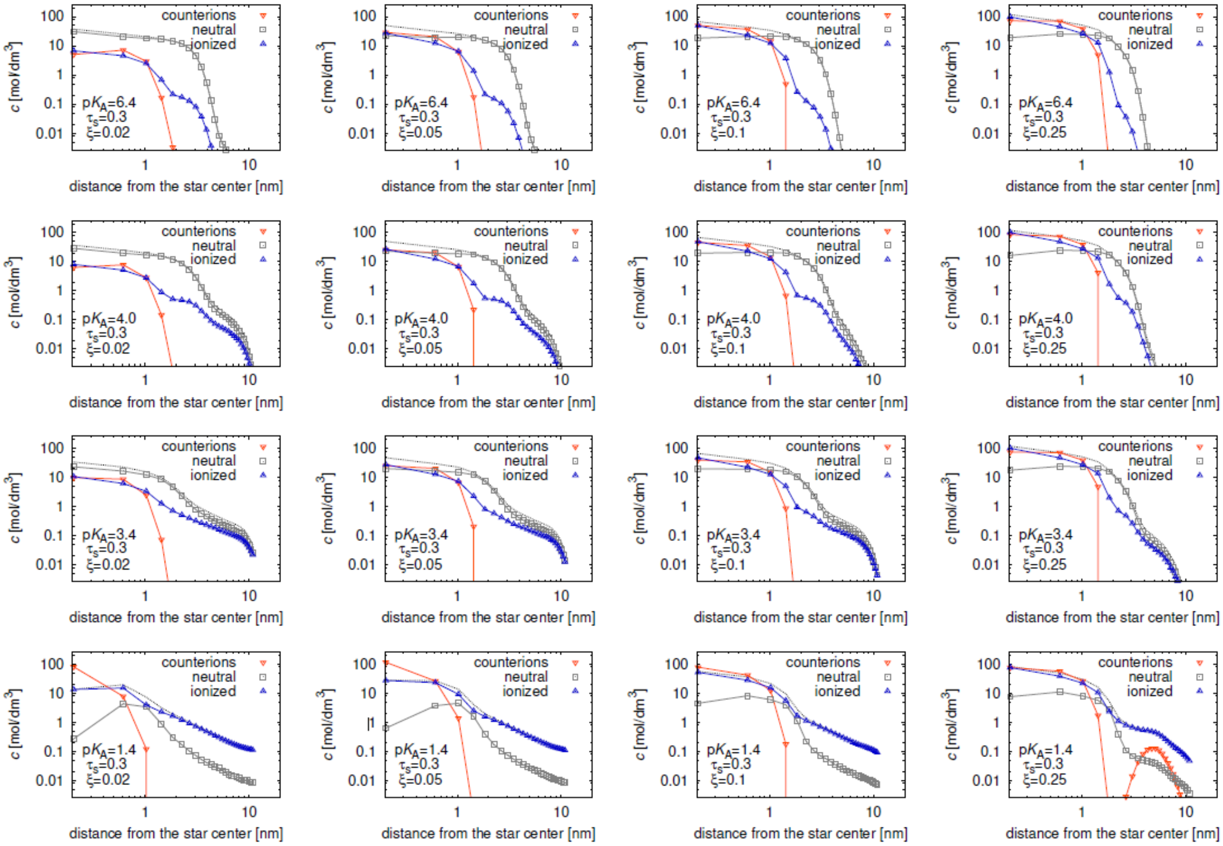

FIG. S4.4.5: Distributions of individual particle types for 20x50 star with hydrophobic salt counterions, τ_s = 0.3. Increasing ξ from left to right; increasing ionization from top to bottom. The colour code matches the simulation snapshots. The dashed line represents all star segments.

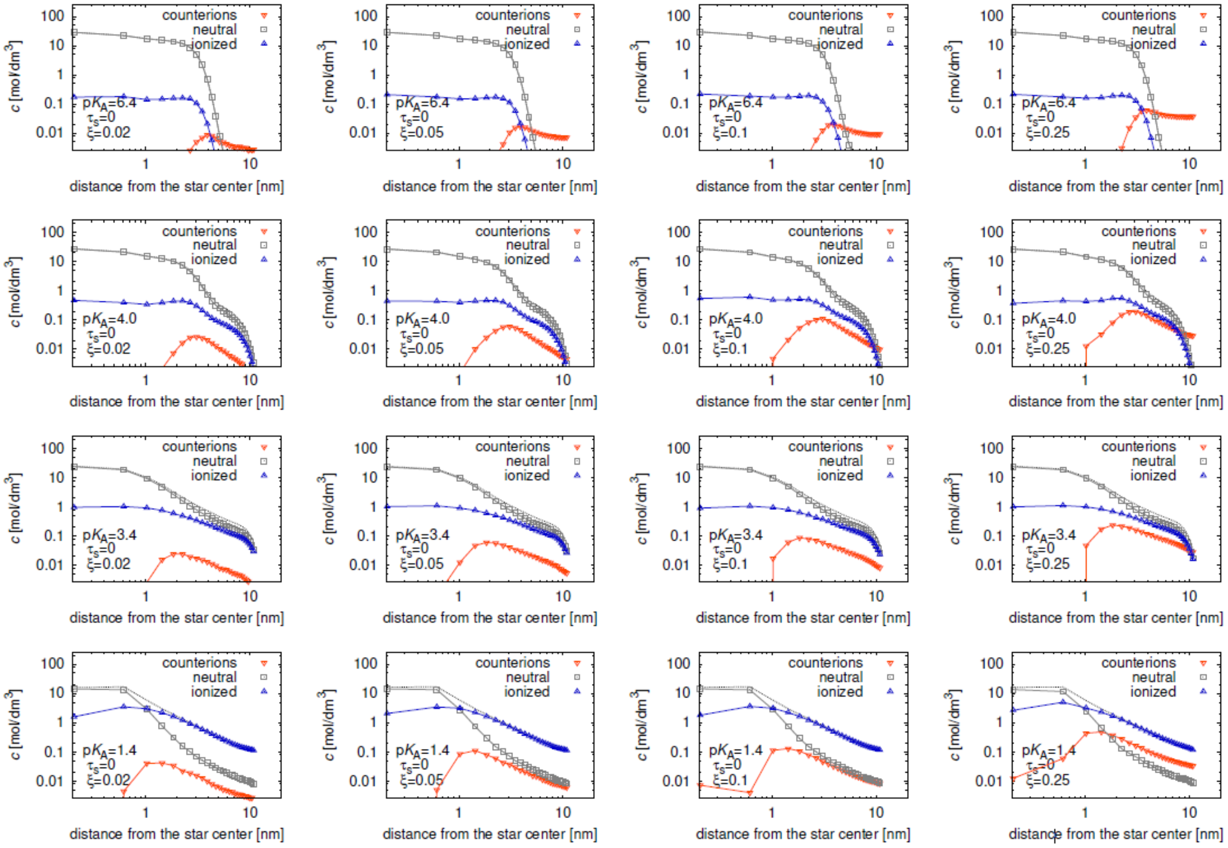

FIG. S4.4.6: Distributions of individual particle types for 20x50 star with hydrophilic salt counterions, τ_s = 0. Increasing τ from left to right; increasing ionization from top to bottom. The colour code matches the simulation snapshots. The dashed line represents all star segments.

C. End-to-end distance probabilities of individual star arms for 20x50 star architecture

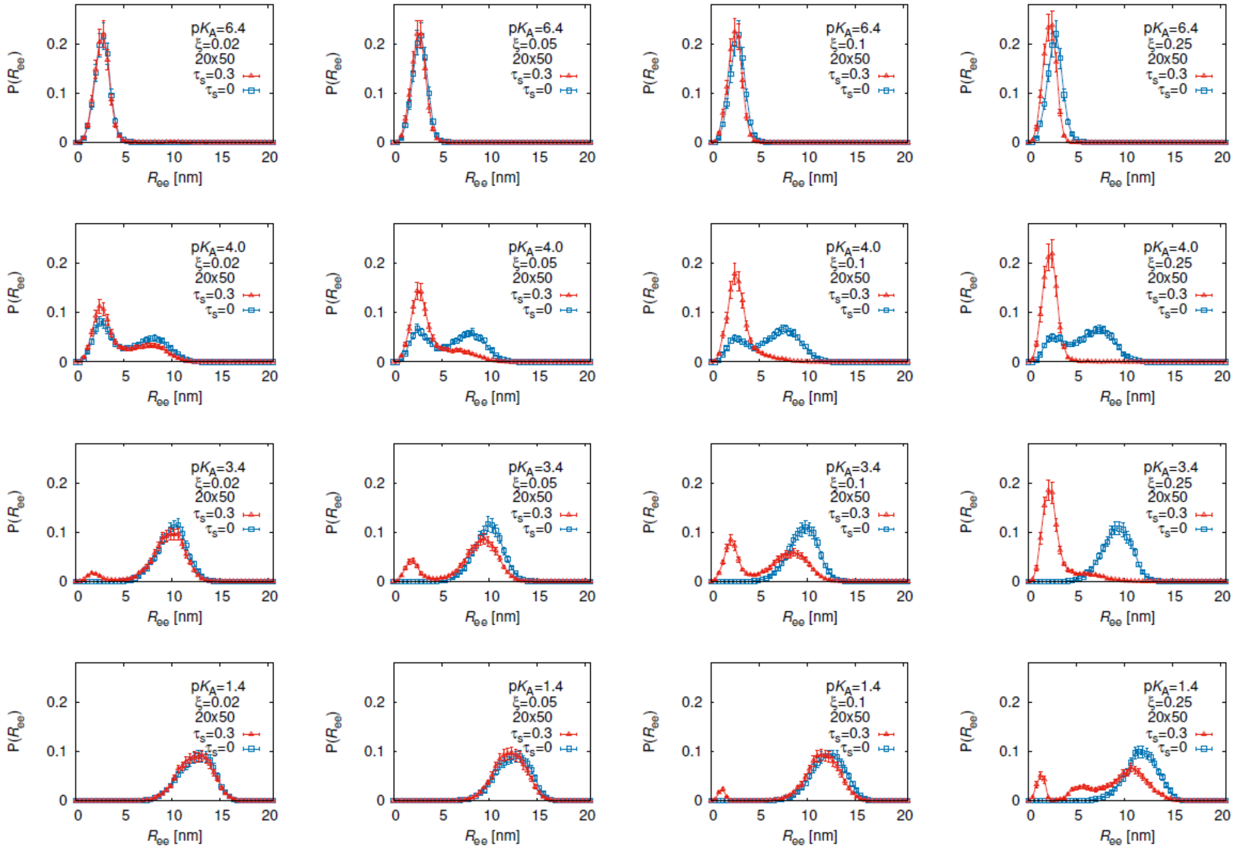

FIG. S4.4.7: End-to-end distance probabilities for 20x50 star. Increasing ξ from left to right; increasing ionization from top to bottom.

D. Conformational and ionization properties of 20x50 star architecture

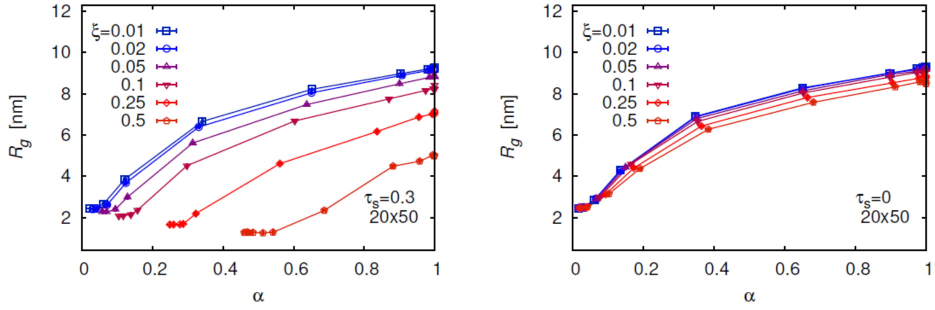

(a) $\tau_s = 0.3$ (b) $\tau_s = 0$

FIG. S4.4.8: Radius of gyration of the star, *Rg*, as a function of the degree of ionization of the star, α for various strengths of counterion hydrophobicity, τ_s.

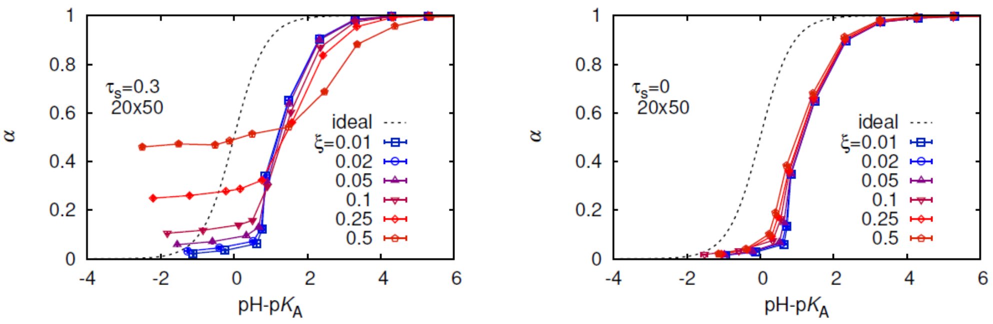

(a) $\tau_s = 0.3$

(b) $\tau_s = 0$

FIG. S4.4.9: Titration curves; degree of ionization, α as a function of pH-pKA for various strengths of counterion hydrophobicity, τ_s.

IV. SIMULATION RESULTS FOR THE 10X20 STAR ARCHITECTURE

A. Simulation snapshots for the 10x20 star architecture

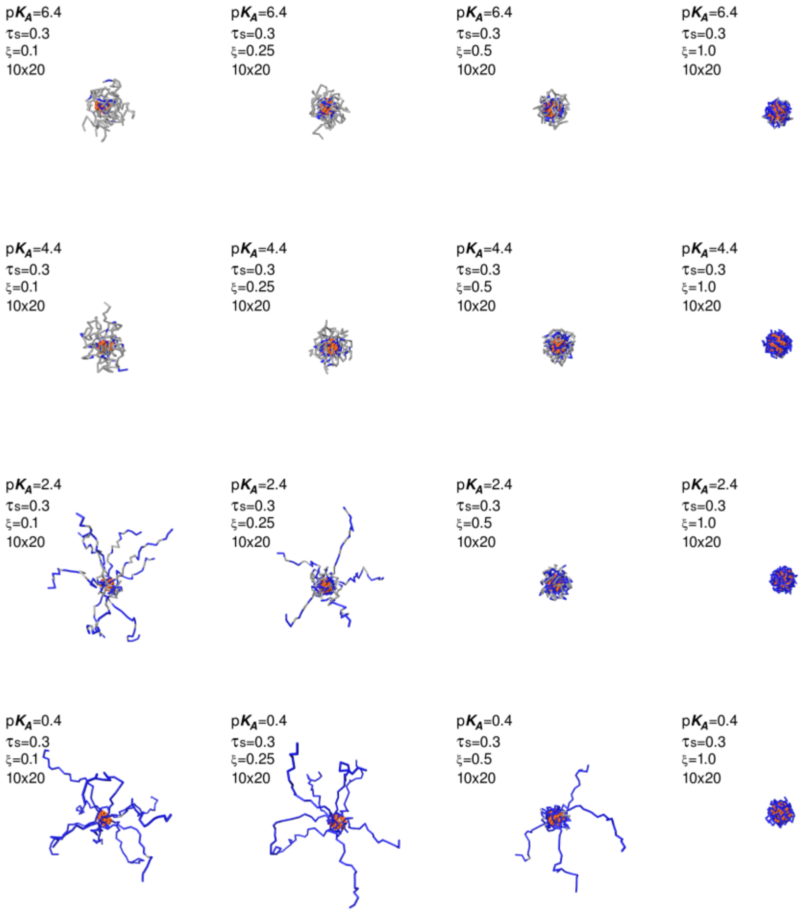

FIG. S4.4.10: Simulation snapshots for 10x20 star with hydrophobic salt counterions, $\tau_s = 0.3$. Increasing ξ from left to right; increasing ionization from top to bottom. Colour code: blue ionized segments, grey non-ionized segments, orange salt counterions.

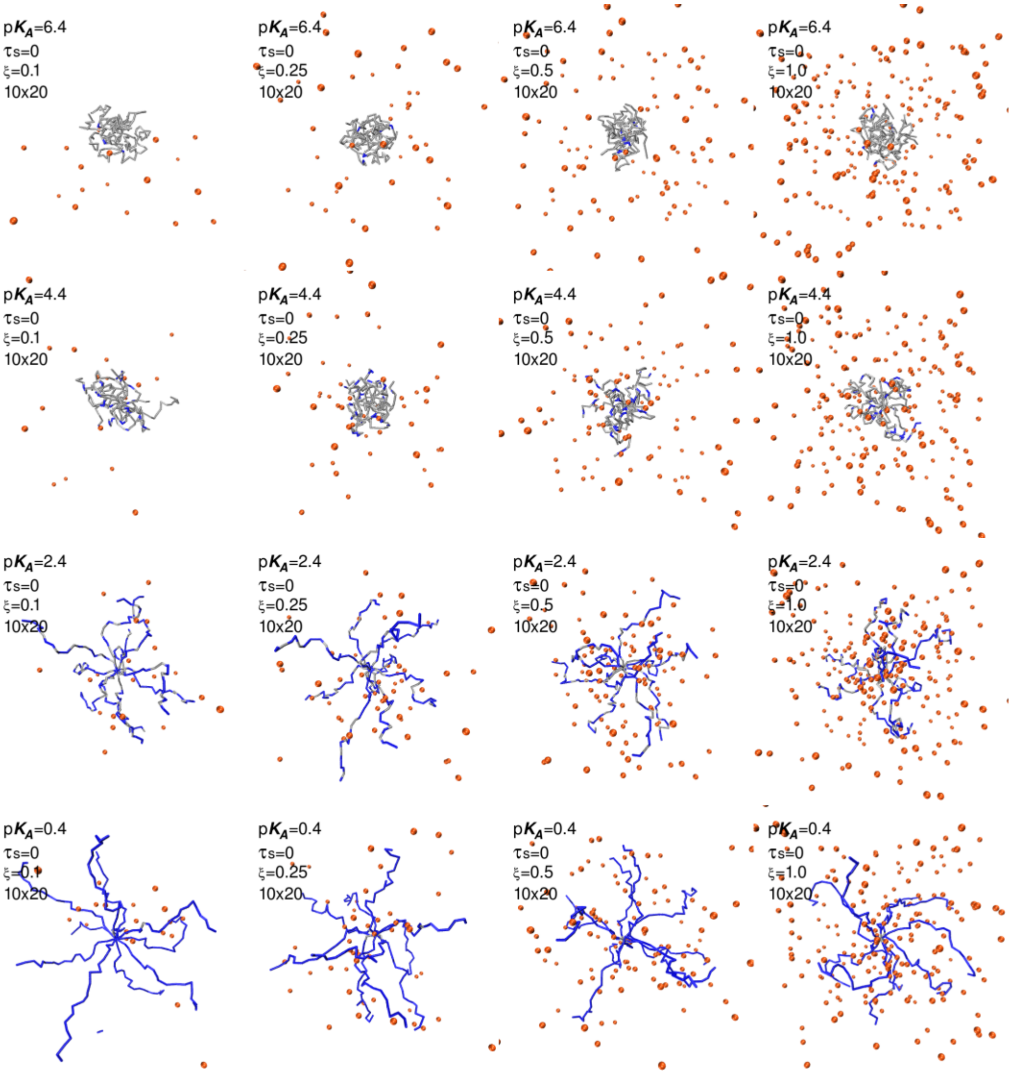

FIG. S4.4.11: Simulation snapshots for 10x20 star with hydrophilic salt counterions, τ_s = 0. Increasing ξ from left to right; increasing ionization from top to bottom. Colour code: blue ionized segments, grey non-ionized segments, orange salt counterions.

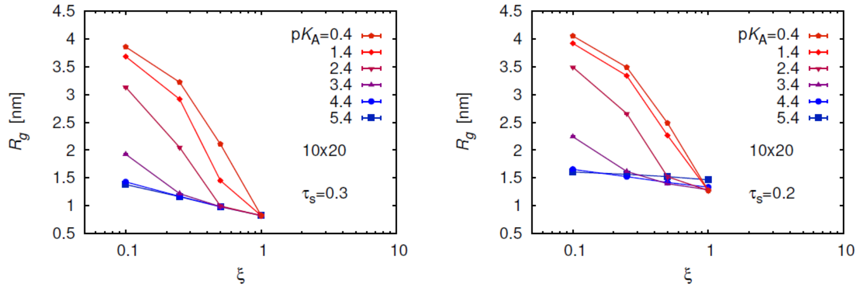

(a) $\tau_s = 0.3$ (b) $\tau_s = 0.2$

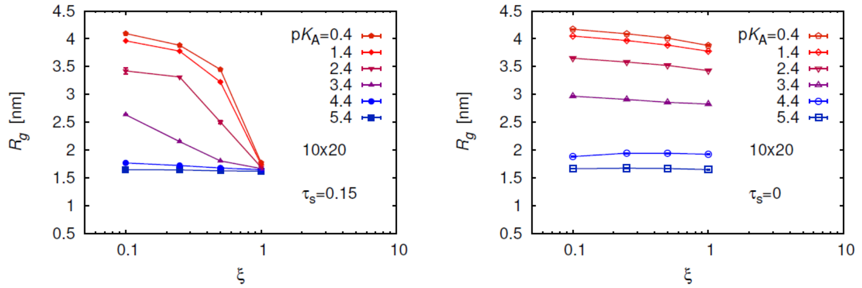

(c) $\tau_s = 0.15$ (d) $\tau_s = 0$

FIG. S4.4.12: Radius of gyration of the star, R_g, as a function of the charge ratio ξ for various ionization constants of the polymer, pK_A, and various strengths of counterion hydrophobicity, τ_s.

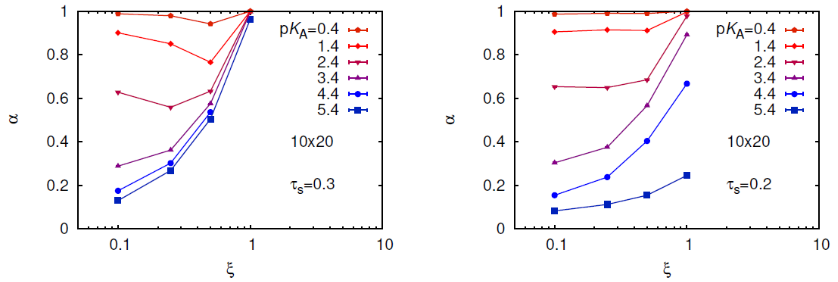

(a) $\tau_s = 0.3$ (b) $\tau_s = 0.2$

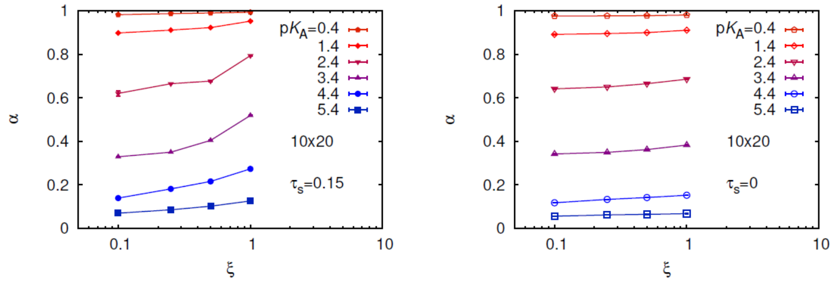

(c) $\tau_s = 0.15$ (d) $\tau_s = 0$

FIG. S4.4.13: Degree of ionization, α, as a function of the charge ratio ξ for various ionization constants of the polymer, pK_A, and various strengths of counterion hydrophobicity, τ_s.

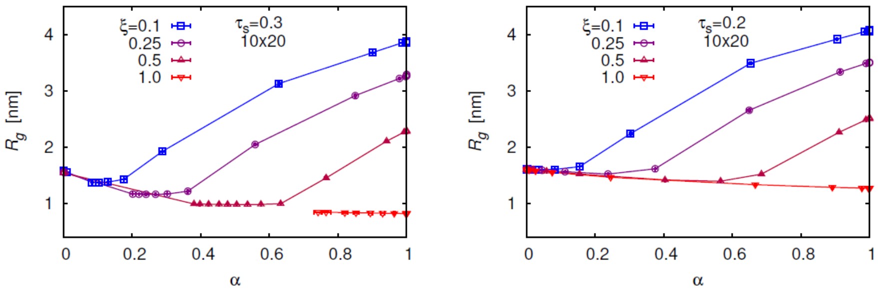

(a) $\tau_s = 0.3$ (b) $\tau_s = 0.2$

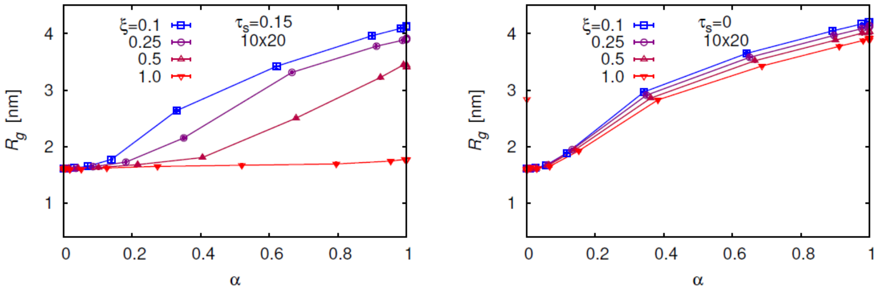

(c) $\tau_s = 0.15$ (d) $\tau_s = 0$

FIG. S4.4.14: Radius of gyration of the star, R_g, as a function of the degree of ionization of the star, for various strengths of counterion hydrophobicity, τ$_s$.

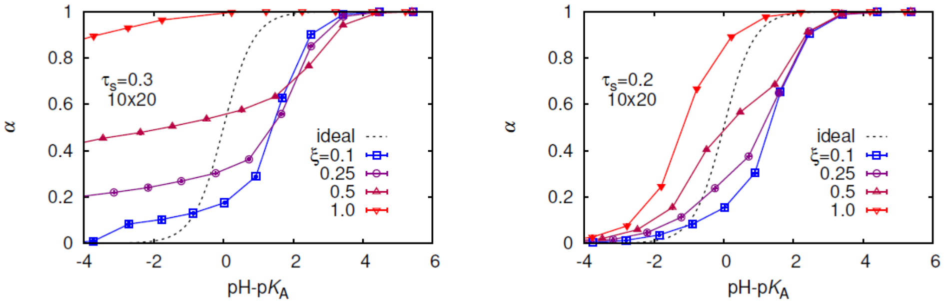

(a) $\tau_s = 0.3$ (b) $\tau_s = 0.2$

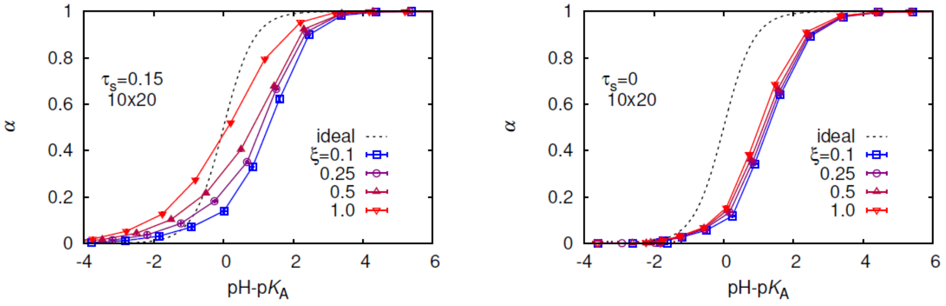

(c) $\tau_s = 0.15$ (d) $\tau_s = 0$

FIG. S4.4.15: Titration curves; degree of ionization, as a function of pH-pK$_A$ for various strengths of counterion hydrophobicity, τ$_s$.

References

[1] A.T. Press, A. Ramoji, M.vd Lühe, A.C. Rinkenauer, J. Hoff, M. Butans, C. Rössel, C. Pietsch, U. Neugebauer, F.H. Schacher, M. Bauer, Cargo–carrier interactions significantly contribute to micellar conformation and biodistribution, NPG Asia Mater. 9 (10) (2017) e444.

[2] A.V.. Dobrynin, M. Rubinstein, S.P. Obukhov, Cascade of transitions of polyelectrolytes in poor solvents, Macromolecules 29 (8) (1996) 2974–2979.

[3] H.J. Limbach, C. Holm, Conformational properties of poor solvent polyelectrolytes, Comp. Phys. Comm. 147 (2002) 321–324.

[4] H.J. Limbach, C. Holm, K. Kremer, Structure of polyelectrolytes in poor solvent, Europhys. Lett. 60 (4) (2002) 566–572.

[5] P. Košovan, Z. Limpouchová, K. Procházka, Charge distribution and conformations of weak polyelectrolyte chains in poor solvents, Coll. Czech. Chem. Commun. 73 (4) (2008) 439–458.

[6] A. Kiriy, G. Gorodyska, Sergiy Minko, W. Jaeger, P. Štepánek, M. Stamm, Cascade of coil-globule conformational transitions of single flexible polyelectrolyte molecules in poor solvent, J. Am. Chem. Soc. 124 (45) (2002) 13454–13462.

[7] F. Uhlík, P. Košovan, E.B. Zhulina, O.V. Borisov, Charge-controlled nanostructuring in partially collapsed star-shaped macromolecules, Soft Matter 12 (2016) 4846–4852.

[8] O.V. Rud, A.A. Mercurieva, F.A.M. Leermakers, T.M. Birshtein, Collapse of polyelectrolyte star. Theory and modeling, Macromolecules 45 (4) (2012) 2145–2160.

[9] J-M. Y. Carrillo, A.V. Dobrynin, Morphologies of planar polyelectrolyte brushes in a poor solvent: molecular dynamics simulations and scaling analysis, Langmuir 25 (22) (2009) 13158–13168.

[10] S.A. Barr, A.Z. Panagiotopoulos, Conformational transitions of weak polyacids grafted to nanoparticles, J. Chem. Phys. 137 (14) (2012) 144704.

[11] A.V. Dobrynin, M. Rubinstein, Theory of polyelectrolytes in solutions and at surfaces, Prog. Polym. Sci. 30 (11) (2005) 1049–1118.

[12] A.V. Dobrynin, Theory and simulartions of charged polymers: from solution properties to polymer nanomaterials, Curr. Opin. Colloid Interface Sci. 13 (2008) 376–388.

[13] O.V. Borisov, E.B. Zhulina, F.A.M. Leermakers, M. Ballauff, A.H.E. Müller, Conformations and solution properties of star-branched polyelectrolytes, in: A.H.E. Müller, Oleg Borisov (Eds.), Self Organized Nanostructures of Amphiphilic Block Copolymers I, Adv. Polym. Sci., vol. 241, Springer, Berlin, Heidelberg, 2011, pp. 1–55.

[14] Yu Mei, M. Hoffmann, M. Ballauff, A. Jusufi, Spherical polyelectrolyte brushes in the presence of multivalent counterions: the effect of fluctuations and correlations as determined by molecular dynamics simulations, Phys. Rev. E 77 (2008) 031805.

[15] A. Jusufi, O. Borisov, M. Ballauff, Structure formation in polyelectrolytes induced by multivalent ions, Polymer 54 (8) (2013) 2028–2035.

[16] M. Quesada-Pérez, J.A. Maroto-Centeno, A. Martín-Molina, Effect of the counterion valence on the behavior of thermo-sensitive gels and microgels: a monte carlo simulation study, Macromolecules 45 (21) (2012) 8872–8879.

[17] R. Schweins, K. Huber, Collapse of sodium polyacrylate chains in calcium salt solutions, Eur. Phys. J. E 5 (1) (2001) 117–126.

[18] R.J. Nap, S.H. Park, I. Szleifer, Competitive calcium ion binding to end-tethered weak polyelectrolytes, Soft Matter (2018).

[19] F. Carnal, S. Ulrich, S. Stoll, Influence of explicit ions on titration curves and conformations of flexible polyelectrolytes: a Monte Carlo study, Macromolecules 43 (5) (2010) 2544–2553.

[20] A. Hanisch, A.H. Gröschel, M. Förtsch, M. Drechsler, H. Jinnai, T.M. Ruhland, F.H. Schacher, A.H.E. Müller, Counterion-mediated hierarchical self-assembly of an abc miktoarm star terpolymer, ACS Nano 7 (5) (2013) 4030–4041.

[21] D.J. Pochan, Z. Chen, H. Cui, K. Hales, K. Qi, K.L. Wooley, Toroidal triblock copolymer assemblies, Science 306 (5693) (2004) 94–97.

[22] Z. Chen, H. Cui, K. Hales, Z. Li, K. Qi, D.J. Pochan, K.L. Wooley, Unique toroidal morphology from composition and sequence control of triblock copolymers, J. Am. Chem. Soc. 127 (24) (2005) 8592–8593.

[23] H. Cui, Z. Chen, K.L. Wooley, D.J. Pochan, Controlling micellar structure of amphiphilic charged triblock copolymers in dilute solution via coassembly with organic counterions of different spacer lengths, Macromolecules 39 (19) (2006) 6599–6607.

[24] H. Cui, Z. Chen, S. Zhong, K.L. Wooley, D.J. Pochan, Block copolymer assembly via kinetic control, Science 317 (5838) (2007) 647–650.

[25] H. Cui, Z. Chen, K.L. Wooley, D.J. Pochan, Origins of toroidal micelle formation through charged triblock copolymer self-assembly, Soft Matter 5 (2009) 1269–1278.

[26] W.K. Kim, A. Moncho-Jordá, R. Roa, M. Kanduc, J. Dzubiella, Cosolute partitioning in polymer networks: effects of flexibility and volume transitions, Macromolecules 50 (16) (2017) 6227–6237.

[27] Q-H. Hao, G. Xia, B. Miao, H-G. Tan, X-H. Niu, L-Y. Liu, Morphological response of a spherical polyelectrolyte brush to solvent quality and electrostatic interaction strength, Macromolecules (2018).

[28] P. Košovan, J. Kuldová, Z. Limpouchová, K. Procházka, E.B. Zhulina, O.V. Borisov, Molecular dynamics simulations of a polyelectrolyte star in poor solvent, Soft Matter 6 (2010) 1872–1874.

[29] G. Bai, M. Nichifor, M. Bastos, Cationic polyelectrolytes as drug delivery vectors: calorimetric and fluorescence study of rutin partitioning, J. Phys. Chem. B 114 (49) (2010) 16236–16243.

[30] P. Mukerjee, The nature of the association equilibria and hydrophobic bonding in aqueous solutions of association colloids, Adv. Colloid Interface Sci. 1 (3) (1967) 242–275.

[31] O. Ikkala, G.t. Brinke, Hierarchical self-assembly in polymeric complexes: towards functional materials, Chem. Commun. 19 (2004) 2131.

[32] M. Uchman, M. Šteˇpánek, S. Prévost, B. Angelov, J. Bednár, M-S. Appavou, M. Gradzielski, K. Procházka, Coassembly of poly(ethylene oxide)-block-poly (methacrylic acid) and n-dodecylpyridinium chloride in aqueous solutions leading to ordered micellar assemblies within copolymer aggregates, Macromolecules 45 (16) (2012) 6471–6480.

[33] S. Pispas, Soluble complexes of sodium poly(isoprene-b-methacrylate) micelles with cationic surfactants in aqueous media, J. Phys. Chem. B 110 (6) (2006) 2649–2655.

[34] J.M. Borreguero, P.A. Pincus, B.G. Sumpter, M Goswami, Unraveling the agglomeration mechanism in charged block copolymer and surfactant complexes, Macromolecules 50 (3) (2017) 1193–1205.

[35] C. Wang, K.C. Tam, New insights on the interaction mechanism within oppositely charged polymer/surfactant systems, Langmuir 18 (17) (2002) 6484–6490.

[36] E. Guzmán, S. Llamas, A. Maestro, L. Fernández-Peña, A. Akanno, R. Miller, F. Ortega, R.G. Rubio, Polymer–surfactant systems in bulk and at fluid interfaces, Adv. Colloid Interface Sci. 233 (2016) 38–64.

[37] A.K. Saxena, N.S. Hosmane, Recent advances in the chemistry of carborane metal complexes incorporating d- and f-block elements, Chem. Rev. 93 (3) (1993) 1081–1124.

[38] J. Plesek, Potential applications of the boron cluster compounds, Chem. Rev. 92 (2) (1992) 269–278.

[39] R.N Grimes, Metallacarboranes in the new millennium, Coord. Chem. Rev. 200–202 (2000) 773–811.

[40] I.B. Sivaev, V.I. Bregadze, Chemistry of cobalt bis(dicarbollides). A review, Collect. Czechoslovak Chem. Commun. 64 (1999) 783–805.

[41] M. Frederick Hawthorne, D.C. Young, P.A. Wegner, Carbametallic boron hydride derivatives. I. Apparent analogs of ferrocene and ferricinium ion, J. Am. Chem. Soc. 87 (8) (1965) 1818–1819.

[42] M. Uchman, A.I. Abrikosov, M. Lepšík, M. Lund, P. Matejícek, Nonclassical hydrophobic effect in micellization: molecular arrangement of nonamphiphilic structures, Adv. Theor. Simul. 1 (1) (2017) 1700002.

[43] R. Fernandez-Alvarez, V. Dordovic, M. Uchman, P. Matejícek, Amphiphiles without head-and-tail design: nanostructures based on the self-assembly of anionic boron cluster compounds, Langmuir 34 (12) (2018) 3541–3554.

[44] K.I. Assaf, W.M. Nau, The chaotropic effect as an assembly motif in chemistry, Angew. Chem. Int. Ed. 57 (43) (2018) 13968–13981.

[45] P. Cígler, M. Kožíšek, P.Řězáčová, J. Brynda, Z. Otwinowski, J. Pokorná, J. Plešek, B. Grüner, L. Dolečková-Marešová, M. Máša, J. Sedláček, J. Bodem, Hans-Georg K., V. Král, J. Konvalinka, From nonpeptide toward noncarbon protease inhibitors: metallacarboranes as specific and potent inhibitors of hiv protease, Proc. Nat. Acad. Sci. 102 (43) (2005) 15394–15399.

[46] J. Brynda, P. Mader, V. Šícha, M. Fábry, K. Poncová, M. Bakardiev, B. Grüner, P. Cígler, P. Rezácová, Carborane-based carbonic anhydrase inhibitors, Angew. Chem. Int. Ed. 52 (51) (2013) 13760–13763.

[47] E. Makrlík, P. Vanura, Applications of the dicarbollylcobaltate(iii) anion in the water/nitrobenzene extraction system, Talanta 32 (5) (1985) 423–429.

[48] B. Gruner, J. Rais, P. Selucky, M. Lucanikova, Recent progress in extraction agents based on cobalt bis(dicarbollides) for partitioning of radionuclides from high-level nuclear waste, in: N.S. Hosmane (Ed.), Boron Science: New Technologies and Applications, CRC Press, New York, 2012, pp. 463–490.

[49] J. Fanfrlík, M. Lepšík, D. Horinek, Z. Havlas, P. Hobza, Interaction of carboranes with biomolecules: formation of dihydrogen bonds, ChemPhysChem 7 (5) (2006) 1100–1105.

[50] J.G. Planas, C. Viñas, F. Teixidor, A. Comas-Vives, G. Ujaque, A. Lledós, M.E. Light, M.B. Hursthouse, Self-assembly of mercaptane-metallacarborane complexes by an unconventional cooperative effect: AC–H···S–H···H–B hydrogen/dihydrogen bond interaction, J. Am. Chem. Soc. 127 (45) (2005) 15976–15982.

[51] P. Matějíček, J. Zedník, K. Ušelová, J. Pleštil, J. Fanfrlík, A. Nykänen, J. Ruokolainen, P. Hobza, K. Procházka, Stimuli-responsive nanoparticles based on interaction of metallacarborane with poly(ethylene oxide), Macromolecules 42 (13) (2009) 4829–4837.

[52] J. Brus, A. Zhigunov, J. Czernek, L. Kobera, M. Uchman, P. Matějíček, Control over the self-assembly and dynamics of metallacarborane nanorotors by the nature of the polymer matrix: a solid-state NMR study, Macromolecules 47 (18) (2014) 6343–6354.

[53] P. Matějíček, J. Brus, A. Jigounov, J. Pleštil, M. Uchman, K. Procházka, M. Gradzielski, On the structure of polymeric composite of metallacarborane with poly(ethylene oxide), Macromolecules 44 (10) (2011) 3847–3855.

[54] R.N. Grimes, Carboranes in the chemist’s toolbox, Dalton Trans. 44 (2015) 5939–5956.

[55] J. Plešek, K. Baše, F. Mareš, F. Hanousek, B. Štíbr, S. Hermánek, Potential uses of metallocarborane sandwich anions for analysis, characterization and isolation of various cations and organic bases, Collect. Czechoslovak Chem. Commun. 49 (1984) 2776–2789.

[56] J. Dubochet, M. Adrian, J-J. Chang, J-C. Homo, J. Lepault, A.W. McDowall, P. Schultz, Cryo-electron microscopy of vitrified specimens, Q. Rev. Biophys. 21 (2) (1988) 129–228.

[57] L. Nová, F. Uhlík, P. Košovan, Local pH and effective pKA of weak polyelectrolytes – insights from computer simulations, Phys. Chem. Chem. Phys. 19 (2017) 14376–14387.

[58] W.R. Smith, B. Trˇíska, The reaction ensemble method for the computer simulation of chemical and phase equilibria. I. Theory and basic examples, J. Chem. Phys. 100 (4) (1994) 3019–3027.

[59] J. Landsgesell, L. Nová, O.V. Rud, F. Uhlík, D. Sean, P. Hebbeker, C. Holm, P. Košovan, Simulations of ionization equilibria in weak polyelectrolyte solutions and gels, Soft Matter 15 (2019) 1155–1185.

[60] J. Pleštil, J. Krízˇ, Z. Tuzar, K. Procházka, Y.B. Melnichenko, G.D. Wignall, M.R. Talingting, P. Munk, S.E. Webber, Small-angle neutron scattering study of onion-type micelles, Macromol. Chem. Phys. 202 (4) (2001) 553–563.

[61] T.J. Martin, K. Procházka, P. Munk, S.E. Webber, ph-dependent micellization of poly(2-vinylpyridine)-block-poly(ethylene oxide), Macromolecules 29 (18) (1996) 6071–6073.

[62] K. Procházka, T.J. Martin, P. Munk, S.E. Webber, Polyelectrolyte poly(tert-butyl acrylate)-block-poly(2-vinylpyridine) micelles in aqueous media, Macromolecules 29 (20) (1996) 6518–6525.

[63] E.B. Zhulina, O.V. Borisov, Theory of block polymer micelles: recent advances and current challenges, Macromolecules 45 (11) (2012) 4429–4440.

[64] P. Matějíček, K. Podhájecká, J. Humpolíčková, F. Uhlík, K. Jelínek, Z. Limpouchová, K. Procházka, M. Špírková, Polyelectrolyte behavior of polystyrene-block-poly(methacrylic acid) micelles in aqueous solutions at low ionic strength, Macromolecules 37 (26) (2004) 10141–10154.

[65] V.Dord'ovič, M. Uchman, M. Reza, J. Ruokolainen, A. Zhigunov, O.I. Ivankov, P. Matejícek, Cation-sensitive compartmentalization in metallacarborane containing polymer nanoparticles, RSC Adv. 6 (2016) 9884–9892.

[66] V. Dord'ovič, B. Verbraeken, R. Hogenboom, S. Kereïche, P. Matejícek, M. Uchman, Tuning of thermoresponsivity of a poly(2-alkyl-2-oxazoline) block copolymer by interaction with surface-active and chaotropic metallacarborane anion, Chem. Asian J. 13 (7) (2018) 838–845.

[67] F. Uhlík, P. Košovan, Z. Limpouchová, K. Procházka, O.V. Borisov, F.A.M. Leermakers, Modeling of ionization and conformations of starlike weak polyelectrolytes, Macromolecules 47 (12) (2014) 4004–4016.

[68] F.A. Plamper, H. Becker, M. Lanzendorfer, M. Patel, A. Wittemann, M. Ballauff, A.H.E. Müller, Synthesis, characterization and behavior in aqueous solution of star-shaped poly(acrylic acid), Macromol. Chem. Phys. 206 (18) (2005) 1813–1825.

[69] P. Matějíček, M. Uchman, J. Lokajová, M. Šteˇpánek, M. Špírková, K. Procházka, Multilayer polymeric nanoparticles based on specific interactions in solution: polystyrene-block-poly(methacrylic acid) micelles with linear poly(2-vinylpyridine) in aqueous buffers, Mater. Manuf. Processes 23 (6) (2008) 557–560.

[70] J.D. Willott, T.J. Murdoch, F.A.M. Leermakers, W.M. de Vos, Behavior of weak polyelectrolyte brushes in mixed salt solutions, Macromolecules 51 (3) (2018) 1198–1206.

[71] R. Kou, J. Zhang, Z. Chen, G. Liu, Counterion specificity of polyelectrolyte brushes: role of specific ion-pairing interactions, ChemPhysChem 19 (11) 0(2018) 1404–1413.

References for Supporting Information

[1] Filip Uhlik, Peter Košovan, Zuzana Limpouchová, Karel Procházka, Oleg V. Borisov, and Frans A. M. Leermakers. Modeling of ionization and conformations of starlike weak polyelectrolytes. Macromolecules, 47(12), 4004-4016, 2014.

[2] Filip Uhlík, Peter Košovan, Ekaterina B. Zhulina, and Oleg V. Borisov. Charge-controlled nano-structuring in partially collapsed star-shaped macromolecules. Soft Matter, 12, 4846-4852, 2016.

[3] W. R. Smith and B. Trska. The reaction ensemble method for the computer simulation of chemical and phase equilibria. I. Theory and basic examples. Journal of Chemical Physics, 100(4), 3019-3027, 1994.

[4] Ulli Wolff. Monte Carlo errors with less errors. Computer Physics Communications, 156(2), 143-153, 2004.

5-Summary and general conclusions

The results of the four papers presented deal with nanostructures made entirely or partially of boron clusters. Publication I and II deal with the fundamental principles involved in the self-assembly of COSAN anions into the simplest of nanostructures, micelles. Publication IV deals with the direct incorporation of *orto*-carborane into the polymer chain of a triblock terpolymer and the effect it has on the polymer self-assembly. At last, in Publication III the unique characteristics of COSAN (hydrophobicity, delocalized charge, interaction with polymers) where exploited to reveal how it interacts with polyelectrolytes in diblock copolymer micelles.

Publication I gathered all the information about COSAN micellization and attempted to unify several diverging theories. First, it attempted to clear the ambiguous description of COSAN as an amphiphile. Hydrotropes, surfactants, amphiphiles and pickering stabilizers were defined in order to contextualize the different terms and relate them to COSAN. Due to similarities to classic surfactants such as sodium dodecyl sulfate (SDS) COSAN was determined to have an inherently amphiphilic structure that determines its surfactant behavior, despite lacking the classic head-and-tail structure. The small ΔS_{mic} of COSAN was explained through three main theories: non-classical hydrophobic effect, chaotropic effect and size-dependant hydration.

Publication II undertook a deeper study into the thermodynamic causes of micellization. The new analysis of ITC curves was used based on the mass action model. This newer model provided refined data compared to that of the first publication. In short, the model allowed the direct determination of aggregation number (*n*) and counterion binding (β) by using them as fitting parameters of the experimental data. In the previous model *n* and β were obtained from SAXS and conductivity measurements respectively. The concentration of COSAN for SAXS experiments was many times that of the CMC. This forced the assumption, onto the previous model, that aggregation number is constant across a very broad range of concentrations. Results confirmed the strong ΔH dependence of micellization. Furthermore, it determined that micellization parameters are barely affected by the choice of counterion (H^+, Li^+, Na^+ or K^+). Additionally, micellization was studied by ITC in the presence of acetonitrile as cosolvent. With the help of simulations, it was determined that acetonitrile prefers interactions with the B-H bonds in COSAN and therefore is accumulated around COSAN rather than evenly distributed in solution. This together with NMR data, helped formulate the theory that individual COSAN molecules prefer their C-H bonds to be facing inwards when micellization occurs.

Publication III the self-assembly of a carborane-containing triblock terpolymer was compared to a diblock copolymer lacking the carborane block. This represents the first synthesis of a triblock terpolymer with carboranes. The carborane block allowed the polymer to adopt different conformation (worms or sphere) depending on the process of preparation. The resulting micelles formed a multi stimuli responsive system.

The middle block made of polyhydroxystyrene responded to pH allowing the activation/deactivation of fluorescence by protonation or deprotonation of the -OH group. This process was reversible. The carborane block responded to fluorine ions (F^-) by undergoing a deboronation process. This process was not reversible.

Lastly, Publication IV entails a very detailed work describing the precipitation of PS-P2VP micelles upon addition of COSAN. The micelles had a PS core and a charged P2VP corona. After addition of COSAN at an amount equal to 10% of the PVP segments the micelles precipitate. Precipitation occurs at the same level of COSAN regardless of the degree of charge in the P2VP chains (controlled by pH of the solution). The expected result was precipitation of the micelles when the charge ratio reached 1:1 of $COSAN^-$:$P2VP^+$. Coarse grained simulations were used to determine the molecular cause of the "early precipitation". In the simulations, COSAN ion was represented as a counterion with an increased degree of hydrophobicity. As hydrophobicity increases, the interactions of the counterions with the charged corona have a more unexpected result. COSAN ions cause the collapse of the charged P2VP chains eventually leading to micelle precipitation. Depending on the degree of charge in the polyelectrolyte different mechanisms of precipitation occur. The hydrophobicity of COSAN was determined as the main cause of such effect. Both experimental and simulations results with "innocent counterions" (Na^+) produced no effect on the micellar composition. The results obtained here can be used as guidelines for the loading of negatively charged Active Pharmaceutical Ingredients into polymeric vectors.

Overall, boron clusters can be divided in two different groups. The large clusters such as COSAN, $B_{21}H_{18}^{2-}$ or $B_{12}H_{12}^{2-}$ are capable of forming nanostructures on their own through self-assembly or simply by mixing with polymers. Their combination of hydrophobicity (relative) and charge gives them unique traits that allow them to interact with different polymers (charged/uncharged, hydrophobic/hydrophilic). The nature of the effect they have on the polymer chain has only begun to be explored (as in Publication IV) and much research is still needed. Meanwhile, other smaller clusters such as carboranes have a more favorable chemistry toolset that facilitates their incorporation into monomers and polymers and can, in this way, form boron nanostructures. This thesis shows some of the effects the addition of boron clusters can have in the polymers. Nonetheless, a deeper study is still necessary to discern in which situations it might be convenient to include them into the polymer chain.
